Analytical Modelling of Formation Damage in One-phase and Two-phase Flows: Applications for Laboratory Experiments

Shuyan Yang, B.Eng. (Hons)

A thesis submitted for the degree of Doctor of Philosophy (Ph.D.)

Australian School of Petroleum and Energy Resources
Faculty of Engineering, Computer & Mathematical Sciences
The University of Adelaide

THE UNIVERSITY of ADELAIDE

November 2021

To

my mother, Xiuli, & my brother, Justen,

who believe in me and have supported me unconditionally

Table of Contents

Abstract

I hereby present a Ph.D. thesis by publication. This thesis includes six journal publications, four of which have been published and two have been submitted for publication.

This thesis is focussed on the application of analytical modelling in laboratory experiments of formation damage in one-phase and two-phase flows in porous media. It targets formation damage with chemical reactions, fines migration, as well as one-dimensional (1D) and two-dimensional (2D) two-phase flows accounting for capillary end effects.

The thesis develops a novel system of fundamental equations for reactive flows with large deposition of solid reaction products. A new class of exact analytical solutions has been derived for reactive flows with any arbitrary stoichiometric coefficients. The analytical solution yields breakthrough concentration and pressure drop type curves, significantly facilitating the interpretation of the laboratory data. The developed system of governing equations has been validated by laboratory modelling and can be used for the prediction of mineral precipitation chemical reactive flows in porous media.

In addition, the three-point pressure method for large scale deposits has been investigated for the first time and the results show that the inclusion of outlet concentration data significantly decreases parameter uncertainty. The large parameter uncertainties without using outlet concentration arise due to the inability for the model to distinguish between a set of deposit profiles.

Laboratory studies applying the three-point pressure method have also been conducted for fines migration in porous media to predict formation damage in a hydraulically

fractured well. The results show that while pressure measurements alone can predict formation damage due to fracture fluid leak-off, breakthrough fines concentration is able to fully predict model functions and coefficients to characterise the system.

The two-phase flow in porous media investigated in this thesis comprises steady-state and transient 1D flow with capillary end effects, and steady-state 2D flow with capillary end effects near a hydraulically fractured production well.

Steady-state analytical solutions, along with transient numerical solutions, have been applied in the so-called steady-state-transient test (SSTT). It includes a three-dimensional (3D) modelling of the SSTT with the treatment of the simulated data by a 1D inverse solver. The main result shows a significant reduction in the 3D flow effects when using an inlet distributor with spiral (or concentric-circle) grooves rather than one with half-moon grooves.

Following this result, two SSTTs were carried out in the laboratory. In the concentric-circle SSTT, a weighting method for water cut measurements at the effluent was used, while in the half-moon SSTT, a visualisation method was used. Based on the results, the use of a concentric-circle distributor and the weighting method in SSTTs is recommended.

Lastly, the exact solution to the steady-state 2D flow towards a fractured well was derived and applied to predict formation damage due to capillary-trapped water, known as water blocking. The results show water blocking is likely to be a significant factor in the productivity decline for the case study conducted.

Declaration

I certify that this work contains no material which has been accepted for the award of any other degree or diploma in my name, in any university or other tertiary institution and, to the best of my knowledge and belief, contains no material previously published or written by another person, except where due reference has been made in the text. In addition, I certify that no part of this work will, in the future, be used in a submission in my name, for any other degree or diploma in any university or other tertiary institution without the prior approval of the University of Adelaide and where applicable, any partner institution responsible for the joint-award of this degree.

I acknowledge that copyright of published works contained within this thesis resides with the copyright holder(s) of those works.

I also give permission for the digital version of my thesis to be made available on the web, via the University's digital research repository, the Library Search and also through web search engines, unless permission has been granted by the University to restrict access for a period of time.

I acknowledge the support I have received for my research through the provision of an Australian Government Research Training Program Scholarship.

Shuyan Yang 30/11/2021

Acknowledgements

First and foremost, I would like to express my sincere gratitude to my supervisor Prof. Pavel Bedrikovetsky for the continuous support, patience, and guidance he has provided throughout the years. I cannot imagine how I could have commenced, much less completed a Ph.D. without him.

I would like to wholeheartedly thank all those who have helped me along my Ph.D. journey. To my co-supervisor Dr. Abbas Zeinijahromi for providing guidance and support when I needed it. To the wonderful Dr. Sara Borazjani for helping me to grow as a researcher and for sharing stories, photos, and videos of her beautiful daughter Eva. To the amazing Dr. Alex Badalyan and Dr. Themis Carageorgos for all the interesting conversations we shared, both academically and personally. Last but not least, to a very special Dr. Thomas Russell, who has gone above and beyond in helping me from day one.

I would also like to extend my gratitude to Dr. Emma McEwin for reviewing and editing my work, sometimes within short time frames/at short notice.

To all those who I have studied with, past and present Ph.D. students, I have learnt so much from each and every one of you. I hope that I have given back as much as I have received. A special acknowledgement to Yazan Arouri, the person I graduated Bachelor's with, and with whom I started a Ph.D. Hopefully, we will qualify for our Ph.D.s at the same time, too.

I would like to take this opportunity to thank all those who have shown me tremendous encouragement and support outside of my studies. To my ahjussi Emerance Ishimwe, who has been the unsung hero of my life for over a decade and always a call away, despite

us being almost 16,000 km and 9.5 hours apart. To the always welcoming and supportive Gina Torkington and the Saturday Kids family; I cannot express how thankful I am to have been a part of this program. It has been my get-away for almost a decade; I will forever treasure the memories created and lessons learnt from this experience/from my time spent with you.

Finally, I would like to unreservedly thank my mother, Xiuli Tan, who has always provided a shoulder for me to lean on, my little brother, Justen Yang, who brings sunshine into my life, and my father, Guoqiang Yang, who has been my designated driver and listening ear. Your unconditional love and support have helped me through all of my study and life challenges. To my family in China, thank you for supporting me through my challenging times, and I hope that you are ready for my next visit because I'll be collecting hongbao.

Thesis by Publication

Published Peer-Reviewed Journal Papers

Yang, S., Osipov, Y., Xu, C., Kuzmina, L., Russell, T. and Bedrikovetsky, P., 2021. Analytical solution for large-deposit non-linear reactive flows in porous media. *Chemical Engineering Journal*, p.132812.

Yang, S., Russell, T., Badalyan, A., Schacht, U., Woolley, M. and Bedrikovetsky, P., 2019. Characterisation of fines migration system using laboratory pressure measurements. *Journal of Natural Gas Science and Engineering*, 65, pp.108-124.

Yang, S., Hemmati, N., Russell, T., Zeinijahromi, A., Borazjani, S., Behr, A., Genolet, L. and Bedrikovetsky, P., 2021. 3D effects in two-phase steady-state tests. *Journal of Petroleum Science and Engineering*, p.109533.

Hemmati, N., Borazjani, S., **Yang, S.**, Badalyan, A., Genolet, L., Behr, A., Zeinijahromi, A., and Bedrikovetsky, P. (2022). Laboratory validation of steady-state-transient test to determine relative permeability and capillary pressure. *Fuel*, 321, 123940.

Naik S, **Yang, S.**, Woolley M, and Bedrikovetsky P., 2019. Analytical modelling of the water block phenomenon in hydraulically fractured wells. *Journal of Natural Gas Science and Engineering*, 67, pp. 56-70.

Journal Paper Accepted for Publication

Yang, S., Russell, T., Vaz, A., and Bedrikovetsky, P., Large-deposit non-linear chemical reactive flows in porous media: Identifiability and observability, *Journal of Natural Gas Science and Engineering*, Accepted for publication.

1. Contextual Statement

Significance of the project The significance and impact of this Ph.D. project lie in the novel formulations of reactive and colloidal transport, analytical modelling of two-phase flows, and their applications in laboratory modelling of formation damage and two-phase flows in porous media. These formulations are supported by experimental works designed to investigate phenomena, confirm the accuracy of modelling efforts, and retrieve the model functions from the corresponding laboratory tests. The formulated governing equations and derived analytical solutions are applied for the development of the laboratory methods to study the corresponding processes. The above analytical modelling and consequential laboratory-test design underpin a strong academic contribution and novel technique for industrial applications.

In the petroleum industry, reaction-induced formation damage encompasses mineral precipitation reactions in geological basins and oilfield scaling during water injection operations. Colloidal formation damage occurs due to both foreign particle injection during injection operations and natural fine particle detachment during production operations. The formation of precipitates and the mobilisation of particles reduce the permeability of the porous media and hence reduce the recovery of oil and gas.

The obtained one-dimensional (1D) analytical solutions in this thesis for the different formation damage processes can be widely used as benchmarks for numerical methods. The analytical solutions have significantly improved techniques for the treatment and the qualitative analysis of experimental results. Another important application of the 1D analytical solutions is obtaining semi-analytical quasi three-dimensional (3D) solutions for chemical and colloidal flows in porous media using the streamline method.

In addition, the proposal and feasibility study for the application of three-point pressure coreflooding experiments for reactive, suspension, and two-phase flows is a significant application for the derived analytical models. During conventional coreflooding experiments, particle (or ion) breakthrough concentrations and pressure drop between the inlet and outlet of the core (i.e., across the core) are measured. In the three-point pressure method, pressure drop measurements across the core, and in its first section, are obtained. The results show that the breakthrough concentration cannot be substituted by the additional pressure measurement in the three-point pressure method. However, the additional pressure drop measurement can significantly improve the quality of matching to the experimental measurements.

The models developed in this thesis for chemical, colloidal, and two-phase flows are vital tools for decision making. They allow for simple and time-efficient predictions and uncertainty analyses based on laboratory experiments for formation damage and two-phase transport. The models have already resulted in significant improvement in laboratory techniques in their respective areas.

State of the art Modelling of reactive, colloidal, and two-phase processes has long attracted attention in industrial and academic research for environmental, chemical, and petroleum applications (Bedrikovetsky, 2013, Civan, 2015, Khilar and Fogler, 1998, Lake, 1989). Numerous analytical solutions have been obtained for one-phase and two-phase flows and applied to determine model parameters from the laboratory experiments.

The governing system of single-phase transport with two reacting components contains the law of acting mass with a constant reaction coefficient and a linear formation damage factor (Bethke, 1996, Drever, 1982). 1D problems for commingled injection of reacting liquids allow for exact solutions, where the outlet concentrations are at steady-state and

the pressure drop across the core linearly grows with time (Altree-Williams et al., 2018, Vaz et al., 2016). However, numerous laboratory experiments show changing breakthrough concentrations and a nonlinear increase in pressure drop during injections (Ahmed, 2004, Ghaderi et al., 2009, Moghadasi et al., 2004). In simpler situations of dissolution chemical reactions, Altree-Williams et al. (2019) recommend introducing the varying reacting solid-fluid surface into the system of equations.

In this thesis, a different approach has been taken. A chemical reaction coefficient depending on the deposit concentration is introduced, which implicitly assumes the reactive surface dependency. The formulated 1D problem allows for an exact solution that is obtained by a nonlinear method of characteristics with first integrals along the trajectories. The extended system of governing equations for large deposit concentrations contains two extra parameters, when compared with the traditional model, the damage exponent in the formation damage factor for permeability and the reaction capacity coefficient. Both parameters are interpreted and described using the percolation and effective medium theory on the microscale. The exact solutions for the direct problem allow for the regularisation of the inverse problem, which makes it possible to use experimental data to determine the model coefficients. The solution of the inverse problem is found to be stable. The obtained values of the tuned model coefficients have the same order of magnitude as those obtained by calculations from the microscale.

For low concentration solid deposits and a traditional linear system of governing equations with steady-state solutions, two laboratory methods to characterise the reactive flow system from the coreflood have been proposed and used in industry. One of the methods is measuring the breakthrough concentration of one of the reacting species and the pressure drop across the core. The other method is the three-point pressure method (Vaz et al., 2017, Vaz et al., 2016). Both methods determine the model coefficients.

However, the first method requires using cumbersome and expensive chromatography tests to measure the breakthrough concentration, while the three-point pressure method uses pressure measurements only, which are simple and more accurate, and widely available laboratory equipment. In this thesis, the three-point pressure method is developed for large deposit reactions using the analytical nonlinear solutions.

The conventional method to calculate model coefficients in the colloidal-suspension model, accounting for fines detachment, migration, and straining in small pores, measures the breakthrough concentrations of fines and the pressure drop across the core (Bedrikovetsky et al., 2011, Bedrikovetsky et al., 2012). Due to the abovementioned advantages of the three-point pressure method, this method was also adopted in this study for fines migration.

Various methods for laboratory determination of capillary pressure and relative permeabilities have been developed during the last half a century. This is largely due to the advancement in reservoir modelling and simulation capabilities of two-phase flows in porous media. The effect of capillary pressure on steady-state experiments, especially for short cores, is significant. However, laboratory methods for determining both capillary pressure and relative permeabilities from coreflooding using the same core are not available. Recently, Borazjani et al. (2021a) and Borazjani et al. (2021b) proposed what they called a steady-state transient test (SSTT), using both steady-state and transient data. In their study, they developed an inverse solver and demonstrated its stability. However, neither the laboratory validation of this method nor the experimental protocol (i.e., the selection of flow velocity, frequency of sampling, sampling volumes, core lengths, etc.) is available. Therefore, in the current study a laboratory investigation of SSTT was carried out, as well as its 3D numerical modelling, and a thorough validation of the method.

Scope of the work In light of the above presentation of state of the art, the main contributions of this thesis are:

- Formulation of novel governing equations for 1D non-equilibrium non-linear large-deposit reactive flows in porous media
- Derivation of new exact solutions for 1D non-equilibrium non-linear large-deposit reactive flows
- Extension of the traditional three-point pressure method for reactive flows for the case of non-equilibrium non-linear large-deposit reactive flows
- Derivation of new exact solutions for 1D fines migration model with applications to hydraulically fractured wells
- Extension of the three-point pressure method for formation damage due to fines migration
- Combining of the 1D semi-analytical SSTT solution with a 3D numerical coreflood model to plan and design commingled water-oil injection experiments
- Validation of the SSTT method through laboratory experiments using the design from the 1D semi-analytical SSTT solution with a 3D numerical coreflood model
- Derivation of a new exact solution for 2D two-phase flow with one immobile phase and its application for inflow performance of a fractured well

1.1. Thesis Structure

This is a Ph.D. thesis by publication. Six publications are presented in this thesis, four of which have been published in journals and two have been submitted for publication.

The thesis body comprises nine chapters. The first chapter includes the contextual statement, introduces the problems addressed in the thesis, and outlines their importance. A detailed literature review is included in the second chapter. Chapters three to eight

present the novel research performed as part of this thesis in the form of submitted and published papers. The journal paper titles, and publication status are provided in Table 1. Chapter nine concludes the thesis and provides recommendations for future studies.

Table 1. Journal paper title and the corresponding publication status in each chapter of the thesis.

Chapter	Title	Status
3	Analytical solution for large-deposit non-linear reactive flows in porous media	Published
4	Large-deposit non-linear chemical reactive flows in porous media: Identifiability and observability	Accepted for publication
5	Characterisation of fines migration system using laboratory pressure measurements	Published
8	3D effects in two-phase steady-state tests	Published
6	Laboratory validation of a steady-state-transition test for determining relative permeability and capillary pressure	Published
7	Analytical modelling of the water block phenomenon in hydraulically fractured wells	Published

1.2. How the Publications are related to the Thesis

The paper "Analytical solution for large-deposit non-linear reactive flows in porous media" has been published in the *Chemical Engineering Journal* (impact factor, IF = 13.273 (2020)) and is presented in Chapter 3 of the thesis. It presents a novel system of a governing equation for 1D non-equilibrium non-linear large-deposit reactive flows in porous media. Analytical solutions to the 1D problem of stoichiometric coefficients being equal to arbitrary values, as well as unity with different injection concentration conditions are derived. The new solutions exhibit time-dependent reactant breakthrough concentrations and nonlinear pressure drop evolution with time, which were observed in laboratory experiments. The analytical solutions were applied to interpret the laboratory data for chemically reactive coreflooding experiments. The study revealed that the tuned model parameters from the laboratory data have the same order of magnitude as those

obtained from micromodels. The results provide greater insight into the nature of large-deposit-concentration chemical-reactive transport in porous media.

The paper "Large-deposit non-linear chemical reactive flows in porous media: Identifiability and observability" has been accepted for publication in the *Journal of Natural Gas Science and Engineering* (IF = 4.965 (2020)) and is presented in Chapter 4 of the thesis. It focuses on the development of laboratory methods to determine model parameters for large-deposit concentrations in reactive flows, using the new analytical solutions derived in Chapter 3. The study investigated the conventional and three-point pressure methods used to conduct experiments for chemically reactive flows in cores, and the application of the analytical solutions for data treatments presented in Chapter 3. The conventional method uses pressure drop and breakthrough concentration of one reacting species, and the three-point pressure method measures two sets of pressure drop data, which are across the core and its first section. Using the exact analytical solution allows regularisation of the inverse problem. The laboratory tests were treated using both methods, and all three sets of data were used. Although the three-point pressure method is less cumbersome, more precise, and cheaper, breakthrough concentration measurements cannot be replaced by the pressure drop measurement across the first section of the core.

The paper "Characterisation of fines migration system using laboratory pressure measurements" has been published in the *Journal of Natural Gas Science and Engineering* (IF = 4.965 (2020)) and is presented in Chapter 5 of the thesis. It investigates the three-point pressure method to characterise the migration of natural clay fine particles in porous media. The explicit formulae for the application of the three-point pressure method were derived based on validated analytical solutions from previous works. The result led to the conclusion that the three-point pressure method cannot fully characterise

the fines migration system. In other words, the additional pressure measurement cannot substitute the breakthrough concentration measurements of effluent. A thorough laboratory investigation of fines migration, along with a detailed microscale characterisation of porous media and migrating clays, was carried out. In this particular case, improving the measurement of second pressure drop yields improved the accuracy of the tuned coefficient.

The paper "3D effects in two-phase steady-state tests" has been published in the *Journal of Petroleum Science and Engineering* (IF = 4.346 (2020)) and is presented in Chapter 6 of the thesis. It studies the 3D effects of laboratory SSTTs accounting for capillary end effects. The important 3D phenomenon of incomplete sweep and non-uniform phase distributions in core cross-sections were discovered. In particular, the 3D effect was more significant for the simulation using an inlet distributor with half-moon geometries than spiral (or concentric-circle) geometries. The results of 1D treatment of the "measured" data, produced by the 3D simulations revealed that the direct problem solution is more sensitive to capillary pressure than that for the inverse problem. This explains the reason why the petroleum industry is using 1D inverse solvers to treat corefloods in short cores.

The paper "Laboratory validation of steady-state-transient test to determine relative permeability and capillary pressure" has been published in *Fuel* (IF = 6.609 (2020)) and is presented in Chapter 7 of the thesis. It evaluates the stability and accuracy of SSTTs. Based on the result of 3D modelling presented in Chapter 6, two coreflood experiments were conducted. For one of the experiments an inlet distributor with half-moon geometries was used, and for the other, concentric-circles geometries. Furthermore, in the half-moon set-up, effluent water cut was determined using the visualisation method, while in the concentric-circle set-up, the weighting method was used. The results clearly

showed the advantages of the latter method, including more closely matched and predicted modelling results compared to the raw laboratory measurements.

The paper "Analytical modelling of the water block phenomenon in hydraulically fractured wells" has been published in the *Journal of Natural Gas Science and Engineering* (IF = 4.965 (2020)) and is presented in Chapter 8 of the thesis. It explores two-phase steady-state flow, accounting for formation damage by the capillary trapped water near a fractured production well. For the first time, an exact solution was derived. The exact solution yields the explicit dependency of the formation damage on rock wettability, and transport coefficients. This revealed that changing the contact angle by wettability alternation can mitigate and even remove the formation damage due to the capillary entrapped water.

1.3. References

AHMED, S. J. 2004. *Laboratory study on precipitation of calcium sulphate in berea sandstone cores.* Master of Science, King Fahd University of Petroleum and Minerals

ALTREE-WILLIAMS, A., BRUGGER, J., PRING, A. & BEDRIKOVETSKY, P. 2018. Exact solution for coupled reactive flow and dissolution with porosity changes. *Transport in Porous Media,* 124, 655-679.

ALTREE-WILLIAMS, A., BRUGGER, J., PRING, A. & BEDRIKOVETSKY, P. 2019. Coupled reactive flow and dissolution with changing reactive surface and porosity. *Chemical Engineering Science,* 206, 289-304.

BEDRIKOVETSKY, P. 2013. *Mathematical theory of oil and gas recovery with applications to ex-USSR oil and gas fields,* Dorbrecht, Kluwer Academic Publishers.

BEDRIKOVETSKY, P., SIQUEIRA, F. D., FURTADO, C. A. & SOUZA, A. L. S. 2011. Modified particle detachment model for colloidal transport in porous media. *Transport in porous media,* 86, 353-383.

BEDRIKOVETSKY, P., ZEINIJAHROMI, A., SIQUEIRA, F. D., FURTADO, C. A. & DE SOUZA, A. L. S. 2012. Particle detachment under velocity alternation during suspension transport in porous media. *Transport in Porous Media,* 91, 173-197.

BETHKE, C. 1996. *Geochemical reaction modeling: Concepts and applications*, Oxford University Press on Demand.

BORAZJANI, S., HEMMATI, N., BEHR, A., GENOLET, L., MAHANI, H., ZEINIJAHROMI, A. & BEDRIKOVETSKY, P. 2021a. Determining water-oil relative permeability and capillary pressure from steady-state coreflood tests. *Journal of Petroleum Science and Engineering,* 205, 108810.

BORAZJANI, S., HEMMATI, N., BEHR, A., GENOLET, L., MAHANI, H., ZEINIJAHROMI, A. & BEDRIKOVETSKY, P. 2021b. Simultaneous determination of gas–water relative permeability and capillary pressure from steady-state corefloods. *Journal of Hydrology,* 598, 126355.

CIVAN, F. 2015. *Reservoir formation damage,* United States, Gulf Professional Publishing.

DREVER, J. I. 1982. The geochemistry of natural waters.

GHADERI, S., KHARRAT, R. & TAHMASEBI, H. 2009. Experimental and theoretical study of calcium sulphate precipitation in porous media using glass micromodel. *Oil & Gas Science and Technology - Rev lFP,* 64, 489-501.

KHILAR, K. C. & FOGLER, H. S. 1998. *Migrations of fines in porous media,* Dordrecht, Kluwer Academic Publishers.

LAKE, L. W. 1989. *Enhanced oil recovery,* Upper Saddle River, NJ, Prentice Hall.

MOGHADASI, J., MÜLLER-STEINHAGEN, H., JAMIALAHMADI, M. & SHARIF, A. 2004. Model study on the kinetics of oil field formation damage due to salt precipitation from injection. *Journal of Petroleum Science and Engineering,* 43, 201-217.

VAZ, A., BEDRIKOVETSKY, P., FERNANDES, P., BADALYAN, A. & CARAGEORGOS, T. 2017. Determining model parameters for non-linear deep-bed filtration using laboratory pressure measurements. *Journal of Petroleum Science and Engineering,* 151, 421-433.

VAZ, A., MAFFRA, D., CARAGEORGOS, T. & BEDRIKOVETSKY, P. 2016. Characterisation of formation damage during reactive flows in porous media. *Journal of Natural Gas Science and Engineering,* 34, 1422-1433.

2. Literature Review

2.1. Introduction

The use of exact analytical solutions in the treatment of laboratory data for the planning and designing of tests, as well as the calculation of model coefficients is a prospective development in various areas of laboratory porous media research. Ill-posed inverse problems can be regularised by using the exact solutions of the direct (or forward) problems. Examples of this application are given by the inverse JBN method (Johnson et al., 1959) for the relative permeability measurements and inverse solutions of the deepbed filtration problems (Alvarez et al., 2005, Alvarez et al., 2007). Well-posed inverse solutions can provide formulae for simple algorithms to retrieve model functions from laboratory tests. Using analytical solutions to plan and design laboratory tests (for example, determining the flow velocity, the frequency for effluent sampling, the placement of different pressure transducers) is an effective method for reducing the number of experimental errors and uncertainties.

However, the use of analytical solutions in laboratory studies in evaluating formation damage is limited. Although two-phase flow tests have attracted intensive research since 1960, attempts have not been made to measure pressure profiles, including the three-point pressure method.

The following literature review reflects on the application of analytical solutions in formation damage due to chemically reactive transport (Chapter 2.2), fines migration with induced formation damage (Chapter 2.3) and two-phase flow accounting for capillary end effects (Chapter 2.4) in porous media.

2.2. Chemical reaction formation damage transport in porous media

Chemical reactions in incompatible fluid flow in porous media typically result in the precipitation of insoluble solids, which induce formation damage by reducing permeability. This affects the productivity in artesian, geothermal, oil, and gas wells (Civan, 2015). Numerous natural mineral precipitation processes can be found in aquifers and under the earth's crust (Lasaga, 2014). In the petroleum industry, salt precipitation, due to incompatible fluid mixing, occurs during water injection, well drilling, and completion. This results in the non-equilibrium precipitation of solid salt deposits near wellbores. Some of the key studies in the literature includes Bethke (2007), Evans (2009), Fogler (2010), Kleinitz et al. (2001), Le and Mahadevan (2011), Mackay (2002), Mackay (2003), Manahan (2017) and Van Dorp et al. (2009).

In this thesis, the chemical reaction between barium ions Ba^{2+} (typically found in formation water) and sulphate ions SO_4^{2-} (typically found in seawater, which is often used as the injection water) that form the insoluble barium sulphate $BaSO_4$ is discussed (shown in Eq. (1)). This is often referred to as oilfield scaling.

$$Ba^{2+} + SO_4^{2-} \rightarrow BaSO_4 \tag{1}$$

The brief literature search in this section presents well-known governing equations and the corresponding analytical solutions (Chapter 2.2.1), as well as the application of the three-point pressure method based on the analytical solutions (Chapter 2.2.2).

Figure 1 presents a schematic of the so-called oilfield scaling formation damage at the reservoir scale. Figure 1a shows the structure of the displacement zone along a given streamline within the waterflooded pattern connecting the injection and production wells. The displacement zone can be divided into three components. In the direction of flow, they are the injected water zone, the mixture zone, and the undisturbed zone. The chemical reaction, described in Eq. (1), occurs in the mixture zone, where the barium-

rich formation water (FW) mixes with the sulphate-rich seawater (SW), and barium sulphate precipitates. This structure of the flow zone is reflected in the analytical solution presented in Chapter 2.2.1. Figure 1b shows the breakdown of the composition of the porous media. The reactants (i.e., barium and sulphate ions) are in the pore space, while the deposit (i.e., barium sulphate precipitates) removes a portion of the pore space.

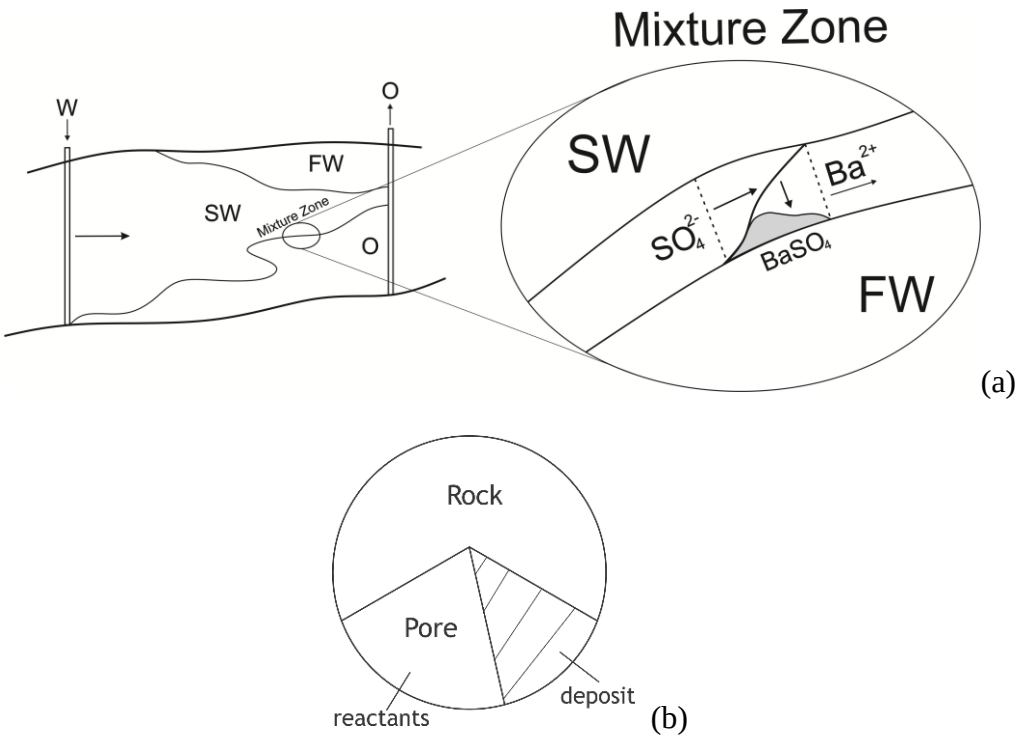

Figure 1. Schematic of oilfield scaling formation damage at the reservoir scale: (a) barium sulphate precipitation of a streamline in the mixing zone due to the injected seawater (SW) displacing formation water (FW) and (b) composition of the porous media (Vaz et al., 2016).

2.2.1. Analytical modelling of reactive flows with insoluble precipitates

The 1D reactive flow in porous media is described by a system of governing equations. The governing equations include two mass balance equations, for barium ions in Eq. (2) and sulphate ions in Eq. (3), a kinetics equation for chemical reactions given by the law of acting masses (Eq. (4)), and a precipitate-dependent modified Darcy's equation (Eq. (5)) (Bethke, 1996, Drever, 1982, Vaz et al., 2016):

$$\phi \frac{\partial c_1}{\partial t} + U \frac{\partial c_1}{\partial x} = -\frac{\partial \sigma}{\partial t} \tag{2}$$

$$\phi \frac{\partial c_2}{\partial t} + U \frac{\partial c_2}{\partial x} = -\frac{\partial \sigma}{\partial t} \tag{3}$$

$$\phi \frac{\rho_\sigma}{M_\sigma} \frac{\partial \sigma}{\partial t} = \lambda U c_1 c_2 \tag{4}$$

$$U = -\frac{k_0}{\mu(1+\beta\sigma)} \frac{\partial p}{\partial x} \tag{5}$$

where, c_1, c_2, and σ are the concentrations for reactants 1, 2, and precipitate, respectively, ϕ and k_0 are the porosity and initial formation permeability of the formation, respectively, U and μ are the velocity and viscosity of the injected fluid, respectively, ρ_σ and M_σ are the precipitate density and molecular weight, respectively, λ and β are the kinetics rate and formation damage coefficients, respectively, p is pressure, t is time, and x is the 1D coordinate.

Substituting dimensionless parameters and variables, shown in (6) and (7),

$$C_1 = \frac{c_1}{c_1^o}, C_2 = \frac{c_2}{c_2^o}, S = \frac{\rho_\sigma}{M_\sigma} \frac{\sigma}{c_1^o}, P = \frac{k_0 p}{U \mu L} \tag{6}$$

$$X = \frac{x}{L},\ T = \frac{Ut}{\phi L},\ \varepsilon_k = \lambda L c_2^o,\ \alpha = \frac{c_1^o}{c_2^o} \tag{7}$$

where the superscript o represents the injected concentration, into Eqs. (2)-(5) transforms the system of governing equations to the dimensionless form (8) - (11):

$$\frac{\partial C_1}{\partial T} + \frac{\partial C_1}{\partial X} = -\varepsilon_k C_1 C_2 \tag{8}$$

$$\frac{\partial C_2}{\partial T} + \frac{\partial C_2}{\partial X} = -\alpha \varepsilon_k C_1 C_2 \tag{9}$$

$$\frac{\partial S}{\partial T} = \varepsilon_k C_1 C_2 \tag{10}$$

$$1 = -\frac{1}{1+\beta\frac{M_\sigma}{\rho_\sigma}c_1^o S}\frac{\partial P}{\partial T} \tag{11}$$

with the boundary (12) and initial (13) conditions:

$$X = 0 : C_1 = C_2 = 1 \tag{12}$$

$$T = 0 : C_1 = C_2 = S = 0 \tag{13}$$

The full derivation of the analytical solution to the problem (8)-(13) is presented in Vaz et al. (2016). The analytical solution for concentrations of reactants 1, 2, and precipitate, as well as pressure drop across the core ΔP are presented in Eqs. (14)-(17).

$$C_1\left(X,T\right) = \frac{(1-\alpha)}{e^{\varepsilon_k(1-\alpha)X} - \alpha} \tag{14}$$

$$C_2\left(X,T\right) = \frac{(1-\alpha)}{1-\alpha e^{-\varepsilon_k(1-\alpha)\mathrm{X}}} \tag{15}$$

$$S\left(X,T\right) = \varepsilon_k\left[\frac{(1-\alpha)^2}{e^{\varepsilon_k(1-\alpha)X} + \alpha(\alpha e^{-\varepsilon_k(1-\alpha)X} - 2)}\right]T \tag{16}$$

$$\Delta P\left(T\right) = 1 + \frac{M_\sigma}{\rho_\sigma}\beta c_1^o\left\{\frac{\alpha\left[e^{\varepsilon_k(\alpha-1)} - 1\right]}{\alpha e^{\varepsilon_k(\alpha-1)} - 1}\right\}T \tag{17}$$

Figure 2 shows the solution space for the governing equations described in Eqs. (8)-(11). The concentration profiles for the reactants and precipitate are shown by the continuous and dashed curves, respectively. The concentration front trajectory on the dimensionless coordinate and time, *X* and *T*, respectively, are represented by the bold straight line and travels with the injected fluid velocity. Behind the concentration front, the reactants and precipitate concentrations are at steady-state. While ahead of the concentration front, the concentrations are equal to zero.

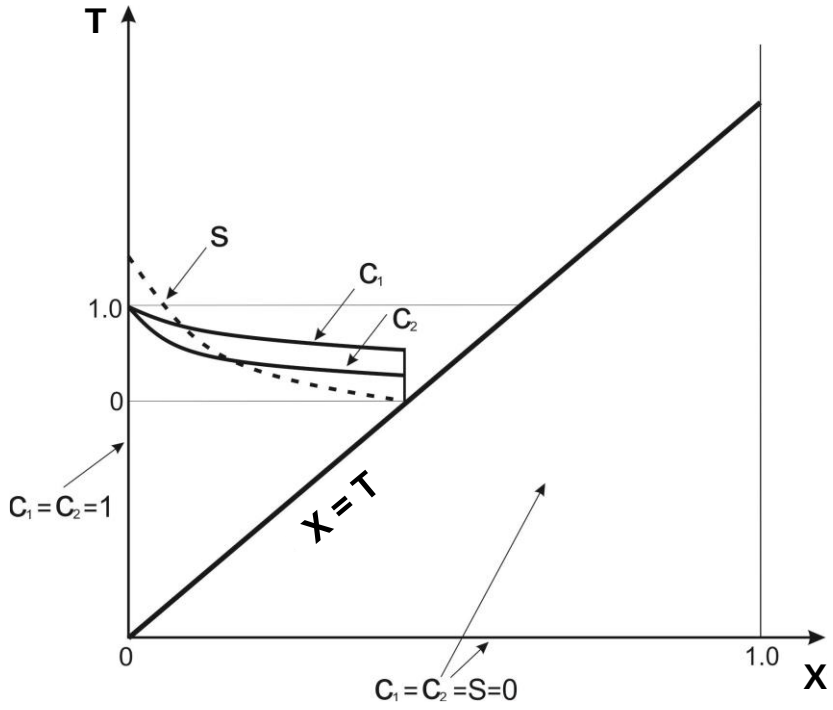

Figure 2. Schematic of the exact solution space for the analytical model of reactive flows with insoluble precipitation (Vaz et al., 2016).

2.2.2. Laboratory modelling of reactive flows with insoluble precipitates – the three-point pressure method

In a conventional coreflooding experiment for reactive flows with insoluble precipitates, pressure drop measurements between the inlet and outlet of the core, as well as the breakthrough concentration of one reactant are obtained. Pressure measurements during corefloods are simple to operate, precise, and use low-cost equipment, while breakthrough concentration measurements are cumbersome, have low accuracy, and use chromatography, which is significantly more costly. The three-point pressure method avoids the need to obtain the breakthrough concentration; it is replaced by the pressure drop across the first section of the core. This method has been applied to deepbed filtration (Bedrikovetsky et al., 2001) and linear low-deposit-concentration oilfield scaling (Vaz et al., 2016).

A schematic of the three-point pressure method experiment performed by Vas (2016) is shown in Figure 3. Breakthrough concentrations for barium ions and four sets of pressure data are recorded. The four sets of pressure data are recorded along the core at positions $x = 0$, $\omega_1 L$, $\omega_2 L$, and L, where L is the length of the core. Three sets of pressure drop data are obtained from the four sets of pressure data, namely Δp (pressure drop across the core), Δp_1 (pressure drop across the first section), and Δp_2 (pressure drop across the second section).

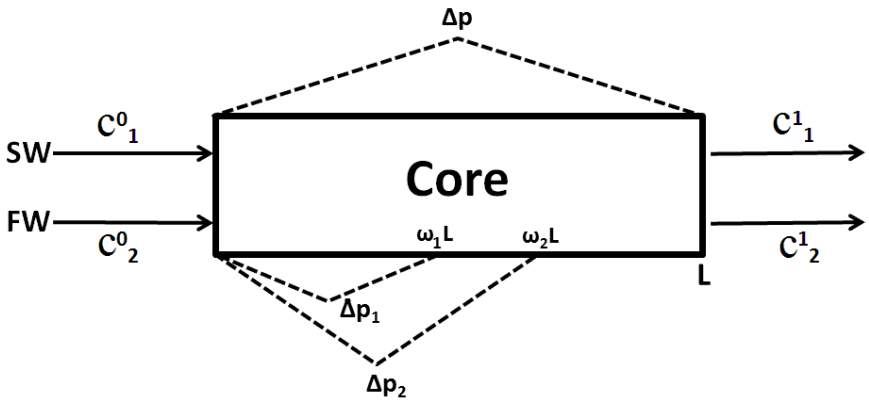

Figure 3. Schematic of the three-point pressure method set-up of the commingled injection of incompatible fluids coreflooding experiment (Vaz et al., 2016).

Figure 4 presents the laboratory set-up for the three-point pressure method used in (Vaz et al., 2016), and is also available at the Australian School of Petroleum and Energy Resources, The University of Adelaide. The purpose of the detailed technical description in Figure 3 and Figure 4 is to show the wide availability of the equipment and, consequently, the feasibility of applying the three-point pressure method to the oilfield scaling. It is also feasible to use this method in any mineral precipitation chemical reactions in porous media.

Figure 4. Photograph of the three-point pressure method set-up of the commingled injection of incompatible fluids coreflooding experiment (Vaz et al., 2016).

Figure 5 presents the sensitivity of dimensionless pressure drop with respect to β and λ by (Vaz et al., 2016). The base values for β and λ are 0.64 and 0.01m^{-1}, respectively. In this model, ΔP varies linearly with T.

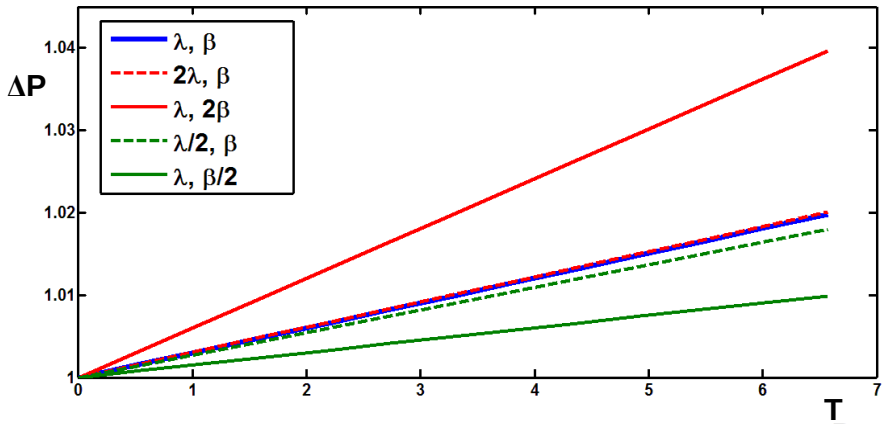

Figure 5. Sensitivity study for the dimensionless pressure drop ΔP with respect to the formation damage β and kinetics rate λ coefficients (Vaz et al., 2016)

However, extensive laboratory studies exhibit significant time-dependent reactant breakthrough concentrations and nonlinear pressure drop evolution with time (Ahmed,

2004, Ghaderi et al., 2009, Moghadasi et al., 2004). This effect can be explained by the change in the surface liquid-solid where the chemical reaction occurs. The corresponding mathematical model is not available in the literature; consequently, neither the analytical model nor the design of the three-point pressure method has been performed.

Replacing the kinetics rate coefficient in Eq. (4) with the deposit-dependent reaction rate function $\lambda(\sigma)$, shown in Eq. (18), addresses the problem.

$$\lambda(\sigma)=\begin{cases}\lambda_0(1-b\sigma), & \sigma<b^{-1}\\ 0, & \sigma>b^{-1}\end{cases} \tag{18}$$

where λ_0 and b are the initial kinetics rate and reaction capacity coefficients, respectively. The reactions are assumed to take place on the reactive surfaces of the porous media. The reaction capacity coefficient represents the variation of available reaction surfaces. As precipitates form, the available reaction surfaces may increase (corresponding to a negative b) or decrease (corresponding to a positive b). Deposit-dependent reaction rate functions are presented in Figure 5. Lines 1, 2, and 3 correspond to the reduction in the reaction rate as σ increases. Line 4 corresponds to the increase in the reaction rate as σ increases. Lines 5 and 6 correspond to the constant reaction rate, which is modelled by Vaz et al. (2016).

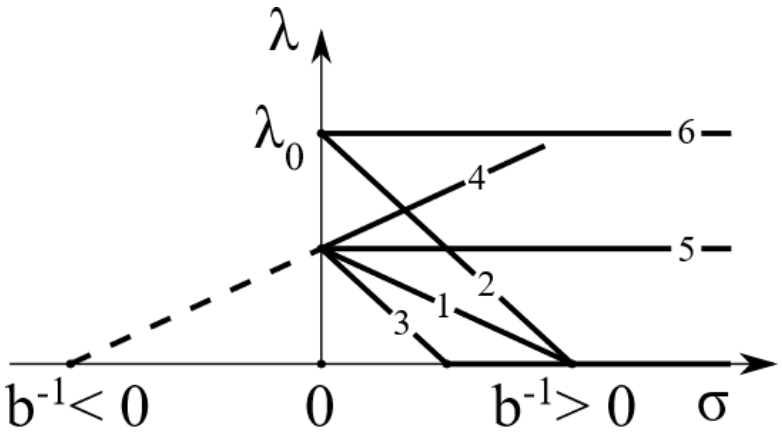

Figure 6. Schematic for three forms of the reaction rate functions $\lambda=\lambda(\sigma)$ (Yang et al., 2022).

The above literature review addresses the importance of developing basic equations for reactive flow with changing solid-liquid surfaces for precipitation. The derivation of the corresponding basic equations, along with the design of the three-point pressure method are important problems in fluid mechanics in porous media. They are also important for the prevention and mitigation of formation damage in industry.

The abovementioned problems are solved in Chapters 3 and **Error! Reference source not found.** of this thesis.

2.3. Fines migration formation damage transport in porous media

The transport of colloidal suspension in porous media occurs in numerous natural and engineering processes. Such processes include particle attachment, where the analytical model and three-point pressure methods are well developed (Bedrikovetsky et al., 2001, Vaz et al., 2017), and fines detachment, where the current state-of-the-art laboratory tests use breakthrough particle concentration (Oliveira et al., 2014, Russell and Bedrikovetsky, 2018).

Figure 7 shows the fines detachment from grain surfaces and the schematic of its mathematical modelling. Figure 7a shows that fines are mobilised by the carrier fluid, pass through pores that are larger than them, while plugging pores that are smaller than them. Figure 7b shows two main forces exerting on an attached fine particle. The attaching forces are electrostatic force and gravity. However, the effects of gravity are neglected in porous media applications. The detaching forces are drag and lifting forces. Although lifting forces may detach fines, they are neglected in the majority of applications. The mechanical equilibrium of a fine particle is shown in Eq. (19).

$$F_d\left(U\right)l_d = F_e\left(\gamma\right)l_n \tag{19}$$

where $F_d(U)$ is the detaching drag force, which depends on the carrier fluid velocity U, $F_e(\gamma)$ is the attaching electrostatic force, which depends on the carrier fluid salinity γ, l_d and l_n are the drag and electrostatic force lever arms, respectively.

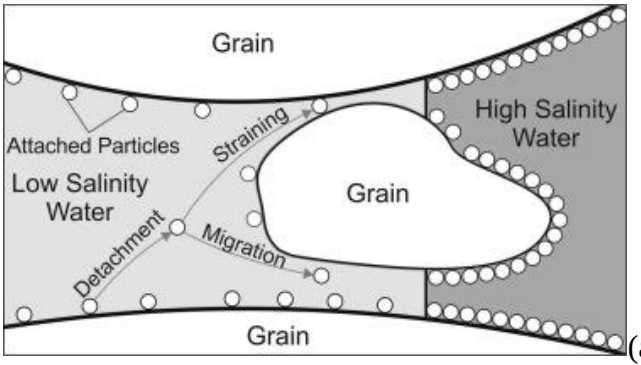

(a)

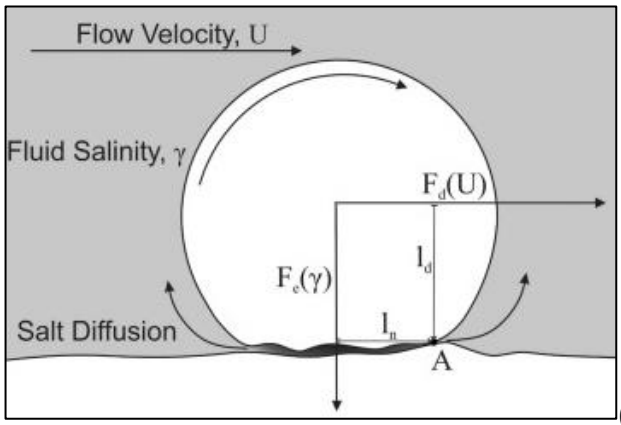

(b)

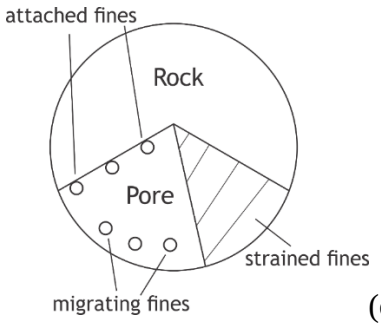

(c)

Figure 7. Schematic of fines migration in a porous medium: (a) the mechanical processes during low salinity water injection, (b) forces and lever arms acting on an attached particle, and (c) composition of the porous medium (Russell and Bedrikovetsky, 2018).

It follows the works of Bedrikovetsky et al. (2011), Bedrikovetsky et al. (2012), Bradford et al. (2013), Civan (2015), and Elimelech et al. (2013).

2.3.1. Analytical modelling of fines migration due to salinity difference

Chequer et al. (2018) derived and solved a system of governing equations describing the 1D linear transport accounting for fines migration due to salinity difference in porous media. This system accounts for fines detachment and consequent permeability damage. It consists of a mass balance equation for particles, shown in Eq. (20):

$$\frac{\partial}{\partial t}\left(\phi c+\sigma_s+\sigma_a\right)+\alpha U\frac{\partial c}{\partial x}=0 \tag{20}$$

where c, σ_s, and σ_a are the concentration of the suspended, strained, and attached particles, respectively, and α is the drift delay factor. The parameter αU models the suspended particle travelling at a slower rate than the carrier fluid.

An expression for the irreversible straining rate of the suspended particles, proportional to the suspended particle flow rate, are shown in Eq. (21):

$$\frac{\partial \sigma_s}{\partial t}=\lambda c\alpha U \tag{21}$$

where λ is the filtration coefficien.

A mass balance equation for the solute, assuming negligible diffusion, is shown in Eq. (22):

$$\phi\frac{\partial \gamma}{\partial t}+U\frac{\partial \gamma}{\partial x}=0 \tag{22}$$

Lastly, accounting for permeability reduction due to strained particles, a modified form of Darcy's equation is shown in Eq. (23):

$$U=-\frac{k_0}{\mu\left(1+\beta\sigma_s\right)}\frac{\partial p}{\partial x} \tag{23}$$

Introducing dimensionless parameters and variables in (24),

$$T=\frac{Ut}{\phi L},\ X=\frac{x}{L},\ C=\frac{c}{\phi\Delta\sigma_{cr}},\ S_a=\frac{\sigma_a}{\phi\Delta\sigma_{cr}},\ S_s=\frac{\sigma_s}{\phi\Delta\sigma_{cr}},\ \Lambda=\lambda L,\ P=\frac{pk_0}{U\mu L} \tag{24}$$

where $\Delta\sigma_{cr}$ is the concentration of a detached particle as a result of the change in salinity from the initial γ_0 to the injected γ_I salinity. This is calculated from the critical retention function, shown in Eq. (25).

$$\Delta\sigma_{cr}=\Delta\sigma_{cr}\left(\gamma_0\right)-\Delta\sigma_{cr}\left(\gamma_I\right) \tag{25}$$

The dimensionless parameters and variables in (24) transform the system of governing equations (19)-(23) into the dimensionless form (26)-(29).

$$\frac{\partial}{\partial T}\left(C+S_a\left(\gamma\right)+S_s\right)+\alpha\frac{\partial C}{\partial X}=0 \tag{26}$$

$$\frac{\partial S_s}{\partial T}=\alpha\Lambda C \tag{27}$$

$$\frac{\partial\gamma}{\partial T}+\frac{\partial\gamma}{\partial X}=0 \tag{28}$$

$$1=-\frac{1}{1+\phi\beta\Delta\sigma_{cr}S_s}\frac{\partial P}{\partial X} \tag{29}$$

The dimensionless governing equations are subjected to the boundary and initial conditions presented in (30) and (31), respectively.

$$X=0:\ \gamma=\gamma_I,\ C=0,\ P=P_0 \tag{30}$$

$$T=0:\gamma=\gamma_0,\ C=0,\ S_s=0 \tag{31}$$

The four equations (26)-(29) determine four unknowns, namely C, S_s, γ, and P. However, the equation for pressure (29) is independent on the rest of the system and the attached particle concentration is solved based on the solutions of C, S_s, and γ. Laboratory

experiments are required to determine the constant coefficients α, λ, β, and $\Delta\sigma_{cr}$ in the model.

Figure 8 shows the two concentration fronts, which divide the flow zone into three regions, for the governing equations described in Eqs (26)-(29). The injected fluid front and the suspended particle front are along the lines of $X = T$ and $X = \alpha T$, respectively. Consequently, regions 0, I, and II are defined as/determined to be ahead of both fronts, between the two fronts, and behind both fronts, respectively.

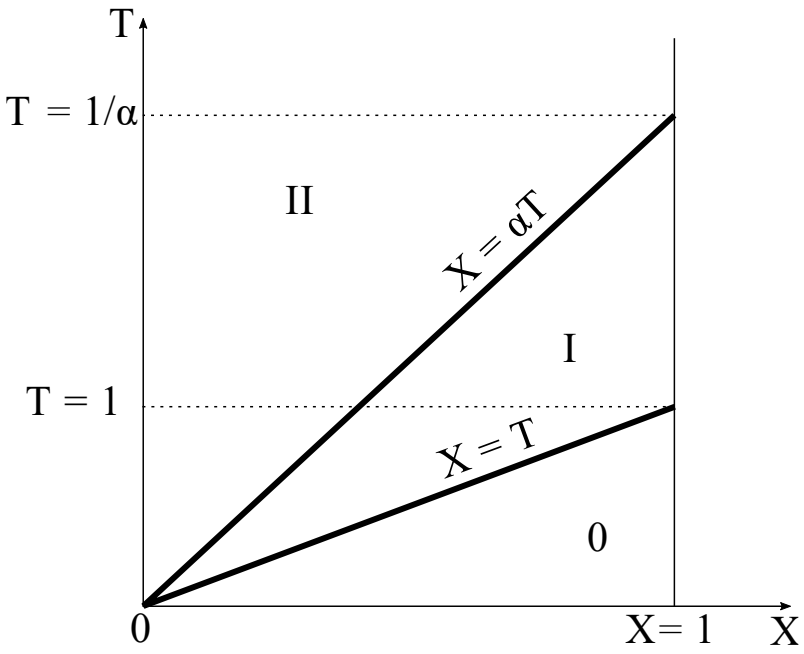

Figure 8. Schematic of the concentration fronts for the analytical model of the 1D linear transport accounting for fines migration due to salinity difference (Yang et al., 2022).

Table 2 presents the explicit solution for pressure drop across the core and accumulated suspended particle concentrations C_a, defined by Eq. (32), in regions 0, I and II.

$$C_a(1,T) = \alpha \int_0^T C(1,y)\,dy \tag{32}$$

Table 2. Exact solution presented by Chequer et al. (2018) for pressure drop across the core and accumulated breakthrough concentration.

	Region	Solution
$\Delta P(T)$	$X > T$	$1+\beta\Delta\sigma_{cr}\left[T+\frac{1}{\Lambda}\left(e^{-\alpha\Lambda T}-1\right)+\frac{(1-\alpha)}{\alpha\Lambda}\left(e^{-\alpha\Lambda T}-1\right)\right]$
	$\alpha T > X > \alpha T$	$1+\beta\Delta\sigma_{cr}\left[1+\frac{1}{\Lambda}\left(e^{-\Lambda\alpha T}-1\right)+\frac{(1-\alpha)}{\alpha\Lambda}\left(e^{-\alpha\Lambda T}-e^{\alpha\Lambda\left(\frac{1-T}{1-\alpha}\right)}\right)\right]$
	$X > \alpha T$	$1+\beta\Delta\sigma_{cr}\left[1+\frac{1}{\Lambda}\left(e^{-\Lambda\alpha T}-1\right)+\frac{(1-\alpha)}{\alpha\Lambda}\left(e^{-\alpha\Lambda T}-e^{\alpha\Lambda\left(\frac{1-T}{1-\alpha}\right)}\right)\right]$
$C_a(T)$	$X > T$	0
	$\alpha T > X > \alpha T$	$-\frac{1}{\Lambda}\left(e^{\frac{\alpha\Lambda(1-T)}{1-\alpha}}-1\right)$
	$X > \alpha T$	$-\frac{1}{\Lambda}\left(e^{-\Lambda}-1\right)$

2.3.2. Laboratory modelling of fines migration due to salinity difference – the three-point-pressure method

In Chapter 2.2.2, the importance and benefits of substituting the breakthrough concentration with an intermediate pressure drop measured along the core were emphasized. In this chapter, the formulation of the three-point pressure method and the application of the fines migration model to the industry are presented.

Figure 9 shows the applicability of the model presented in Chapter 2.3.1. Figure 9a presents the schematic for the fines migration experiment using the three-point pressure method. The core is initially saturated with the formation water of investigation. Then, the injection of fines-free water with a salinity lower than the formation water begins. During the experiment, pressure data are measured at the inlet ($x = 0$), midpoint ($x = \omega L$), and outlet ($x = L$) of the core, hence two sets of pressure drop, ΔP_L of the core and $\Delta P_{\omega L}$, are obtained. In addition, the breakthrough concentration of fines is also measured. Figure 9b shows the applicability of this model to a hydraulically fractured well, where fines

migration occurs in the leak-off zone due to the salinity difference in the fracturing and formation fluids.

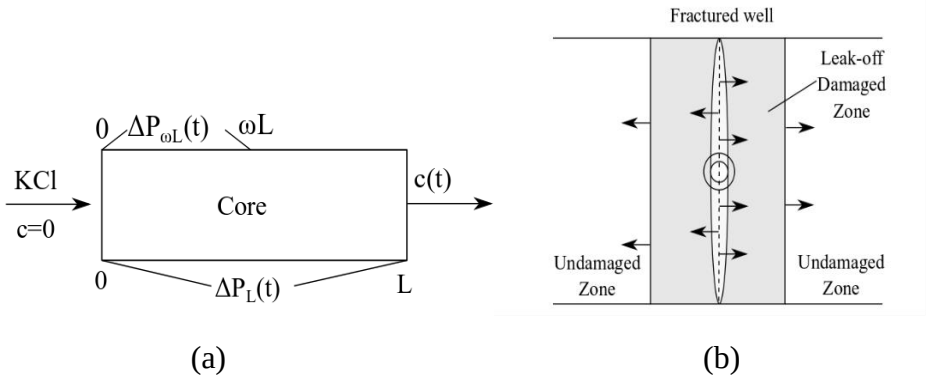

Figure 9. Schematic of the applications of the 1D linear transport accounting for fines migration due to salinity difference: (a) the three-point pressure method and (b) the leak-off zone around a hydraulically fractured well (Yang et al., 2022).

Figure 10 shows SEM images of a core before and after a low-salinity coreflood experiment. The comparison between Figure 10a and Figure 10b reveals that some particles were detached, shown in the solid red circles, and that a pore was plugged by strained fines, shown in the dashed red circles. This figure illustrates the main physics mechanism of fines detachment and formation damage reflected in the mathematical model.

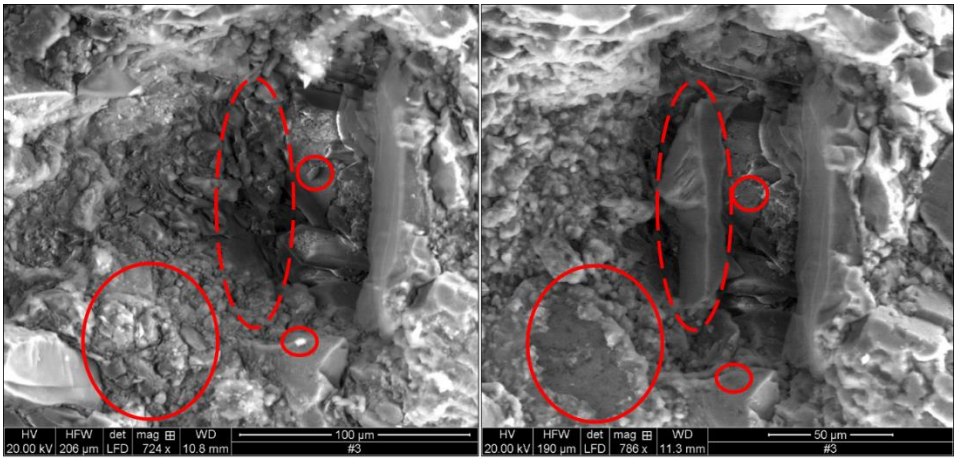

Figure 10. SEM images of a core: (a) before and (b) after a low-salinity coreflood experiment (Yang et al., 2022).

The above literature review on fines migration in porous media and consequent formation damage shows that the three-point pressure method, as developed previously for deepbed filtration and reactive flows, can significantly improve the quality of prediction of formation damage fines migration. This method for fines migration is not available. This thesis closes the gap. A detailed presentation of the results is given in Chapter 5.

2.4. Laboratory tests based on analytical model for two-phase flows in porous media

Two-phase flow in a porous medium is defined as two immiscible fluids which occupy the same pore space. Of the two phases, the wetting phase (often water) is more wetting to the porous medium than the other phase, the non-wetting phase (often oil or gas). A simple schematic of such a composition in a porous medium is shown in Figure 11.

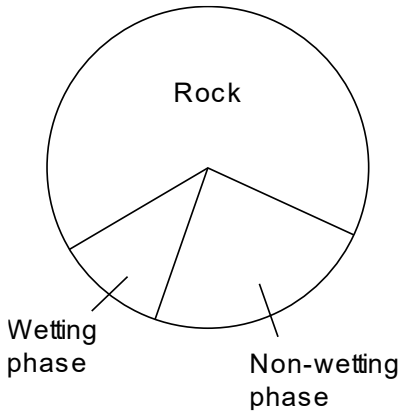

Figure 11. Schematic of the composition of a porous medium under two-phase immiscible flow.

Relative permeability k_r and capillary pressure p_c, which are functions of water saturation s, are the two main model functions for describing two-phase flow in porous media. These functions form an input into reservoir simulation in oil and gas production, water resources management, plant irrigation, and geothermal projects (Lake, 1989, Rabinovich, 2019, Raoof and Hassanizadeh, 2012, Sorey et al., 1980). The Rapoport-

Leas equation (Barenblatt et al., 1990), shown in Eq. (33), describes the 1D two-phase transport accounting for capillary effects and solves the unknown *s*:

$$\phi \frac{\partial s}{\partial t} + U \frac{\partial f(s)}{\partial x} = -\frac{\sqrt{k\phi}\sigma \cos\theta}{\mu_n} \frac{\partial}{\partial x}\left(f(s) k_{rn}(s) \frac{\partial J(s)}{\partial x} \right) \tag{33}$$

$$f(s) = \left(1 + \frac{k_{rn}(s)\mu_w}{k_{rw}(s)\mu_n} \right)^{-1} \tag{34}$$

$$J(s) = \frac{p_c \sqrt{k\phi}}{\sigma \cos\theta} \tag{35}$$

where $f(s)$ and $J(s)$ are the fractional flow and Leverett functions, respectively, σ is the interfacial tension between the wetting and non-wetting phase, θ is the contact angle, μ is the viscosity, and subscripts w and n represent the wetting and non-wetting phase, respectively.

Assuming the total velocity for the two phases is constant and summative, applying Darcy's equation accounting for two-phase flow and Eq. (35) results in Eq. (36), which allows for the determination of the wetting phase pressure:

$$U = -k\left(\frac{k_{rw}(s)}{\mu_w} + \frac{k_{rn}(s)}{\mu_n} \right) \frac{\partial p_w}{\partial x} - \frac{k k_{rn}(s)}{\sqrt{\frac{k}{\phi}}\mu_n} \frac{\partial \left(\sigma \cos\theta J(s) \right)}{\partial x} \tag{36}$$

For a given injected water fraction F_n, it is defined as:

$$F_n = \frac{U_w}{U_w + U_n} \tag{37}$$

Figure 12 presents a schematic for the laboratory test determining relative permeabilities of a SSTT. Figure 12a shows the simultaneous measurements of pressure drop across the core and breakthrough water cut for the given injected water fraction F_n under steady-state condition, while Figure 12c shows the next injected water fraction F_{n+1}. Figure 12b

illustrates the transition between the two steady states. Schematics of a steady-state coreflooding experiment are shown in Figure 12a and Figure 12c.

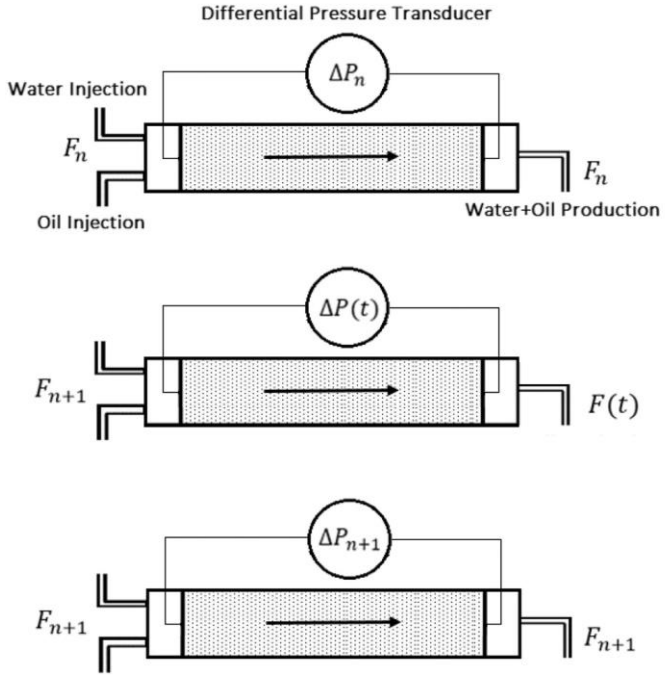

Figure 12. Schematics of a two-phase steady-state-transient test: (a) steady-state flow with injected water fraction F_n, b) transient state flow with F_{n+1}, and c) steady-state flow with F_{n+1}, where n=1,2…(Borazjani et al., 2021a).

Introducing dimensionless parameters and variables, shown in (38),

$$X=\frac{x}{L},\ T=\frac{Ut}{\phi L},\ P_n=\frac{kp_n}{UL\mu_n},\ P_w=\frac{kp_w}{UL\mu_w},\ \varepsilon=\frac{\sqrt{k\phi}\sigma\cos\theta}{UL\mu_n} \tag{38}$$

transforms Eqs. (33) and (36) into the dimensionless form;

$$\frac{\partial s}{\partial T}+\frac{\partial f(s)}{\partial X}=\varepsilon\frac{\partial^2\psi(s)}{\partial X^2} \tag{39}$$

$$\frac{\partial P_w}{\partial X}=-\left(1+\varepsilon k_{rn}(s)\frac{\partial J}{\partial X}\right)\left(\frac{k_{rw}(s)\mu_n}{\mu_w}+k_{rn}(s)\right)^{-1} \tag{40}$$

where

$$\frac{\partial\psi(s)}{\partial s}=-k_{rn}(s)\,f(s)\frac{\partial J(s)}{\partial s} \tag{41}$$

The capillary pressure is equal to zero downstream from the core, in the set-up shown in Figure 12, as the two phases enter an open space. With the assumption of pressure continuity within the system, the outlet capillary pressure is also equal to zero. This corresponds to the outlet boundary condition being:

$$X = 1:\ J(s) = 0 \tag{42}$$

At the inlet, equality between the wetting phase velocity for the current stage, where F_n, and the next stage, where $F_n + \delta = F_{n+1}$, must be achieved. Therefore, the inlet boundary condition is:

$$X = 0:\ f(s) - \varepsilon \frac{\partial \psi(s)}{\partial X} = F_n + \delta, \qquad \delta \ll 1 \tag{43}$$

Assuming Eq. (39) is under a steady state, integrating Eq. (39) with respect to X allows for the initial condition for the transient state solution:

$$T = 0:\ \frac{1 - X}{\varepsilon} = \int_{s}^{s(J=0)} \frac{k_{rn}(s) f(s) J'(s)}{F_n - f(s)} ds \tag{44}$$

The dimensionless constant ε on the right-hand-side of Eq. (39) is the capillary-viscous ratio, a ratio between the capillary and viscous forces. In large-scale approximations, where L is very large, ε becomes very small, i.e., $\varepsilon \ll 1$; therefore, the effects of capillary pressure become negligible. This allows for the use of the Buckley-Leverett equation to describe the 1D two-phase transport (Lake, 1989):

$$\frac{\partial s}{\partial T} + \frac{\partial f(s)}{\partial X} = 0 \tag{45}$$

The solution for Eq. (45) is presented in works by Barenblatt et al. (1990) and Lake (1989).

2.4.1. 1D steady-state-transient test

For sufficiently long cores, low capillary pressure, or high viscous force, the large-scale approximation conditions are fulfilled during the unsteady-state water injection (Al-Sarihi et al., 2020, Bedrikovetsky, 2013). The unsteady-state Welge-JBN method, using the inverse solution for the direct problem of the Buckley-Leverett solution, determines $k_{rw}(s)$ and $k_{rn}(s)$. The laboratory measurements for the Welge-JBN method are pressure drop across the core and water-cut history at the core outlet (Johnson et al., 1959, Welge, 1952).

The accuracy of the Welge-JBN method has been investigated numerically by Al-Sarihi et al. (2020). When the capillary-viscous ratio is less than 0.5, relative permeabilities obtained from data generated by the numerical Rapoport-Leas model do not significantly change from the data generated by the Buckley-Leverett model. This important result significantly widens the area of applicability of the Welge-JBN method. However, values of the capillary viscous ratio can go up to 30 in natural cores (Al-Sarihi et al., 2020, Lake, 1989).

Hussain et al. (2012) obtained explicit formulae for wetting-phase saturation along the core, accounting for capillary pressure, using the method of matched asymptotic expansions. However, this solution is only valid for a small capillary-viscous ratio. The capillary pressure function must be defined in order to solve the system. This means that capillary pressure must be defined independently of the steady-state coreflood test. The results can be inconsistent with the data obtained from the coreflooding. Although the traditional porous plate (Greder et al., 1997, Vavra et al., 1992) or centrifuge methods (Donaldson et al., 1991, Hoffman, 1963, Slobod et al., 1951) have high accuracy, the filling conditions are different from the coreflood (Brown, 1951, Reed and Maas, 2018, van der Post et al., 2000). Furthermore, the capillary pressure is not usually measured in

the same core, where waterflooding has been conducted; rather, the sister cores are usually used, which also yields some inconsistencies. The above facts explain the shortcoming of the asymptotic method for determining relative permeabilities for the core tests. Nevertheless, the asymptotic method is significantly more effective than history matching from numerical simulation inverse solvers.

The steady-state method essentially involves directly calculating relative permeability from Darcy's equation for two-phase flow. Figure 12a and Figure 12c show the schematic of this method. Typically, the number of steady-state tests varies from 4 to 15. A limitation of the steady-state test for determining relative permeability is that it can be determined only between the inlet wetting phase saturation (which can be significantly larger than the initial wetting phase saturation) and 1-s_{nr}, where s_{nr} is the residual non-wetting phase saturation. As mentioned above, capillary pressure must be determined separately by the porous plate or centrifuge method from a sister core. Therefore, the steady-state method does not allow for the simultaneous determination of relative permeability and capillary pressure functions.

Gupta and Maloney (2015) presented a solution to the above-mentioned steady-state test shortcomings by alternating between two injection velocities. This allows for the relative permeability and capillary pressure functions to de-couple. While using the third velocity can significantly increase the accuracy of the test and decrease data scattering, it also significantly increases the time needed to conduct the test.

Another method to simultaneously determine the relative permeability and capillary functions is through the use of X-ray computational tomography (CT) to obtained in-situ water saturations along the core (Hussain, 2012, Hussain et al., 2014). This avoids the

issue of inconsistent systems for determining the two functions; however, X-ray CT equipment is expensive and not readily available.

The closed system for 1D two-phase flow accounting for capillary effects is defined by Eqs. (39) and (40), subjected to boundary conditions, (42) and (43), while the initial condition (44) is defined and has been solved uniquely. For an oil and water system, the procedure for the solution can be found in Borazjani et al. (2021a), while for a gas and water system, the solution can be found in Borazjani et al. (2021b). Both procedures allow for the simultaneous determination of relative permeability and capillary pressure functions based on measurements of breakthrough water-cut and pressure drop across the core. These methods use both the steady-state and transient state of the measured data, and hence the name steady-state-transient test (SSTT). Chapters 6 and 7 of this thesis validate this method by analysing the 3D effects on the SSTT method and laboratory testing with accuracy and uncertainty control, respectively.

2.4.2. 2D Steady-state flows near wells

Figure 9b shows that near a fractured well, 1D flow approximation can be used. However, the well drainage radius can be significantly higher than the 1D flow radius, as shown in Figure 13.

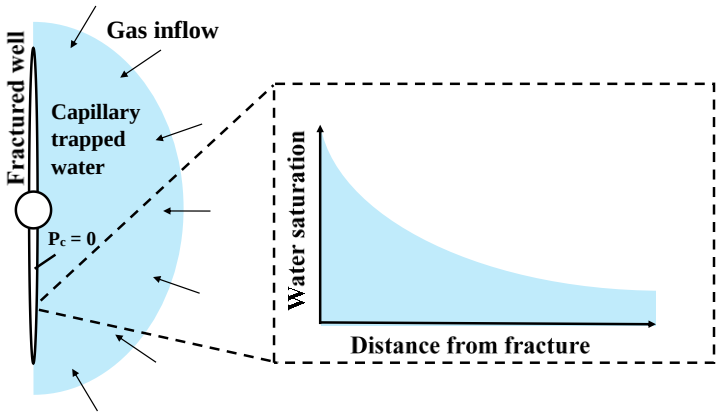

Figure 13. Schematic of steady-state two-phase flow accounting for capillary end effects near a hydraulically fractured production well (Naik et al., 2019).

An exact 2D solution for the steady-state two-phase flow would describe the effect of capillary trapped water on oil or gas production more precisely than the 1D flow solution. This complex 2D solution would be able to describe formation damage due to blocking by the wetting phase near a hydraulically fractured production well. Thus, a skin factor could be predicted and different well stimulation techniques could be used to remove the capillary trapped water. However, this analytical solution is not available.

Steady-state solutions for single-phase flow problems in complex 2D geometries have been solved for different well configurations (Bear, 1988, Bedrikovetsky, 2013). Approximate analytical solutions for two-phase flow problems in complex 2D geometries using streamline methods are cumbersome to use. The exact solution for two-phase flow towards a fractured well, including the particular case of one immobile phase, has not been derived.

Naik et al. (2018, 2015) discussed a solution for 1D two-phase steady-state flows and their applications, accounting for compressibility of the non-wetting phase. 1D solutions were presented for both linear and radial flows. It was found that wettability alternation, as well as 2D effects during flow towards a fractured producer, are of paramount importance in well stimulation. However, the effects on steady-state flows have not been investigated. Chapter 8 presents the exact solution for two-phase steady-state flow towards a hydraulically fractured well and studies the effects of contact angle (wettability) on the well index.

2.5. References

AHMED, S. J. 2004. *Laboratory study on precipitation of calcium sulphate in berea sandstone cores.* Master of Science, King Fahd University of Petroleum and Minerals

AL-SARIHI, A., YOU, Z., BEHR, A., GENOLET, L., KOWOLLIK, P., ZEINIJAHROMI, A. & BEDRIKOVETSKY, P. 2020. Admissible parameters for two-phase coreflood and Welge–JBN method. *Transport in Porous Media,* 131, 831-871.

ALVAREZ, A., BEDRIKOVETSKY, P., HIME, G., MARCHESIN, A., MARCHESIN, D. & RODRIGUES, J. 2005. A fast inverse solver for the filtration function for flow of water with particles in porous media. *Inverse problems,* 22, 69.

ALVAREZ, A. C., HIME, G., MARCHESIN, D. & BEDRIKOVETSKY, P. G. 2007. The inverse problem of determining the filtration function and permeability reduction in flow of water with particles in porous media. *Transport in Porous Media,* 70, 43-62.

BARENBLATT, G. I., ENTOV, V. M. & RYZHIK, V. M. 1990. *Theory of fluid flows through natural rocks,* Dordrecht, Springer Science+Business Media.

BEAR, J. 1988. *Dynamics of fluids in porous media,* New York, Dover Publications.

BEDRIKOVETSKY, P. 2013. *Mathematical theory of oil and gas recovery with applications to ex-USSR oil and gas fields,* Dorbrecht, Kluwer Academic Publishers.

BEDRIKOVETSKY, P., MARCHESIN, D., SHECAIRA, F., SOUZA, A., MILANEZ, P. & REZENDE, E. 2001. Characterisation of deep bed filtration system from laboratory pressure drop measurements. *Journal of Petroleum Science and Engineering,* 32, 167-177.

BEDRIKOVETSKY, P., SIQUEIRA, F. D., FURTADO, C. A. & SOUZA, A. L. S. 2011. Modified particle detachment model for colloidal transport in porous media. *Transport in porous media,* 86, 353-383.

BEDRIKOVETSKY, P., ZEINIJAHROMI, A., SIQUEIRA, F. D., FURTADO, C. A. & DE SOUZA, A. L. S. 2012. Particle detachment under velocity alternation during suspension transport in porous media. *Transport in Porous Media,* 91, 173-197.

BETHKE, C. 1996. *Geochemical reaction modeling: Concepts and applications*, Oxford University Press on Demand.

BETHKE, C. M. 2007. *Geochemical and biogeochemical reaction modeling*, Cambridge university press.

BORAZJANI, S., HEMMATI, N., BEHR, A., GENOLET, L., MAHANI, H., ZEINIJAHROMI, A. & BEDRIKOVETSKY, P. 2021a. Determining water-oil relative permeability and capillary pressure from steady-state coreflood tests. *Journal of Petroleum Science and Engineering,* 205, 108810.

BORAZJANI, S., HEMMATI, N., BEHR, A., GENOLET, L., MAHANI, H., ZEINIJAHROMI, A. & BEDRIKOVETSKY, P. 2021b. Simultaneous determination of gas–water relative permeability and capillary pressure from steady-state corefloods. *Journal of Hydrology,* 598, 126355.

BRADFORD, S. A., TORKZABAN, S. & SHAPIRO, A. 2013. A theoretical analysis of colloid attachment and straining in chemically heterogeneous porous media. *Langmuir,* 29, 6944-6952.

BROWN, H. W. 1951. Capillary pressure investigations. *Journal of Petroleum Technology,* 3, 67-74.

CHEQUER, L., VAZ, A. & BEDRIKOVETSKY, P. 2018. Injectivity decline during low-salinity waterflooding due to fines migration. *Journal of Petroleum Science and Engineering,* 165, 1054-1072.

CIVAN, F. 2015. *Reservoir formation damage,* United States, Gulf Professional Publishing.

DONALDSON, E. C., EWALL, N. & SINGH, B. 1991. Characteristics of capillary pressure curves. *Journal of Petroleum Science and Engineering,* 6, 249-261.

DREVER, J. I. 1982. The geochemistry of natural waters.

ELIMELECH, M., GREGORY, J. & JIA, X. 2013. *Particle deposition and aggregation: measurement, modelling and simulation*, Butterworth-Heinemann.

EVANS, A. M. 2009. *Ore geology and industrial minerals: an introduction*, John Wiley & Sons.

FOGLER, H. S. 2010. *Essentials of chemical reaction engineering,* Upper Saddle River, NJ, Pearson Education.

GHADERI, S., KHARRAT, R. & TAHMASEBI, H. 2009. Experimental and theoretical study of calcium sulphate precipitation in porous media using glass micromodel. *Oil & Gas Science and Technology - Rev lFP,* 64, 489-501.

GREDER, H., GALLATO, V., CORDELIER, P., LARAN, D., MUNOZ, V. & D'ABRIGEON, O. 1997. Forty comparisons of mercury injection data with oil/water capillary pressure measurements by the porous plate technique. *Society of Core Analysis, SCA*, 9710.

GUPTA, R. & MALONEY, D. Applications of the intercept method to correct steady-state relative permeability for capillary end-effects. International Symposium of the Society of Core Analysts 2015 Canada. 16-21.

HOFFMAN, R. N. 1963. A technique for the determination of capillary pressure curves using a constantly accelerated centrifuge. *Society of Petroleum Engineers Journal*, 3, 227-235.

HUSSAIN, F. 2012. *Testing Predictive Value of Image-Based Predictions for Two-Phase Drainage Relative Permeability*. Citeseer.

HUSSAIN, F., CINAR, Y. & BEDRIKOVETSKY, P. 2012. A semi-analytical model for two phase immiscible flow in porous media honouring capillary pressure. *Transport in porous media*, 92, 187-212.

HUSSAIN, F., PINCZEWSKI, W. V., CINAR, Y., ARNS, J.-Y., ARNS, C. & TURNER, M. 2014. Computation of relative permeability from imaged fluid distributions at the pore scale. *Transport in porous media*, 104, 91-107.

JOHNSON, E., BOSSLER, D. & NAUMANN, V. 1959. Calculation of relative permeability from displacement experiments. *Transactions of the AIME*, 216, 370-372.

KLEINITZ, W., KOEHLER, M. & DIETZSCH, G. The precipitation of salt in gas producing wells. SPE European formation damage conference, 2001. OnePetro.

LAKE, L. W. 1989. *Enhanced oil recovery*, Upper Saddle River, NJ, Prentice Hall.

LASAGA, A. C. 2014. *Kinetic theory in the earth sciences*, Princeton university press.

LE, D. & MAHADEVAN, J. 2011. Productivity loss in gas wells caused by salt deposition. *SPE Journal*, 16, 908-920.

MACKAY, E. 2003. Predicting in situ sulphate scale deposition and the impact on produced ion concentrations. *Chemical Engineering Research and Design*, 81, 326-332.

MACKAY, E. J. Modelling of in-situ scale deposition: The impact of reservoir and well geometries and kinetic reaction rates. International Symposium on Oilfield Scale, 2002. OnePetro.

MANAHAN, S. 2017. *Environmental chemistry*, CRC press.

MOGHADASI, J., MÜLLER-STEINHAGEN, H., JAMIALAHMADI, M. & SHARIF, A. 2004. Model study on the kinetics of oil field formation damage due to salt precipitation from injection. *Journal of Petroleum Science and Engineering*, 43, 201-217.

NAIK, S., YANG, S., WOOLLEY, M. & BEDRIKOVETSKY, P. 2019. Analytical modelling of the water block phenomenon in hydraulically fractured wells. *Journal of Natural Gas Science and Engineering*, 67, 56-70.

NAIK, S., YOU, Z. & BEDRIKOVETSKY, P. 2015. Rate enhancement in unconventional gas reservoirs by wettability alteration. *Journal of Natural Gas Science and Engineering*, 26, 1573-1584.

NAIK, S., YOU, Z. & BEDRIKOVETSKY, P. 2018. Productivity index enhancement by wettability alteration in two-phase compressible flows. *Journal of Natural Gas Science and Engineering*, 50, 101-114.

OLIVEIRA, M. A., VAZ, A. S., SIQUEIRA, F. D., YANG, Y., YOU, Z. & BEDRIKOVETSKY, P. 2014. Slow migration of mobilised fines during flow in reservoir rocks: laboratory study. *Journal of Petroleum Science and Engineering*, 122, 534-541.

RABINOVICH, A. 2019. An analytical solution for cyclic flow of two immiscible phases. *Journal of Hydrology*, 570, 682-691.

RAOOF, A. & HASSANIZADEH, S. 2012. A new formulation for pore-network modeling of two-phase flow. *Water Resources Research*, 48.

REED, J. & MAAS, J. Review of the intercept method for relative permeability correction using a variety of case study data. The International Symposium of the Society of Core Analysts, 2018.

RUSSELL, T. & BEDRIKOVETSKY, P. 2018. Colloidal-suspension flows with delayed fines detachment: Analytical model & laboratory study. *Chemical Engineering Science*, 190, 98-109.

SLOBOD, R., CHAMBERS, A. & PREHN, W. 1951. Use of centrifuge for determining connate water, residual oil, and capillary pressure curves of small core samples. *Journal of Petroleum Technology*, 3, 127-134.

SOREY, M. L., GRANT, M. A. & BRADFORD, E. 1980. Nonlinear effects in two-phase flow to wells in geothermal reservoirs. *Water Resources Research*, 16, 767-777.

VAN DER POST, N., MASALMEH, S., COENEN, J., VAN DER GIJP, K. & MAAS, J. Relative permeability, hysteresis and I-Sw measurements on a carbonate prospect. 14th International Symposium of the Society of Core Analyst, Abu Dhabi, 2000.

VAN DORP, Q. T., SLIJKHUIS, M. & ZITHA, P. L. J. Salt precipitation in gas reservoirs. 8th European Formation Damage Conference, 2009. OnePetro.

VAVRA, C. L., KALDI, J. G. & SNEIDER, R. M. 1992. Geological applications of capillary pressure: a review. *AAPG bulletin*, 76, 840-850.

VAZ, A., BEDRIKOVETSKY, P., FERNANDES, P., BADALYAN, A. & CARAGEORGOS, T. 2017. Determining model parameters for non-linear deep-bed filtration using laboratory pressure measurements. *Journal of Petroleum Science and Engineering*, 151, 421-433.

VAZ, A., MAFFRA, D., CARAGEORGOS, T. & BEDRIKOVETSKY, P. 2016. Characterisation of formation damage during reactive flows in porous media. *Journal of Natural Gas Science and Engineering*, 34, 1422-1433.

WELGE, H. J. 1952. A simplified method for computing oil recovery by gas or water drive. *Journal of Petroleum Technology*, 4, 91-98.

YANG, S., OSIPOV, Y., XU, C., KUZMINA, L., RUSSELL, T. & BEDRIKOVETSKY, P. 2022. Analytical solution for large-deposit non-linear reactive flows in porous media. *Chemical Engineering Journal*, 430, 132812.

3. Analytical solution for large-deposit non-linear reactive flows in porous media

Yang, S., Osipov, Y., Xu, C., Kuzmina, L., Russell, T. and Bedrikovetsky, P.

Chemical Engineering Journal, p.132812.

Statement of Authorship

Title of Paper	Analytical solution for large-deposit non-linear reactive flows in porous media
Publication Status	☑ Published ☐ Accepted for Publication ☐ Submitted for Publication ☐ Unpublished and Unsubmitted work written in manuscript style
Publication Details	Yang, S., Osipov, Y., Xu, C., Kuzmina, L., Russell, T. and Bedrikovetsky, P., 2021. Analytical solution for large-deposit non-linear reactive flows in porous media. Chemical Engineering Journal, p.132812.

Principal Author

Name of Principal Author (Candidate)	Shuyan Yang		
Contribution to the Paper	Literature search for laboratory data, data matching and interpretation, development and derivation of micromodels for fitting parameters, manuscript preparation		
Overall percentage (%)	70%		
Certification:	This paper reports on original research I conducted during the period of my Higher Degree by Research candidature and is not subject to any obligations or contractual agreements with a third party that would constrain its inclusion in this thesis. I am the primary author of this paper.		
Signature		Date	13/11/2021

Co-Author Contributions

By signing the Statement of Authorship, each author certifies that:

i. the candidate's stated contribution to the publication is accurate (as detailed above);

ii. permission is granted for the candidate in include the publication in the thesis; and

iii. the sum of all co-author contributions is equal to 100% less the candidate's stated contribution.

Name of Co-Author	Yuri Osipov		
Contribution to the Paper	Derivation of the analytical solution		
Signature		Date	11/11/21

Name of Co-Author	Chengyuan Xu		
Contribution to the Paper	Literature search for laboratory data, data matching		
Signature		Date	11/11/21

Name of Co-Author	Liudmila Kuzmina		
Contribution to the Paper	Derivation of the analytical solution, problem formulation		
Signature		Date	11/11/21

Name of Co-Author	Thomas Russell		
Contribution to the Paper	Development and derivation of micromodels for fitting parameters, manuscript preparation and editing		
Signature		Date	13/11/2021

Name of Co-Author	Pavel Bedrikovetsky		
Contribution to the Paper	Problem formulation, supervision of the development of the work, manuscript preparation and revision		
Signature		Date	11/11/21

Chemical Engineering Journal 430 (2022) 132812

Contents lists available at ScienceDirect

Chemical Engineering Journal

journal homepage: www.elsevier.com/locate/cej

Analytical solution for large-deposit non-linear reactive flows in porous media

Shuyan Yang [a], Yuri Osipov [b], Chengyuan Xu [a,c], Liudmila Kuzmina [d], Thomas Russell [a], Pavel Bedrikovetsky [a,*]

[a] The University of Adelaide, Australia
[b] Moscow State University of Civil Engineering, Russia
[c] Southwest Petroleum University, China
[d] National Research University Higher School of Economics, Russia

ARTICLE INFO

Keywords:
Porous media
Reactive flow
Exact solution
Laboratory study
Rate coefficient
Permeability

ABSTRACT

We discuss reactive flows in porous media that exhibit an irreversible chemical reaction between two components, resulting in large solid-product deposition. Previous works used the analytical solution for the linear problem with low deposition to determine model parameters from the reactant breakthrough concentrations and pressure drop growth across the core during laboratory coreflood. The present work derives an exact analytical solution for the non-linear problem with large solid-product deposition. We use the solution for interpretation of the laboratory data, and determination of the type curves for the measured values. Seven sets of experimental data are shown to closely match the data from the analytical model, which validates the analytical model.

1. Introduction

Reactive flows in porous media occur in numerous technological processes of chemical, environmental, and petroleum engineering. The incomplete list of examples includes commingled flows of incompatible waters with different ion compositions in aquifers, saline water intrusion into natural water reservoirs, water injection into geothermal reservoirs in enhanced energy projects, waterflooding in oilfields, etc. [1–4]. These chemical reactions alter the reactant concentrations during geochemical flows; the precipitation of solid products causes permeability reduction and consequent formation damage [4,5]. For oil displacement by water, the reactions can enhance oil recovery, whereas permeability decline reduces well productivity [5]. For example, injection of sulphate-rich seawater into oilfields causes incompatibility with metal-rich formation water, yielding precipitation of insoluble salts, leading to decline in well injectivity and productivity (Fig. 1a and 1b) [6,7].

Consider an irreversible reaction between two species that produces solid product deposition in a porous medium:

$$qQ + rR \rightarrow D \tag{1}$$

where Q and R represent reactants 1 and 2 with their corresponding stoichiometric coefficients q and r, and D is the deposit [1,4].

The reaction rate is given by the law of mass action [1–3,8]:

$$\frac{\partial \sigma}{\partial t} = \lambda(\sigma) U c_1^q c_2^r \tag{2}$$

where σ, c_1, and c_2 are the molar concentrations of the deposit, reactant 1, and reactant 2, respectively, U is the Darcy velocity, and $\lambda(\sigma)$ is the kinetics rate function (Fig. 1c). The product λU is called the reaction rate constant. Eq. (2) is applicable at different reservoir scales [9]. Varying $\lambda(\sigma)$ reflects changes in the solid–liquid interface shape and area during deposition [4,10,11].

The deposition causes permeability damage. Consider the power law form of the permeability damage ratio [12]:

$$\frac{k_0}{k(\sigma)} = (1 + \beta\sigma)^n \tag{3}$$

where k_0 is the initial permeability, β is the formation damage coefficient, and n is the damage exponent. The "default" case $n = 1$ corresponds to keeping the first two terms in Taylor's expansion for the function of σ in right hand side of Eq. (3).

At low deposit concentrations, where the model coefficients λ and β can be assumed to be constant, and $n = 1$, the analytical solution for the one-dimensional (1D) reactive flow problem provides explicit formulae for the concentrations and pressure drop across the core [13]. The

* Corresponding author.
E-mail address: pavel.bedrikovetsky@adelaide.edu.au (P. Bedrikovetsky).

https://doi.org/10.1016/j.cej.2021.132812
Received 14 September 2021; Received in revised form 1 October 2021; Accepted 3 October 2021
Available online 10 October 2021

Nomenclature

a	surface area, L^2, m^2
A_v	specific internal surface area
b	reaction capacity coefficient constant, L^3 mol^{-1}, m^3 mol^{-1}
c	molar concentration of reactant, mol L^{-3}, mol m^{-3}
C	dimensionless molar concentration of reactant
C_v	coefficient of variation
c^0	injected molar concentration of reactant, mol L^{-3}, mol m^{-3}
f	probability density function for pore size
g	conductance, L^4, m^4
k	permeability, L^2, m^2
L	core length, L, m
M	molecular weight, g/mol
n	permeability damage exponent
p	pressure, $ML^{-1}T^{-2}$, N m^{-2}
p_c	percolation threshold
q	stoichiometric coefficient of reactant 1
r	stoichiometric coefficient of reactant 2
r_e	effective radius, L, m
r_{min}	minimum pore throat radius, L, m
r_s	precipitate particle radius, L, m
S	dimensionless molar deposit concentration
t	time, T, s
T	dimensionless time, T, s
U	Darcy flow velocity, L T^{-1}, ms^{-1}
v	volume of one precipitate, L^3, m^3
V	volumetric concentration
x	coordinate, L, m
X	dimensionless coordinate
z	coordination number

Greek Letters

α, γ	dimensionless parameters
β	formation damage coefficient
δp	pressure drop across the core, $ML^{-1}T^{-2}$, N m^{-2}
δP	dimensionless pressure drop across the core
η	fraction of pores which are conductive
κ	power-law exponent
$\lambda(\sigma)$	reaction rate function
λ_0	reaction rate coefficient, $L^{3q+3r-4}$ mol^{1-q-r}, $m^{3q+3r-4}$ mol^{1-q-r}
Λ_0	dimensionless reaction rate coefficient
μ	viscosity, $ML^{-1}T^{-1}$, kg m^{-1} s^{-1}
ν	correlation radius index
ρ	density, ML^{-3}, kg/m^3
σ	deposit molar concentration, mol L^{-3}, mol m^{-3}
τ	Lagrangian coordinate or tortuosity
ϕ	porosity

Subscript

0	initial (for area, permeability and pressure)
1	first reactant
2	second reactant
av	averaged value
r	rock
σ	precipitate/solid

solution exhibits steady-state profiles of the reacting species and also shows that the growth in deposit concentration and the pressure drop versus time are linear; the breakthrough time is equal to one pore volume injected (PVI) and the breakthrough concentration (BTC) curves stabilize at the breakthrough moment instantly [13]. Further in the text, we refer to this case as "linear reactive flow". However, in numerous laboratory tests time-varying breakthrough concentrations and non-linear pressure drop variations are observed, which are attributed to large deposit concentrations [14–16]. We refer to this case as "non-linear reactive flow".

For non-linear reactive flows, the deposit accumulation alters the rock surface where the reactions occur, yielding variation of the kinetics rate function, i.e. $\lambda = \lambda(\sigma)$ [4,10,11]. For large deposits, where the linear Taylor's approximation is not valid, the damage exponent n is not equal to one. The non-linear pressure drop variation versus time and the non-steady-state breakthrough concentrations during reactive flow tests are attributed to changes in the deposit-dependent kinetics rate function.

Mathematical modelling using laboratory-based values of the kinetics rate function $\lambda(\sigma)$, formation damage coefficient β, and damage exponent n is an important step in the design and implementation of numerous chemical, environmental, and petroleum engineering technologies that involve reactive flows in porous media. The kinetics rate function, formation damage coefficient, and damage exponent are empirical parameters reflecting the form of the deposit and complex geometry of porous rocks. Therefore, these parameters can be determined only by tuning the laboratory data from reactive flow tests (Fig. 2) using mathematical modelling. This involves solving the inverse problems for the governing system of reactive flows in porous media that

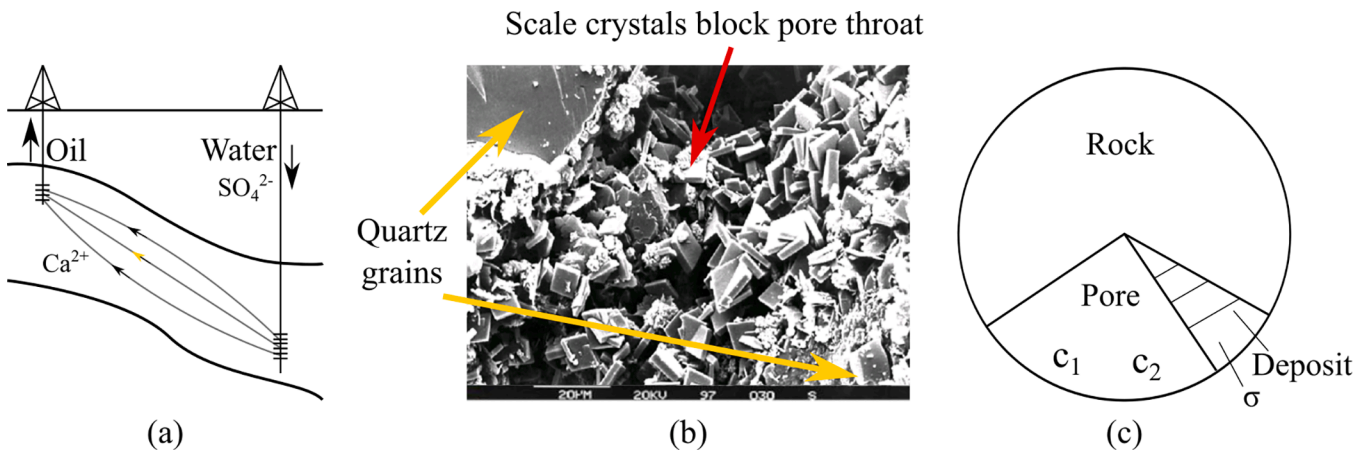

Fig. 1. Schematic for reactive flows in subterranean reservoirs: (a) streamlines during injection of incompatible water in oil reservoir; (b) precipitated barium sulphate crystals on the quartz grain surfaces; (c) two reactants and solid deposit in porous space.

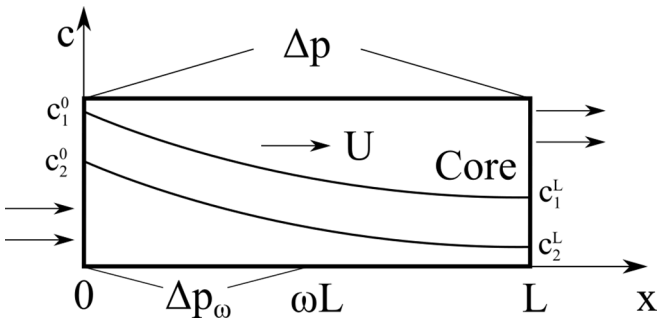

Fig. 2. Schematic for laboratory coreflood by commingled injection of two incompatible waters.

includes Eqs. (2) and (3).

The inverse solution is based on an iterative minimization algorithm for the best match that includes the solution of the direct problem at each iteration, making the inverse problem cumbersome and computationally expensive. Besides, non-uniqueness of inverse solutions and ill-posed inverse problems are significant obstacles for the determination of the model functions from the laboratory data.

One way of dealing with this problem is the analytical modelling of 1D transport, describing the laboratory reactive-flow tests. Exact solutions of direct 1D problems can regularise inverse problems, yielding stable and unique inverse solutions. The examples of suspension transport in porous media [17,18] and two-phase immiscible displacement [5,19] show that the exact solution of the direct problem can significantly simplify the problem of system characterisation from the measured laboratory data. Moreover, an exact solution can regularize the ill-posed inverse problem. Besides, exact solutions can benchmark numerical models, and facilitate extra-fast quasi 3D streamline modelling [20]. This explains the intensive research on analytical modelling of reactive flows in porous media [5,21,22].

However, the mathematical model for deposit-dependent reaction kinetics and the corresponding analytical solution for 1D reactive transport are not available.

In the current work, we derive an exact solution for 1D non-linear reactive flow with large deposits. Several transformations and mappings of the independent variables and unknown functions simplify the governing system up to a first-order hyperbolic equation, which is analytically solved by the method of characteristics. An exact analytical solution is derived for a linear deposit-concentration-dependent kinetics rate function. We apply this solution to tune the model parameters, interpret laboratory data by defining the type curves for measured values, and validate the analytical model.

The structure of the text is as follows. Section two discusses the main model assumptions, formulates the basic governing equations, and derives the analytical solution. Section three presents type curves for concentration and pressure drop profiles, and histories for non-linear and linear reactive flows. Section four develops simplifies models to estimate the model coefficients. Section five matches seven laboratory data sets on reactive flows with the analytical model and tunes the model coefficients. Discussion of the model validity in section six and conclusions on the hydrodynamics of non-linear reactive flows in section seven finalize the paper.

2. Mathematical model

In this section, we present the mathematical model for 1D transport with an irreversible chemical reaction between two aqueous components [3,6,7,13]. Section 2.1 discusses the main assumptions. Section 2.2 formulates the governing equations. Section 2.3 presents the exact solution for the general case of arbitrary stoichiometric coefficients; for which the derivations are performed in Appendices A and B. Section 2.4 shows the exact solutions for the particular case where the stoichiometric coefficients are equal to one.

2.1. Assumptions

Molar concentrations of two reactants and deposit are assumed to be small enough not to change the volumetric balance of incompressible carrier water, i.e. the suspension/colloidal density is assumed to be constant. For large concentrations, we introduce volumetric fractions of both reactants, deposit, and carrier water, and assume volume additivity with mixing, reaction, and precipitation (Amagat's law). The individual densities of both reactants, deposit, and of carrier water are assumed to be constant. Adding the volumetric balance equations for both reactants, deposit, and of carrier water results in conservation of the total rate $U = U(t)$ [5]. The above yields the same transport equation for volumetric concentrations as that for small molar concentrations of both reactants, deposit, and of carrier water.

Here we discuss the particular case of flow with constant velocity, U. The reaction kinetics of two species obeys the law of mass action (Eq. (2)) with stoichiometric coefficients q and r for components 1 and 2, respectively. The reaction rate constant is assumed to be proportional to the flow velocity.

The solid precipitate can take the form of individual crystals, pore lining, and dendrites, the form of which can change during precipitation. The dependency $\lambda = \lambda(\sigma)$ is due to the variation of the form and area of the solid–liquid interface [11,23,24]. Fig. 3 presents three different types of kinetic rate function $\lambda(\sigma)$. The case of costant kinetics rate coefficient corresponds to small deposit concentrations, where the precipitation does not change the reaction kinetics (lines 5 and 6). The kinetics rate function becomes a linear function of deposit concentration σ when retaining only the first two terms in the Taylor's series for $\lambda = \lambda(\sigma)$ (lines 1–4). Lines 1–3 correspond to the Langmuir blocking reaction kinetics where the reaction probability is proportional to the amount of vacancies that remains after the deposition, and b^{-1} is the total of vacancies in the clean bed. The lines 1–6 differ by the values of constants λ_0 and b^{-1}, which will be used in sensitivity analysis in section 3. The kinetics of chemical reaction and solid deposition in the incompressible fluid is assumed to be independent of pressure.

The varying permeability $k(\sigma)$ is given by Eq. (3). It is also assumed that the deposit concentration is significantly smaller than porosity and smaller than the percolation threshold where deposition stops the flow [25]. Rock dispersivity coefficient is assumed to be negligible compared to the core size, allowing dispersion/diffusion of reactants to be ignored [26–28]. The porosity of the rock is assumed to remain constant.

2.2. Governing equations

The mathematical model for one-dimensional reactive flow in porous media consists of mass balance equations for the two reactants in the aqueous phase, kinetics equation for the reaction rate, and a modified

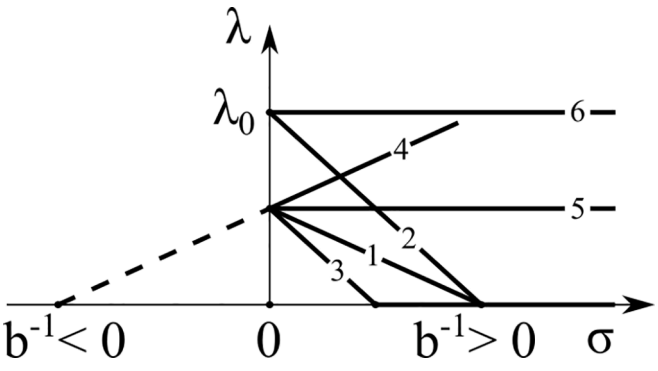

Fig. 3. Three types of reaction rate functions $\lambda = \lambda(\sigma)$.

form of Darcy's law to account for permeability damage due to the reaction product precipitation [1,2,13,27,29]:

$$\phi\frac{\partial c_1}{\partial t}+U\frac{\partial c_1}{\partial x}=-\frac{\partial \sigma}{\partial t} \tag{4}$$

$$\phi\frac{\partial c_2}{\partial t}+U\frac{\partial c_2}{\partial x}=-\frac{\partial \sigma}{\partial t} \tag{5}$$

$$\frac{\partial \sigma}{\partial t}=\lambda(\sigma)Uc_1^q c_2^r,\ \ \lambda(\sigma)=\begin{cases}\lambda_0(1-b\sigma), & \sigma<b^{-1}\\ 0, & \sigma>b^{-1}\end{cases} \tag{6}$$

$$U=-\frac{k_0}{\mu(1+\beta\sigma)^n}\frac{\partial p}{\partial x} \tag{7}$$

Here p is the pressure, μ is the carrier water viscosity, and ϕ is the formation porosity. We retain the first two terms in the Taylor series for the kinetics rate function $\lambda(\sigma)$ in Eq. (2), so in Eq. (6), the initial kinetics rate coefficient is $\lambda_0=\lambda(0)$ and the reaction capacity coefficient is $b=-\lambda'(0)/\lambda(0)$.

We introduce the following dimensionless variables and parameters:

$$X=\frac{x}{L},\ T=\frac{Ut}{\phi L},\ C_1=\frac{c_1}{c_1^0},\ C_2=\frac{c_2}{c_2^0},\ S=b\sigma,\ P=\frac{k_0 p}{U\mu L},$$
$$\Lambda_0=\lambda_0 bL\phi\left(c_1^0\right)^q\left(c_2^0\right)^r,\ \alpha=\frac{1}{c_1^0 b\phi},\ \gamma=\frac{1}{c_2^0 b\phi} \tag{8}$$

where L is the core length, and $c_1{}^0$ and $c_2{}^0$ are the injection concentrations of reactants 1 and 2, respectively.

In the linear case, where $b=0$, we define the dimensionless precipitate concentration S, the initial kinetics rate coefficient Λ_0, and the ratio between the injected concentrations γ as:

$$S=\frac{\sigma}{\phi c_1^0},\ \Lambda_0=\lambda_0 Lc_2^0,\ \gamma=\frac{c_1^0}{c_2^0} \tag{9}$$

and $\alpha=1$.

Introduction of dimensionless parameters (8) transforms system (4-7) to the following dimensionless system:

$$\frac{\partial C_1}{\partial T}+\frac{\partial C_1}{\partial X}=-\alpha\frac{\partial S}{\partial T} \tag{10}$$

$$\frac{\partial C_2}{\partial T}+\frac{\partial C_2}{\partial X}=-\gamma\frac{\partial S}{\partial T} \tag{11}$$

$$\frac{\partial S}{\partial T}=\Lambda(S)C_1^q C_2^r,\ \Lambda(S)=\begin{cases}\Lambda_0(1-S), & S<1\\ 0, & S>1\end{cases} \tag{12}$$

$$1=-\frac{1}{\left(1+\frac{\beta S}{b}\right)^n}\frac{\partial P}{\partial X} \tag{13}$$

The initial and boundary conditions corresponding to the commingled injection of two reactants into a clean bed are:

$$T=0:\ C_1=C_2=S=0 \tag{14}$$

$$X=0:\ C_1=C_2=1,\ P=\frac{k_0 p_0}{U\mu L} \tag{15}$$

The governing equations (10-13) for the four unknowns C_1, C_2, S, and P, subject to initial (14) and boundary (15) conditions, describe 1D reactive commingled flow of two reactants with solid product deposition. Yet, due to pressure independence of the reaction kinetics, Eq. (13) can be separated from the system (10-12). Thus, the reactants and deposit concentrations are determined by the problem (10-12, 14 and 15). For known solution of the 3 × 3 system (10-12), pressure distribution along the core during the injection is found from Eq. (13).

The model contains four empirical coefficients: the initial kinetics rate coefficient, λ_0, the reaction capacity coefficient, b, the formation damage coefficient, β, and the damage exponent, n. These empirical coefficients can only be determined from laboratory data matching due to the lack of clear relations to core properties [13].

2.3. Exact solution for arbitrary stoichiometric coefficients

The derivation of the exact solution for the problem (10-12, 14 and 15) with arbitrary stoichiometric coefficients, q and r, utilises transformation of the system, introduction of a new independent variable τ, $\tau = T\text{-}X$, and reduction to a first order hyperbolic equation, which is solved by method of characteristics. The derivations are presented in Appendices A and B. The solution is characterised by two flow regions, separated by the injected fluid front ($X=T$): region 0 (ahead of the front, $X>T$) and region I (behind the front, $X<T$), as shown in Fig. 4.

The final solution for the concentration of the first reactant, C_1, in coordinates (X,T) is:

$$C_1(X,T)=\begin{cases}0, & X>T\\ \int_{C_0(X)}^{C_1(X,T)}\frac{dC}{(1-C)C^q(\gamma C-\gamma+\alpha)^r}=\frac{\Lambda_0}{\alpha^r}(T-X), & X<T\end{cases} \tag{16}$$

where the concentration on the front $C_0(X)=C_1(X,X)$ as a function of X is given by either of Eqs. (A12) or (A13).

The concentration of the second reactant, C_2, follows from Eq. (A20):

$$C_2(X,T)=\begin{cases}0, & X>T\\ \int_{C_0(X)}^{\frac{\alpha C_2(X,T)-\alpha+\gamma}{\gamma}}\frac{dC}{(1-C)C^q(\gamma C-\gamma+\alpha)^r}=\frac{\Lambda_0}{\alpha^r}(T-X), & X<T\end{cases} \tag{17}$$

Riemann invariant (B3) for system (10-12) is calculated in Appendix B. From (B3) follows the explicit formula for deposit concentration, S, as expressed via solution $C_1(X,T)$:

$$S(X,T)=\frac{C_1(X,T)-C_0(X)}{1-C_0(X)} \tag{18}$$

Taking the expression for the pressure gradient from Eq. (13) and integrating over X from zero to one yields the dimensionless pressure drop across the core, ΔP:

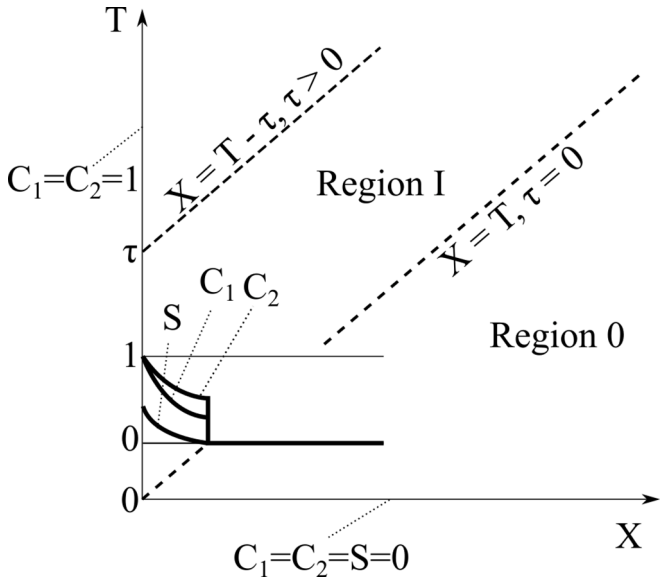

Fig. 4. Reaction front and profiles for reactants and deposit in the (X,T)-plane.

$$\Delta P(T) = \int_0^1 \left(1 + \frac{\beta S(X,T)}{b}\right)^n dX \tag{19}$$

2.4. Exact solution for stoichiometric coefficients equal to one

This section presents exact solutions for four cases of unitary stoichiometric coefficients: $q = r = 1$. All concentrations are equal to zero in region 0 ($X > T$) (Appendix A). Consequently, here we derive the analytical solutions for region I ($X < T$) only.

Case A. *Consider the case where the injected reactant concentrations are not equal,* ${c_1}^0 \neq {c_2}^0$.

The implicit expression for integral (A12) leads to the following explicit formula for initial concentration $C_0(X)$:

$$C_0(X) = \frac{\gamma - \alpha}{\gamma - \alpha exp(\Lambda_0(\alpha - \gamma)X)}, \quad \tau = 0 \tag{20}$$

Expressions (16) and (17) for the two reactants become:

$$\gamma ln\left|\frac{\gamma(C_1(X,T) - 1) + \alpha}{\gamma(C_0(X) - 1) + \alpha}\right| - (\gamma - \alpha) ln\left|\frac{1 - C_1(X,T)}{1 - C_0(X)}\right| - \alpha ln\left|\frac{C_1(X,T)}{C_0(X)}\right| = (\gamma - \alpha)\Lambda_0(T - X) \tag{21}$$

$$\gamma ln\left|\frac{\alpha(C_2(X,T) - 1) + \gamma}{\gamma(C_0(X) - 1) + \alpha}\right| - (\gamma - \alpha) ln\left|\frac{\alpha(1 - C_2(X,T))}{\gamma(1 - C_0(X))}\right| - \alpha ln\left|\frac{\alpha(C_2(X,T) - 1) + \gamma}{\gamma C_0(X)}\right| = (\gamma - \alpha)\Lambda_0(T - X) \tag{22}$$

With $C_0(X)$ and $C_1(X,T)$ determined from Eq. (20) and (21) respectively, the solution for the deposit concentration $S(X,T)$ is obtained from Eq. (18).

Case B. *Consider the case where the injected reactant concentrations are equal,* ${c_1}^0 = {c_2}^0$.

For $C_1 = C_2 = C$, system (10-12) becomes:

$$\frac{\partial C}{\partial T} + \frac{\partial C}{\partial X} = -\alpha\Lambda_0(1 - S)C^2 \tag{23}$$

$$\frac{\partial S}{\partial T} = \Lambda_0(1 - S)C^2 \tag{24}$$

Mapping Eqs. (23) and (24) from (X,T) to (X,τ) using $\tau = T\text{-}X$ (Eq. (A3)), expressing S from Eq. (23), substituting the resulting equation for S into Eq. (24), and using separation of variables for C and X, yields the expressions for reactant concentrations C_0 and C [30,31]:

$$C_0(X) = \frac{1}{1 + \alpha\Lambda_0 X}, \quad \tau = 0 \tag{25}$$

$$\frac{1}{C_0(X)} - \frac{1}{C(X,T)} + ln\left|\frac{C(X,T)(1 - C_0(X))}{C_0(X)(1 - C(X,T))}\right| = \Lambda_0(T - X) \tag{26}$$

The solution for deposit concentration $S(X,T)$ is determined by Eq. (18).

Case C. *Consider the case where the concentration of reactant* 1 *is significantly smaller than the concentration of reactant* 2, $C_1 \ll C_2$.

For this case, we assume that $C_2 = 1$. So, system (10-12) becomes:

$$\frac{\partial C_1}{\partial T} + \frac{\partial C_1}{\partial X} = -\alpha\Lambda_0(1 - S)C_1 \tag{27}$$

$$\frac{\partial S}{\partial T} = \Lambda_0(1 - S)C_1 \tag{28}$$

Introducing the independent variable τ from Eq. (A3), expressing S from Eq. (27), substituting S into Eq. (28), and performing separation of variables results in the following solution:

$$C_0(X) = exp(-\alpha\Lambda_0 X), \ \tau = 0 \tag{29}$$

$$C_1(X,T) = \frac{C_0(X)}{C_0(X)(exp(\Lambda_0(T - X)) - 1) + 1} \tag{30}$$

Similar to the previous cases, Eq. (18) determines the solution for deposit concentration $S(X,T)$ for known $C_0(X)$ and $C_1(X,T)$.

Case D. *Consider the case of linear chemical reactive flow at low deposit concentration, which corresponds to* $b = 0$ *in Eq.* (6).

The solution for the linear case, with dimensionless parameters and variables defined by (9), is as follows [13]:

$$C_1(X) = \frac{1 - \gamma}{exp(\Lambda_0(1 - \gamma)X) - \gamma} \tag{31}$$

$$C_2(X) = \frac{1 - \gamma}{1 - \gamma exp(\Lambda_0(\gamma - 1)X)} \tag{32}$$

$$S(X,T) = \Lambda_0\left[\frac{(1 - \gamma)^2}{exp(\Lambda_0(1 - \gamma)X) + \gamma(\gamma exp(\Lambda_0(\gamma - 1)X) - 2)}\right]T \tag{33}$$

$$\Delta P(T) = 1 + \beta\phi c_1^0 \int_0^1 S(X,T)dX \tag{34}$$

The reactant concentrations (31) and (32) are steady-state behind the reaction front, and the breakthrough concentrations are constant before and after the front's arrival. Therefore, it follows from Eq. (6) that the deposit concentration is proportional to the volume of injected water (Eq. (33)). The pressure drop across the core is, therefore, also proportional to the volume of injected water Eq. (34).

2.5. Comparison between the analytical and numerical models

We solved the governing system (10-13) subject to initial and boundary conditions (14 and 15) numerically. The numerical algorithm implements a two-step Lax–Friedrichs finite-difference method [32,33]. The computer code, implemented in Matlab, with the detailed description is available from http://faculty.smu.edu/shampine/current.html.

Fig. 5 shows the comparison of the analytical solution for Case A, given by Eqs. (20) and (21), and the numerical data. The following values have been used for the analytical and numerical modelling: $b = 0.2$ m^3/mol, $\lambda_0 = 1$ m^2/mol, ${c_1}^0 = 25$ mol/m^3, ${c_2}^0 = 50$ mol/m^3, $L = 0.05$ m, $\phi = 0.2$. Close agreement between the exact and numerical

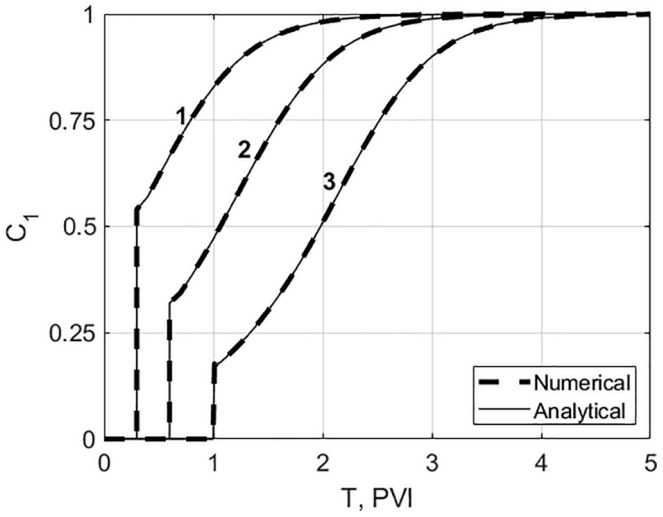

Fig. 5. Comparison between numerical and analytical solutions for BTCs at three core ports with $X = 0.3$, 0.6, and 1.0.

solutions for BTCs at three core points ($X = 0.3$, 0.6, and 1.0 corresponding to curves 1, 2, and 3, respectively) is observed near the concentration shock, where the numerical dispersion smooths the shock. The close match suggests low numerical dispersion. There is also strong agreement between the exact and numerical solutions for the second reactant concentration, deposit concentration, and pressure drop across the core. Assuming validity of the basic system (10-13), high accuracy of matching validates the analytical model.

3. Type curves for the reactive flow with large deposit

In this section, we present the type curves for reactant breakthrough concentration, deposit concentration profile and history, and the history for pressure drop across the core (Figs. 6a, 6b, 6c, and 6d, respectively), and analyse the effects of the reaction rate function on these curves. Here we discuss three types of reaction rate functions, one that decreases with deposition, one that increases with deposit concentration, and one with constant rate coefficient, that correspond to curves 1–6 in Fig. 3.

For all calculations presented in Fig. 6, the following values are used: $L = 0.05$ m, $\phi = 0.2$, and $n = 1$. BTCs in Fig. 6a are taken at the effluent $X = 1$, the deposition profiles in Fig. 6b correspond to the moment $T = 10$ PVI, and the deposit histories in Fig. 6c are taken at $X = 0.1$.

All BTCs are equal to zero before the arrival of the concentration front at $T = 1$ PVI and jump up at the moment of the front arrival (Fig. 6a). For the declining reaction rate curves, the BTCs monotonically increase and asymptotically tend to unity as time tends to infinity, which corresponds to a vanishing of the reaction rate function and thus a complete halt to reaction within the core. For an increasing reaction rate function, the BTC decreases monotonically after $T = 1$ and tends to zero as time tends to infinity (curve 4). The BTCs stabilise at the breakthrough moment for constant reaction rate coefficients (curves 5 and 6).

The deposit concentration is equal to zero ahead and on the concentration front for all functions $\lambda(\sigma)$. Fig. 6b shows the deposition profiles at $T = 10$ PVI, when the profiles for the reaction rate functions 1, 2, and 3 have approximately stabilised. The profile for increasing $\lambda(\sigma)$ steeply decreases near to the core entrance due to an accelerating reaction rate. The profiles decline more gradually for constant rate coefficients.

At any fixed position in the core, the deposited concentration is equal to zero before the arrival of the concentration front. Fig. 6c shows that the deposit concentration at $X = 0.1$ for the reaction rate functions 1, 2, and 3 approximately stabilise within 10 PVI. For an increasing $\lambda(\sigma)$, the deposit concentration also stabilises due to accelerating consumption of the ions by the chemical reaction close to the inlet (curve 4). Deposit concentrations grow linearly with time for constant reaction rate coefficients.

Deposit concentration increases monotonically with time for all functions $\lambda(\sigma)$, so the pressure drop increases also. It stabilises for the cases of decreasing reaction rate functions and grows unlimitedly for increasing $\lambda(\sigma)$. The pressure drop grows linearly with time for constant reaction rate coefficients. The same type curves are valid for pressure drop across the core section with length ωL (Fig. 2); these data are used

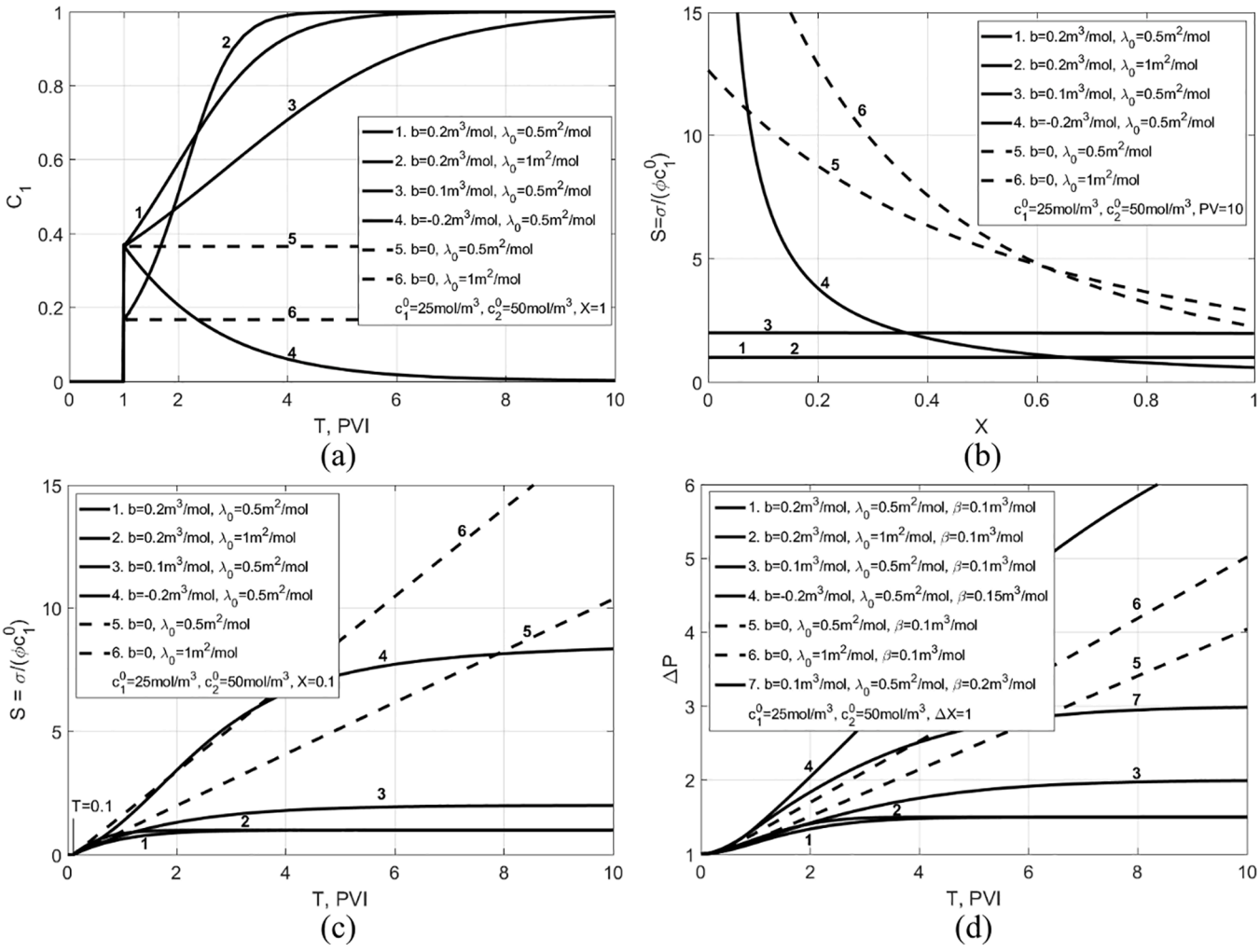

Fig. 6. Type curves for concentration and pressure drop profiles and histories: (a) breakthrough concentration for the first reactant, $C_1(1,T)$; (b) deposit concentration profile along the core, $S(X,10)$; (c) deposit concentration at the core outlet, $S(0.1,T)$; (d) the history of the pressure drop across the core, $\Delta P(T)$.

in laboratory three-point-pressure method [12,45].

Now let us compare the effect of the magnitude of each parameter on the system behaviour. Consider the effects of λ_0 for decreasing reaction rate functions (curves 1 and 2). The BTC at the arrival time is completely determined by λ_0; the higher the λ_0 the higher the reaction rate and thus, the smaller the BTC. The more intensive reaction leads to faster stabilisation, so curve 2 exceeds curve 1 at large times. The deposition profiles in Fig. 6b stabilise at the same value, which is independent of the reaction rate coefficient, which determines only the rate at which the curves stabilise. The deposit concentration for larger λ_0 (curve 2) stabilises faster than curve 1 (Fig. 6c). The same conclusion applies to pressure drop – curve 2 stabilises before curve 1, but to the same value.

Next, we discuss the effect of the reaction capacity coefficient b by comparing curves 1 and 3. As the reaction progresses, the precipitate concentration, S, tends to b^{-1}, the reaction rate will decrease. When b is higher, the reaction rate decreases faster, resulting in more precipitate, and thus a smaller outlet concentration of suspended ions, as shown in Fig. 6a. The retention profiles shown in Fig. 6b for curves 1 and 3 have already stabilized, illustrating that higher values of b result in lower values of the stabilized precipitate concentration. This analysis also explains the higher pressure drop presented in Fig. 6d.

For linear reactive flows with $b = 0$ and $n = 1$, the higher is the reaction rate coefficient, the lower is the BTC (curves 5 and 6 in Fig. 6a). Curve 5 of the deposition profile is located lower than curve 6 near to inlet and lays above curve 6 further within the core. This is the result of two competitive effects of the reaction rate coefficient on the reaction rate: intuitively, increasing λ_0 results in an increase of the reaction rate; however, it also yields a decrease in reagent concentrations and, consequently, in the reaction rate. The time-dependencies of deposited concentration and pressure drop are linear and exhibit higher slopes as the reaction rate coefficient increases – curve 6 is above curve 5 in Figs. 6c and 6d.

The curvature of the pressure drop curves is highly affected by the damage coefficient n. For the small deposit linear model with $n = 1$, the pressure drop grows linearly, as shown in curves 5 and 6. For $n < 1$, the curves would be concave, while $n > 1$ would result in convex curves. This arises from a diminishing or compounding effect of precipitate on permeability decline, respectively. When the deposition rate also decelerates or accelerates with deposit concentration ($b \neq 0$), then the curvature of the pressure drop curve is a more complex function of the magnitude of the model parameters.

4. Qualitative evaluation of the model coefficients

Various forms of pore space are encountered in different engineering applications. Depending on the pore space geometry, network connectivity, micro-heterogeneity, etc., different mathematical models of porous media for conductivity evaluation are applied. In this section, to estimate the formation damage coefficient β, we introduce solid deposit into two porous-media conductivity models (sections 4.1 and 4.2) and compare them to the linear theory used in the previous sections. Section 4.3 presents the estimate of the reaction capacity coefficient b.

In the models presented here, we approximate the porous media with a three-dimensional cubic lattice of cylindrical tubes. We assume that the lattice has constant bond length which can be determined from

$$l = 15\frac{\sqrt{k}}{\phi} \tag{35}$$

With known bond length, l, and pore radii, r, we can use Poiseuille's equation to relate the flow to the pressure drop across the bond

$$\Delta p = q\left(\frac{\pi r^4}{8\mu l}\right)^{-1} \tag{36}$$

The bonds have a distribution of radii, $f(r)$, which we assume to be known.

4.1. Effective medium theory

The essence of effective medium theory is to replace a lattice consisting of distributed bond radii with an equivalent one with a constant, effective, bond radius. The assumptions of the model are as follows. The porous medium (Berea sandstone) can be described by a simple cubic lattice with constant bond length and a distribution of bond radii, which is the pore throat size distribution. The bonds in the lattice are cylindrical and the walls are smooth, with length given by Eq. (35). The random conductor network can be represented by a homogeneous effective network. The mean potential difference across a bond in the random conductor network must be equal to the constant potential difference across a bond in the homogeneous effective network. Permeability is calculated from $k = r^2\phi/(8\tau)$, the single-phase, one-dimensional permeability component determined from Darcy's and Poiseuille's relationship.

Based on assumption 4, that the potential difference across the original network, and the effective network must be the same, combined with Poiseuille's equation, we arrive at the following expression:

$$\int_0^{\infty} \frac{r_e^4 - r^4}{r^4 + \left(\frac{z}{2} - 1\right) r_e^4} f(r)dr = 0 \tag{37}$$

where r_e is the effective pore radius of the homogeneous network, and z is the coordination number of the lattice ($z = 6$ for a cubic lattice).

Next, we introduce the solid deposit into the porous lattice. We assume that deposit builds in pores of increasing size. Thus, for any deposit concentration, S, we can define a radius, r_{min}, below which all pores are filled with deposit, and above which the pores are deposit-free. Given that deposit-filled pores will have zero conductivity, Eq. (37) becomes:

$$\frac{\eta(S)}{\frac{z}{2} - 1} + \int_{r_{min}}^{r_\infty} \frac{r_e^4 - r^4}{r^4 + \left(\frac{z}{2} - 1\right) r_e^4} f(r)dr = 0 \tag{38}$$

The volume of precipitate is considered to consist of discrete particles, such that pore blockage occurs when one particle fills one pore. Then the fraction of filled pores, η, can be defined as:

$$\eta(\sigma) = \frac{M_\sigma}{\rho_\sigma}\frac{\sigma}{v_\sigma} l^3, \quad v_\sigma = \frac{4}{3}\pi r_s^3 \tag{39}$$

Here M_σ and ρ_σ are the molecular mass and density of the precipitate, and v_σ is the volume of an individual precipitate particle. In terms of dimensionless deposit concentrations, Eq. (39) becomes:

$$\eta(S) = M_\sigma \phi c_1^0 S l^3/\rho_\sigma v_\sigma \tag{40}$$

Lastly, the permeability of the porous medium is related to the effective pore radius by:

$$k = \frac{\phi r_e^2}{8\tau} \tag{41}$$

where τ is the tortuosity.

Eqs. (38)-(41) relate the permeability of the porous medium to the precipitate concentration.

4.2. Percolation theory

Percolation studies revolve around the identification and analysis of infinite clusters, connected networks of conducting bonds that extend from one end of the system to another. Infinite clusters are necessary for fluid flow to occur. The fraction of conducting bonds required for an infinite cluster is called the percolation threshold. Analysis of the nature of the infinite cluster allow us to derive an expression for the overall conductivity of the network [5,34].

Above the percolation threshold, it is possible to segment the cross-section into cells, such that within each cell, the cluster of conductive

bonds resembles an infinite cluster at the percolation threshold.

The assumptions of the model are as follows. Porous medium (Berea sandstone) can be described by a simple cubic lattice with constant bond length and a distribution of bond radii, which is the pore throat size distribution. The bonds in the lattice are cylindrical and the walls are smooth, with length given by Eq. (35). The infinite cluster can be divided into boxes with width R, the correlation radius, and length equal to that of the network. Within each box, the cluster resembles an infinite cluster at the percolation threshold, η_c. There is only one chain of bonds (an r-chain) that extends from one edge to another. Removal of a few bonds will reduce the cluster to finite clusters. The bonds within an r-chain are in series, while the r-chains in the network are in parallel. No interflow between the conducting parallel chains.

As before, suppose that precipitate is introduced such that pores are filled by increasing size. This allows us to define the minimum radius, r_{min}, below which pores are not conductive, and above which they are. We can relate the fraction of conducting pores, η_σ, to this radius using the following formula:

$$\eta(r_{min}) = \int_{r_{min}}^{\infty} f(r)dr \tag{42}$$

Here $f(r)$ is the probability distribution function for pore radii; the deposit concentration σ corresponding to r_{min} is defined by Eq. (39). The value of r_{min} which corresponds to $\eta(r_{min}) = \eta_c$, the percolation threshold, is referred to as r_c. When r_{min} lies above this value, the set of conducting bonds does not form an infinite cluster.

With η-th fraction of bonds conducting, the conducting network will approximately resemble a number of chains which extend infinitely in the direction of flow. The distance in each cross-section between each chain is given by percolation theory [5,34]:

$$R(r_{min}) = l\left[\frac{1-\eta_c}{\eta(r_{min})-\eta_c}\right]^{\nu} \tag{43}$$

where l is the bond length as above, and ν is the correlation radius index, a general property of percolation networks, which is equal to 0.9 for 3D networks.

The number of r-chains within a cross-section is then:

$$N(r_{min}) = R(r_{min})^{-2} \tag{44}$$

Suppose the minimum radius is decreased, then the number of chains, N, will increase. This increase is attributed to new conducting chains whose minimum radius is less than the original r_{min}. Thus, the set of all conducting r-chains can be characterized by the minimum conducting radius within each chain. The quantity $N(r_{min})$ is then the cumulative density of these chains. Taking the derivative with respect to r_{min} results in the normalized distribution function for each cross-section:

$$F(r_{min}) = -\frac{dN(r_{min})}{dr_{min}} = \frac{2\nu f(r_{min})}{\left(l[1-\eta_c]^{\nu}\right)^2}\left(\int_{r_{min}}^{r_c} f(r)dr\right)^{(2\nu-1)} \tag{45}$$

The conductivity of each r-chain is equal to the harmonic average of the conductivity of each bond within the chain, as evaluated from Poiseuille's equation:

$$g(r_{min}) = \frac{\pi}{8}\frac{\int_{r_{min}}^{\infty} f(r)dr}{\int_{r_{min}}^{\infty} r^{-4}f(r)dr} \tag{46}$$

The initial permeability (no precipitate) is the weighted average of the conductivity of each r-chain:

$$k_0 = \int_0^{r_c} g(r)F(r)dr \tag{47}$$

Introduction of precipitate means that all chains whose minimum radius is between 0 and r_{min} will no longer be conducting, resulting in the following expression for permeability:

$$k(r_{min}(S)) = \int_{r_{min}(S)}^{r_c} g(r)F(r)dr \tag{48}$$

For a fixed precipitate concentration, S, the value of r_{min} is determined from Eqs. (39) and (42).

4.3. Estimate of the reaction capacity coefficient

Next, we present a physical basis for the reaction capacity coefficient, b, and present how it depends on the intrinsic properties of the system. We do so by conceptualizing deposit formation as occurring on the internal surface of the porous medium. As precipitate forms, it will either increase or decrease the available surface area, thus altering the area available for further reaction. The following geometry of precipitant is assumed. The reaction surfaces created or consumed are squares with length equal to the sphere diameter. Each precipitate formed creates or consumes 4 units of the square areas from the matrix. Decrease in reaction surfaces with deposition assumes the precipitates form in the cavities of the reaction surface, Fig. 7a. Smooth reaction surfaces result in the increase of reaction surfaces with reaction, Figs. 7b and 7c.

Suppose the porous medium has an internal surface area (available for reaction) $a(S)$. When a precipitate particle is deposited, $a(S)$ changes by some value a_σ. Fig. 7 presents three conceptual cases for this. Fig. 7a shows an internal cavity in the internal porous media surface. Five square reactive surfaces are highlighted in grey. When a particle precipitates in this space, the $5(2r_s)^2$ reactive area is covered, and $(2r_s)^2$ of new surface is created by the deposited particle and thus $a_\sigma = ((2r_s)^2\text{-}5(2r_s)^2) = \text{-}4(2r_s)^2$. The resulting decrease in reactive area reduces the reaction rate, resulting in a positive value of the reaction capacity coefficient, b. On the contrary, the scenarios shown in Figs. 7b and 7c show growth of precipitate particles on the solid surface, in this case, the change in surface area is $a_\sigma = (5(2r_s)^2\text{-}(2r_s)^2) = 4(2r_s)^2$ for the single particle case (Fig. 7b) and $a_\sigma = (4(2r_s)^2\text{-}2(2r_s)^2) = 2(2r_s)^2$ for the case of a particle forming next to another (Fig. 7c). These two cases correspond to an increasing reaction surface area, and thus a negative value of b.

Consider now the normalized total internal surface area of the porous medium:

$$\frac{a(\sigma)}{a_0} = 1 \pm \frac{a_\sigma}{a_0}\frac{V_\sigma}{v_\sigma} \tag{49}$$

where a_0 is the total reactive surface available on the matrix, V_σ is the total volume of precipitates, and v_σ is the unit spherical volume of a precipitate.

The initial reactive surface area is given by:

$$a_0 = f_c A_v \rho_r \tag{50}$$

where f_c is the clay content of the matrix, A_v is the specific surface area, and ρ_r is the matrix density. The total precipitate volume is given by:

$$V_\sigma(\sigma) = \frac{M_\sigma}{\rho_\sigma}\sigma, \quad V_\sigma(S) = \frac{M_\sigma \phi c_1^0}{\rho_\sigma}S \tag{51}$$

where σ and S are dimensional and dimensionless deposit concentrations, respectively, M_σ is the molecular weight of the precipitate, and ρ_σ is the density of the precipitate.

For cubic particles similar to those shown in Fig. 1b, the individual particle volume is given by:

$$v_\sigma = 8r_s^3 \tag{52}$$

resulting in an explicit expression for b:

$$b = \pm\frac{2M_\sigma}{r_s f_c \rho_r A_v \rho_\sigma} \tag{53}$$

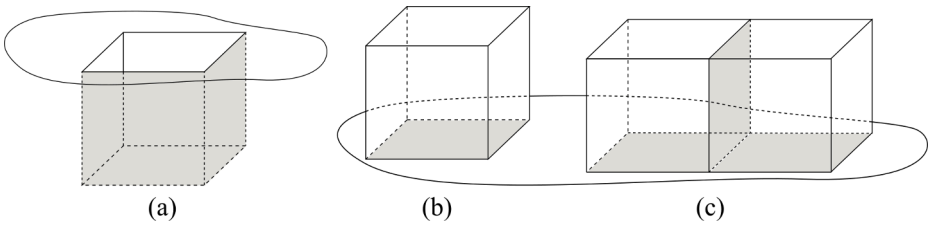

Fig. 7. Qualitative evaluation of the reaction variation coefficients b from change in the surface area during deposition: a) filling in the pit in the rock surface by the crystal of deposited solid, resulting in the surface area decrease ($b < 0$); b) deposition of a single crystal on the rock surface yielding the surface increase ($b > 0$); c) the rock surface increases due to deposition of two neighbouring crystals ($b > 0$).

4.4. Comparison with linear model

In the previous sections, a physical basis has been presented for both the formation damage coefficient, β, and the reaction capacity coefficient, b. What remains is to compare these formulations with experimental data to confirm their validity. To the end, simultaneous fitting was conducted for test 9 from the study by Ahmed [14] with damage exponent $n = 1$. The fitted values for λ_0, β, and b are 2.73x10^{-3} m^2/mol, 2.03x10^{-1}, and 3.39x10^{-5} m^3/mol, respectively.

A Berea sandstone was used for the experiment and the precipitate formed was $CaSO_4$. As such, parameter values for the matrix were taken from typical Berea sandstones and for precipitates were taken from typical values of $CaSO_4$, namely density and molecular weight. The specific surface area A_v for Berea sandstones ranged from 0.79 m^2/g to 1.23 m^2/g and clay content (f_c) ranged from 6% to 8% [35]. The average values of A_v and f_c were chosen to calculate b.

Estimates for β rely on knowing the pore size distribution. Two estimates of this distribution for Berea sandstones are presented here: one truncated normal distribution with coefficient of variation, $C_v = 0.64$ and mean pore throat size of 5.15 μm [36], and one lognormal distribution with $C_v = 0.64$ and a mean pore throat size of 11.05 μm [37]. Both curves are presented in Fig. 8a.

Estimates for the particle size, r_s, are not widely available for precipitate formed during simultaneous injection. As such, EMT and Eq. (53) were tuned to the experimental values of β and b to obtain an optimal value of r_s, which was found to be 31.4 μm. The resulting estimate for b is 4.1 × 10^{-5} m^3/mol.

While neither the EMT or percolation theory models presented above necessarily demonstrate a linear relationship between k_0/k and S, calculations presented in Fig. 8b show an approximately linear tendency for all cases. These calculated points have been fit with straight lines with y-intercept of 1 which shows good agreement. The values of β vary between 1.81 × 10^{-1} to 4.37 × 10^{-1}.

5. Matching experimental data

In this section, we will discuss the matching of seven sets of laboratory data obtained from the literature using solutions from the different sub-cases. Section 4.1 discusses the simultaneous fitting of breakthrough concentration and pressure drop values from six sets of data using the non-linear Case A model. Section 4.2 shows the simultaneous fitting of two sets of pressure drop data and one set of pressure drop prediction using the non-linear Case B model. Section 4.3 presents the results from simultaneously fitting two sets of linear pressure drop data using the non-linear Case A model. The solution to the linear model, Case D, is also used to fit all laboratory data for comparison.

5.1. Simultaneous fitting of breakthrough concentration and pressure drop data

Ahmed [14] performed commingled injection of calcium chloride ($CaCl_2$) and sodium sulphate (Na_2SO_4) into Berea sandstone cores with simultaneous measurements of breakthrough concentration of calcium ions (c_1) and pressure drop (Δp) across the core. The cores had the following properties: $L = 0.051$ m, $d = 0.038$ m, $k_{av} = 2.15 \times 10^{-13}$ m^2, and $\phi_{av} = 0.24$.

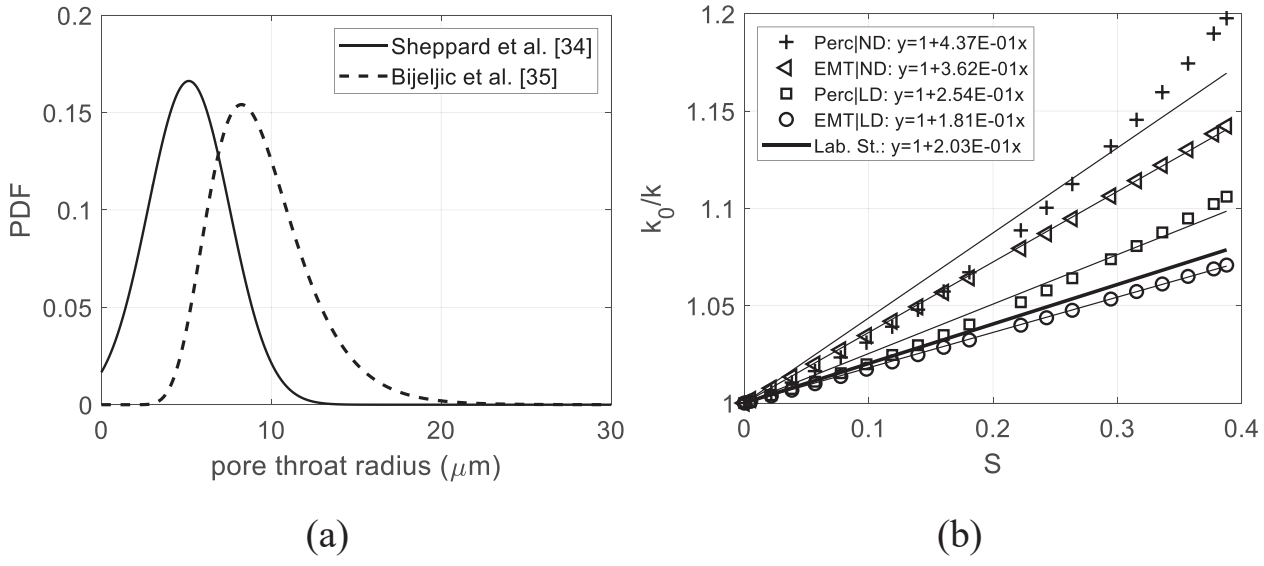

Fig. 8. Estimates of permeability decline due to solid precipitation: (a) pore throat size distributions of Berea sandstone; (b) the curves for reciprocal normalised permeability (i.e. different values of formation damage coefficient β) obtained from the micromodels: Perc – percolation, EMT – effective medium theory, ND – normal distribution, LD – lognormal distribution.

Results from 5 of the tests conducted by Ahmed [14], namely tests 8, 9, 10, 11 and 14, were used in this study. All 5 tests were conducted under a constant injection rate of 10 ml/min. In tests 8, 9, and 14, the injected concentrations of $CaCl_2$ (c_1^0) and Na_2SO_4 (c_2^0) were 54.5 mol/m^3 and 12.5 mol/m^3, 76.8 mol/m^3 and 18.8 mol/m^3, and 92 mol/m^3 and 22.5 mol/m^3, respectively. All three tests were conducted at 95 °C. Tests 10 and 11 were conducted under 70 °C and 45 °C, respectively. Both of these tests involved injecting $CaCl_2$ at 76.8 mol/m^3 and Na_2SO_4 at 18.8 mol/m^3.

The reaction is one to one, $q = r = 1$, with different injection concentrations, $c_1^0 \neq c_2^0$, therefore the solution to the non-linear model Case A is used for the fitting of these tests.

Fig. 9 presents the laboratory data and matching results by the non-linear Case A and linear Case D models for the varying injection concentration test series. The dimensionless breakthrough concentration data (C_1) for the three tests (Figs. 9a, 9c, and 9e for tests 8, 9, and 14, respectively) increased as injection concentrations (c_1^0) increase. Similarly, the dimensionless pressure drop data (ΔP) also increased with c_1^0. In addition, the three tests have distinctively different ΔP shapes: test 8 is concave (Fig. 9b), test 9 is convex (Fig. 9d) and test 14 is almost linear (Fig. 9f).

Fig. 10 presents the laboratory data and matching results by the non-linear Case A and linear Case D models for the varying operating temperature test series. C_1 decreased as temperature increases, which indicates the reaction intensity increases with temperature (Figs. 9c, 10a, 10c for tests 9, 10, and 11, respectively). ΔP for both tests (10 and 11) reached a similar magnitude at dimensionless time $T = 130$, however, for test 10 (temperature is 70 °C), ΔP is convex (Fig. 10b), while the ΔP in test 11 (temperature is 45 °C) is concave (Fig. 10d).

Both C_1 and ΔP curves were simultaneously fitted to obtain the tuning parameters for each test. The tuned parameter values and coefficients of determination, R^2, for Case A and Case D are presented in Table 1. The fitting has improved by using the non-linear Case A model across all five tests compared to the linear Case D model. This is observable from Figs. 9 and 10 as well as values of R^2.

To validate the model, we use a criterion relating a number of degrees of freedom of the measured data, i.e. a topological dimension of the data array (m) and a number of independent model parameters (n). For example, $m = 2$ for a linear line, $m = 3$ for quadratic parabola, etc. Consider mapping from the space of model parameters into the space of constants that parametrize the measured data array. If high match was achieved for $n < m$, i.e. higher dimension array can be matched by lower number of parameters, the matching has "predictive" feature, which validates the model. For $n \geq m$, close match can be achieved by numerous sets of model parameters. In this case, one can claim only that the model reproduces the process; more measurements must be performed for the model validation. For well-posed inverse problems, small perturbation of the measured data does not change the sign of inequality between n and m.

The BTCs have three degrees of freedom because the breakthrough concentration and two parameters describing the parabolic increase are independent constants. Yet, the breakthrough data are scattered, thus the curve is considered two-parametric. The dimensionless pressure drop curves also have two free parameters. Therefore, the laboratory data for each experiment have four degrees of freedom. The data is successfully matched by tuning four parameters (namely λ_0, β, b, and n) for the non-linear Case A model.

5.2. Simultaneous fitting of pressure drop data with equal injection concentrations

Ghaderi et al. [15] simultaneously injected $CaCl_2$ and Na_2SO_4 into a glass micro model and measured pressure drop across the model (Fig. 8). The glass model had the following properties: $L = 0.0075$ m, $k_{av} = 2.15 \times 10^{-13}$ m^2, and $\phi_{av} = 0.39$. The injection rate was 0.008 ml/min and the test was conducted at 80 °C. The injected concentrations of $CaCl_2$ (c_1^0) and Na_2SO_4 (c_2^0) were the same, and equal to 50 mol/m^3, 15 mol/m^3, and 70 mol/m^3 in tests 2, 4, and 5, respectively. As the injected reactant concentrations are equal, $c_1^0 = c_2^0$, the non-linear model used for this fitting is Case B.

The dimensionless pressure drop curves, shown in Fig. 11, have a parabolic form and started at point (0,1). Therefore, each curve has two degrees of freedom.

Given that Ghaderi et al. [15] did not measure BTCs, and that we do not expect that we can uniquely determine the model parameters from a single ΔP curve, we simultaneously matched two curves that corresponded to $c_1^0 = c_2^0 = 15$ mol/m^3 and $c_1^0 = c_2^0 = 70$ mol/m^3 using the non-linear Case B and linear Case D models. The tuned parameter values as well as R^2 are shown in Table 1. Similar to the results presented in Section 4.1, the non-linear model showed better fitting than the linear model. In addition, the number of tuned parameters equals to the number of degrees of freedom of laboratory data. Therefore, high agreement between modelling and experimental data supports the model validity.

Fig. 11 shows pressure drop prediction by the non-linear Case B and linear Case D models for the case of injected concentration equal to 50 mol/m^3. Parameters used in predicting the pressure drop were taken from the fitting of the 15 mol/m^3 and 70 mol/m^3 tests. High agreement between the predictive modelling and laboratory data also validates the non-linear model (Eqs. (10)-(13)).

5.3. Simultaneous fitting of pressure drop data with different injection concentrations

Moghadasi et al. [16] simultaneously injected incompatible waters containing calcium nitrate $Ca(NO_3)_2$ and Na_2SO_4 into a glass-bead column. The glass model had the following properties: $L = 0.415$ m, $k_{av} = 159 \times 10^{-12}$ m^2, and $\phi_{av} = 0.38$. The injection concentrations for Ca$(NO_3)_2$ (c_1^0) and Na_2SO_4 (c_2^0) for test A were 108.1 mol/m^3 and 27.1 mol/m^3 and for test B were 216.2 mol/m^3 and 54.2 mol/m^3. Both experiments were conducted at 70 °C with an injection rate of 50 ml/min.

Both pressure drop curves exhibited almost linear growth as shown in Fig. 12. Laboratory data was tuned using the non-linear Case A and linear Case D models, with the tuning parameters and R^2 values presented in Table 1. Similar to the previous two studies (shown in Sections 5.1 and 5.2), better matching was observed in the non-linear Case A model than the linear Case D model (averaged $R^2 = 0.83$ versus averaged $R^2 = 0.72$).

The obtained rate and formation damage coefficients were within the interval of commonly observed results [13,38] .

6. Summary and discussion

Governing system of equations. Alteration of rock surfaces during reaction product deposition and the corresponding change in the reaction rate can be expressed by the deposit-dependency of the kinetics rate (Eq. (2)). Retaining the first two terms in the Taylor series of the kinetics rate function $\lambda(\sigma)$ for small deposit yielded a linear dependency of the kinetics rate function versus deposit concentration (Eq. (6)). In this case, the 1D reactive flow problem allows for an exact analytical solution.

The analytical solution obtained is valid for any time varying injection rate. Any dependency $U(t)$ in dimensional system (4-7) results in dimensionless form (10-13) after introduction of dimensionless variables and parameters, given by (8).

For arbitrary stoichiometric coefficients, the analytical model provides implicit expressions for reactant and deposited concentrations and for pressure drop across the core (Eqs. (A12) and (16-19)). The expressions become explicit for linear second order chemical reactions with unitary stoichiometric coefficients (Eqs. (29)-(34)).

The exact solution shows that in the case where the derivative of the reaction rate function remains finite even at $S = 1$, then the deposit concentration tends to $S = 1$ asymptotically as $T \to \infty$ [39]. An illustrative

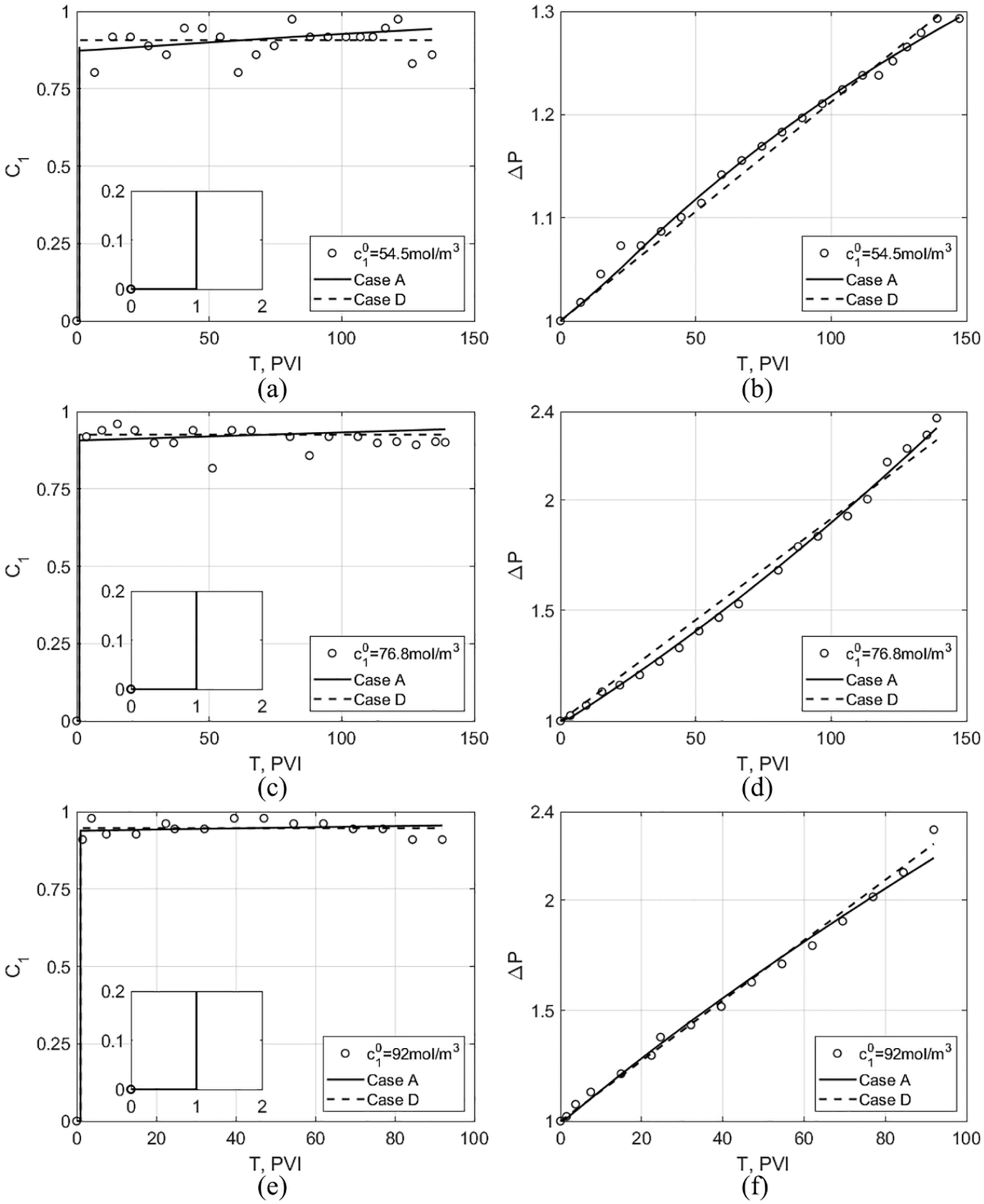

Fig. 9. Model fitting for commingled injection of $CaCl_2$ and $NaSO_4$ into sandstone cores (Ahmed [14]): (a), (c), (e) breakthrough concentrations of calcium cations, C_1; (b), (d), (f): pressure drop across the core, ΔP. Figures (a, b), (c, d), and (e, f) correspond to experiments 8, 9, and 14, respectively.

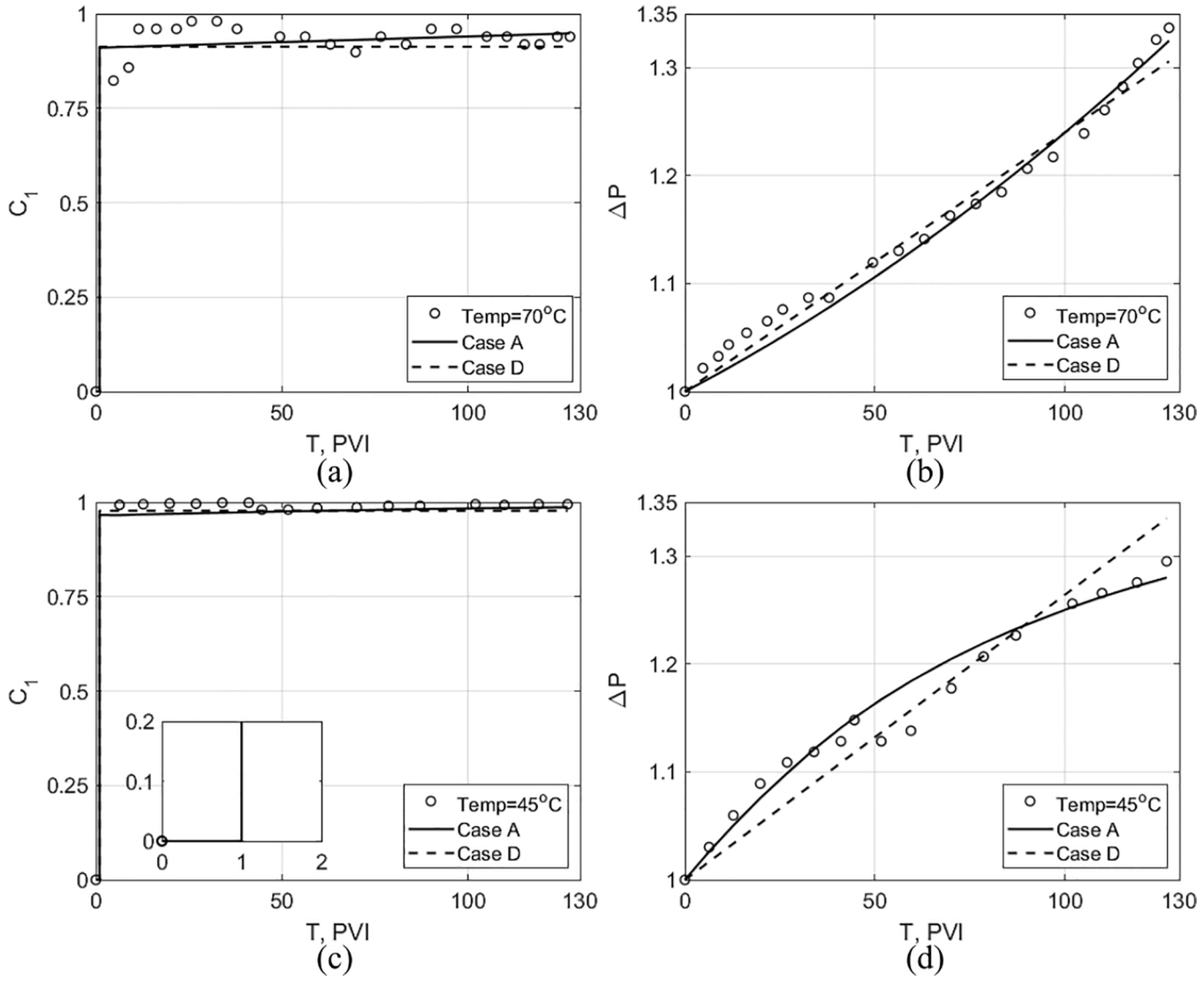

Fig. 10. Model fitting for commingled injection of $CaCl_2$ and $NaSO_4$ into sandstone cores (Ahmed [14]): (a), (c) breakthrough concentration of calcium cations, C_1; (b), (d) pressure drop across the core, ΔP. Figures (a, b) and (c, d) correspond to experiments 10 and 11 respectively.

Table 1
Tuning the model coefficients from the experimental data.

Reference	Test	λ_0(m^2/mol) Nonlinear / Linear	β(-) Nonlinear / Linear	b(m^3/mol) Nonlinear / Linear	n(-) Nonlinear / Linear	R^2_{C1} Nonlinear / Linear	$R^2_{\Delta P}$ Nonlinear / Linear	$R^2_{\Delta P}$ Nonlinear n = 1
Ahmed [14]	9	4.10E-02 / 9.77E-02	5.90E-02 / 6.57E-03	4.02E-03 / 0	1.87 / 1	0.95 / 0.95	0.99 / 0.94	0.90
	8	3.16E-01 / 1.98E-01	1.92E-01 / 1.82E-03	1.13E-01 / 0	0.53 / 1	0.94 / 0.89	0.99 / 0.92	0.93
	10	1.21E-02 / 5.44E-02	3.40E-03 / 2.32E-03	1.14E-02 / 0	1.54 / 1	0.95 / 0.87	0.98 / 0.96	0.94
	11	2.11E-03 / 7.42E-03	3.15E-02 / 6.27E-03	1.20E-02 / 0	0.25 / 1	0.99 / 0.99	0.96 / 0.92	0.92
	14	3.42E-02 / 5.40E-02	1.78E-02 / 1.19E-02	3.09E-03 / 0	0.76 / 1	0.97 / 0.97	0.99 / 0.96	0.98
Ghaderi et al. [15]	2	4.57E-03 / 1.76E-01	9.96E-02 / 4.64E-03	6.99E-03 / 0	0.57 / 1	–	0.95 / 0.70	0.94
	4					–	0.97 / 0.97	0.92
	5					–	0.98 / 0.87	0.94
Moghadasi et al. [16]	A	9E-05 / 5.1E-04	1.20E-01 / 2.19E-02	5.0E-04 / 0	1 / 1	–	0.84 / 0.69	0.84
	B					–	0.82 / 0.75	0.82

example is the case where the reaction rate function has the form:

$$\lambda(\sigma) = \lambda_0(1 - b\sigma)^{\kappa} \tag{54}$$

In this case, asymptotic stabilisation occurs if the reaction rate function has a power-law shape with exponent $\kappa > 1$, i.e. the reaction rate decreases slowly near the maximum deposit. Otherwise, for $\kappa < 1$,

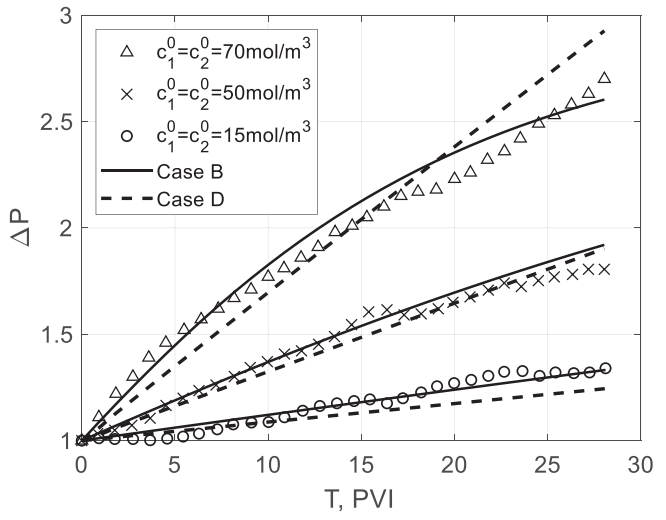

Fig. 11. Commingled injection of two incompatible aqueous solutions of CaCl2 and NaSO4 into a glass micro-model (Ghaderi et al. [15]). The three tests have been performed with different injection concentrations. The solid and dashed curves show the matching results by nonlinear Case B and linear Case D models. The curves from experimental data points '△' and '○' show the matching results by the linear and nonlinear models. The curves from experimental data '×' correspond to the tuned model prediction.

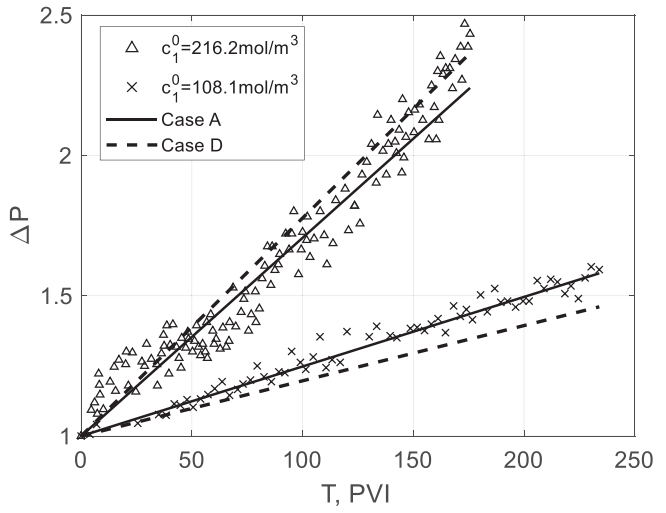

Fig. 12. Simultaneous injection of incompatible waters with $Ca(NO_3)_2$ and $NaSO_4$ into a glass-bead column (Moghadasi et al. [16]). The solid and dashed curves show the matching results by nonlinear Case A and linear Case D models. Parameters λ_0, β, and b were tuned by simultaneously fitting both pressure drop curves.

where the reaction rate vanishes rapidly close to $S = 1$, the deposit concentration and pressure drop stabilise at a finite time. The case of $\kappa < 1$ corresponds to a sufficiently high deposit concentration such that the fraction of conducting pores is close to the percolation threshold of the pore network [25].

Model parameters and laboratory studies. Laboratory coreflood tests usually involve the measurement of component concentrations at the effluent and pressure drop across the core [38,40–45]. The initial kinetics rate coefficient, λ_0, is a kinematic property, allowing it to be determined from the breakthrough concentration, C_1 [17,40,46]. The formation damage coefficient, β, is a dynamic property and is determined from pressure drop measurement, ΔP [13,18]. These two parameters can be determined from the breakthrough concentrations and pressure drop across the core during commingled injection of two incompatible waters [12,13]. Thus, the exact solution (A12, 16, and 17) can be used for determining the reaction rate coefficient λ_0 and the reaction capacity coefficient, b, from C_1, and calculation of β and the damage exponent n from ΔP (Eq. (19)).

However, pressure measurements are less cumbersome and involve significantly simpler and lower-cost equipment than the concentration measurements. Substitution of the BTC measurements of suspended particles by measurements of the pressure drop between the core inlet and an intermediate point in the core, proposed in work [45], has been shown to improve the coreflood test quality for colloid-suspension-nanoparticle and reactive transport in porous media.

As it follows from the exact solution, given by Eqs. (16)-(18), reactive flow with commingled injection of two reactants is not self-similar [5]. Thus the deposit profile at one moment cannot be obtained from the profile at another moment. Therefore, as it follows from Eq. (19), the pressure drop between the inlet and an intermediate point along the core is independent of the pressure drop across the overall core. Using the three-point-pressure method allows increasing the number of independent measured data, more reliably adjust the model, or using more detailed mathematical models for the model functions $\lambda(\sigma)$ or $k(\sigma)$ (Fig. 2, Eqs. (2) and (3)). The above-mentioned features have been proven for low- and high-concentration colloids [45,11] and reactive flows [12] in porous media.

Matching the experimental data. The analytical non-linear model exhibits unsteady-state concentrations of reactants behind the reaction front, and non-linear growth of deposit and pressure drop across the core; whereas the linear model shows steady-state concentrations of reactants behind the reaction front, and linear growth of deposit and pressure drop across the core. Seven sets of laboratory experiments (shown in Section 4.1 and 4.2) exhibited the above-mentioned non-linear behaviour.

When matching the results from the seven sets of laboratory data using non-linear models, the deposit-dependent kinetics rate function $\lambda(\sigma)$, monotonically decreased with time. Thus, precipitate deposition slowed the chemical reaction.

In addition, the number of degrees of freedom of the experimental curves was equal to the number of tuned model parameters. Therefore, the high agreement between the experimental data and non-linear modelling allowed claiming the model validity.

Ahmed [14] measured breakthrough concentration of one reactant and pressure drop across the core simultaneously throughout the experiments. Both sets of laboratory data increased with time. Using the non-linear model allowed for more accurate fitting to the pressure drop curvature and breakthrough concentration growth. Close examination of the fitting parameter values and testing conditions revealed the initial kinetics rate coefficient λ_0 increased with temperature for both the non-linear and linear models. However, β and b showed no clear dependency on the effects of temperature and injection concentration.

From the tests conducted by Ghaderi et al. [15], the pressure drop curve of the intermediate injection concentration was accurately predicted by the non-linear model, tuned from two other curves. This also validated the model.

It should be noted that in all cases, improved fitting of the model with $b \neq 0$ compared to the linear model where the reaction rate function is constant, is expected, given that the case of $b = 0$ is part of the possible solutions explored by the optimisation algorithm when using the non-linear model. In some cases, similar results for the quality of match between the two models suggests approximately linear behaviour. However several of the studies shown here, such as those presented by Ghaderi et al., show clear non-linearity, and in these cases, only the inclusion of non-linearity allows for the behaviour of the system to be accurately described by modelling.

The laboratory study conducted by Moghadasi et al. [16] exhibited linear behaviour at significantly higher injected concentrations and larger volumes of injected water when compared to the other two studies. Yet, the tuned value of the initial kinetics rate coefficient was

two or three orders of magnitude lower than in the other two studies. The slowness of the chemical reaction would explain the linear behaviour of the reactive flow system.

Scale dependencies and upscaling techniques. When reactants are well mixed at the micro-scale, exact upscaling of reaction-transport equations is applicable. Battiato and Tartakovsky [29] have shown that when the Péclet number is significantly larger than the Damköhler number, macro-scale equations can accurately describe the micro-scale processes. Under such a condition, scale separation is established and the micro- and macro-scale equations are decoupled. When the exact upscaling condition is not satisfied, iterative hybrid modelling can be the solution to link between the micro- and macro-scale [27]. The multiscale analysis platform (MAP) flowchart, presented by Scheibe et al. [47], can be used for the selection of a suitable hybrid modelling technique. In addition, there are numerous geochemical numerical simulators developed for solving reactive transport equations (such as TOUGHREACT, PHREEQC, and ChemPlugin from the Geochemist's Workbench) [48–50]. However, systematic discrepancies may arise from the numerical method and sequential coupling scheme used by the simulator.

Another case of exact upscaling corresponds to small concentration of one of reactants, $C_1 \ll C_2$, where constant concentration $C_2 = {C_2}^0$ can be assumed. The problem becomes equivalent to that of deep bed filtration of colloids and suspensions [51,52]. Consider multiple chemical reactions with the same stoichiometric coefficient, where k different suspended ions react with species 1 to create k unique precipitates:

$$\frac{\partial S^{(k)}}{\partial T} = \Lambda^{(k)}\left(S^{(1)},\, S^{(2)}...S^{(n)}\right)(C_1)^q\left(C_2^{(k)0}\right)^{r_k} \tag{55}$$

Introduction of the total deposit concentration S instead of time in Eq. (55):

$$S = \sum_{k=1}^{n} S^{(k)},\quad \Lambda(S) = \sum_{k=1}^{n} \Lambda^{(k)}\left(S^{(k)},\, S^{(2)},\, ...S^{(n)}\right)\left(C_2^{(k)0}\right)^{r_k} \tag{56}$$

yields the system of ordinary differential equations:

$$\frac{dS^{(k)}}{dS} = \frac{\Lambda^{(k)}\left(S^{(1)},\, S^{(2)}...S^{(n)}\right)\left(C_2^{(k)0}\right)^{r_k}}{\sum_{k=1}^{n}\Lambda^{(k)}\left(S^{(1)},\, S^{(2)}...S^{(n)}\right)\left(C_2^{(k)0}\right)^{r_k}},\, S = 0:\;\; S^{(k)} = 0 \tag{57}$$

The solution $S^{(k)}(S)$ of the problem (57) allows expressing the total reaction rate function versus S [53]. The averaged (upscaled) governing 2×2 system:

$$\frac{\partial}{\partial T}\left[C_1 + \sum_{k=1}^{n}\alpha^{(k)}S^{(k)}(S)\right] + \frac{\partial C_1}{\partial X} = 0,\;\; \frac{\partial S}{\partial T} = \Lambda(S)C_1^q \tag{58}$$

is solved with respect to two unknowns $C_1(X,T)$ and $S(X,T)$. The one-dimensional problem for system (58) subject to initial and boundary conditions (14 and 15) for $q = 1$ allows for an exact solution for any arbitrary reaction rate function $\Lambda(S)$ [53,54]. This exact solution allows for downscaling, i.e. determining the individual deposit concentrations from the concentrations $C_1(X,T)$ and $S(X,T)$ [54].

More cases for exact upscaling of reactive flows are derived in [11,55–57].

Further developments and other applications. The exact solutions derived can be used for data treatment of three-point-pressure tests on reactive flows with large deposit concentrations, Fig. 2 [11,12]. The obtained model coefficients λ_0, β, b, and n can be used for prediction of behaviour of production wells [58] and injection wells [59] for oilfield scaling and water resources management.

Chemical reactions (1) with two-phase multicomponent flow occur in numerous processes of geo-chemical transport and enhanced oil recovery [5,7,40–42,60]. The splitting procedure reduces two-phase reactive flow equations to the one-phase system given by Eqs. (10)-(13) [61]. This allows transforming the analytical solution (A12, 16, and 17) for two-phase reactive flow [5].

The obtained analytical solution for reactive flow in porous media can be used for stream-line modelling of commingled injection of incompatible waters in aquifers, geothermal reservoirs, and oil fields (Fig. 1a) [5,62].

7. Conclusions

Analytical modelling and analysis of experimental data for 1D nonlinear reactive flow in porous media with high deposit concentration allows drawing the following conclusions:

- One-dimensional second-order reactive flow in porous media with linear reaction-kinetics function allows for an exact analytical solution.
- The solution yields implicit formulae for reactant and deposit concentrations for any arbitrary stoichiometric coefficients.
- The exact solution exhibits reaction-front propagation with the carrier-water velocity and all concentrations equal to zero ahead of the front.
- In the nonlinear case of high deposit concentration, the concentration profiles for reactants are non-steady-state and the deposit profile and pressure drop grow non-linearly with time. In contrast, for linear flow with low deposit concentration, the concentration profiles for reactants are steady-state while the deposit profile and pressure drop grow linearly with time.
- For seven investigated laboratory studies, the analytical model matches the experimental data with high accuracy; the number of degrees of freedom of the experimental data are equal to the number of tuned model constants. This indicates validity of the analytical model.

Declaration of Competing Interest

The authors declare that they have no known competing financial interests or personal relationships that could have appeared to influence the work reported in this paper.

Acknowledgements

The authors are grateful to Dr. Alex Laurence Altree-Williams (Australian School of Petroleum and Energy Resources) for useful discussions and cooperation. Many thanks are due to David H. Levin (Murphy, NC, USA) who provided professional English-language editing of this article.

Appendix A. Derivation of analytical solution for any stoichiometric coefficients

In this Appendix we present the derivation of the analytical solution for arbitrary stoichiometric coefficients. Using the Lagrangian coordinate instead of time in system (Eqs. (10)-(12)), constructing the equation for the conservation of mass for the linear combination of two component concentrations to obtain first integral, and using the non-linear method of characteristics allows us to obtain an exact solution for the 1D reactive transport problem (14 and 15) [28,30,31].

Region 0:

Consider region 0, where $0 < T < X$, ahead of the injected fluid front ($X = T$) in the (X,T)-plane, as shown in Fig. 4. Substitution of Eq. (12) into Eqs. (10) and (11) and rewriting the obtained equations in the characteristic form yields:

$$\frac{dX}{dT} = 1,\ \frac{dC_1}{dT} = -\alpha\Lambda_0(1-S)C_1^qC_2^r,\ \frac{dC_2}{dT} = -\gamma\Lambda_0(1-S)C_1^qC_2^r \tag{A1}$$

Solving the system of two ordinary differential equations (ODE) (A1) with zero initial conditions (14) and any solution $S(X,T)$ for deposit results in solution with zero reactant concentrations, leading to zero deposition concentration:

$$C_1(X,T) = C_2(X,T) = S(X,T) = 0 \tag{A2}$$

Region I:

Now let us consider region I, $0 < X < T$, which is located behind the injected fluid front ($X = T$). Let us introduce a new independent (Lagrangian) variable, τ, which at point X counts as time since the concentration front passed this point:

$$\tau = T - X \tag{A3}$$

Therefore, the domain $0 < X < T$ becomes $0 < X$, $0 < \tau$. Boundary condition (15), for $\tau = 0$, remains the same in the new domain.

Transforming the governing system Eqs. (10)-(12) to the mobile reference system (X,τ):

$$\frac{\partial C_1}{\partial X} = -\alpha\Lambda_0(1-S)C_1^qC_2^r \tag{A4}$$

$$\frac{\partial C_2}{\partial X} = -\gamma\Lambda_0(1-S)C_1^qC_2^r \tag{A5}$$

$$\frac{\partial S}{\partial \tau} = \Lambda_0(1-S)C_1^qC_2^r \tag{A6}$$

Multiplying Eq. (A4) by γ and Eq. (A5) by -α, and taking the summation of the resultant equations yields:

$$\gamma\frac{\partial C_1}{\partial X} - \alpha\frac{\partial C_2}{\partial X} = 0 \tag{A7}$$

Integrating Eq. (A7) with respect to X and applying boundary condition (15) yields the following relationship between the unknown functions:

$$C_2(X,\tau) = \frac{\gamma C_1(X,\tau) - \gamma + \alpha}{\alpha} \tag{A8}$$

Substituting Eq. (A8) into system (A4-A6) reduces it to a system of two equations:

$$\frac{\partial C_1}{\partial X} = -\alpha\Lambda_0(1-S)C_1^q\left(\frac{\gamma C_1 - \gamma + \alpha}{\alpha}\right)^r \tag{A9}$$

$$\frac{\partial S}{\partial \tau} = \Lambda_0(1-S)C_1^q\left(\frac{\gamma C_1 - \gamma + \alpha}{\alpha}\right)^r \tag{A10}$$

with unknowns C_1 and S.

Axis $\tau = 0$, which is an image of concentration front in (X, τ)-plane, is a characteristic line for system Eqs. (A4)-(A6) [5]. From Eq. (12), it follows that the deposit concentration S is continuous along this front. As the deposit concentration is zero ahead of this front (for $\tau < 0$), S equals zero along the front. Thus, the characteristic form of Eq. (A9) becomes:

$$\frac{dC_1(X,0)}{dX} = -\alpha\Lambda_0C_1^q\left(\frac{\gamma C_1 - \gamma + \alpha}{\alpha}\right)^r \tag{A11}$$

Separation of variables in the ODE (A11) and integration in X accounting for boundary condition (15) yields the implicit expression:

$$\int_{C_0(X)}^{1} \frac{dC}{\Lambda_0C^q\left(\frac{\gamma C-\gamma+\alpha}{\alpha}\right)^r} = \alpha X,\ C_0(X) = C_1(X,0) \tag{A12}$$

Solution (A12) for $C_0(X)$ can be rewritten as:

$$\varphi(1) - \varphi(C_1(X,0)) = \alpha X,\quad \varphi'(C_1) = \frac{1}{\Lambda_0C_1^q\left(\frac{\gamma C_1-\gamma+\alpha}{\alpha}\right)^r} \tag{A13}$$

For any integers q and r, the integral (A12) can be expressed explicitly.

Multiplying Eq. (A10) by α and adding the result to Eq. (A9) results in the following conservation law form for system (A9) and (A10):

$$\alpha\frac{\partial S}{\partial \tau} + \frac{\partial C_1}{\partial X} = 0 \tag{A14}$$

Expressing S from Eq. (A9) for S yields:

$$S(X,\tau)=\frac{1}{\alpha\Lambda_0 C_1^q\left(\frac{\gamma C_1-\gamma+\alpha}{\alpha}\right)^r}\frac{\partial C_1}{\partial X}+1=\frac{1}{\alpha}\frac{\partial\varphi(C_1)}{\partial X}+1 \tag{A15}$$

Substituting the obtained expression (A15) into Eq. (A14) yields

$$\frac{\partial}{\partial\tau}\left(\frac{\partial\varphi(C_1)}{\partial X}\right)+\frac{\partial C_1}{\partial X}=0 \tag{A16}$$

Changing the order of derivatives in the first term of Eq. (A16), integrating with respect to X, and accounting for boundary conditions (15) results in:

$$\frac{\partial\varphi(C_1)}{\partial\tau}+C_1=1 \tag{A17}$$

Separating variables in Eq. (A17) and integrating in τ while accounting for initial condition (A13) result in solution $C_1(X,\tau)$:

$$\int_{C_0(X)}^{C_1}\frac{\varphi'(C)dC}{(1-C)}=\tau \tag{A18}$$

Where $C_0(X)=C_1(X,0)$ is given by expressions (A12) or (A13). Accounting for expression (A13), solution (A18) can be rewritten as:

$$\int_{C_0(X)}^{C_1}\frac{dC}{\Lambda_0(1-C)C^q\left(\frac{\gamma C-\gamma+\alpha}{\alpha}\right)^r}=\tau \tag{A19}$$

Finally, the concentration of the first reactant in coordinates (X,T) follows from Eq. (A19):

$$\int_{C_0(X)}^{C_1}\frac{dC}{\Lambda_0(1-C)C^q\left(\frac{\gamma C-\gamma+\alpha}{\alpha}\right)^r}=T-X \tag{A20}$$

where $C_0(X)$ as a function of X is given by either of Eqs. (A12) or (A13). Upon the return to coordinates (X,T), concentration $C_0(X)=C_1(X,0)$ at $\tau=0$ becomes a concentration behind the front $C_1(X,X)$, $T=X$. However, expressions (A12) and (A13) still can be used for the lower limit in integral (A19).

The concentration of the second reactant can be found from Eqs. (A8) and (A19):

$$\int_{C_0(X)}^{\frac{\alpha C_2-\alpha+\gamma}{\gamma}}\frac{dC}{\Lambda_0(1-C)C^q\left(\frac{\gamma C-\gamma+\alpha}{\alpha}\right)^r}=T-X \tag{A21}$$

For the known concentration of the first reactant $C_1(X,T)$, the expression for deposit concentration $S(X,T)$ is presented in the next Appendix.

Appendix B. Riemann invariant

Differentiation of Eq. (A1) with respect to X yields

$$\frac{\varphi'(C_1)}{1-C_1}\frac{\partial C_1}{\partial X}=\frac{\varphi'(C_0)}{1-C_0}\frac{dC_0}{dX} \tag{B1}$$

where $\varphi'(C)$ and $C_0(X)$ are defined by Eqs. (A13) and (A12), respectively.

For $\tau=0$, Eq. (A15) takes the form

$$0=\frac{1}{\alpha}\frac{d\varphi(C_0)}{dX}+1 \tag{B2}$$

Substituting second equality of Eqs. (A15) and (B2) into (B1) results in

$$\frac{S(X,\tau)-1}{1-C_1(X,\tau)}=-\frac{1}{1-C_0(X)} \tag{B3}$$

Formula (B3) determines the Riemann invariant for system Eqs. (A9) and (A10). It yields explicit expression for solution $S(X,T)$ via $C_1(X,T)$, given by Eqs. (A19) and (A13).

References

[1] C. Bethke, Geochemical reaction modeling: concepts and applications, Oxford University Press, New York, 1996.

[2] J.I. Drever, The geochemistry of natural waters, 3rd ed., Prentice Hall Englewood Cliffs, NJ, 1997.

[3] D.A. Frank-Kamenetskii, Diffusion and heat transfer in chemical kinetics, 2nd ed., Plenum Press, New York, 1969.

[4] H.S. Fogler, Essentials of chemical reaction engineering, 4th ed., Pearson Education, Upper Saddle River, NJ, 2010.

[5] P. Bedrikovetsky, Mathematical theory of oil & gas recovery, Springer Science & Business Media, Dordrecht, 2013.

[6] E.J. Mackay, M.M. Jordan, Impact of brine flow and mixing in the reservoir on scale control risk assessment and subsurface treatment options: Case histories, J. Energy Resour. Technol. 127 (2005) 201–213.

[7] K.S. Sorbie, E.J. Mackay, Mixing of injected, connate and aquifer brines in waterflooding and its relevance to oilfield scaling, J. Pet. Sci. and Eng. 27 (1-2) (2000) 85–106.
[8] Y.B. Zeldovich, G.I. Barenblatt, V.B. Librovich, G.M. Makhviladze (Eds.), The Mathematical Theory of Combustion and Explosions, Springer US, Boston, MA, 1985.
[9] P.E. Kechagia, I.N. Tsimpanogiannis, Y.C. Yortsos, P.C. Lichtner, On the upscaling of reaction-transport processes in porous media with fast or finite kinetics, Chem. Eng. Sci. 57 (13) (2002) 2565–2577.
[10] P.C. Lichtner, D.M. Tartakovsky, Stochastic analysis of effective rate constant for heterogeneous reactions, Stoch. Env. Res. Risk Assess 17 (6) (2003) 419–429.
[11] A. Altree-Williams, J. Brugger, A. Pring, P. Bedrikovetsky, Coupled reactive flow and dissolution with changing reactive surface and porosity, Chem. Eng. Sci. 206 (2019) 289–304.
[12] A. Vaz, P. Bedrikovetsky, P.D. Fernandes, A. Badalyan, T. Carageorgos, Determining model parameters for non-linear deep-bed filtration using laboratory pressure measurements, J. Pet. Sci. and Eng. 151 (2017) 421–433.
[13] A. Vaz, D. Maffra, T. Carageorgos, P. Bedrikovetsky, Characterisation of formation damage during reactive flows in porous media, J. Nat. Gas Sci. and Eng. 34 (2016) 1422–1433.
[14] S.J. Ahmed, Laboratory study on precipitation of calcium sulphate in Berea sandstone cores, King Fahd University of Petroleum and Minerals, Dhahran, Saudi Arabia, 2004.
[15] S.M. Ghaderi, R. Kharrat, H.A. Tahmasebi, Experimental and theoretical study of calcium sulphate precipitation in porous media using glass micromodel, Oil Gas Sci. Technol. 64 (4) (2009) 489–501.
[16] J. Moghadasi, H. Müller-Steinhagen, M. Jamialahmadi, A. Sharif, Model study on the kinetics of oil field formation damage due to salt precipitation from injection, J. Pet. Sci. Eng. 43 (3-4) (2004) 201–217.
[17] A.C. Alvarez, P.G. Bedrikovetsky, G. Hime, A.O. Marchesin, D. Marchesin, J. R. Rodrigues, A fast inverse solver for the filtration function for flow of water with particles in porous media, Inverse Problems 22 (1) (2006) 69–88.
[18] A.C. Alvarez, G. Hime, D. Marchesin, P.G. Bedrikovetsky, The inverse problem of determining the filtration function and permeability reduction in flow of water with particles in porous media, Transp. in Porous, Media 70 (1) (2007) 43–62.
[19] S. Borazjani, A. Behr, L. Genolet, P. Kowollik, P. Bedrikovetsky, Ion-exchange inverse problem for low-salinity coreflooding, Transp. in Porous, Media 128 (2) (2019) 571–611.
[20] S. Oladyshkin, J.-J. Royer, M. Panfilov, Effective solution through the streamline technique and HT-splitting for the 3D dynamic analysis of the compositional flows in oil reservoirs, Transp. in Porous, Media 74 (3) (2008) 311–329.
[21] J. Pérez Guerrero, L. Pimentel, T. Skaggs, M.T.J.I.j.o.h. Van Genuchten, m. transfer, Analytical solution of the advection–diffusion transport equation using a change-of-variable and integral transform technique, Int. J. Heat and Mass Transf. 52 (2009) 3297.
[22] J.S. Pérez Guerrero, E.M. Pontedeiro, M.Th. van Genuchten, T.H. Skaggs, Analytical solutions of the one-dimensional advection–dispersion solute transport equation subject to time-dependent boundary conditions, Chem. Eng. J 221 (2013) 487–491.
[23] A.C. Lasaga, Kinetic theory in the earth sciences, Princeton Univ. Press, Princeton, NJ, 2014.
[24] D.M. Tartakovsky, M. Dentz, P.C. Lichtner, Probability density functions for advective-reactive transport with uncertain reaction rates, Water Resour. Res. 45 (7) (2009), https://doi.org/10.1029/2008WR007383.
[25] H. Yuan, A. Shapiro, Z. You, A. Badalyan, Estimating filtration coefficients for straining from percolation and random walk theories, Chem. Eng. J 210 (2012) 63–73.
[26] A.H. Benneker, A.E. Kronberg, I.C. Lansbergen, K.R. Westerterp, Mass dispersion in liquid flow through packed beds, Ind. Eng. Chem. Res. 41 (7) (2002) 1716–1722.
[27] I. Battiato, D.M. Tartakovsky, A.M. Tartakovsky, T.D. Scheibe, Hybrid models of reactive transport in porous and fractured media, Adv. Water Resour. 34 (9) (2011) 1140–1150.
[28] A. Polyanin, V.V. Dilman, Methods of modeling equations and analogies in chemical engineering, CRC Press, Boca Raton, FL, 1994.
[29] I. Battiato, D.M. Tartakovsky, Applicability regimes for macroscopic models of reactive transport in porous media, J. Contam. Hydrol. 120-121 (2011) 18–26.
[30] A.D. Polyanin, A.V. Manzhirov, Handbook of mathematics for engineers and scientists, Chapman & Hall/CRC, Boca Raton, FL, 2006.
[31] A.D. Polyanin, V.F. Zaitsev, Handbook of nonlinear partial differential equations, Chapman & Hall/CRC, Boca Raton, FL, 2006.
[32] L.F. Shampine, Solving hyperbolic PDEs in MATLAB, Appl. Num. Anal. & Comp. Math. 2 (3) (2005) 346–358.
[33] L.F. Shampine, Two-step Lax-Friedrichs method, Appl. Math. Lett. 18 (10) (2005) 1134–1136.
[34] V. Selyakov, V. Kadet, Percolation models for transport in porous media: with applications to reservoir engineering, Springer Science & Business Media, Dordrecht, 2013.
[35] P. Churcher, P. French, J. Shaw, L. Schramm, Rock properties of Berea sandstone, Baker dolomite, and Indiana limestone, California, SPE Inter. Symp. on Oilfield Chem. Anaheim, 1991, pp. 431–446.
[36] A.P. Sheppard, J.-Y. Arns, M.A. Knackstedt, W.V. Pinczewski, Volume Conservation of the Intermediate Phase in Three-Phase Pore-Network Models, Transp. in Porous, Media 59 (2) (2005) 155–173.
[37] B. Bijeljic, A.H. Muggeridge, M.J. Blunt, Pore-scale modeling of longitudinal dispersion, Water Resour. Res. 40 (11) (2004), https://doi.org/10.1029/2004WR003567.
[38] P.G. Bedrikovetsky, R.P. Lopes Jr., P.M. Gladstone, F.F. Rosario, M.C. Bezerra, E. A. Lima, Barium sulphate oilfield scaling: mathematical and laboratory modelling, Society of Petroleum Engineers, Aberdeen, United Kingdom, SPE Int. Symp. on Oilfield Scale, 2004, p. 14.
[39] V.E. Nazaikinskii, P.G. Bedrikovetsky, L.I. Kuzmina, Y.V. Osipov, Exact solution for deep bed filtration with finite blocking time, SIAM J. on Appl. Math. 80 (5) (2020) 2120–2143.
[40] R. Farajzadeh, A. Ameri, M.J. Faber, D.W. Van Batenburg, D.M. Boersma, J. Bruining, Effect of continuous, trapped, and flowing gas on performance of Alkaline Surfactant Polymer (ASP) flooding, SPE Enhanc. Oil Recovery Conf. Kuala Lumpur, Malaysia, 2013.
[41] R. Farajzadeh, P.L.J. Zitha, J. Bruining, Enhanced mass transfer of CO2 into water: experiment and modeling, Ind. Eng. Chem. Res. 48 (13) (2009) 6423–6431.
[42] R. Farajzadeh, A. Andrianov, P.L.J. Zitha, Investigation of immiscible and miscible foam for enhancing oil recovery, Ind. Eng. Chem. Res. 49 (4) (2010) 1910–1919.
[43] C.V. Chrysikopoulos, V.E. Katzourakis, Colloid particle size-dependent dispersivity, Water Resour. Res. 51 (6) (2015) 4668–4683.
[44] M. Asraf-Snir, V. Gitis, Tracer studies with fluorescent-dyed microorganisms—A new method for determination of residence time in chlorination reactors, Chem. Eng. J 166 (2) (2011) 579–585.
[45] M.D. Becker, Y. Wang, K.D. Pennell, L.M. Abriola, A multi-constituent site blocking model for nanoparticle and stabilizing agent transport in porous media, Environ. Sci. 2 (2015) 155–166.
[46] A. Shapiro, H. Yuan, Application of stochastic approaches to modelling suspension flow in porous media, Statistical mechanics and random walks: Principles, processes and applications, Nova Science Publishers (2012) 1–36.
[47] T.D. Scheibe, E.M. Murphy, X. Chen, A.K. Rice, K.C. Carroll, B.J. Palmer, A. M. Tartakovsky, I. Battiato, B.D. Wood, An analysis platform for multiscale hydrogeologic modeling with emphasis on hybrid multiscale methods, Ground Water 53 (1) (2015) 38–56.
[48] C. Bethke, ChemPlugin User's Guide, Aqueous Solutions LLC, Champaign, Illinois, 2018.
[49] D.L. Parkhurst, C. Appelo, User's guide to PHREEQC (Version 2): A computer program for speciation, batch-reaction, one-dimensional transport, and inverse geochemical calculations, U.S. Geol. Surv. Water Resour. Invest. Rep. 99-4259, Denver, Colorado, 1999.
[50] T. Xu, N. Spycher, E. Sonnenthal, L. Zheng, K. Pruess, TOUGHREACT user's guide: a simulation program for non-isothermal multiphase reactive transport in variably saturated geologic media, version 2.0, Earth Sciences Division, Lawrence Berkeley Natl. Lab., Berkeley, California, 2012.
[51] H. Yuan, A.A. Shapiro, Modeling non-Fickian transport and hyperexponential deposition for deep bed filtration, Chem. Eng. J 162 (3) (2010) 974–988.
[52] H. Yuan, A.A. Shapiro, A mathematical model for non-monotonic deposition profiles in deep bed filtration systems, Chem. Eng. J 166 (1) (2011) 105–115.
[53] H. Zhang, G.V.C. Malgaresi, P. Bedrikovetsky, Exact solutions for suspension-colloidal transport with multiple capture mechanisms, Int. J. of Non-Linear Mech. 105 (2018) 27–42.
[54] P. Bedrikovetsky, Z. You, A. Badalyan, Y. Osipov, L. Kuzmina, Analytical model for straining-dominant large-retention depth filtration, Chem. Eng. J 330 (2017) 1148–1159.
[55] A.A. Shapiro, Continuous upscaling and averaging, Chem. Eng. J 234 (2021) 116454, https://doi.org/10.1016/j.ces.2021.116454.
[56] P. Bedrikovetsky, Y. Osipov, L. Kuzmina, G. Malgaresi, Exact upscaling for transport of size-distributed colloids, Water Resour. Res. 55 (2) (2019) 1011–1039.
[57] A.P. Reverberi, M. Vocciante, B. Fabiano, Scaling effects and front propagation in a class of reaction-diffusion equations: From classic to anomalous diffusion, Chem. Eng. J 377 (2019), 121154.
[58] P. Bedrikovetsky, R.M. Silva, J.S. Daher, J.A. Gomes, V.C. Amorim, Well-data-based prediction of productivity decline due to sulphate scaling, J. Pet. Sci. and Eng. 68 (2009) 60-70.
[59] P.G. Bedrikovetsky, E.J. Mackay, R.M. Silva, F.M. Patricio, F.F. Rosário, Produced water re-injection with seawater treated by sulphate reduction plant: Injectivity decline, analytical model, J. Pet. Sci. and Eng. 68 (2009) 19-28.
[60] F. Civan, Reservoir formation damage, 3rd ed., Gulf Professional Publishing, Oxford, 2015.
[61] S. Borazjani, A.J. Roberts, P. Bedrikovetsky, Splitting in systems of PDEs for two-phase multicomponent flow in porous media, Appl. Math. Lett. 53 (2016) 25–32.
[62] S. Oladyshkin, M. Panfilov, Streamline splitting between thermodynamics and hydrodynamics in a compositional gas–liquid flow through porous media, C. R. Mécanique 335 (1) (2007) 7–12.

4. Large-deposit non-linear chemical reactive flows in porous media: Identifiability and observability

Yang, S., Russell, T., Vaz, A. and Bedrikovetsky, P.

Accepted for publication in Journal of Natural Gas Science and Engineering

Statement of Authorship

Title of Paper	Large-deposit non-linear chemical reactive flows in porous media: Identifiability and observability
Publication Status	☐ Published ☑ Accepted for Publication ☐ Submitted for Publication ☐ Unpublished and Unsubmitted work written in manuscript style
Publication Details	Yang, S., Russell, T., Vaz, A., and Bedrikovetsky, P., Large-deposit non-linear chemical reactive flows in porous media: Identifiability and observability, Journal of Natural Gas Science and Engineering, Accepted for Publication

Principal Author

Name of Principal Author (Candidate)	Shuyan Yang		
Contribution to the Paper	Performed model fitting to laboratory test results, unidentifiability studies, result analysis		
Overall percentage (%)	70%		
Certification:	This paper reports on original research I conducted during the period of my Higher Degree by Research candidature and is not subject to any obligations or contractual agreements with a third party that would constrain its inclusion in this thesis. I am the primary author of this paper.		
Signature		Date	08/05/2022

Co-Author Contributions

By signing the Statement of Authorship, each author certifies that:

i. the candidate's stated contribution to the publication is accurate (as detailed above);

ii. permission is granted for the candidate in include the publication in the thesis; and

iii. the sum of all co-author contributions is equal to 100% less the candidate's stated contribution.

Name of Co-Author	Thomas Russell		
Contribution to the Paper	Technical discussions, problem formulation, manuscript preparation		
Signature		Date	08/05/2022

Name of Co-Author	Alexandre Vaz		
Contribution to the Paper	Design and performed laboratory experiments		
Signature		Date	12/05/2022

Name of Co-Author	Pavel Bedrikovetsky		
Contribution to the Paper	Problem formulation, technical discussions, supervision of the project		
Signature		Date	09/05/2022

Large-deposit non-linear chemical reactive flows in porous media: Identifiability and observability

Shuyan Yang[a], Thomas Russell[a], Alexandre Vaz[b], Pavel Bedrikovetsky[a]

[a] *Australian School of Petroleum and Energy Resources, University of Adelaide, Adelaide, SA 5005, Australia*

[b] *Laboratory of Exploration and Production Engineering LENEP, North Fluminense State University UENF, Macae, RJ, Brazil*

Abstract

This work discusses the use of additional pressure drop measurements in the characterisation of chemical reactive flow in porous media resulting in insoluble solid deposition. Previous studies of this problem have used outlet breakthrough concentration of one species and pressure drop across the sample during the commingled injection of reacting species, to determine model coefficients. In this work, we consider the introduction of additional measurements of pressure drop across subsections of the sample. The recently derived analytical model is compared to laboratory data to demonstrate the validity of both the model and additional measurement data. The effect of measuring different quantities is assessed by considering the identifiability of the model parameters. All parameters exhibit finite confidence intervals, however, datasets neglecting breakthrough concentration result in higher parameter uncertainty. Higher parameter uncertainty is shown to result in uncertainty in deposit profiles and prediction of pressure drop at higher length scales, demonstrating the importance of limiting parameter uncertainty through experimental design.

Nomenclature

A_i	lower limit of investigation for parameter θ_i	*Greek letters*	
b	reaction capacity coefficient, $L^3\,mol^{-1}$, $m^3\,mol^{-1}$	α, γ	dimensionless parameters
B_i	upper limit of investigation for parameter θ_i	β	formation damage coefficient
c	molar concentration of reactant, mol L^{-3}, mol m^{-3}	δ_b	perturbation of reaction capacity coefficient
c_0	injected molar concentration of reactant, mol L^{-3}, mol m^{-3}	δ_λ	perturbation of reaction rate coefficient
C	dimensionless molar concentration of reactant	Δp	pressure drop across the core, $ML^{-1}T^{-2}$, N m^{-2}
C_0	dimensionless molar concentration of reactant along the injection front	Δ_α	tolerance
D	deposit	ε	degree of confidence
d_k	number of sets of measurement data	θ	set of model parameters
J	impedance	$\theta_{i,max}$	upper limit of confidence interval for parameter i
k	permeability, L^2, m^2	$\theta_{i,min}$	lower limit of confidence interval for parameter i
L	core length, L, m	$\hat{\theta}$	optimal model parameter set
m	number of datapoints within a set of measurement data	$\lambda(\sigma)$	reaction rate function
n	formation damage exponent	$\Lambda(S)$	dimensionless reaction rate function
p	fluid pressure, $ML^{-1}T^{-2}$, N m^{-2}	λ_0	reaction rate coefficient, $L^{3q+3r-4}mol^{1-q-r}$, $m^{3q+3r-4}mol^{1-q-r}$
P	dimensionless fluid pressure	Λ_0	dimensionless reaction rate coefficient

$Q()$	quartile function	σ	solid deposit concentration, mol L^{-3}, mol m^{-3}
q,r	stoichiometric coefficients of reactant 1 and 2	σ_{ki}	measurement error of dataset k at time t_i
Q,R	reactants 1 and 2	χ^2	chi-squared
R^2	coefficient of determination	χ^2_{min}	minimum value of chi-squared (corresponding to optimum θ)
S	dimensionless deposit concentration	ω	fraction of the core across which pressure drop is measured
t	time, T, s		
T	dimensionless time	*Subscript*	
U	darcy flow velocity, LT^{-1}, ms^{-1}	0	initial
x	coordinate, L, m	1	first reactant
X	dimensionless coordinate, L, m	2	second reactant
$y_k(t)$	measurement data		
$y_k(t,\theta)$	model prediction		

1. Introduction

The flow of reactive species through porous media, and the subsequent deposition of insoluble solids, occurs frequently in a number of gas and oil production processes. This commonly occurs during the injection of non-native species into natural reservoirs such as during CO_2 injection for storage purposes [1-6], hydrogen storage [7], water injection in enhanced geothermal projects and waterflooding in oilfields [8-10], or even in the natural incursion of seawater into coastal freshwater aquifers [11-13]. It also occurs when a number of fluids are co-injected into a reservoir, and react during their commingled flow in the porous media [14, 15]. The list of other applications of reactive transport in gas and oil production includes well acidizing and acid- fracturing [16-18], gas production from coals [19, 20], ionic exchange and mineral-dissolution reactions with consequent fines migration [21-25], and oilfield sulphate scaling [26].

The reaction between different ionic species suspended in the fluids decreases their concentrations as the concentrations of reaction products increases. When the reaction between two suspended ions results in an insoluble product, solid precipitate is formed within the porous media, which can clog the internal fluid pathways and reduce the permeability of the porous media [27, 28]. This reduction of permeability can increase oil recovery by delaying water breakthrough and increasing sweep efficiency. More commonly, the decrease in permeability decreases injection or production potential, thus decreasing the viability of projects. This is often seen in oilfields, where sulphate-rich injected seawater mixes with the metal-rich natural reservoir waters to produce insoluble salts, reducing well injectivity/productivity [29, 30].

Central to the understanding and prediction of these phenomena is an accurate mathematical framework for the underlying processes.

Suppose we have an irreversible chemical reaction between two species (Q,R) that results in an insoluble solid (D):

$$qQ + rR \rightarrow D \tag{1}$$

where q and r represent the stoichiometric coefficients for species Q and R, respectively. For this reaction, the reaction rate is given by the law of mass action [13, 31]:

$$\frac{\partial \sigma}{\partial t} = \lambda U c_1^q c_2^r, \tag{2}$$

where σ is the deposit concentration, t is time, λ is the reaction rate coefficient, U is the fluid velocity, and c_1 and c_2 are the concentrations of the two reacting species. The reaction rate constant in this case is λU.

The decrease in permeability as a result of the deposit growth is given by:

$$\frac{k_0}{k(\sigma)} = (1 + \beta\sigma)^n \tag{3}$$

where k_0 is the initial, undamaged permeability, β is the formation damage coefficient, and n is the formation damage exponent. The classical form of $n=1$ is obtained by a Taylor's series expansion, but more recent studies have made use of the formation damage exponent to extend the applicability of the formula [32]. Similarly, the reaction rate coefficient, λ has been posited to be a function of the deposit concentration, with Eq. (2) representing the limit of small deposit concentration [33].
This definition of the deposit concentration assumes spatial averaging over a number of pores, similar to the scale required for Darcy's law to be valid. While the inclusion of the formation damage exponent allows for diminishing or intensifying formation damage with higher deposit concentrations, the model does not account for the co-occurrence of different damage mechanisms. For example, deposit which forms a uniform film on the internal porous surface will induce less damage than deposit which plugs pore throats. In situations where the deposit accumulates in multiple ways, the concentrations of each deposit type would need to be modelled explicitly. This limitation also applies to dual-porosity porous media, in which deposits within meso- and macro-porosity will have significantly different effects on the overall rock permeability [34, 35].

The Eqs. (2,3) along with conservation laws for the reacting species, and Darcy's law for the fluid velocity, present a closed system of equations for the reacting species, fluid velocity and pressure, and the deposit concentration. An exact solution, along with analysis of a limited number of cases, has recently been presented [32].

The primary use of these equations is to make predictions and perform optimisation/design of field processes. In order to do so, accurate estimates need to be made of the model coefficients. To this end, experimentalists have developed techniques to simulate flow environments analogous to those in reservoir conditions, and measure species concentrations, as well as fluid pressures and velocities, in order to study the system.

The linear case, where λ is constant and n is one has been studied previously [36] and exhibits relatively simple behaviour. The outlet concentration of one reacting species exhibits a constant breakthrough concentration determined entirely by the reaction rate coefficient. Measurements of the deposit concentration, or more commonly, the fluid pressure drop across a sample, shows a linear growth, with a slope determined by both λ and β. Thus, by measuring both the outlet concentration of one reacting species and the total pressure drop across the core, the two system parameters can be uniquely identified.

In the study of formation damage due to the injection of suspended particles, the system is also characterised by a rate coefficient (filtration coefficient) and a formation damage coefficient, describing the damage caused by each particle [37, 38]. Researchers in this field have similarly measured the outlet concentration of particles and pressure drop in order to determine the model parameters [39, 40]. However, given that the measurement of particle concentrations is more cumbersome, and often less accurate than pressure measurements, some researchers have developed a technique which uses two pressure drops, one measured over the total core length, and one measured over a smaller portion of the sample [33, 41]. This is referred to as the three-point pressure method although the technique has been generalised to include the measurement of pressure at more than two points in the core. This method has been shown to produce accurate estimates of the parameters, and parameter uncertainty has been linked analytically to the measurement uncertainty [42].

However, in some cases, it has been shown that the three-point pressure provides insufficient information to characterise the system. When analysing fines migration, where formation damage

occurs due to the dislodgement of natural particles from the internal porous surface, it has been shown that not measuring the outlet concentration of particles prevents the system from being uniquely characterised [43]. Thus, it is not yet known under what circumstances the inclusion of additional pressure drop measurements can circumvent the need to measure species concentration at the outlet.

One such system of interest is the chemical reactive flow defined by Eqs. (2,3), wherein we permit non-linearity through some function $\lambda(\sigma)$ and a value of n not equal to one. For this case, the breakthrough concentration is no longer constant, and the deposit concentration, or pressure drop curves, are non-linear. In this case it is not yet known whether outlet concentration measurements are necessary. Presenting a system for experimental characterisation of chemical reactive flow in porous media using only pressure drop measurements would allow faster, more accurate, and potentially on-site identification of model parameters. An analytical solution for this system has been derived in a previous work [32]. Leveraging this analytical solution, this paper aims to resolve the question of the necessity of outlet concentration, and, more broadly, prescribe a set of measurement data sufficient for experimentally characterising the system.

The structure of the paper is as follows. Section 2 outlines the problem of determining the model parameters from experimental data. Section 3 presents a series of experimental data and assesses the validity of the model through inverse modelling. Section 4 presents a quantitative study of the uniqueness of derived parameters and their uncertainty using synthetically generated data. Section 5 discusses the results, and Section 6 concludes the work.

2. Formulation of the problem

Following the new mathematical model presented by Yang, Osipov, Xu, Kuzmina, Russell and Bedrikovetsky [32] which describes non-linear chemical reactive flow in porous media, this study aims to evaluate various methods for estimating the model parameters from laboratory data. In particular, focus is placed on the use of additional pressure drop measurements following the success of this methodology in studying particle-based formation damage as well as the superior accuracy of pressure measurements compared with species' concentrations.

The details of the system that we are interested in is as follows. A homogeneous porous media saturated with water is injected with two commingled fluids containing a mix of suspended ions, which, when combined, result in the formation of insoluble salts and thus, the formation of solid precipitate. The deposition of this solid precipitate on the internal surface of the porous media results in both a decrease in the fluid permeability, and a change in the chemical reaction rate. The nature of this decline in permeability and variation of the chemical reaction rate are the primary sources of non-linearity in measurements, and thus are a key focus for the experimental characterisation of the system.

The decrease in permeability is defined by Eq. (3). The formation damage coefficient, β, describes the magnitude of permeability damage per unit of deposit. The formation damage exponent, n, describes the acceleration or deceleration of permeability decline with increasing deposit concentration.

The rate of deposit growth is given by:

$$\frac{\partial \sigma}{\partial t} = \lambda(\sigma) U c_1^q c_2^r, \quad \lambda(\sigma) = \begin{cases} \lambda_0 (1 - b\sigma), & \sigma < b^{-1} \\ 0, & \sigma > b^{-1} \end{cases} \tag{4}$$

The reaction rate coefficient, λ_0, describes the initial chemical reaction kinetics, in the absence of any deposit. The reaction capacity coefficient, b, describes the change in the reaction rate with deposit concentration. Where the deposit growth helps catalyse the reaction by creating a larger internal surface, b is negative, resulting in an increasing deposition rate. Conversely, when the deposit reduces the concentration of highly reactive surface sites, b is positive, and the reaction rate decreases with the deposit concentration. A more rigorous physical interpretation of both b and β is presented in [32].

In Appendix A we provide the full system of governing equations for non-linear chemical reactive flow in porous media and the exact solution is presented in Appendix B.

The set of parameters (λ_0,b,β,n) are the unknowns for the system of equations. Given a set of measurements of the system, we wish to solve the inverse problem of determining these four parameters uniquely and accurately. Given the complexity of the exact solution, no analytical inverse solution is known for this problem. Thus, the inverse solution is solved numerically using an optimisation procedure. The minimisation procedures utilised here involve the minimisation of squared deviation between the error

$$\sum_{k=1}^{m}\sum_{i=1}^{d_k}\left(y_k\left(t_i\right)-y_k\left(t_i,\theta\right)\right)^2 \tag{5}$$

where $y_k(t_i)$ is the measured data, $y_k(t_i,\theta)$ are the model predictions at time i based on the set of model unknowns, θ ,and summation is performed over each data point, $i = 1\ldots d_k$ within each data set $k = 1\ldots m$. The set of parameters $\hat{\theta}$ which minimises this function is considered the 'true' set of parameters.

The assumption that the minimisation of the squared error in Eq. (5) will result in the 'true' parameter set is not always satisfied. For this study, as the error structure of the data from the laboratory study is not known, we choose to assume that the error is homoscedastic (constant for all data) and uncorrelated.

For the study of chemical reactive flows in porous media, the data sets consists of the concentration of one dissolved species at the outlet (referred to as breakthrough concentration), as well as the pressure drop across the core, measuring the extent of permeability decline. In this paper, we also include the pressure drop measured across an intermediary portion of the core. Previous works have referred to this as the three-point pressure method [36], however in our study, both in the laboratory and in the synthetic data sets, we used three sets of pressure drop data, collected by pressure transducers at four points across the core. A schematic representation of the core setup and chemical reaction is presented in Fig. 1.

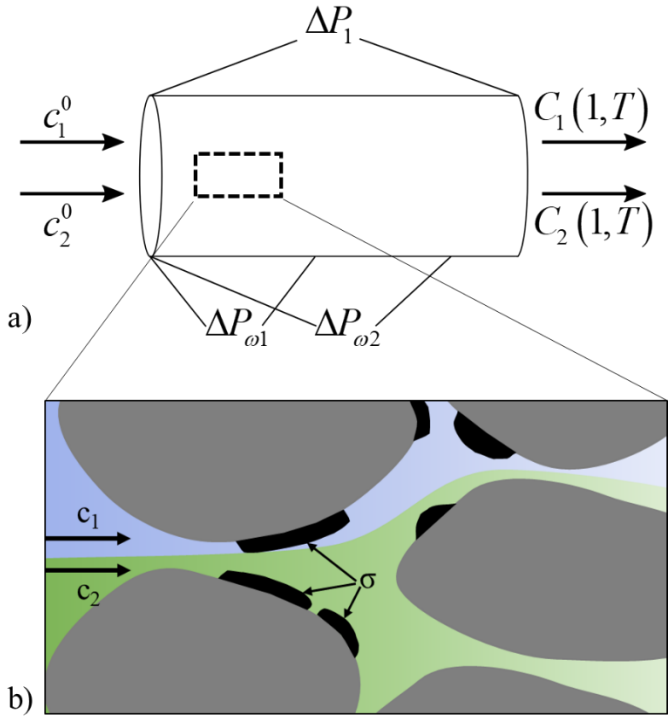

Figure 1. Schematic of chemical reaction in porous media during commingled injection, a) core setup including injection (c_1^0, c_2^0) and outlet (C_1, C_2) concentrations, and total (Δp) and intermediate (Δp_ω) pressure drops, b) flow of two reactants through porous media and the precipitation of the solid deposit, σ.

If the solution for non-linear chemical reactions in porous media was self-similar, then the pressure change at any point could be used to recalculate the pressure change at any other point, and thus additional pressure measurements would provide no new information. However, as was proven by Yang, Osipov, Xu, Kuzmina, Russell and Bedrikovetsky [32], the solution used in this work is not self-similar, and thus the investigation of additional pressure drop measurements has merit. For other models which are self-similar, this exercise would not be fruitful.

It is common for measurements of pressure drop to have much greater accuracy than those of concentration, especially when high concentrations of dissolved ions are studied, which, when measured using ion chromatography, need to be heavily diluted. Thus, we first evaluated the appropriateness of the three-point pressure method by comparing it with laboratory data. We then analysed the effectiveness of additional pressure measurements in the identification of the system parameters and compared it to the traditional approach of measuring the concentration of one species at the outlet.

3. Laboratory study and inverse modelling

In order to assess the assumptions of the model, several sets of laboratory data are presented here and compared with the model. All laboratory data were taken from [36]. The tests in these studies involved the co-injection of 'Formation water', rich in $BaCl_2$ and NaCl, and 'Seawater', rich in Na_2SO_4 and NaCl. Mixing these two fluids results in the formation of the insoluble salt $BaSO_4$ as per the reaction given in Eq. (6) below.

$$BaCl_2(aq) + Na_2SO_4(aq) \rightarrow BaSO_4 + 2NaCl \quad (6)$$

Cores used in this study were Berea sandstones, a type of core that is commonly used to emulate typical sandstone reservoir properties. A summary of the properties of the tests analysed in this study is presented below in Table 1. While we assumed homogeneity for each core sample, we did not make direct comparisons between each test analysed, and so it was not necessary for each core to have the same properties. Note that while the injected concentrations in Table 1 seem to differ from those presented by Vaz et al. in their study, they provide the concentrations of each ion within the 'formation water' and 'sea water' prior to their commingled injection.

Table 1. Core properties and test conditions for three laboratory tests from Vaz et al. 2016

	Q (cm^3/min)	k (md)	ϕ	c_{Ba} (ppm)	c_{SO4} (ppm)
Test 2	6	102	0.1766	305	945
Test 5	6	75.48	0.1691	200	1889
Test 7	4	97.98	0.1739	115	1417

The outlet concentration of Ba^{2+} was measured during the test (hereafter referred to as C_1), as well as the pressure drop across the whole length of the core (Δp_1 or $\omega=1$), across the first 49% of the core length ($\Delta p_{0.49}$ or $\omega=0.49$), and across the first 12% of the core length ($\Delta p_{0.12}$ or $\omega=0.12$). A complete description of the laboratory setup and methodology is presented by Vaz, Maffra, Carageorgos and Bedrikovetsky [36].

As described in the previous section, determination of the model parameters, (λ_0,b,β,n), involves the minimisation of the squared deviation between the model and measurement data, Eq. (6). Breakthrough concentrations are presented in dimensionless form, normalised by the injected concentration for that

species. Pressure drops are presented in dimensionless form as the impedance, defined by Eq. (A.5) in Appendix A. The curves are plotted against the number of pore volumes injected, a dimensionless measure of time (see Eq. (A.5)).

Optimisation was done using the Levenberg-Marquadt algorithm implemented in Matlab. This is a gradient based algorithm that requires an initial guess, which was varied to ensure that the true optimal fit was obtained. Lower bounds of zero were placed on the parameters λ_0, β, and n as there is no physical reason for any of these parameters being negative. The parameter b had no bounds as both positive and negative values are physically possible. The results of the fitting are shown in Fig. 2.

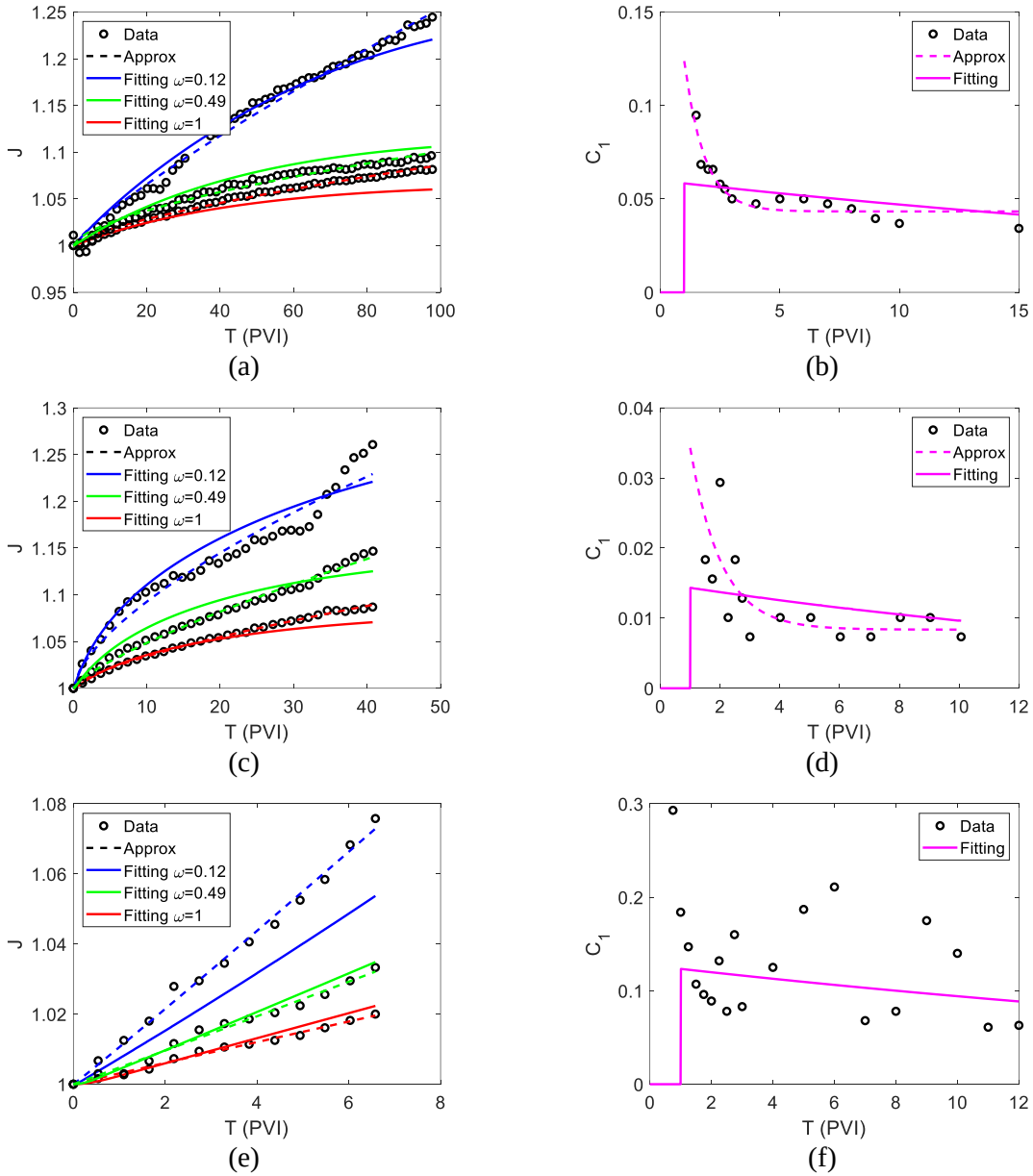

Figure 2. Fitting of experimental data: (a), (c), and (e) are the impedance fitting results from tests 2, 5, and 7, respectively; (b), (d), and (f) are the breakthrough concentration fitting results from tests 2, 5, and 7, respectively. Experimental data is taken from [36].

We note that the normalised concentration of barium (C_1) begins at 1 as the core was initially saturated with the 'formation water'. Beyond ~1 PVI, this has no effect on the modelling and so only data beyond the breakthrough is considered for tuning.

The experimental data exhibits the key characteristics of non-linear reactive flow. Namely, the breakthrough concentration is not constant, and the impedance curves grow non-linearly.

The parameters obtained from the fitting are presented in Table 2.

Table 2. Fitting parameters and coefficient of determination (R^2) obtained from the experimental data.

	b	β	λ_0	n	R^2 C_1	R^2 $J(\omega=0.12)$	R^2 $J(\omega=0.49)$	R^2 $J(\omega=1)$
Test 2	-0.0176	0.084	1.02	0.032	0.448	0.98	0.88	0.76
Test 5	-0.0145	0.0247	0.777	0.11	-12.09	0.99	0.29	0.998
Test 7	-0.005	0.09	0.39	0.051	-333.6	-0.09	0.99	1.00

The quality of fit in Fig. 2 demonstrates reasonable agreement between the model and the laboratory data. Poor quality of fit for concentration, as demonstrated by R^2 values in Table 2 are partly due to the large scattering of the concentration data. Slight mismatch in pressure drops for Test 2 (Fig. 2 a) and Test 7 (Fig. 2 e) indicate slightly sharper declines in deposit concentrations along the core than predicted by the model.

The tuning produces negative values of b for all three tests, in contrast with the positive values in the laboratory data of [44, 45]. These negative b values are consistent with the decreasing breakthrough concentration of Barium as observed in Fig. 2 (b,d,f).

4. Identifiability study

In the previous section we demonstrated that the inclusion of additional pressure drop measurements along with breakthrough concentrations can be used to characterise the non-linear chemical reaction. In this section we develop this further by assessing the identifiability of the parameter estimates and quantifying the uncertainty in each parameter. In order to avoid any systematic errors introduced by deviations between the model and measurements, we use synthetic data, generated by the model, to which we add uniformly distributed errors.

To assess the importance of each data set, we analysed seven different scenarios, each containing a different subset of the available measurement data. The notation (C_1,Δp_1,$\Delta p_{0.49}$,$\Delta p_{0.12}$) is used to designate the case where the outlet concentration of dissolved species 1, as well as pressure drop curves for ω=1, 0.49, and 0.12, are used.

The problem of optimisation involves the minimisation of some measure of the deviation between the model predictions and the data by changing the model parameters. For the purposes of assessing identifiability, we minimise the χ^2, defined as

$$\chi^2(\theta) = \sum_{k=1}^{m} \sum_{i=1}^{d_k} \frac{1}{\sigma_{ki}^2} \left(y_k(t_i) - y_k(t_i, \theta) \right)^2 \tag{7}$$

where σ_{ki} is the measurement error and summation is performed over each data point, $i = 1 \ldots d_k$ within each data set $k = 1 \ldots m$.

The correct approach to parameter identification involves the maximisation of the likelihood, or the maximisation of the probability of observing the measured data given that they were generated by a model with parameters, θ [46]. In general, this procedure involves the construction of a generative model that can simulate both the expected value of the data (obtained from the mathematical model) as well as the uncertainties associated with each point. In this work we restrict ourselves to the particular case where these uncertainties are gaussian, with standard deviations given by σ_{ki}. In this particular case,

the maximisation of the likelihood corresponds exactly to the minimisation of the χ^2 [46]. This assumption is common in engineering applications [47] but may not always be satisfied. For very simple cases, the covariance matrix of the χ^2 matrix can be used to derive confidence intervals, however choose not to use this technique to allow for more generality.

Thus, the problem is to find a set of parameters, θ such that χ^2 is minimum. We refer to the optimal parameter set as $\hat{\theta}$.

The principle of the following identifiability analysis is that while optimisation procedures might identify a set of model parameters that are a global minimum of χ^2, there might be other parameter sets that allow an equally close match to the data, or a sufficiently close match that these parameters should also be considered valid. If there are multiple parameter sets with equally good matches to the data, we say that the problem is structurally unidentifiable. Even in cases where this isn't true, as a result of measurement uncertainty, parameter sets whose χ^2 are sufficiently close to the optimal value are also considered permissible. In this sense we consider that each set of parameters has a certain probability of being the true value. The higher this probability is, the better the fit to the data (lower χ^2). Thus, the value of χ^2 computed over the space of all θ allows us to construct a probability distribution over the same space which represents the uncertainty in the true parameter values. It is possible to construct a region within the θ space, within which we have a certain degree of confidence that the true value lies within this region. The projection of this region onto a single parameter provides the confidence interval for that parameter. When the confidence interval for a parameter is infinite, we say that the parameter is practically unidentifiable.

To assess the identifiability of each parameter, we use the profile likelihood method [48, 49]. It is important to note that while referred to as the profile 'likelihood', the calculated quantity is in fact χ^2. As discussed earlier, the optimal parameter set maximises the likelihood, and in the case of gaussian measurement uncertainty, it also minimises the χ^2.

The profile likelihood is defined as:

$$\chi^2_{PL}(\theta) = \min_{\theta_{j\neq i}} \left[\chi^2(\theta) \right] \tag{8}$$

It is computed by fixing one parameter and tuning the remaining parameters. By repeating this procedure across a range of the fixed parameter, we can construct a profile $\chi^2(\theta_i)$ allowing the identifiability of the parameter to be assessed. The set of permissible parameters is defined by the confidence interval for the parameter:

$$\left\{ \theta \mid \chi^2(\theta) - \chi^2\left(\hat{\theta}\right) < \Delta_\varepsilon \right\} \tag{9}$$

where the tolerance Δ_ε follows from the quantiles of the χ^2 distribution:

$$\Delta_\varepsilon = Q\left(\chi^2_{df}, 1-\varepsilon\right) \tag{10}$$

where *df* is the number of degrees of freedom of the χ^2 distribution, here set as 1 given that only one of the variables is fixed [50].

A (1-ε)th quantile of the χ^2 distribution corresponds to the (1-ε)% confidence interval, or the range of the parameter θ_i such that we can be (1-ε)% confident that the parameter belongs within the interval. A complete procedure for calculating the profile likelihood is presented in Appendix C.

The width of the confidence interval for identifiable parameters provides a quantifiable measure of the quality of information derived from an experiment. This is the primary criteria we used to compare the value obtained from measuring different quantities during experiments.

The identifiability study was conducted on two synthetic data sets, one for an accelerating reaction (negative *b*), as in the laboratory data in this work, and one for a decelerating reaction (positive *b*), as was reported for a previous work [32].

4.1 Identifiability for accelerating reactions

A data set for studying negative *b* was generated using the parameter values of (λ_0,*b*,β,*n*)=(0.5,-0.5,0.6,0.8). Three point-pressure measurement locations are the same as those of the laboratory data presented in Section 3 (i.e. ω=1, ω=0.49, ω=0.12). The data, as well as the results of tuning the data with the model, are presented in Fig. 3. The model shows excellent agreement with the data, which demonstrates the ability of the model to accurately tune the data without issue. The obtained parameters are close to the input values. The ability of the model to find the global minimum in the χ^2 space is an important assumption for the subsequent analysis and has been verified for all cases.

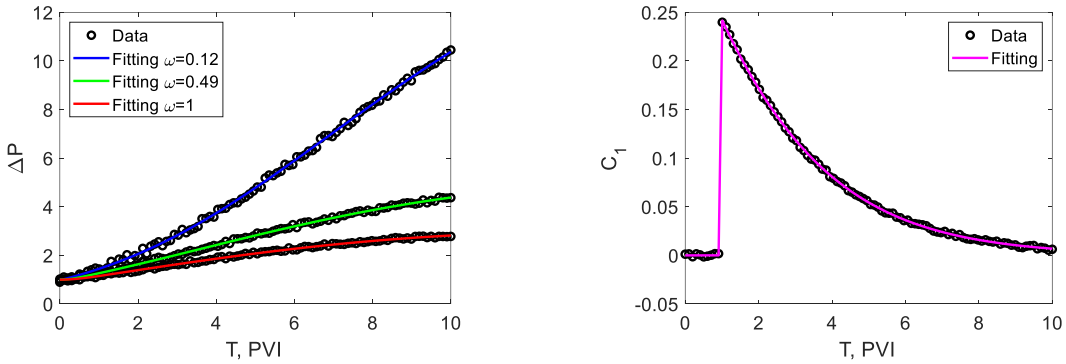

Figure 3. Synthetic experimental data set for negative *b* as well as model predictions following least-squared optimisation.

The profile likelihoods for all four parameters have been calculated according to the methodology describe above. The results, when tuning all four available data sets, are presented in Fig. 4.

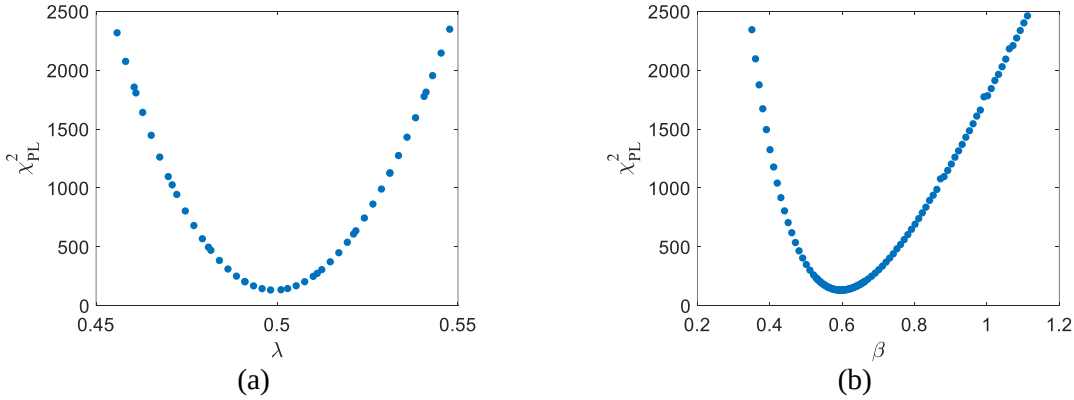

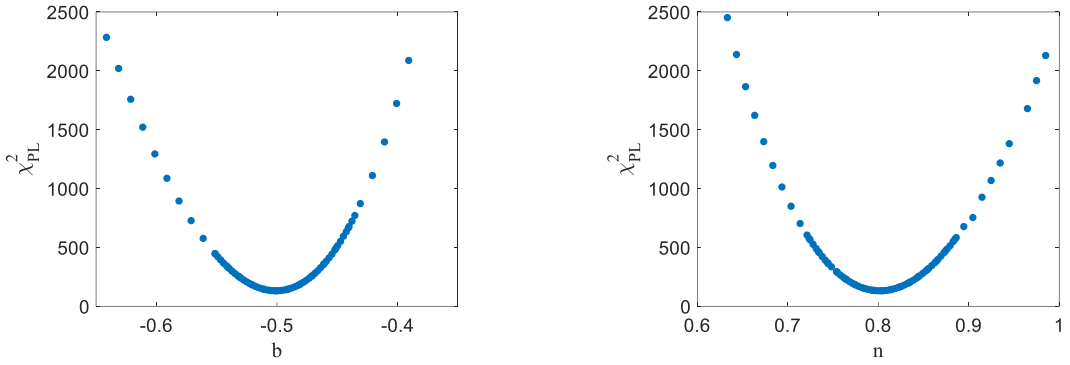

(c) (d)

Figure 4. χ^2_{PL} profiles for each parameter using the synthetic experimental dataset consisting of (C_1,Δp_1,$\Delta p_{0.49}$,$\Delta p_{0.12}$) for a negative value of the reaction capacity coefficient, b.

The curves in Fig. 4 are approximately quadratic, with some deviation, especially for β. The next step is to use Eq. (10) to determine the threshold value of χ^2_{PL} that corresponds to certain confidence intervals for each parameter. For this work, 95% and 99% confidence intervals are used, which correspond to Δ_ε values of approximately 3.84 and 6.63 respectively. The confidence intervals are determined by the intersection of quadratic approximations of the above curves around the minimum, and the lines $\chi^2_{PL} = \chi^2_{PL,min} + \Delta_\varepsilon$. This analysis for the curves in Fig. 4 is shown in Fig. 5.

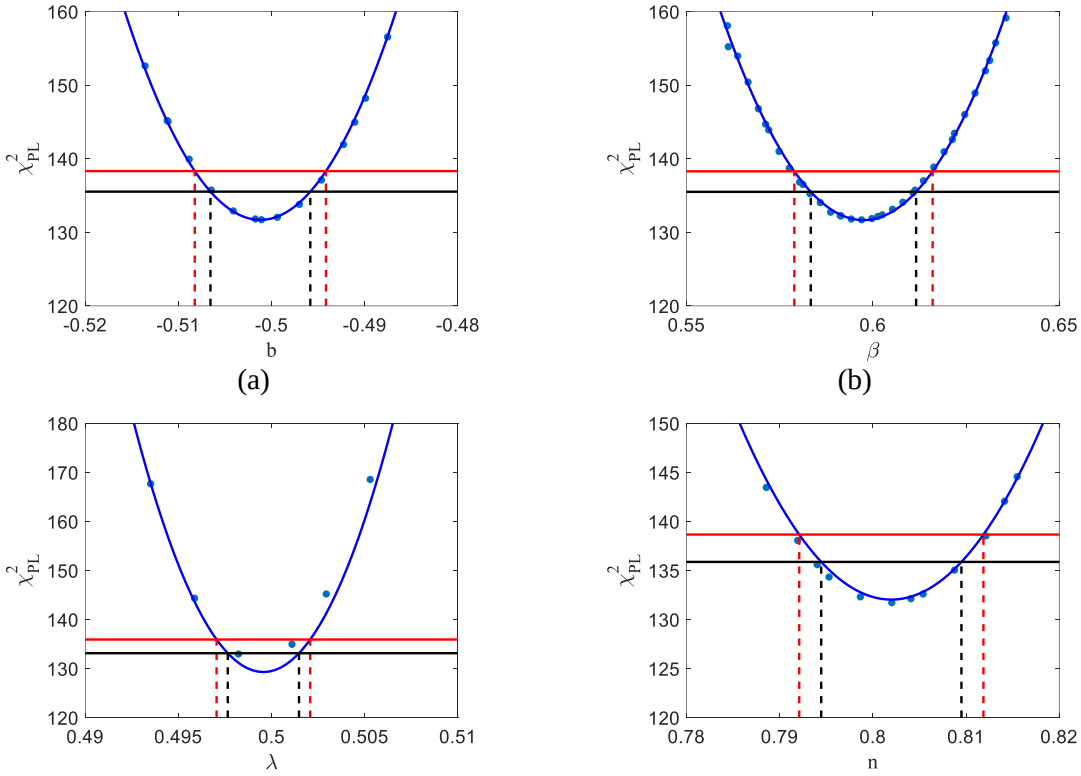

(a) (b)

(c) (d)

Figure 5. χ^2_{PL} profiles and confidence intervals for each parameter using the synthetic experimental dataset consisting of (C_1,Δp_1,$\Delta p_{0.49}$,$\Delta p_{0.12}$) for a negative value of the reaction capacity coefficient, b.

The derived confidence intervals are presented in Table 3, as well as those determined when fitting different subsets of the four availablej experimental curves.

Table 3. Upper and lower bounds of confidence intervals derived from the χ^2_{PL} profiles for the synthetic data set with an accelerating reaction.

Fitting Data	CI	Accelerating reaction							
		b		*β*		λ_0		*n*	
		Lower	Upper	Lower	Upper	Lower	Upper	Lower	Upper
C_1, ΔP_1, $\Delta P_{0.49}$, $\Delta P_{0.12}$	99%	-0.509	-0.496	0.581	0.618	0.497	0.502	0.792	0.812
	95%	-0.508	-0.497	0.585	0.613	0.498	0.501	0.794	0.81
ΔP_1, $\Delta P_{0.49}$, $\Delta P_{0.12}$	99%	-0.62	-0.414	0.557	0.637	0.432	0.56	0.786	0.819
	95%	-0.591	-0.435	0.567	0.627	0.447	0.545	0.79	0.816
ΔP_1, $\Delta P_{0.12}$	99%	-0.646	-0.403	0.55	0.64	0.421	0.567	0.785	0.823
	95%	-0.61	-0.427	0.561	0.629	0.439	0.549	0.789	0.819
C_1, ΔP_1, $\Delta P_{0.12}$	99%	-0.504	-0.497	0.578	0.619	0.497	0.502	0.792	0.813
	95%	-0.503	-0.498	0.583	0.614	0.497	0.501	0.794	0.81
ΔP_1, $\Delta P_{0.49}$	99%	-0.762	-0.388	0.54	0.65	0.384	0.586	0.779	0.839
	95%	-0.707	-0.424	0.553	0.637	0.404	0.557	0.786	0.832
C_1, ΔP_1, $\Delta P_{0.49}$	99%	-0.51	-0.495	0.56	0.631	0.496	0.502	0.783	0.824
	95%	-0.508	-0.497	0.568	0.623	0.497	0.501	0.788	0.819
C_1, ΔP_1	99%	-0.51	-0.495	0.56	0.624	0.496	0.502	0.785	0.825
	95%	-0.509	-0.497	0.567	0.616	0.497	0.501	0.79	0.82

It is particularly important that the confidence intervals for each parameter are finite. This indicates that for each of the datasets studied here, all parameters are both structurally and practically identifiable (to the levels of 95 and 99% confidence).

In order to facilitate comparison between the datasets and different parameters, we divided the range of the confidence interval by the optimised value, to be used as a measure of the coefficient of variation. The results are shown in Table 4.

Table 4. Range of confidence intervals normalised by the optimal value for each parameter derived from the χ^2_{PL} profiles for the synthetic data set with negative *b*.

	Accelerating reaction									
	95% CI					99% CI				
	b	*β*	λ_0	*n*	sum	*b*	*β*	λ_0	*n*	sum
C_1, ΔP_1, $\Delta P_{0.49}$, $\Delta P_{0.12}$	0.021	0.047	0.008	0.019	0.094	0.027	0.061	0.01	0.025	0.123
ΔP_1, $\Delta P_{0.49}$, $\Delta P_{0.12}$	0.313	0.101	0.195	0.031	0.641	0.413	0.133	0.256	0.041	0.844
ΔP_1, $\Delta P_{0.12}$	0.367	0.114	0.222	0.037	0.739	0.484	0.15	0.291	0.048	0.974
C_1, ΔP_1, $\Delta P_{0.12}$	0.01	0.051	0.008	0.02	0.089	0.014	0.067	0.01	0.026	0.117
ΔP_1, $\Delta P_{0.49}$	0.564	0.14	0.307	0.055	1.066	0.702	0.183	0.409	0.072	1.366
C_1, ΔP_1, $\Delta P_{0.49}$	0.023	0.09	0.008	0.039	0.16	0.031	0.119	0.01	0.051	0.211
C_1, ΔP_1	0.023	0.081	0.008	0.036	0.148	0.03	0.107	0.01	0.047	0.195

The cells have been colour coded for each of the two confidence intervals to demonstrate the relative magnitude of each value.

By definition, the values for the 99% confidence intervals are larger than the values for the 95% confidence intervals. We note that reducing the confidence intervals to a single value ignores the non-symmetrical nature of some of the confidence intervals. The values in Table 4 are presented for the purpose of comparison; reporting of the uncertainty for each parameter involves explicitly providing the confidence interval as per Table 3.

The values in Table 4 are neatly grouped into two categories: datasets that include the breakthrough concentration, C_1, and those that do not. Including the breakthrough concentration results in significantly smaller confidence intervals which greatly improved our ability to identify the parameters.

Within the sets of data that include concentration, the uncertainty is lowest for the reaction rate coefficient, λ_0 and the reaction capacity coefficient, b. Uncertainties for all parameters are low for each of these datasets. Overall parameter uncertainty is lower when the dataset includes both Δp_1 and $\Delta p_{0.12}$, indicating that a greater distance between the pressure measurement points along the core improves model determination.

When the concentration is not included, identifying each parameter is more difficult. The most substantial effect is noted in the confidence intervals for b and λ_0. Similar to the datasets with the concentration, including $\Delta p_{0.12}$ in the dataset provides better results than including $\Delta p_{0.49}$ with the best results in this case being when both are included.

Generally, the inclusion of additional pressure drop measurements improves the fitting process by decreasing the width of the confidence intervals.

4.2 Identifiability for decelerating reactions

While the experimental data tuned in this work exhibits behaviour consistent with negative values of b, previous works have presented data which exhibits positive b [44, 45]. Therefore, we include here a set of synthetic data with positive b to maintain generality. The parameters used to generate the data are, $(\lambda_0,b,\beta,n)=(1,0.5,0.6,0.8)$. Experimental data, along with model predictions following tuning, are presented in Fig. 6.

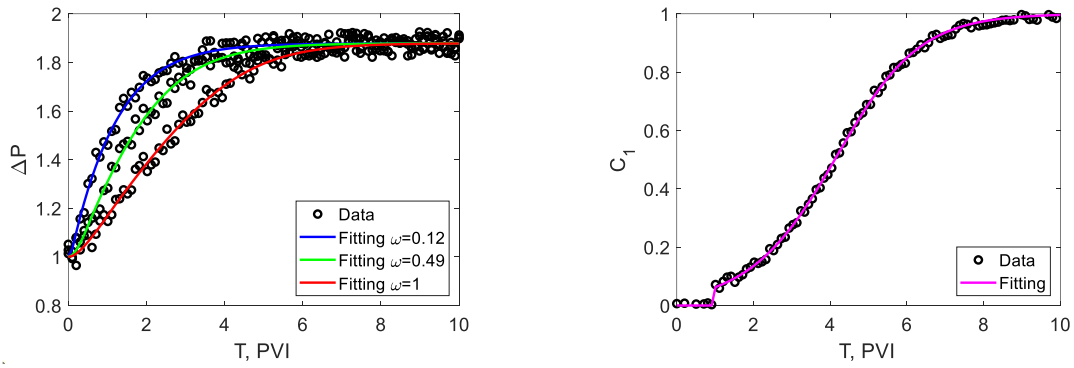

Figure 6. Synthetic experimental data set for a decelerating reaction as well as model predictions following least-squared optimisation.

A defining characteristic of the case with positive reaction capacity coefficient is the stabilisation of the system due to cessation of the chemical reaction as σ tends to b^{-1}. This is observed through a convergence of all pressure drop curves to a single stabilised value (defined by $\sigma=b^{-1}$) and the tendency of the breakthrough concentration to 1. The experimental data presented in Fig. 6 includes sufficiently large time frames such that stabilisation is observed, although this is not necessarily true for all laboratory data [44, 45, 51].

The profile likelihoods for the case where all datasets are used (C_1,Δp_1,$\Delta p_{0.49}$,$\Delta p_{0.12}$) are presented in Fig. 7.

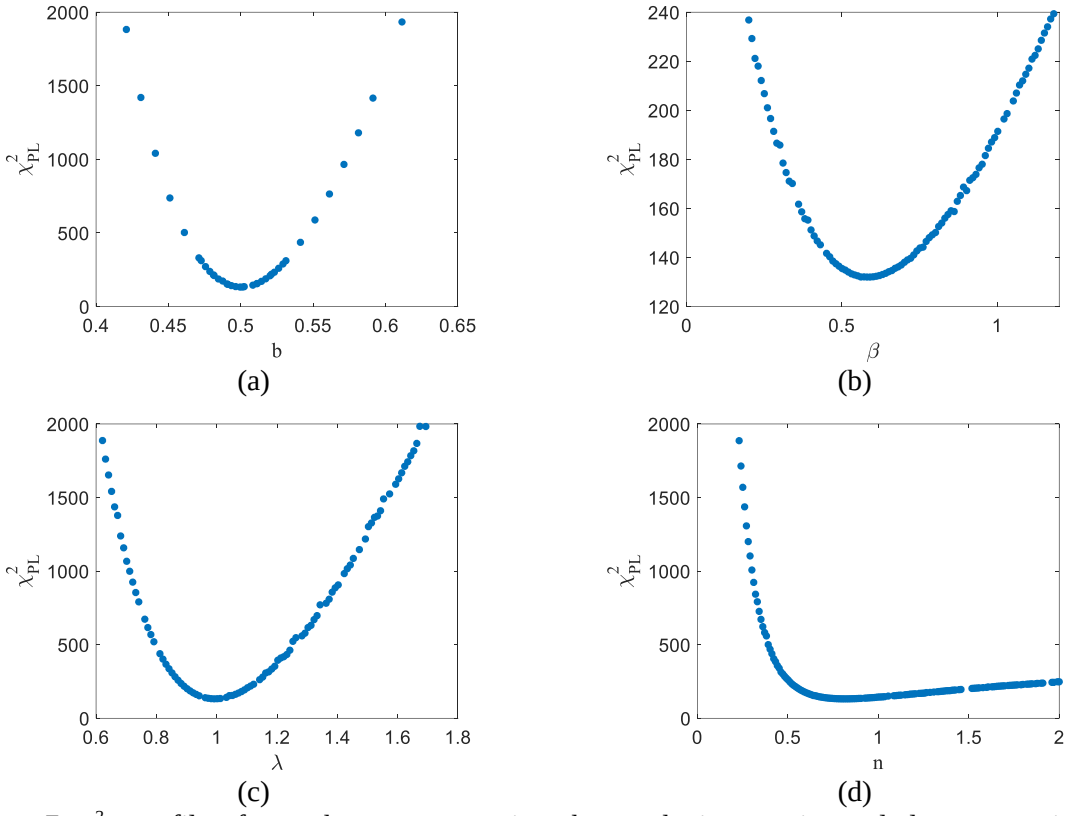

Figure 7. χ^2_{PL} profiles for each parameter using the synthetic experimental dataset consisting of (C_1,Δp_1,$\Delta p_{0.49}$,$\Delta p_{0.12}$) for a positive value of the reaction capacity coefficient, *b*.

As with the case of an accelerating reaction, each profile shows a single minimum. The curves here show greater deviation from a quadratic curve, especially for the formation damage exponent, *n*. For this case, the χ^2_{PL} profiles along with χ^2_{PL} thresholds are presented in Fig. 8.

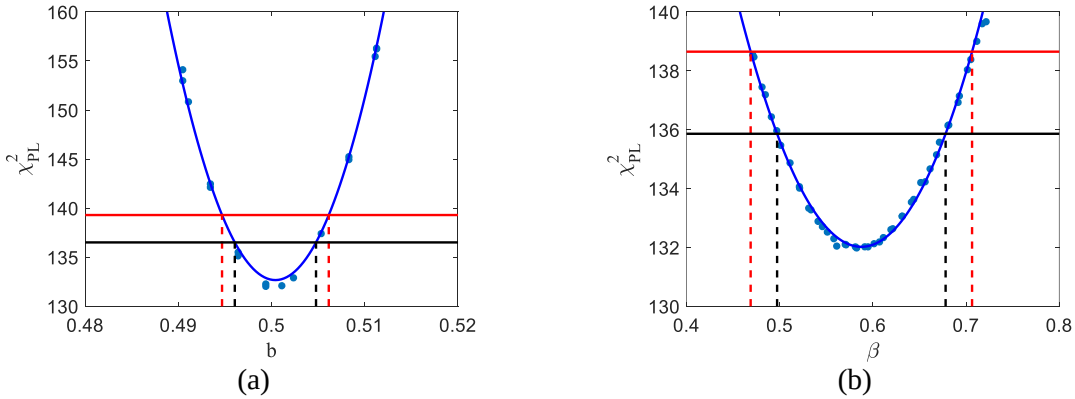

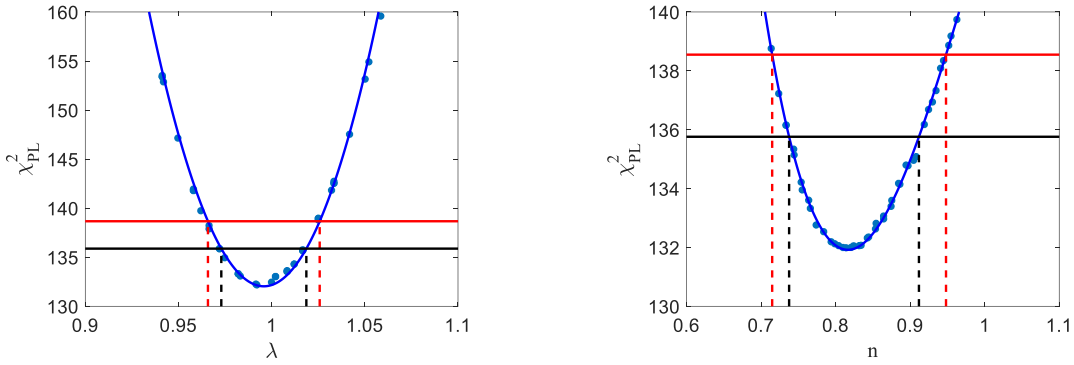

(c) (d)

Figure 8. χ^2_{PL} profiles and confidence intervals for each parameter using the synthetic experimental dataset consisting of (C_1,Δp_1,$\Delta p_{0.49}$,$\Delta p_{0.12}$) for a positive value of the reaction capacity coefficient, *b*.

Each curve shows reasonable agreement with a parabola in the region surrounding the minimum. The confidence intervals arising from the intersection between the likelihood profile curves and the χ^2_{PL} thresholds are presented in Table 5.

Table 5. Upper and lower bounds of confidence intervals derived from the χ^2_{PL} profiles for the synthetic data set with a decelerating reaction.

		Decelerating reaction							
Fitting Data	CI	*b*		*β*		λ_0		*n*	
		Lower	Upper	Lower	Upper	Lower	Upper	Lower	Upper
C_1, ΔP_1, $\Delta P_{0.49}$, $\Delta P_{0.12}$	99%	0.495	0.507	0.472	0.712	0.964	1.029	0.715	0.948
	95%	0.497	0.506	0.501	0.683	0.972	1.021	0.738	0.912
ΔP_1, $\Delta P_{0.49}$, $\Delta P_{0.12}$	99%	0.43	0.572	0.207	1.277	0.811	1.199	0.461	2.574
	95%	0.444	0.552	0.25	1.097	0.852	1.146	0.514	1.643
ΔP_1, $\Delta P_{0.12}$	99%	0.434	0.583	0.183	1.367	0.82	1.244	0.471	18.99
	95%	0.45	0.562	0.189	1.138	0.864	1.185	0.538	3.012
C_1, ΔP_1, $\Delta P_{0.12}$	99%	0.494	0.505	0.433	0.689	0.977	1.039	0.709	1.062
	95%	0.496	0.504	0.46	0.654	0.984	1.031	0.74	1.006
ΔP_1, $\Delta P_{0.49}$	99%	0.404	0.566	0.262	1.391	0.781	1.341	0.351	1.699
	95%	0.418	0.538	0.364	1.214	0.838	1.263	0.401	1.259
C_1, ΔP_1, $\Delta P_{0.49}$	99%	0.494	0.505	0.393	0.643	0.98	1.042	0.703	1.11
	95%	0.495	0.504	0.419	0.609	0.987	1.034	0.739	1.044
C_1, ΔP_1	99%	0.495	0.506	0.416	0.872	0.965	1.027	0.624	1.043
	95%	0.496	0.505	0.459	0.804	0.972	1.019	0.658	0.968

The confidence intervals for *n* for the dataset (Δp_1,$\Delta p_{0.12}$) are an outlier, showing an upper bound with an order of magnitude higher for the 99% confidence interval than for other datasets. The χ^2_{PL} profile for this case is shown in Fig. 9.

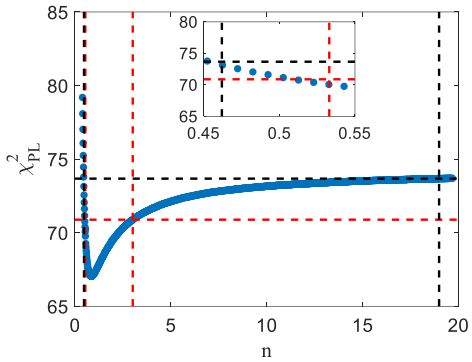

Figure 9. χ^2_{PL} profile for the formation damage exponent, n, for the dataset (Δp_1,$\Delta p_{0.12}$) for a decelerating reaction.

The profile shows significant asymmetry around the minimum, with the curve tending towards a horizontal line as n gets larger. It cannot be concluded from the numerical study here whether the curve has a horizontal asymptote as n gets infinitely large. The curve crosses the necessary χ^2_{PL} threshold to achieve a finite 99% confidence interval, but for most practical purposes, the range of permissible values of n could be considered arbitrarily large.

As with the accelerating reaction, we simplify the comparison by considering the range of the confidence intervals normalised by the optimal value for each parameter. The results are presented in Table 6.

Table 6. Range of confidence intervals normalised by the optimal value for each parameter derived from the χ^2_{PL} profiles for the synthetic data set with a decelerating reaction.

	Decelerating reaction									
	95% CI					99% CI				
	b	β	λ_0	n	sum	b	β	λ_0	n	sum
C_1, ΔP_1, $\Delta P_{0.49}$, $\Delta P_{0.12}$	0.018	0.307	0.049	0.21	0.585	0.024	0.405	0.065	0.281	0.776
ΔP_1, $\Delta P_{0.49}$, $\Delta P_{0.12}$	0.215	1.533	0.287	1.417	3.453	0.284	1.937	0.379	2.653	5.252
ΔP_1, $\Delta P_{0.12}$	0.225	1.545	0.323	3.095	5.187	0.297	1.926	0.426	23.167	25.816
C_1, ΔP_1, $\Delta P_{0.12}$	0.017	0.35	0.046	0.34	0.753	0.022	0.46	0.061	0.452	0.995
ΔP_1, $\Delta P_{0.49}$	0.241	1.411	0.423	1.074	3.15	0.324	1.875	0.558	1.689	4.447
C_1, ΔP_1, $\Delta P_{0.49}$	0.017	0.353	0.047	0.382	0.799	0.022	0.464	0.061	0.509	1.056
C_1, ΔP_1	0.017	0.563	0.048	0.373	1.001	0.023	0.743	0.063	0.504	1.333

Compared to the accelerating reaction case, the overall ranges of the confidence intervals are larger for the decelerating reaction.

The results show a similar distinction between the datasets that contain the concentration and those that do not, as was observed in the accelerating reaction case. Not including the breakthrough concentration results in significantly larger confidence intervals for all parameters.

With concentration measurements, the inclusion of additional pressure drop measurements improves the parameter identifiability, and as with the accelerating reaction, the inclusion of $\Delta p_{0.12}$ provides better results than when including $\Delta p_{0.49}$. This trend is not true for the datasets without concentration, although generally the inclusion of additional pressure drop measurements decreases the uncertainty in the parameters.

4.3 Non-observability

The uncertainty in parameters, as described by the confidence intervals, translates directly into uncertainty of model variables, such as concentrations of dissolved species or solid deposit. The extent to which a parameter cannot be determined thus relates directly to the degree to which internal states of the model cannot be determined to a certain degree of accuracy [49]. We consider variables that cannot be determined accurately due to parameter unidentifiability as non-observable. Structural unidentifiability directly leads to any model states dependent on this variable being non-observable. Practical non-identifiability does not directly imply that any internal states are non-observable; however, quantities that are strongly dependent on non-identifiable (or highly uncertain) parameters might not be well determined. Any dataset that is included in the fitting is observable.

For the model of non-reactive flow studied in this work, parameters that are not directly tuned, typically because they are difficult to measure, include the concentrations of dissolved species within the core, deposit profiles along the core and their variation with time, and pressure drop growth measured at points other than $0.12L$, $0.49L$, and L.

Non-observability of deposit profiles

While no practical non-identifiabilities have been found in this work, the high variability in parameter confidence intervals indicates a potential for underlying model states to be non-observable when using specific experimental datasets. Two cases for both the accelerating (C_1,Δp_1,$\Delta p_{0.49}$,$\Delta p_{0.12}$), (Δp_1,$\Delta p_{0.49}$) and decelerating (C_1,Δp_1,$\Delta p_{0.49}$,$\Delta p_{0.12}$), (Δp_1,$\Delta p_{0.49}$,$\Delta p_{0.12}$) reaction rates are presented to investigate the observability of the deposit profiles. The deposit profiles are calculated for parameter sets along the χ^2_{PL} profiles within the 99% confidence χ^2 thresholds. The profiles are calculated at time T = 3.13 PVI and are presented in Fig. 10.

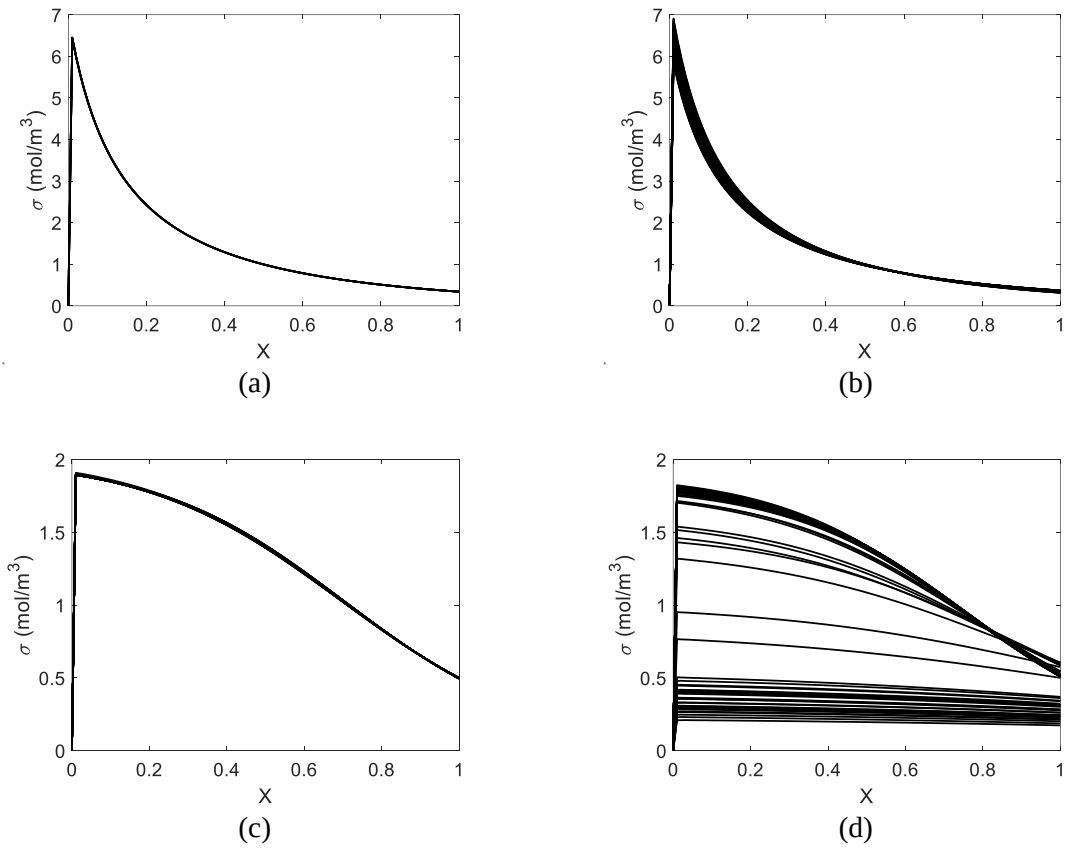

Figure 10. Deposit profiles calculated for the parameter sets along the χ^2_{PL} profiles within the 99% confidence intervals, a) accelerating reaction, (C_1,Δp_1,$\Delta p_{0.49}$,$\Delta p_{0.12}$), b) accelerating reaction, (Δp_1,$\Delta p_{0.49}$), c) decelerating reaction, (C_1,Δp_1,$\Delta p_{0.49}$,$\Delta p_{0.12}$), d) decelerating reaction, (Δp_1,$\Delta p_{0.49}$,$\Delta p_{0.12}$).

The deposit profiles are not dependent on the formation damage coefficient, β, or the formation damage exponent, n. Thus, only the confidence intervals of the remaining parameters, (b,λ_0) directly affect the observability of the deposit profiles.

For the two cases which include breakthrough concentration in the fitting dataset (Fig. 10 a,c), the set of deposit profiles taken along the χ^2_{PL} profile are almost coincident. For the two cases which do not include breakthrough concentration (Fig. 10 b,d), the sets of deposit profiles show some variation. The deceleration reaction case shows substantial variation between deposit profiles, indicating that this measurement is non-observable.

The confidence intervals for both b and λ_0 are wider for these two cases than those which contain breakthrough concentration. This suggests that the width of these confidence intervals contributes to non-observability of the deposit profiles. The inability of the model to distinguish between the different profiles in Fig. 10 suggests an incomplete characterisation of the system. Model predictions made beyond the data used in tuning are thus subject to similar degrees of uncertainty. Deposit profiles, in particular, are important as the remediation of injectivity/productivity issues due to solid deposit formation rely on accurate predictions of the deposit distribution in the porous reservoir. For example, acidizing efforts designed for the lower curves in Fig. 10 d might prioritise acid penetration deep into the reservoir while the higher deposit profiles might be treated using a smaller volume of stronger acid, given that the deposit is more strongly concentrated towards the inlet.

Despite higher relative uncertainty for b and λ_0, the accelerating reaction case (Fig. 10 b) shows greater observability of the deposit profiles than for the decelerating reaction case (Fig. 10 d). This result highlights the importance not only of parameter uncertainty ranges, but of the interdependence between parameters within the region of permissible parameter sets. For the decelerating reaction case, a value of λ_0 higher than the true value would shift the pressure drop curves higher. In order to improve the fitting, a higher value of b could be used to decrease the growth in pressure drop. This interdependency is only approximate, and is permitted by the model only to some degree dependent on the model uncertainty. The degree to which these two parameters can be substituted is diminished greatly in those datasets which include breakthrough concentration, as noted in the narrower confidence intervals. For the accelerating case the same is true; an increasing in λ_0 would require an increase in b in order to better model the increasing pressure drop. That is to say that when treating only pressure drop data, the permissible space of parameters (λ_0,b) is positively correlated.

Suppose the perturbation of the reaction rate coefficient results in a value of $(1+\delta_\lambda)\lambda_0$, while the subsequent perturbation of the reaction capacity coefficient results in a value of $(1+\delta_b)b$ (or $(1-\delta_b)b$ for the case where b is negative), where δ_λ and δ_b are positive constants. When the deposit concentration is low, Eq. (4) shows that the deposit growth rate is approximately proportional to $\lambda_0 c_1 c_2$, thus, in the perturbed case the deposition rate would deviate from the true value by $\delta_\lambda c_1 c_2$. When the deposit concentration grows large, the decelerating reaction rate tends to 0, with the deposit concentration equal to the inverse of b, and thus the perturbation is inversely proportional to $(1+\delta_b)$. In the accelerating reaction case however, the deposition rate tends to $\lambda_0 b c_1 c_2$. In this case, the perturbation of the deposition rate is $(1+\delta_\lambda)(1-\delta_b)c_1 c_2$, proportional to $(\delta_\lambda-\delta_b) -\delta_\lambda\delta_b$. For small perturbations the second term can be neglected. Thus, in the case where b is positive, the perturbations increase the initial deposit growth rate and decrease the final deposit concentration, while in the negative b case, the perturbations partially cancel out at high deposit concentrations. This explains why the higher uncertainties on λ_0 and b in the accelerating reaction case, nonetheless, lead to smaller non-observability issues for the deposit profiles.

The high deposit profiles, which change sharply with X, and the low deposit profiles, which are approximately constant in Fig. 10 d, both produce feasible predictions for the three pressure drop curves

(Δp_1,$\Delta p_{0.49}$,$\Delta p_{0.12}$) within the 99% confidence intervals. This is achieved due to variation in the formation damage exponent, *n*. Values of *n* below 1 gradually reduce the impact of deposit on the permeability with growing deposit. Thus the excess deposit in the early sections of the sample (small *X*) compared with sections near the outlet (large *X*) does not produce significant differences in permeabilities across the sample when *n* is small. This explains how deposit profiles that vary quickly with *X*, and those that do not, can produce similar pressure drop values measured across different sections of the core.

Non-observability of internal pressure growth

Some practitioners may be interested only in making calculations of pressure drop/permeability and thus observability of additional pressure measurements, not included in the experimental datasets, is of interest. Unlike the deposit profiles, pressure profiles not included in the fitting datasets are influenced by the identifiability of all four parameters. Two cases are of interest, pressure drop measured at some point within the investigated region ($X<1$ for this work), and pressure measured at some point outside of this region ($X<0$ or $X>1$). These are understood analogously as interpolation and extrapolation of the existing information, respectively. An internal pressure drop curve is constructed by taking the pressure drop across the first 75% of the core. The observability graphs for the above 4 datasets are presented in Fig. 11.

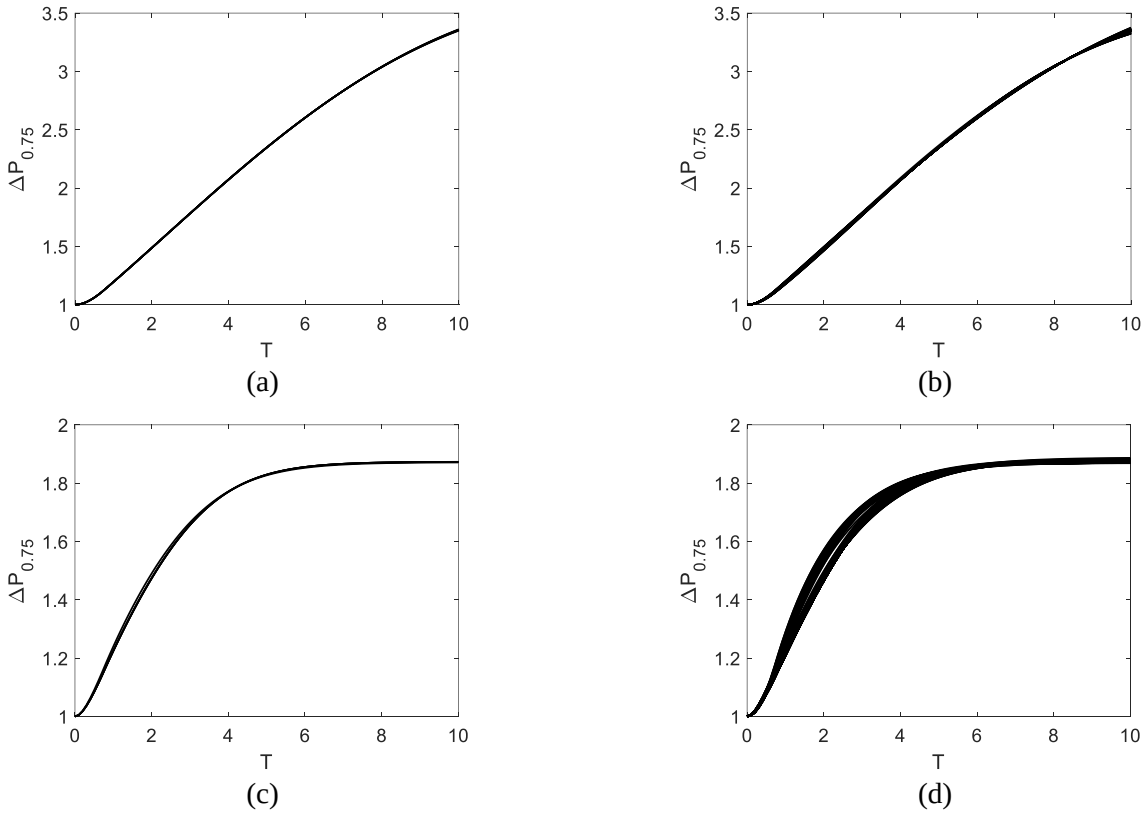

Figure 11. Pressure drop along the first 75% of the core calculated for the parameter sets along the χ^2_{PL} profiles within the 99% confidence intervals, a) accelerating reaction, (C_1,Δp_1,$\Delta p_{0.49}$,$\Delta p_{0.12}$), b) accelerating reaction, (Δp_1,$\Delta p_{0.49}$), c) decelerating reaction, (C_1,Δp_1,$\Delta p_{0.49}$,$\Delta p_{0.12}$), d) decelerating reaction, (Δp_1,$\Delta p_{0.49}$,$\Delta p_{0.12}$).

The results show a similar trend to the deposit profiles, namely that datasets which include breakthrough concentration show almost no variation, while some variation is present when breakthrough concentration is neglected. The key difference here is that while significant deviation was noted in the deposit profiles for the case in Fig. 11 d (decelerating reaction, (Δp_1,$\Delta p_{0.49}$,$\Delta p_{0.12}$)), the pressure drop at $0.75L$ shows less variation. This is expected given the use of pressure drop curves evaluated at $0.49L$ and L for the tuning process. The approximate correlations between parameters within the confidence

regions allowed for permissible treatment of the 'experimental' data, and it is reasonable to assume that the same correlations would limit uncertainty in pressure profiles within the observed region.

The deviation in Fig. 11 d is primarily in the shape of the curve, not in the final value. This is likely due to the relatively large portion of the experimental data (see Fig. 6) which includes stabilised or roughly stabilised values. In cases where the experiment is not run until complete stabilisation, the shape of the confidence region, and the underlying parameter uncertainties, may not provide as good an estimate of the system behaviour at stabilisation. The non-observability behaviour leads to an uncertainty in $\Delta p_{0.75}$ which varies non-monotonically with time; initially it is zero, it grows, and then decreases as the system tends towards stabilisation.

Observability of external pressure growth

In most practical applications, experimental data is obtained from core samples, ranging between centimetres to metres long. Application of models for field design typically involves predictions of system variables across distances in the order metres to kilometres. Thus, while good observability of pressure within the investigated region is a good case for any experiment, observability of pressure outside this region is also critical. Pressure drop profiles are constructed across the first 500% of the experiment, i.e., the pressure difference is calculated between the points $X=5L$ and $X=0$. The profiles are calculated for parameters along the χ^2_{PL} profiles within the 99% confidence intervals. The results are presented in Fig. 12. Note that the number of pore volumes injected, T, is still calculated based on the core length, L.

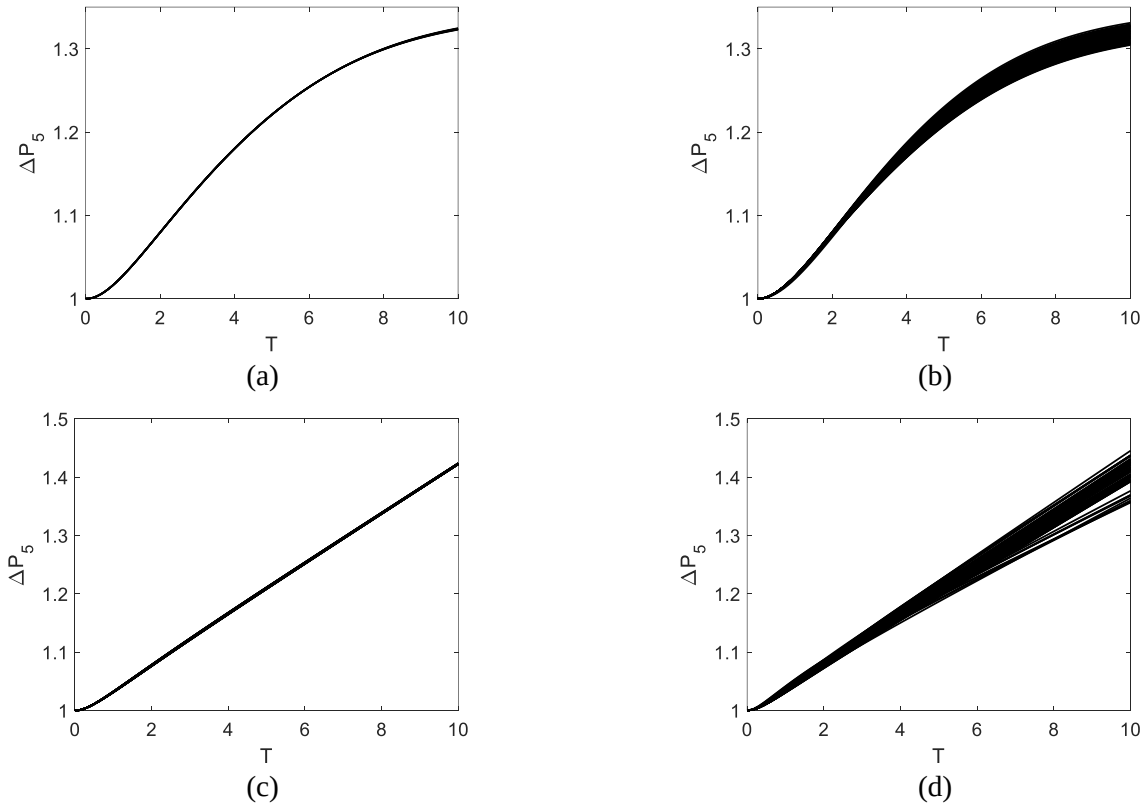

Figure 12. Pressure drop along the first 75% of the core calculated for the parameter sets along the χ^2_{PL} profiles within the 99% confidence intervals, a) accelerating reaction, (C_1,Δp_1,$\Delta p_{0.49}$,$\Delta p_{0.12}$), b) accelerating reaction, (Δp_1,$\Delta p_{0.49}$), c) decelerating reaction, (C_1,Δp_1,$\Delta p_{0.49}$,$\Delta p_{0.12}$), d) decelerating reaction, (Δp_1,$\Delta p_{0.49}$,$\Delta p_{0.12}$).

The results present differing conclusions to the internal pressure growth curves in Fig. 12. First, the accelerating reaction case that does not include breakthrough concentration (Fig. 12 b) here exhibits

some non-observability, perhaps even more so than the deposit profiles presented in Fig. 10. The decelerating reaction case without breakthrough concentration (Fig. 12 d) exhibits higher uncertainty than when predicting $\Delta p_{0.75}$. This uncertainty grows with time, similar to Fig. 11 d, however, in this case stabilisation is not observed. Injection into large reservoirs can continue for several years without injecting 1 pore volume, and thus stabilisation is not always expected. For both accelerating and decelerating reactions, the uncertainty grows with time, implying that the uncertainty in field scale measurements is larger the further out the prediction is made.

5. Discussion

An implication of the identifiability analysis presented above is that all parameters are uniquely identifiable using any of the presented subsets of experimental data. That is, the set of parameters with admissible χ^2 values is finite. This is supported by the analysis of the Jacobian matrix, which shows that in all cases, the Jacobian is full rank (the rank is equal to the number of parameters). This analysis proves only the structural identifiability, meaning that the space of optimal solutions (min χ^2) is simply one set of parameters. Further, even using a single pressure drop measurement results in a full rank Jacobian, while using only the breakthrough concentration does not.

The choice of the number of degrees of freedom as one in Eq. (10) for the χ^2_{df} distribution allows determining confidence intervals for each parameter individually [52]. If, instead, the shape of the confidence region was desired, a larger set of parameters could be fixed, leading to a larger value for the degrees of freedom. Information about the shape of the confidence region can illustrate correlations between parameters [53, 54] and is a useful tool for model evaluation although this is not an aim of the present study.

The cases studied in the work all result in a single minimum in the $\chi^2(\theta)$ space. This is not guaranteed, and in particular, structural model error or highly complex measurement error structures could lead to multiple minima. In this case it is possible that the intersection between the χ^2_{PL} profile and the χ^2 threshold could lead to a disjointed set of admissible parameters. Analysis of this phenomenon and others, such as parameter correlations, could be achieved by a full mapping of the $\chi^2(\theta)$ space, which is avoided by the method employed in this work. This can be achieved efficiently using a Monte Carlo Markov Chain technique, as has been explored by others [55].

Additional investigation into the phenomena studied here is warranted. Researchers in particle filtration commonly measure the deposit profiles directly at the end of the coreflooding experiment [56]. The deposit profile provides an additional source of information that has not been studied in this paper, and the effects of using the deposit profile instead of breakthrough concentration or pressure drop are not clear. In addition, all pressure drop measurements included here are between the inlet and some point further in the core. It is possible to take pressure drop measurements across any arbitrary section of the core. Measurements of the pressure drop across the central part of the core may improve the characterisation of the non-linearities in the model, and thus improve model determination. The current study does not include analysis of varying measurement error or frequency in measurement data, both of which can affect parameter uncertainty. The observability of the internal pressure drop in Section 4 also highlights the importance of the synthetic experimental data stabilising (for the decelerating reaction). This is not guaranteed for experiments, and its importance should be investigated. Lastly, for dissolved species it might be possible to measure even the concentration of the reactants at multiple points across the core, which might lead to more reliable parameter estimation.

While the results presented here may not provide strong support for neglecting breakthrough concentration measurements, they do show that without concentration the model parameters can still be determined uniquely and within finite confidence intervals. This is preliminary evidence that solid deposit formation due to in-situ chemical reactions may be characterised by downhole wellbore pressures during injection operations. Direct field-scale measurement of reservoir parameters is not only

convenient, but also provides effective parameters for the region of influence around the well, avoiding the problem of a heterogeneous porous media that is not addressed in this study.

The information in this study leads to several recommendations for practitioners and experimentalists studying reactive flow in porous media. In an industrial context, the parameter intervals are likely only useful to the extent that they translate to non-observability or uncertainty in the quantities to be predicted. The results show that neglecting breakthrough concentration can be used to tune laboratory data and make predictions of pressure decline on larger scales, albeit with higher uncertainty. For practitioners looking to avoid breakthrough concentration, careful attention should be paid to the uncertainty induced in any quantitative predictions made. Contrastingly, the results show that fitting data with breakthrough concentration and multiple pressure drops results in highly precise estimation of system parameters and low uncertainty in predicted deposit profiles and pressure drop.

Now let us discuss the applications of the analysis of identifiability and observability to determine the model functions / parameters from coreflood tests as described in this work. The computations of χ^2_{PL} profiles rely on fast direct problem modelling. Otherwise, the necessity for a large number of function evaluations results in prohibitively large computation times. One of ways around this problem is using analytical models based on explicit formulae for direct solution. An incomplete list of cases where identifiability and observability analysis can be applied to determine model parameters from the coreflood data, due to availability of the analytical models, includes: relative permeability calculations [57-59], lab-based prediction of well injectivity during CO_2 injection or water flooding [60-62], and deep bed filtration with induced formation damage during drilling [63] and water injection [64-66], fines migration [21-24, 67], and nanoparticle injection [68-72].

6. Conclusions

Tuning of 3-point pressure laboratory data and identifiability analysis of the tuned parameters along with consideration of the observability of deposit profiles and pressure drop curves allows us to draw the following conclusions.

- Using a non-linear chemical reaction model allows close fitting to data containing 3 sets of pressure drops and outlet concentration of one species
- Identifiability analysis shows that using any subset of at least two data sets from those used in the laboratory section results in uniquely determining the four model parameters, (λ_0,b,β,n)
- Confidence intervals determined for each parameter demonstrate that including outlet concentration data significantly decreases parameter uncertainty
- With or without concentration data, including additional pressure drop measurements generally reduces parameter uncertainty
- The parameter uncertainty obtained by tuning datasets without breakthrough concentration leads to an inability of the model to distinguish between a wide set of deposit profiles. The same issue is not present when outlet concentration is included in the inverse modelling
- Parameter uncertainties lead to minimal uncertainty in pressure drop predictions within the experiment, but significant uncertainties when predicting pressure beyond the experiment core length. In both cases, including concentration provides high uncertainty in predicted quantities

CRediT authorship contribution statement

S. Yang: Software, Methodology, Formal analysis, Investigation, Visualization. **T. Russell:** Methodology, Investigation, Writing – Original Draft, Visualization. **A. Vaz:** Conceptualization, Investigation, Resources. **P. Bedrikovetsky:** Methodology, Writing – Review & Editing, Supervision

Appendix A. Governing equations for commingled flow of reacting liquids in porous media

The mathematical model for one-dimensional reactive flow in porous media consists of mass balances for the two suspended species and the solid deposit, as well as a modified form of Darcy's law expressing the formation damage induced by the formation of deposit:

$$\phi\frac{\partial c_1}{\partial t}+U\frac{\partial c_1}{\partial x}=-\frac{\partial\sigma}{\partial t}, \tag{A.1}$$

$$\phi\frac{\partial c_2}{\partial t}+U\frac{\partial c_2}{\partial x}=-\frac{\partial\sigma}{\partial t}, \tag{A.2}$$

$$\frac{\partial\sigma}{\partial t}=\lambda(\sigma)Uc_1^q c_2^r,\ \ \lambda(\sigma)=\begin{cases}\lambda_0(1-b\sigma), & \sigma<b^{-1}\\ 0, & \sigma>b^{-1}\end{cases}, \tag{A.3}$$

$$U=-\frac{k_0}{\mu(1+\beta\sigma)^n}\frac{\partial p}{\partial x}. \tag{A.4}$$

where ϕ is the rock porosity, t is time, x is the spatial dimension, U is the fluid velocity, c_1 and c_2 are the concentrations of the two dissolved species, σ is the deposit concentration, λ is the reaction rate function, q and r are the stoichiometric coefficients of the reaction, λ_0 is the reaction rate coefficient, b is the reaction capacity coefficient, k_0 is the initial permeability, μ is the fluid viscosity, β is the formation damage coefficient, n is the formation damage exponent, and p is the fluid pressure.

We introduce the following dimensionless coordinates, assuming that $b\neq0$:

$$\begin{aligned}&X=\frac{x}{L},T=\frac{Ut}{\phi L},C_1=\frac{c_1}{c_1^0},C_2=\frac{c_2}{c_2^0},S=b\sigma,P=\frac{k_0 p}{U\mu L},\\&\Lambda_0=\lambda_0 bL\phi\left(c_1^0\right)^q\left(c_2^0\right)^r,\alpha=\frac{1}{c_1^0 b\phi},\gamma=\frac{1}{c_2^0 b\phi}\end{aligned} \tag{A.5}$$

In the case where $b=0$, the dimensionless deposit concentration and filtration coefficient, S and Λ_0, as well as the new coefficient γ, must be defined differently:

$$S=\frac{\sigma}{\phi c_1^0},\Lambda_0=\lambda_0 Lc_2^0,\gamma=\frac{c_1^0}{c_2^0} \tag{A.6}$$

In this case α is 1.

Expressing the system of equations (A.1-A.4) using the dimensionless coordinates (A.5) results in the dimensionless system:

$$\frac{\partial C_1}{\partial T}+\frac{\partial C_1}{\partial X}=-\alpha\frac{\partial S}{\partial T}, \tag{A.7}$$

$$\frac{\partial C_2}{\partial T}+\frac{\partial C_2}{\partial X}=-\gamma\frac{\partial S}{\partial T}, \tag{A.8}$$

$$\frac{\partial S}{\partial T}=\Lambda(S)C_1^q C_2^r,\Lambda(S)=\begin{cases}\Lambda_0(1-S), & S<1\\ 0, & S>1\end{cases}, \tag{A.9}$$

$$1=-\frac{1}{\left(1+\frac{\beta S}{b}\right)^{n}}\frac{\partial P}{\partial X}. \tag{A.10}$$

The initial and boundary conditions correspond to the injection of both dissolved species into a core which initially contains no dissolved species or deposit:

$$T=0: C_1=C_2=S=0, \tag{A.11}$$

$$X=0: C_1=C_2=1, P=\frac{k_0 p_0}{U\mu L}. \tag{A.12}$$

Equations (A.7-A.10) subject to initial and boundary conditions (A.11,A.12) are a closed system of 4 equations in four unknowns (C_1,C_2,S,P).

Appendix B. Analytical solution for commingled flow of reacting liquids in porous media

In a previous work, the system of Eqs. (A.7-A.10) subject to boundary conditions (A.11,A.12) was solved analytically [32]. The full details of the solution are omitted here, and only the final result is presented. Briefly, the equations are solved by the introduction of a new variable, $\tau=T-X$, reducing the system to a first order hyperbolic equation, which is then solved by the method of characteristics.

The value of the concentration of the first reactant is given by:

$$C_1\left(X,T\right)=\begin{cases}0, & X>T\\ \int\limits_{C_0(X)}^{C_1(X,T)}\frac{dC}{\left(1-C\right)C^{q}\left(\gamma C-\gamma+\alpha\right)^{r}}=\frac{\Lambda_0}{\alpha^{r}}\left(T-X\right), & X<T\end{cases} \tag{B.1}$$

where C_0 is the concentration of reactant C_1 on the front $X=T$, $C_0(X)=C_1(X,X)$ and is given by:

$$\int\limits_{C_0(X)}^{1}\frac{dC}{\Lambda_0 C^{q}\left(\frac{\gamma C-\gamma+\alpha}{\alpha}\right)^{r}}=\alpha X \tag{B.2}$$

The concentration of the second reactant, C_2 is given by:

$$C_2\left(X,T\right)=\begin{cases}0, & X>T\\ \int\limits_{C_0(X)}^{\alpha C_2(X,T)-\alpha+\gamma/\gamma}\frac{dC}{\left(1-C\right)C^{q}\left(\gamma C-\gamma+\alpha\right)^{r}}=\frac{\Lambda_0}{\alpha^{r}}\left(T-X\right), & X<T\end{cases} \tag{B.3}$$

The deposit concentration is obtained following the solution of the first reactant:

$$S\left(X,T\right)=\frac{C_1\left(X,T\right)-C_0\left(X\right)}{1-C_0\left(X\right)} \tag{B.4}$$

Lastly the pressure drop is obtained by integrating the modified form of Darcy's law (Eq. (A.10)) over X:

$$\Delta P\left(T\right)=\int_0^1\left(1+\frac{\beta S\left(X,T\right)}{b}\right)^{n}dX \tag{B.5}$$

For the chemical reaction studied in this work, the stoichiometric coefficients, q and r, are equal to one, and the injected concentrations of each species are not equal. In this case, the equations simplify greatly. The concentration along the front is given by:

$$C_0(X) = \frac{\gamma - \alpha}{\gamma - \alpha \exp\left(\Lambda_0 (\alpha - \gamma) X\right)} \tag{B.6}$$

and the concentrations of each reactant are determined by solving separately the following algebraic equations:

$$\gamma \ln\left|\frac{\gamma\left(C_1(X,T)-1\right)+\alpha}{\gamma\left(C_0(X)-1\right)+\alpha}\right| - (\gamma-\alpha)\ln\left|\frac{1-C_1(X,T)}{1-C_0(X)}\right| - \alpha \ln\left|\frac{C_1(X,T)}{C_0(X)}\right| = (\gamma-\alpha)\Lambda_0 (T-X) \tag{B.7}$$

$$\gamma \ln\left|\frac{\alpha\left(C_2(X,T)-1\right)+\gamma}{\gamma\left(C_0(X)-1\right)+\alpha}\right| - (\gamma-\alpha)\ln\left|\frac{\alpha\left(1-C_2(X,T)\right)}{\gamma\left(1-C_0(X)\right)}\right| - \alpha \ln\left|\frac{\alpha\left(C_2(X,T)-1\right)+\gamma}{\gamma C_0(X)}\right| = (\gamma-\alpha)\Lambda_0 (T-X)$$

(B.8)

The deposit concentration and pressure drop are, as in the general case, obtained using Eqs. (B.4) and (B.5) respectively.

Simplified expressions for other cases are presented by Yang, Osipov, Xu, Kuzmina, Russell and Bedrikovetsky [32].

Appendix C. Procedure to calculate confidence intervals for model parameters

Following previous works on identifiability [48, 49], here we describe the algorithm to calculate confidence intervals $[\theta_{i,min},\theta_{i,max}]$ for the model parameters θ_i, i=1,2… for a given confidence ε:

1. Determine optimal parameters $\hat{\boldsymbol{\theta}}$ by minimizing $\chi^2(\theta)$;
2. Choose a suitable range for each parameter $A_i<\theta_i<B_i$;
3. For each value of θ_i, determine the optimal values for all other parameters θ_j, j≠i, by minimizing χ^2;
4. Plot the minimum value of χ^2 against θ_i;
5. Repeat steps 3-4 for all parameters i=1,2…
6. For a given level of confidence ε, determine the tolerance Δ_ε using Eq. (10);
7. Find the two roots, $\theta_{i,min}$ and $\theta_{i,max}$, of equation
   $$\chi^2_{PL}(\theta_i) = \chi^2_{PL,\min} + \Delta_\varepsilon \tag{C.1},$$
   located around the optimal value $\hat{\theta}_i$;
8. If $\theta_{i,min}$ and $\theta_{i,max}$ appear to be outside the chosen interval $A_i<\theta_i<B_i$, the interval must be expanded, and calculations 2-7 repeated.

The calculated roots $\theta_{i,min}$ and $\theta_{i,max}$ determine the confidence interval for each model parameter. If Eq. (C.1) has less than two roots, the parameter θ_i is unidentifiable.

References

[1] Y. Zhang, Z. Zhang, M. Arif, M. Lebedev, A. Busch, M. Sarmadivaleh, S. Iglauer, Carbonate rock mechanical response to CO2 flooding evaluated by a combined X-ray computed tomography–DEM method, J. Nat. Gas Sci. and Eng., 84 (2020) 103675.
[2] B. Niu, W. Yan, A.A. Shapiro, E.H. Stenby, Phase identification and saturation determination in carbon dioxide flooding of water flooded chalk using X-Ray computed tomography, in: Paper SCA2009-19 presented at the International Symposium of the Society of Core Analysts held in Noordwijk, The Netherlands, 2009, pp. 27-30.
[3] B. Niu, W. Yan, A.A. Shapiro, E.H. Stenby, Coupling Miscible Flow and Geochemistry for Carbon Dioxide Flooding into North Sea Chalk Reservoir, in: European Comsol Conference 2009, 2009.
[4] W. Yan, S. Huang, E.H. Stenby, Measurement and modeling of CO2 solubility in NaCl brine and CO2–saturated NaCl brine density, Int. J. of Greenh. Gas Control, 5 (2011) 1460-1477.
[5] F. Othman, M.A. Naufaliansyah, F. Hussain, Effect of water salinity on permeability alteration during CO_2 sequestration, Advances in water resources, 127 (2019) 237-251.
[6] J. Ge, X. Zhang, F. Le-Hussain, Fines migration and mineral reactions as a mechanism for CO2 residual trapping during CO2 sequestration, Energy, 239 (2022) 122233.
[7] R.R. Ratnakar, B. Dindoruk, A. Harvey, Thermodynamic modeling of hydrogen-water system for high-pressure storage and mobility applications, J. Nat. Gas Sci. and Eng., 81 (2020) 103463.
[8] A. Shapiro, H. Yuan, Application of stochastic approaches to modelling suspension flow in porous media, in: Statistical mechanics and random walks: Principles, processes and applications, Nova Science Publishers, 2012, pp. 1-36.
[9] A. Zahid, A. Shapiro, E.H. Stenby, W. Yan, Managing injected water composition to improve oil recovery: A case study of North Sea chalk reservoirs, Energy & fuels, 26 (2012) 3407-3415.
[10] X. Liu, W. Yan, E.H. Stenby, E. Thormann, Release of crude oil from silica and calcium carbonate surfaces: on the alternation of surface and molecular forces by high-and low-salinity aqueous salt solutions, Energy & Fuels, 30 (2016) 3986-3993.
[11] C. Bethke, Geochemical reaction modeling: Concepts and applications, Oxford University Press, New York, 1996.
[12] J.I. Drever, The geochemistry of natural waters, 3rd ed., Prentice Hall Englewood Cliffs, NJ, 1997.
[13] H.S. Fogler, Essentials of chemical reaction engineering, 4th ed., Pearson Education, Upper Saddle River, NJ, 2010.
[14] P.G. Bedrikovetsky, R.P. Lopes, Jr., P.M. Gladstone, F.F. Rosario, M.C. Bezerra, E.A. Lima, Barium sulphate oilfield scaling: mathematical and laboratory modelling, in: SPE Int. Symp. on Oilfield Scale, Society of Petroleum Engineers, Aberdeen, United Kingdom, 2004, pp. 14.
[15] E.J. Mackay, I. Collins, M. Jordan, N. Feasey, PWRI: Scale formation risk assessment and management, in: International Symposium on Oilfield Scale, OnePetro, 2003.
[16] M. Farrokhrouz, A. Taheri, A. Keshavarz, Numerical reactive flow transport simulation on core samples during acid fracturing in carbonaceous shale, J. Nat. Gas Sci. and Eng., 84 (2020) 103615.
[17] Z. Luo, L. Cheng, L. Zhao, Y. Xie, Study on the mechanism of reactive acid transport in fractured two-mineral carbonate rocks, J. Nat. Gas Sci. and Eng., 94 (2021) 104118.
[18] H. Al-Arji, A. Al-Azman, F. Le-Hussain, K. Regenauer-Lieb, Acid stimulation in carbonates: A laboratory test of a wormhole model based on Damköhler and Péclet numbers, J. Pet. Sci. and Eng., 203 (2021) 108593.
[19] R. Zagorščak, H.R. Thomas, Dynamic transport and reaction behaviour of high-pressure gases in high-rank coal, J. Nat. Gas Sci. and Eng., 71 (2019) 102978.
[20] Z. Guo, P.N.H. Vu, F. Hussain, A laboratory study of the effect of creep and fines migration on coal permeability during single-phase flow, International Journal of Coal Geology, 200 (2018) 61-76.
[21] Z. Guo, F. Hussain, Y. Cinar, Physical and analytical modelling of permeability damage in bituminous coal caused by fines migration during water production, J. Nat. Gas Sci. and Eng., 35 (2016) 331-346.

[22] F. Othman, M. Yu, F. Kamali, F. Hussain, Fines migration during supercritical CO2 injection in sandstone, J. Nat. Gas Sci. and Eng., 56 (2018) 344-357.
[23] X. Zhang, J. Ge, F. Kamali, F. Othman, Y. Wang, F. Le-Hussain, Wettability of sandstone rocks and their mineral components during CO2 injection in aquifers: Implications for fines migration, J. Nat. Gas Sci. and Eng., 73 (2020) 103050.
[24] K.O.K. Prempeh, L. Chequer, A. Badalyan, P. Bedrikovetsky, Effects of the capillary-entrapped phase on fines migration in porous media, J. Nat. Gas Sci. and Eng., 73 (2020) 103047.
[25] J. Ge, X. Zhang, F. Othman, Y. Wang, H. Roshan, F. Le-Hussain, Effect of fines migration and mineral reactions on CO2-water drainage relative permeability, Int. J. of Greenh. Gas Control, 103 (2020) 103184.
[26] S. Naseri, J. Moghadasi, M. Jamialahmadi, Effect of temperature and calcium ion concentration on permeability reduction due to composite barium and calcium sulfate precipitation in porous media, J. Nat. Gas Sci. and Eng., 22 (2015) 299-312.
[27] P. Bedrikovetsky, Mathematical Theory of Oil & Gas Recovery, Springer Science & Business Media, Dordrecht, 2013.
[28] B. Shabani, J. Pashin, J. Vilcáez, TOUGHREACT-CO2Bio–A new module to simulate geological carbon storage under biotic conditions (Part 2): The bio-geochemical reactive transport of CO2-CH4-H2-H2S gas mixtures, J. Nat. Gas Sci. and Eng., 76 (2020) 103190.
[29] E.J. Mackay, M.M. Jordan, Impact of brine flow and mixing in the reservoir on scale control risk assessment and subsurface treatment options: Case histories, J. Energy Resour. Technol., 127 (2005) 201-213.
[30] K. Sorbie, E. Mackay, Mixing of injected, connate and aquifer brines in waterflooding and its relevance to oilfield scaling, J. Pet. Sci. Eng., 27 (2000) 85-106.
[31] D.A.b. Frank-Kamenetskii, Diffusion and heat transfer in chemical kinetics, 2nd ed., Plenum Press, New York, 1969.
[32] S. Yang, Y. Osipov, C. Xu, L. Kuzmina, T. Russell, P. Bedrikovetsky, Analytical solution for large-deposit non-linear reactive flows in porous media, Chemical Engineering Journal, 430 (2022) 132812.
[33] A. Vaz, P. Bedrikovetsky, P. Fernandes, A. Badalyan, T. Carageorgos, Determining model parameters for non-linear deep-bed filtration using laboratory pressure measurements, J Petrol Sci Eng, 151 (2017) 421-433.
[34] H. Ott, M. Andrew, J. Snippe, M.J. Blunt, Microscale solute transport and precipitation in complex rock during drying, Geophys Res Lett, 41 (2014) 8369-8376.
[35] H. Ott, J. Snippe, K. De Kloe, H. Husain, A. Abri, Salt precipitation due to Sc-gas injection: single versus multi-porosity rocks, Energy Procedia, 37 (2013) 3319-3330.
[36] A. Vaz, D. Maffra, T. Carageorgos, P. Bedrikovetsky, Characterisation of formation damage during reactive flows in porous media, J. Nat. Gas Sci. Eng., 34 (2016) 1422-1433.
[37] K.C. Khilar, H.S. Fogler, Migration of fines in porous media, Kluwer Academic Publishers, Dordrecht, 1998.
[38] P. Bedrikovetsky, N. Caruso, Analytical model for fines migration during water injection, Transport Porous Med, 101 (2014) 161-189.
[39] L. Chequer, A. Vaz, P. Bedrikovetsky, Injectivity decline during low-salinity waterflooding due to fines migration, J Petrol Sci Eng, (2018).
[40] M.A. Oliveira, A.S. Vaz, F.D. Siqueira, Y. Yang, Z. You, P. Bedrikovetsky, Slow migration of mobilised fines during flow in reservoir rocks: Laboratory study, J Petrol Sci Eng, 122 (2014) 534-541.
[41] S.S. Bhattacharya, J. Paitaridis, A. Pedler, A. Badalyan, Y.L. Yang, T. Carageorgos, P. Bedrikovetsky, D. Warren, N. Lemon, Fines Mobilisation by Low-Salinity Water Injection: 3-Point-Pressure Tests, in: SPE International Conference & Exhibition on Formation Damage Control, Lafayette, Louisiana, USA, 2016.
[42] A. Badalyan, L. Chequer, T. Russell, T. Carageorgos, A. Zeinijahromi, Z. You, P. Bedrikovetsky, Uncertainties associated with laboratory-based predictions of well index and formation damage, Measurement, 170 (2021) 108731.

[43] S. Yang, T. Russell, A. Badalyan, U. Schacht, M. Woolley, P. Bedrikovetsky, Characterisation of fines migration system using laboratory pressure measurements, J. Nat. Gas Sci. and Eng., 65 (2019) 108-124.
[44] S.J. Ahmed, Laboratory study on precipitation of calcium sulphate in Berea sandstone cores, in, King Fahd University of Petroleum and Minerals, Dhahran, Saudi Arabia, 2004.
[45] S. Ghaderi, R. Kharrat, H. Tahmasebi, Experimental and theoretical study of calcium sulphate precipitation in porous media using glass micromodel, Oil Gas Sci. Technol., 64 (2009) 489-501.
[46] D.W. Hogg, J. Bovy, D. Lang, Data analysis recipes: Fitting a model to data, arXiv preprint arXiv:1008.4686, (2010).
[47] E. Ranaee, L. Moghadasi, F. Inzoli, M. Riva, A. Guadagnini, Identifiability of parameters of three-phase oil relative permeability models under simultaneous water and gas (SWAG) injection, J Petrol Sci Eng, 159 (2017) 942-951.
[48] A. Raue, C. Kreutz, T. Maiwald, J. Bachmann, M. Schilling, U. Klingmüller, J. Timmer, Structural and practical identifiability analysis of partially observed dynamical models by exploiting the profile likelihood, Bioinformatics, 25 (2009) 1923-1929.
[49] A. Raue, C. Kreutz, T. Maiwald, U. Klingmüller, J. Timmer, Addressing parameter identifiability by model-based experimentation, IET systems biology, 5 (2011) 120-130.
[50] M.C. Neale, M.B. Miller, The use of likelihood-based confidence intervals in genetic models, Behavior genetics, 27 (1997) 113-120.
[51] J. Moghadasi, H. Müller-Steinhagen, M. Jamialahmadi, A. Sharif, Model study on the kinetics of oil field formation damage due to salt precipitation from injection, J. Pet. Sci. Eng., 43 (2004) 201-217.
[52] W.H. Press, S.A. Teukolsky, B.P. Flannery, W.T. Vetterling, Numerical recipes in Fortran 77: volume 1, volume 1 of Fortran numerical recipes: the art of scientific computing, Cambridge university press, 1992.
[53] S. Berg, E. Unsal, H. Dijk, Sensitivity and Uncertainty Analysis for Parameterization of Multiphase Flow Models, Transport in Porous Media, (2021) 1-31.
[54] S. Berg, E. Unsal, H. Dijk, Non-uniqueness and uncertainty quantification of relative permeability measurements by inverse modelling, Computers and Geotechnics, 132 (2021) 103964.
[55] D.W. Hogg, D. Foreman-Mackey, Data analysis recipes: Using markov chain monte carlo, The Astrophysical Journal Supplement Series, 236 (2018) 11.
[56] C. Shani, N. Weisbrod, A. Yakirevich, Colloid transport through saturated sand columns: Influence of physical and chemical surface properties on deposition, Colloids Surfaces A: Physicochemical Engineering Aspects, 316 (2008) 142-150.
[57] M. Farahani, H. Aghaei, S.R. Asadolahpour, Sensitivity of unsteady-state gas-water relative permeability to experimental artefacts and interpretation techniques; case study from a gas reservoir in south Iran, J. Nat. Gas Sci. and Eng., 71 (2019) 102998.
[58] Y. Xiangdong, S. Jiang, L. YanLu, G. Wei, L. Jungang, W. Peng, M. Litao, Impact of pore structure and clay content on the water-gas relative permeability curve within tight sandstones: A case study from the LS block, eastern Ordos Basin, China, J. Nat. Gas Sci. and Eng., 81 (2020) 103418.
[59] Y. Wang, Y. Yang, K. Wang, L. Tao, J. Liu, C. Wang, J. Yao, K. Zhang, W. Song, Changes in relative permeability curves for natural gas hydrate decomposition due to particle migration, J. Nat. Gas Sci. and Eng., 84 (2020) 103634.
[60] D. Li, X. Jiang, Y. Zhong, A. Liu, Coupling effects of native H2S and different co-injected impurities on CO2 sequestration in layered saline aquifers, J. Nat. Gas Sci. and Eng., 88 (2021) 103846.
[61] L. Valle, C. Grima, R. Rodriguez, C. Llopis, Effect of scCO2-brine mixture on injectivity and storage capacity in rock samples of naturally fractured carbonate formations, J. Nat. Gas Sci. and Eng., 81 (2020) 103452.
[62] Q. Feng, H. Chen, X. Wang, S. Wang, Z. Wang, Y. Yang, S. Bing, Well control optimization considering formation damage caused by suspended particles in injected water, J. Nat. Gas Sci. and Eng., 35 (2016) 21-32.
[63] M.G. Temraz, I. Hassanien, Mineralogy and rheological properties of some Egyptian bentonite for drilling fluids, J. Nat. Gas Sci. and Eng., 31 (2016) 791-799.

[64] H. Yuan, A. Shapiro, Z. You, A. Badalyan, Estimating filtration coefficients for straining from percolation and random walk theories, Chem. Eng. J, 210 (2012) 63-73.
[65] H. Yuan, A.A. Shapiro, A mathematical model for non-monotonic deposition profiles in deep bed filtration systems, Chem. Eng. J, 166 (2011) 105-115.
[66] H. Yuan, A.A. Shapiro, Modeling non-Fickian transport and hyperexponential deposition for deep bed filtration, Chem. Eng. J, 162 (2010) 974-988.
[67] T. Russell, D. Pham, M.T. Neishaboor, A. Badalyan, A. Behr, L. Genolet, P. Kowollik, A. Zeinijahromi, P. Bedrikovetsky, Effects of kaolinite in rocks on fines migration, J. Nat. Gas Sci. and Eng., 45 (2017) 243-255.
[68] A. Bera, H. Belhaj, Application of nanotechnology by means of nanoparticles and nanodispersions in oil recovery-A comprehensive review, J. Nat. Gas Sci. and Eng., 34 (2016) 1284-1309.
[69] S. Medhi, D. Gupta, J.S. Sangwai, Impact of zinc oxide nanoparticles on the rheological and fluid-loss properties, and the hydraulic performance of non-damaging drilling fluid, J. Nat. Gas Sci. and Eng., 88 (2021) 103834.
[70] B. Yuan, R.G. Moghanloo, Analytical modeling nanoparticles-fines reactive transport in porous media saturated with mobile immiscible fluids, AIChE Journal, 65 (2019) e16702.
[71] B. Yuan, R.G. Moghanloo, Nanofluid precoating: an effective method to reduce fines migration in radial systems saturated with two mobile immiscible fluids, SPE Journal, 23 (2018) 998-1018.
[72] B. Yuan, R.G. Moghanloo, Nanofluid pre-treatment, an effective strategy to improve the performance of low-salinity waterflooding, J. Pet. Sci. and Eng., 165 (2018) 978-991.

5. Characterisation of fines migration system using laboratory pressure measurements

Yang, S., Russell, T., Badalyan, A., Schacht, U., Woolley, M. and Bedrikovetsky, P.

Journal of Natural Gas Science and Engineering, 65, pp.108-124

Statement of Authorship

Title of Paper	Characterisation of fines migration system using laboratory pressure measurements
Publication Status	☑ Published ☐ Accepted for Publication ☐ Submitted for Publication ☐ Unpublished and Unsubmitted w ork w ritten in manuscript style
Publication Details	Yang, S., Russell, T., Badalyan, A., Schacht, U., Woolley, M. and Bedrikovetsky, P., 2019. Characterisation of fines migration system using laboratory pressure measurements. Journal of Natural Gas Science and Engineering, 65, pp.108-124.

Principal Author

Name of Principal Author (Candidate)	Shuyan Yang		
Contribution to the Paper	Performed laboratory tests, data matching and interpretation, derivation of skin factor for formation damage during fracturing, contribution to writing		
Overall percentage (%)	70%		
Certification:	This paper reports on original research I conducted during the period of my Higher Degree by Research candidature and is not subject to any obligations or contractual agreements with a third party that would constrain its inclusion in this thesis. I am the primary author of this paper.		
Signature		Date	13/11/2021

Co-Author Contributions

By signing the Statement of Authorship, each author certifies that:

i. the candidate's stated contribution to the publication is accurate (as detailed above);

ii. permission is granted for the candidate in include the publication in the thesis; and

iii. the sum of all co-author contributions is equal to 100% less the candidate's stated contribution.

Name of Co-Author	Thomas Russell		
Contribution to the Paper	Derivation of skin factor for formation damage during fracturing, manuscript editing and revision		
Signature		Date	13/11/2021

Name of Co-Author	Alex Badalyan		
Contribution to the Paper	Design of laboratory experiment, performed laboratory experiments		
Signature		Date	15.11.2021.

Name of Co-Author	Ulrike Schacht		
Contribution to the Paper	Rock and mineral interpretation		
Signature		Date	15/11/21

Name of Co-Author	Matthew Woolley		
Contribution to the Paper	Problem formulation, supervision of the development of the work		
Signature		Date	11/11/21

Name of Co-Author	Pavel Bedrikovetsky		
Contribution to the Paper	Problem formulation, supervision of the development of the work, manuscript revision		
Signature		Date	11/11/21

Journal of Natural Gas Science and Engineering 65 (2019) 108–124

Contents lists available at ScienceDirect

Journal of Natural Gas Science and Engineering

journal homepage: www.elsevier.com/locate/jngse

Characterisation of fines migration system using laboratory pressure measurements

Shuyan Yang[a], Thomas Russell[a], Alexander Badalyan[a], Ulrike Schacht[a], Matthew Woolley[b], Pavel Bedrikovetsky[a,*]

[a] The University of Adelaide, South Australia, Australia
[b] Santos Ltd, Adelaide, South Australia, Australia

ARTICLE INFO

Keywords:
Fines migration
Formation damage
3-point pressure method
Laboratory coreflood
Fractured well

ABSTRACT

The focus of this study is formation damage due to fines migration induced by the leak-off of low salinity potassium chloride (KCl) fracturing fluids. The importance of this topic is determined by the wide utilization of KCl in drilling and fracturing fluids, as well as for fines fixing, and the widely reported skin in gas and oil wells. Scanning electron microscopy (SEM) imaging and energy dispersive X-ray (EDX) analyses from this study clearly indicated clay fines mobilisation, migration and straining, resulting in permeability decline. The breakthrough fines concentration was measured during the coreflooding experiments. The installation of a pressure sensor in the middle of the core allowed for pressure drop measurements across the first core section and the overall core. Permeability decline was observed during the injection of water with piecewise-constant decreasing KCl salinity. An analytical model based on the exact solution for one-dimensional fines transport was used to match the laboratory data. Close agreement between the laboratory and modelling data was observed. Moreover, the tuned model coefficients vary in the range of commonly reported values. It was found that neglecting fines breakthrough concentration (BTC) measurements permits laboratory-based prediction of formation damage during fracture fluid leak-off. However, fines BTC must be measured to fully characterise the fines migration system.

1. Introduction

Fines migration is one of the most common causes for formation damage in gas and oil fields. The lifting, migrating, and straining of the initially attached reservoir fines yield permeability decline, resulting in well index impairment for gas and oil production and injection wells. Byrne and Waggoner (2009) presented a case study of fines migration for gas wells, while Civan (2015) provided a comprehensive review for different formation damage mechanisms, including a detailed discussion of fines migration, in oil wells, and Khilar and Fogler (1998) investigated fines migration in artesian wells.

The accumulation of common natural reservoir fines, such as kaolinite, illite, and chlorite, in narrow grain crevices, cracks and other immobile-fluid zones (Civan, 2015), or coat the grain surfaces (Khilar and Fogler, 1998). Therefore, their detachment does not cause a significant increase in permeability. On the contrary, mobilised fines migrate in porous media until straining or size exclusion in thin pores occurs, which hinders fluid flow and yields significant permeability reduction (Fig. 1(a)).

An attached fine particle in a natural reservoir is primarily subject to drag and electrostatic forces (F_d and F_e, respectively in Fig. 1(b)). Typically, an extended form of the traditional DLVO equations (Derjaguin and Landau, 1941; Verwey and Overbeek, 1948) are used to calculate the electrostatic force (Elimelech et al., 2013). Expressions used for drag force on attached particles can be found in the work of Bedrikovetsky et al. (2010). Lifting, gravitational, and Brownian forces are negligibly small when compared with F_d and F_e. It is assumed that the fine particle rotates around the neighbouring particle or asperity at the moment of detachment. Bradford et al. (2013) presented the mechanical equilibrium of the fine particle on the rock surface, which is determined by the torque balance of the drag and electrostatic forces:

$$F_d(U)l = F_e(\gamma), \quad l = {l_d}/{l_n}, \tag{1}$$

where the lever arm for the electrostatic attraction, l_n, is defined by either the mutual grain-rock deformation under the attaching force, F_e, or the distance to asperity; the lever arm for drag force, l_d, for low-deformable solid particle and rock is insignificantly smaller than the fine-particle radius.

The drag force is proportional to the flow velocity, U, thus as a

* Corresponding author.
E-mail addresses: pavel@asp.adelaide.edu.au, pavel.russia@gmail.com (P. Bedrikovetsky).

https://doi.org/10.1016/j.jngse.2019.02.005
Received 8 October 2018; Received in revised form 18 January 2019; Accepted 18 February 2019
Available online 22 February 2019
1875-5100/

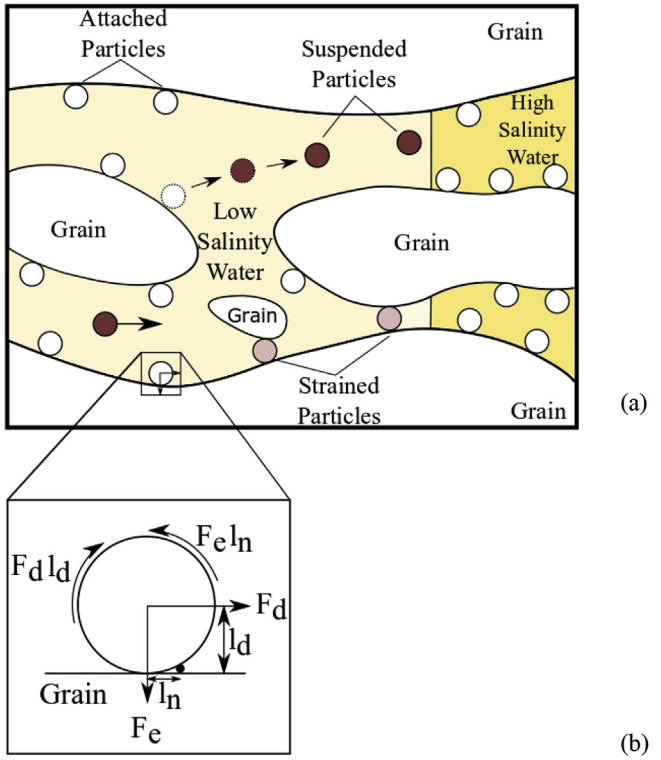

Fig. 1. Schematic of fines migration in rocks: (a) attached, suspended, and strained particles during low-salinity water injection; (b) torque balance for electrostatic and drag forces on an attached particle.

result, attached particles can be lifted under high flow rates (Civan, 2015). The electrostatic force decreases as the ionic strength decreases, meaning that attached particles can be mobilised if a low fluid salinity, γ, is injected. Impairment of production gas and oil wells during high-rate production or after the breakthrough of low-salinity water are widely presented in the literature (see studies presented by Akhmetgareev and Khisamov (2015), Civan (2015), Morrow and Buckley (2011), and Sarkar and Sharma (1990)). Injectivity decline during low-salinity water injection has also been widely reported (Civan, 2015; Chequer et al., 2018; Song and Kovscek, 2016; Sarkar and Sharma, 1990).

Eq. (1) allows for determining whether a fine particle, of any size and shape, is attached in any part of the porous space, remains attached, or is detached under a given velocity, U, and salinity, γ. Calculating the total of attached fines results in the critical retention function, σ_{cr}:

$$\sigma_a = \sigma_{cr}(\gamma, U), \tag{2}$$

where σ_a is the attached particle concentration.

Several analytical models for fines migration based on Eq. (2) have been developed. Bedrikovetsky et al. (2010) presented the model and solution for detachment of particles on an internal cake or matrix surface in a porous medium. Chequer et al. (2018) developed 1D analytical models for linear and radial flows. In the book chapter by Yang et al. (2018), mathematical models were derived and laboratory studies were conducted to investigate the effects of injection velocity and salinities on fines migration. Yuan et al. (2016) used analytical modelling to evaluate the effectiveness of nanoparticles in mitigating fines migration. These models can be fitted to the laboratory data by tuning the model coefficients.

Laboratory studies of fines migration under low ionic strength have been carried out with regards to varying sodium chloride (NaCl) concentrations (Assef et al., 2014; Chequer et al., 2018; Habibi et al., 2012; Othman et al., 2018; Qiao et al., 2016; Rosenbrand et al., 2014; Russell et al., 2018; Yang et al., 2018). However, it is potassium chloride (KCl) that has been widely used in fracturing and drilling fluids, where fines migration can cause significant formation damage (Civan, 2015). In addition, KCl is used for fines fixing in reservoir rocks prior and/or during production or injection (Assef et al., 2014; Bera and Belhaj, 2016; Habibi et al., 2012). Despite that, a combination of systematic laboratory studies of fines migration and rigorous mathematical modelling of the laboratory data has not yet been performed for KCl solutions.

Micro-scale visualisation tests using scanning electron microscopy (SEM) (Rosenbrand et al., 2014), computer tomography (CT) (Lagasca and Kovscek, 2014), and surface-functionalised micromodels (Song and Kovscek, 2016) have also been performed for fluids of varying NaCl concentrations, but are limited for KCl based fluids.

Pressure drop across the core and fines breakthrough concentration (BTC) are measured during the coreflood experiments. Pressure drop measurements are precise and simple, while fines BTC exhibits significant scatter and the measurement is cumbersome and expensive. The same situation occurs during laboratory injectivity decline tests, due to the injection of solid and liquid suspensions and colloids (Bedrikovetsky et al., 2001) and compatibility tests for oilfield scaling (Vaz et al., 2016). In both cases, simultaneous measurements of differential pressure across the first half of the core section and the overall core length, allow for the substitution of fines BTC measurements, yielding simpler and more reliable three-point-pressure tests (Fig. 2(a)). However, application of the three-point-pressure test to fines migration is not available.

In this work we aim to fill the above-mentioned gaps. A comprehensive study of fines-migration induced formation damage during KCl-based salinity decrease was performed. SEM imaging of the rock before and after flooding, along with energy dispersive X-ray (EDX) analysis of produced solids, allowed for the observation of fines lifting, migration and straining. The presented laboratory study includes pressure

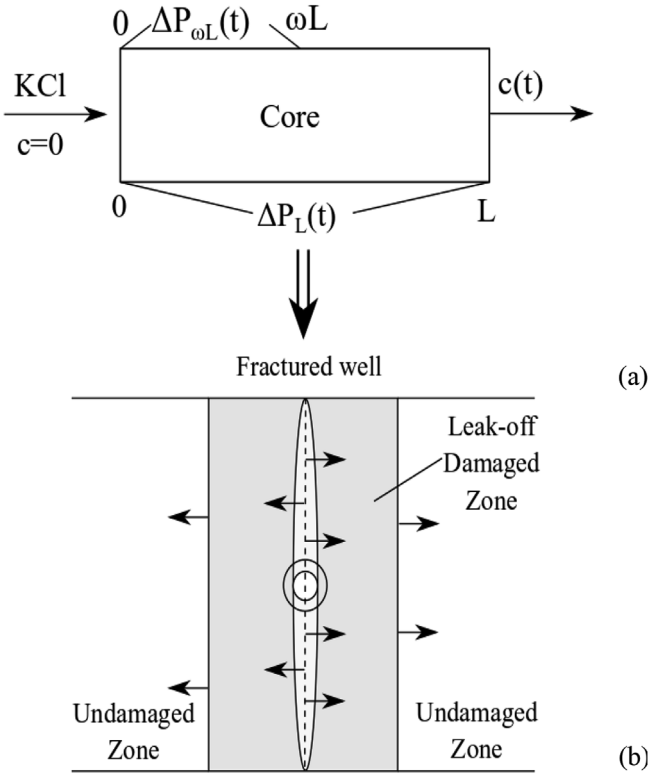

Fig. 2. Schematic of: (a) coreflood experiment with measurements of fines breakthrough concentration and the three-point pressures; (b) leak-off damage zone in the reservoir.

measurements across the core and its first section, and fines BTC. The matching of the derived laboratory data with an analytical model was found to provide high level of accuracy. The fitted model parameters varied within common intervals. Probabilistic estimations of the gas-well skin factor induced by fines migration using laboratory results were also performed.

The structure of the text is as follows. The materials and methodology of the laboratory study are described in Section 2, and the results from the laboratory study are discussed in Section 3. The mathematical model used to describe one-dimensional fines migration due to low salinity coreflooding is presented in Section 4. The treatment of the laboratory data with the mathematical model to determine model parameters is shown in Section 5. The model used for estimating the skin factor due to fines migration is given in Section 6. The discussion and conclusions of the study are given in Sections 7 and 8, respectively.

2. Laboratory material and methodology

In this section, we present the laboratory study of formation damage due to fines migration as a result of low-KCl salinity coreflooding.

2.1. Rocks and fluids

Three Permian consolidated (sandstone) cores from the Patchawarra Formation (Core 1 and 2) and Tirrawarra Formation (Core 3) in the Cooper Basin (Australia) were selected to conduct the coreflooding experiment. Core properties are presented in Table 1.

The injection solutions were prepared using KCl salt (laboratory grade, purity > 99.0%) and Milli-Q deionized water (DIW). The coreflooding experiments consisted of four injection cycles for each core. The four injected solutions, in order of injection, were 2% KCl, 1.2% KCl, 0.4% KCl, and DIW. Percentages given for fluid salinity refer to weight percentage. The 2% KCl solution was used first to saturate the core and prevent fines detachment to achieve permeability stabilisation. 1.2% KCl and 0.4% KCl were the approximate salinities for the formation and the proposed fracturing fluid, respectively. During the final injection cycle, DIW was injected to test the sensitivity of the cores to low salinity water and to produce a sufficient volume of fines to perform SEM studies with EDX analyses.

2.2. Laboratory methodology

SEM imaging was conducted to visualise and identify the fines mineralogical composition of all three core samples. This was conducted on the Quanta 450 SEM, using a beam voltage of 20 kV and spot size 4. EDX analysis was conducted using the Oxford Ultim Max EDS detector with AZtec software. Carbon was used to coat the effluent samples for the EDX analysis. SEM images of the inlet face of the cores were taken before and after each coreflooding experiment. SEM-EDX analysis of effluents was performed after the coreflooding experiments to determine the mineral composition of the fine particles collected.

Mineral content characterisation of the cores was performed by quantitative X-ray diffraction (XRD) analysis. This was conducted by the Bruker D8 ADVANCE Powder X-ray Diffractometer with a Cu-radiation source. Data was processed using Bruker DIFFRAC.EVA software and Crystallography Open Database reference patterns for identifying mineral phases. Quantification was calculated against an internal standard of zinc oxide at 10% using RockJock software.

Saturation of the cores involved drying at 60 °C for 24 h, evacuating them using a vacuum pump for a further 24 h, and then exposing the core to 2% KCl solution while still under vacuum. The porosity of the cores was determined by the weight difference between the dry and 2% KCl saturated core.

The coreflooding experiments were carried out in an air-conditioned laboratory with temperature controlled within 22 °C ± 0.5 °C. The confining pressure for the experiment was maintained at 1000 psi, while the outlet pressure was atmospheric. Flooding of each core started with the injection of 2% KCl at a lower rate of 3.33×10^{-9} m/s, then followed by the injection of 2% KCl at a higher rate of 3.33×10^{-8} m/s. With the injection rate maintained at 3.33×10^{-8} m/s, three injection cycles, with solutions containing 1.2% KCl, 0.4% KCl, and DIW respectively, were conducted sequentially. Each injection cycle was completed when a stabilised pressure drop was achieved.

Each of the four injection cycles had an injection period of approximately 200 pore volumes injected (PVI). Two sets of differential pressure measurements were recorded throughout the experiment. The first set measured the differential pressure across the entire core length, and the second measured the pressure difference across the first 2.7 cm of the core. In the text below these are referred to as the full core and half core differential pressure measurements respectively. The collected effluent samples were processed to determine the BTC, which was used to generate the accumulated breakthrough curve for each core.

2.3. Laboratory set-up

Photographs and a schematic of the laboratory set-up are shown in Fig. 3(a)-(b) and Fig. 3(c), respectively. The set-up consisted of a sandstone core (1) placed inside a Viton sleeve (2), fixed in position by two stainless steel flow distributors (3) in a high-pressure stainless steel coreholder (4). Overburden pressure, measured by an absolute pressure transmitter (7), was generated by compressing distilled water (5) with a manual pressure generator (6).

A high-performance liquid chromatography (HPLC) pump (8) delivered the injection solution (9) through a three-way valve (10) to the core. The back-pressure regulator (11) ensured a smooth operation of the HPLC pump, maintained reliable pressure measurements, and helped to remove any air remaining in the core. The required back-pressure over the diaphragm in the back-pressure generator was provided by the compressed air cylinder (12). The differential pressure across the half core was measured by two differential pressure transmitters (DPTs) (13) and (14) with measurement ranges 0–0.6 psi and 0–14.5 psi, respectively. The differential pressure across the full core was measured by another two DPTs (15) and (16) with measurements ranges 0–72.5 psi and 0–500 psi, respectively. All DPTs were re-zeroed using the three-way manual valves (17–20) prior to measurements. Absolute pressures at the core inlet, half core, and core outlet were measured by absolute pressure transmitters (21–23). When the differential pressures exceeded the DPT ranges, readings from the absolute pressure transmitters were used to calculate the respective differential pressures.

Data collected from pressure transmitters and DPTs was transmitted to a real-time data acquisition module (24) connected to a signal converter (25) and a personal computer (26) with custom built software based on ADVANTECH ADAMView. A fraction collector (27) was used to collect effluent fluid samples in 15 and 50 mL centrifuge plastic tubes (28). The particle concentration of the samples was measured by portable particle counter (29).

Table 1
Properties of the cores.

Properties	Core 1	Core 2	Core 3
Formation	Patchawarra	Patchawarra	Tirrawarra
Depth (ft)	9427.2	9301.3	9754.0
Porosity (%)	11.5	10.7	11.8
Permeability (mD)	4.47	2.39	0.95
Core length (cm)	4.38	4.51	4.38
Core diameter (cm)	3.87	3.79	3.86
Grain density (g/cc)	2.648	2.654	2.647

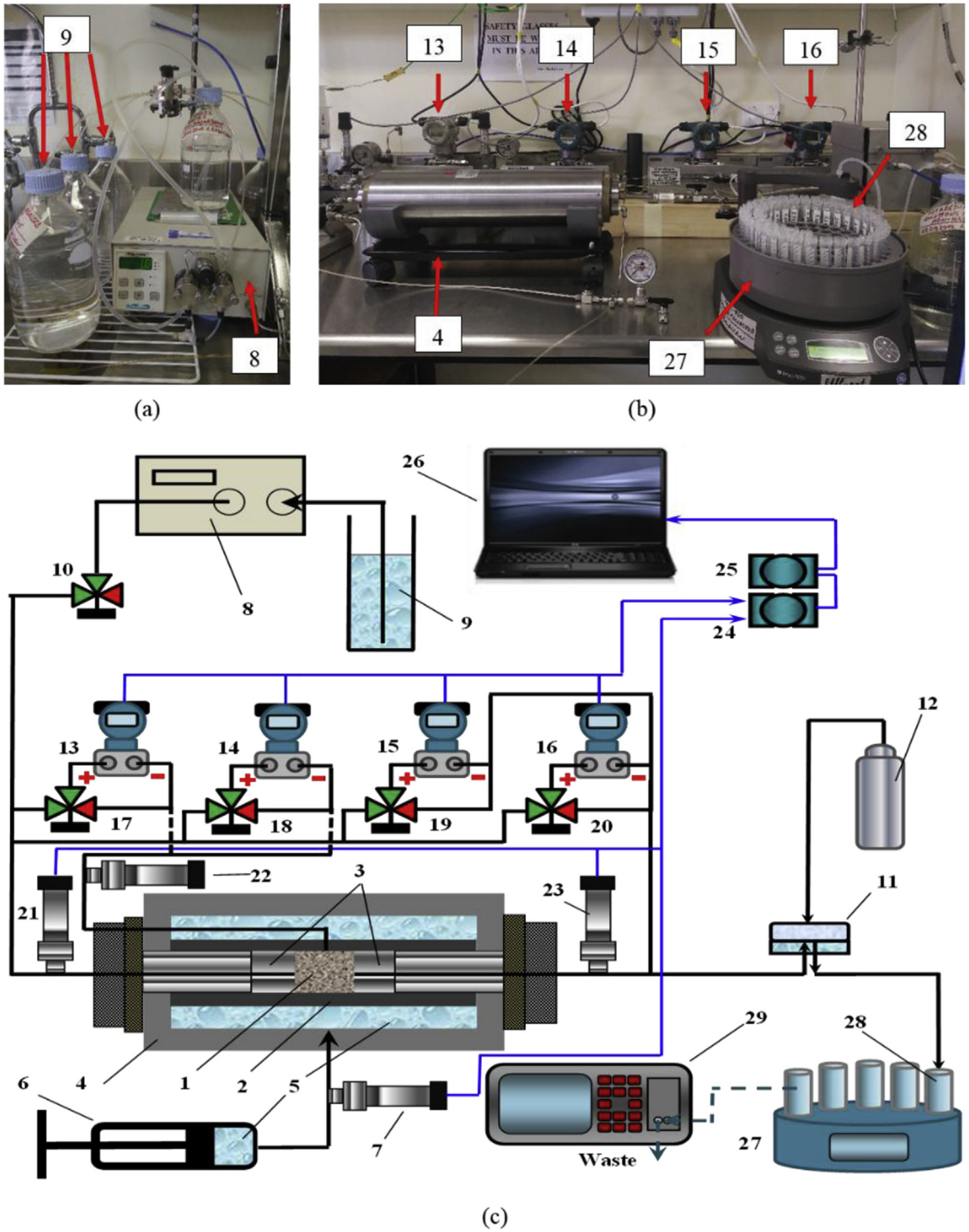

Fig. 3. Laboratory set-up for coreflooding with three-point pressure measurements: (a) and (b) photographs of the set-up; (c) schematic of equipment used: 1 – core sample, 2 – Viton sleeve, 3 – stainless steel distributors, 4 – high-pressure stainless steel core holder, 5 – distilled water to develop overburden pressure, 6 – overburden pressure generator, 7, 21–23 – absolute pressure transmitters, 8 – high-performance liquid chromatography (HPLC) pump, 9 – injection solution, 10, 17-20 – three-way manual valves, 11 – back-pressure regulator, 12 – compressed air cylinder, 13–16 – differential pressure transducers, 24 – real-time data acquisition module, 25 – signal converter, 26 – PC, 27 – sample collector, 28 – centrifuge plastic tubes, 29 – portable particle counter.

3. Laboratory results

In this section, the results from the SEM-EDX and XRD studies, as well as the coreflood experiment are presented.

3.1. SEM-EDX, XRD study on cores

Table 2 presents the results from whole rock XRD analysis. Core 1 and 2 contained a total of 6.89% and 7.79% clay minerals, respectively, namely disordered kaolinite and illite. Core 3 contained a total of 10.88% clay minerals, namely dickite and illite. The absence of smectite group clay from all three cores allows for the exclusion of the possibility

Table 2
Results from the XRD study.

Minerals	Core 1	Core 2	Core 3
Quartz (%w/w)	93.11	92.21	89.12
Kaolinite (%w/w) (disordered)	2.68	4.47	0
Illite (%w/w)	4.21	3.32	5.95
Dickite (%w/w)	0	0	4.93
TOTAL (%w/w)	**100**	**100**	**100**

of formation damage due to swelling clays.

The SEM study provided direct evidence of particle detachment and capture. SEM images of Core 1 taken at the same location before and after coreflooding are given in Fig. 4. Fine particles that have disappeared are shown in solid red circles, and the appearance of a particle is shown by the dashed red circle. This newly appeared particle has most likely migrated here from a neighbouring pore.

The disappearance and appearance of fines are also observable in the before and after coreflooding SEM images of Core 2, shown in Fig. 5. However, due to technical difficulties, the before and after coreflooding of SEM images at the same location for Core 3 were not obtained, and therefore are not presented in the paper.

3.2. SEM-EDX study on effluents

SEM-EDX studies were conducted on the filtered effluent samples collected from each core to identify the types of clay minerals produced due to the reduction of injection solution salinity. SEM-EDX results of Core 1 are shown in Fig. 6. The SEM image of effluent is shown in Fig. 6(a). The EDX spectra obtained from Core 1 effluent, given in Fig. 6(b)-(d), show the presence of potassium (K), iron (Fe), and magnesium (Mg), with titanium (Ti) impurities. This is an indication of illite, which shows that some fraction of the illite in Core 1 was colloidal and detached during the coreflooding experiment.

Effluent SEM-EDX studies were also conducted for Core 2 with SEM image shown in Fig. 7(a). The three EDX spectra obtained from Core 2 effluent showed different but distinctive responses. The dominant Si peak on the EDX spectrum in Fig. 7(b) indicates a quartz particle. The near equal peak heights of Si and Al in Fig. 7(c) confirms the presence of a kaolinite particle with some Fe impurities. Fig. 7(d) shows similar EDX spectra as those in Fig. 6(d) with sulphur (S) impurities, which is an indication of illite. From this analysis, it is clear that both of the primary clay minerals in the core (kaolinite and illite) have detached during the injection of low-salinity water. In addition, the presence of quartz at the outlet suggests that some of the quartz fraction identified in the XRD study was colloidal in nature. However, the effluent study performed on Core 3 was unsuccessful due to contamination, and hence not included in the paper.

3.3. Coreflood experiment

Results from the coreflooding experiments are shown in Fig. 8. Permeability decline, as shown in Fig. 8(a), was observed in each core, with a more noticeable decline during the injection of lower salinity solutions. The permeability of Cores 1, 2 and 3 reduced by 36.5%, 17.6% and 14.4% for 0.4% KCl injection from the initial permeability, and 95.7%, 76.0% and 58.3% for DIW injection, respectively. The experimental uncertainty in permeability measurements is 3.09% (Badalyan et al., 2012).

Fig. 8(b) shows the accumulated breakthrough concentration of each core during the experiment. Particle concentrations in this study refer to volumetric concentrations. Overall, Core 1 produced the least amount of fines, and Core 2 produced the most. Fines production was most significant during the injection of DIW for Core 1 and 2, while most of the fines produced from Core 3 were collected during the 0.4% KCl injection. The difference in fines production in response to salinity change could be due to the differences in the origin of the cores, i.e. Core 1 and 2 were from the Patchawarra Formation, while Core 3 was taken from the Tirrawarra Formation.

We measured concentration and particle size distribution in effluent fluid samples using a POLA-2000 particle counter (Particle and Surface Sciences, Australia). For Cores 1, 2, and 3, the mean particle radii, $< r_s >$, are 1.36, 1.75, and 0.69 μm, with variance 0.068, 0.108, and 0.277, respectively. The mean pore radius, $< r_p >$, is calculated by the Kozeny-Carman equation assuming tortuosity of 2 (Lake, 1989). The mean pore radii for Cores 1, 2, and 3 are: 9.04, 7.43, and 4.0 μm, respectively. The resulting jamming ratios are $< r_s > / < r_p > = 0.15$, 0.23, and 0.17, which indicate straining and size exclusion of fines by the rock yielding significant permeability damage by fines migration (van Oort et al., 1993).

4. Mathematical model

In this section we present the mathematical model for fines migration during low-salinity water injection during linear flow.

4.1. Assumptions

The main assumptions for the mathematical model of one-dimensional linear flow of fine particles in porous media under fluid salinity

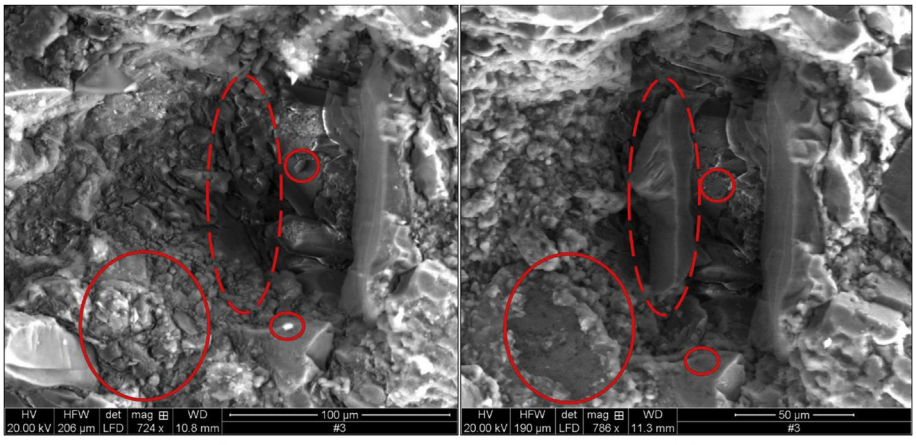

(a) (b)

Fig. 4. Inlet SEM images of Core 1: (a) taken before the coreflooding experiment and (b) taken afterwards. Here the solid circles show those particles that are present in (a) but have disappeared in (b). The dashed circle in (b) highlights a newly captured particle after the experiment.

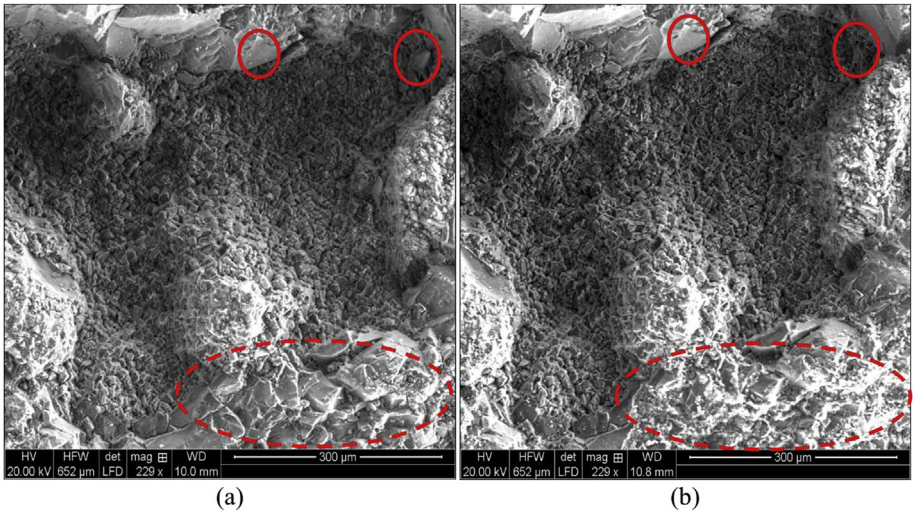

Fig. 5. Inlet SEM images of Core 2: (a) taken before the coreflooding experiment and (b) taken afterwards. Here the solid circles show those particles that are present in (a) but have disappeared in (b). The dashed circle in (b), highlights newly captured particles after the experiment.

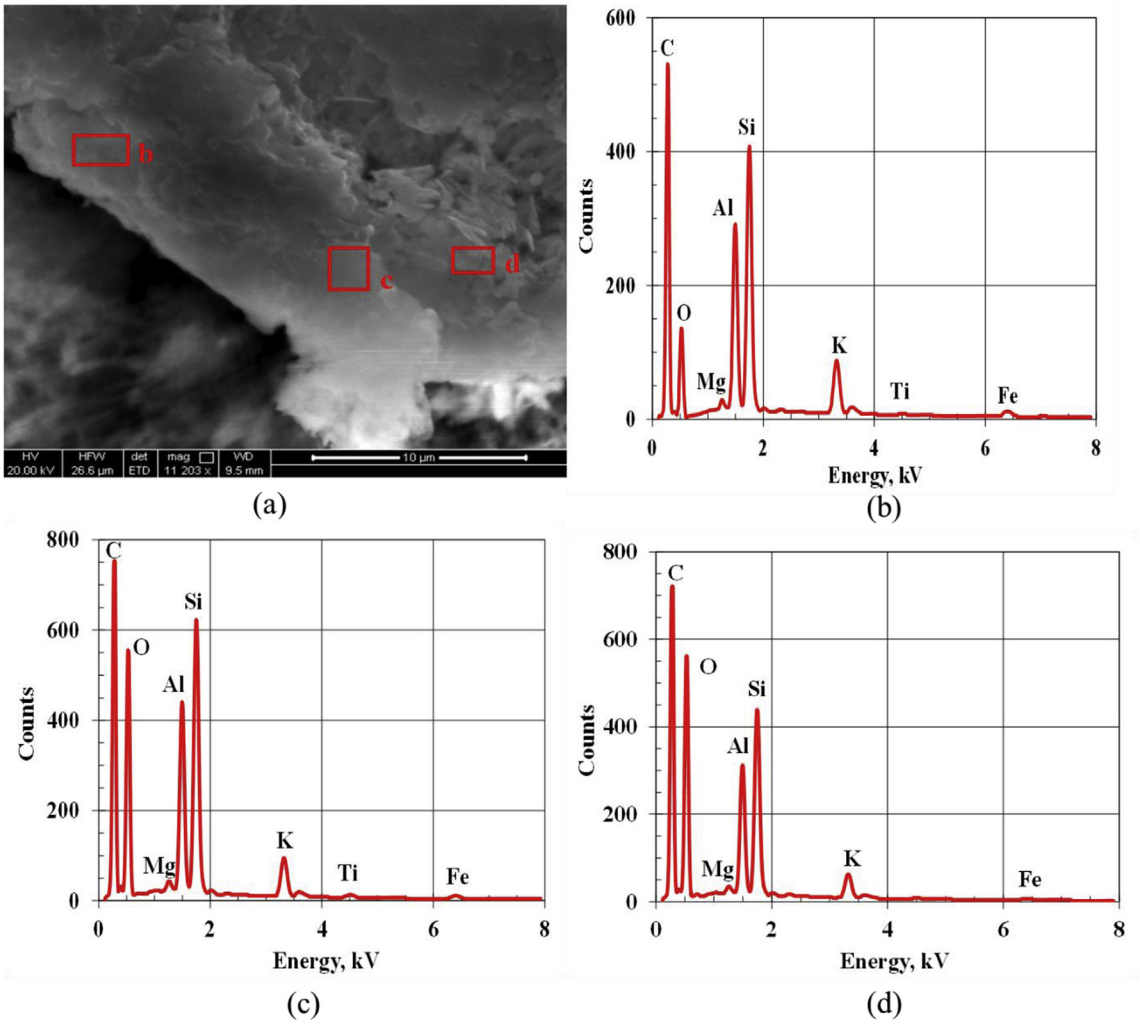

Fig. 6. Effluent collected from Core 1 after the coreflooding experiment: (a) SEM image; (b), (c) and (d) represent EDX graphs of the effluent at locations b, c and d, respectively.

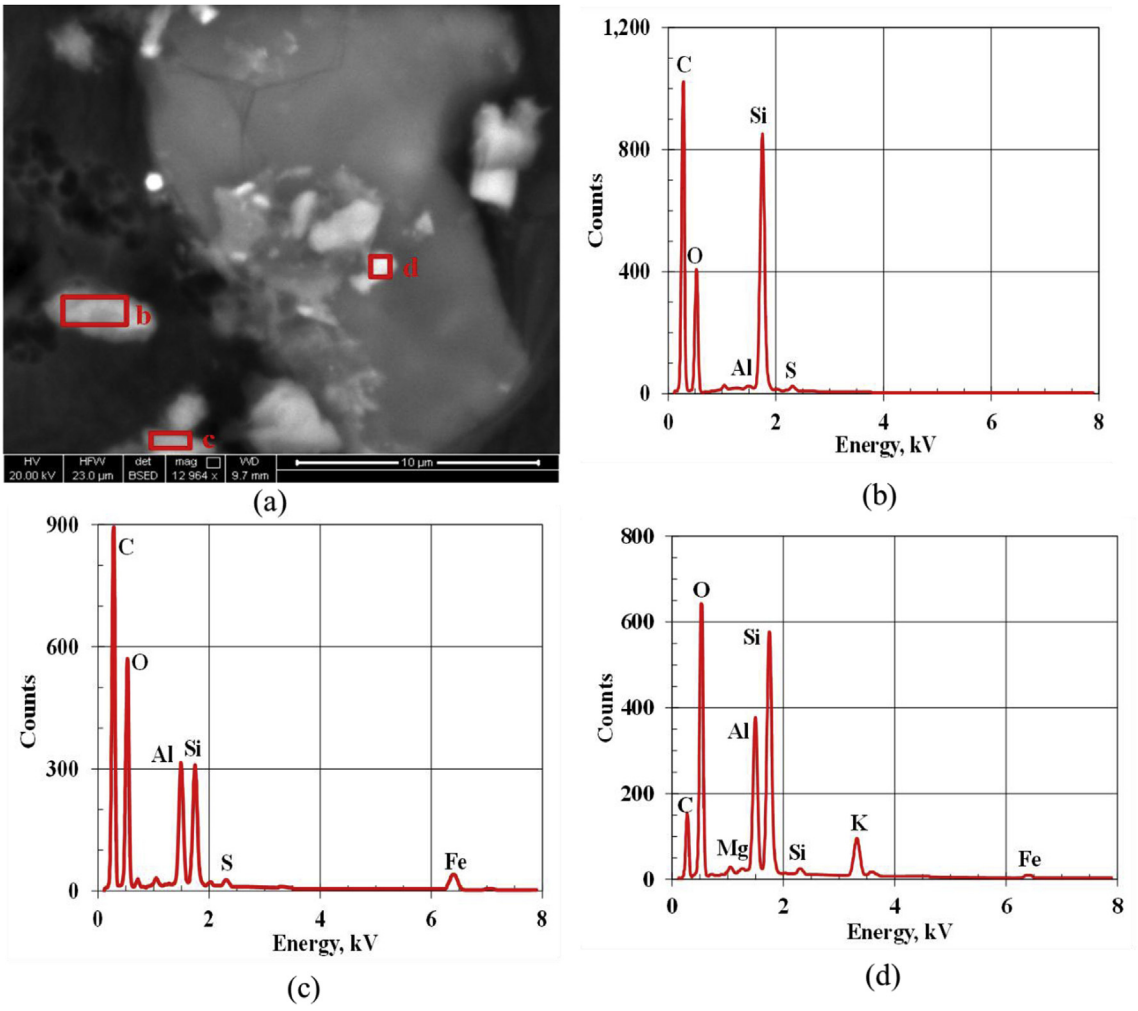

Fig. 7. Effluent collected from Core 2 after the coreflooding experiment: (a) SEM image; (b), (c) and (d) represent EDX graphs of the effluent at locations b, c and d, respectively.

variation are as following:

- Small suspension particle concentration yielding constant fluid density and viscosity
- Small retention concentration, yielding constant porosity and constant flux of incompressible suspension
- Diffusion and dispersion are negligible for both the suspended particles and the solute, i.e. the cores are sufficiently homogeneous and long
- Instantaneous and irreversible particle detachment defined by the critical retention function (Bedrikovetsky et al., 2010)
- Suspended particles travel at a significantly slower velocity compared to the injected solution (Oliveira et al., 2014; Yang et al., 2016)
- Permeability damage due to attached particles is negligible when compared to strained particles, therefore the permeability increase due to particle detachment is ignored

4.2. Basic equations

The governing system of equations for one-dimensional (1D) linear flow for fine particles in a porous medium accounting for salt transport consists of the following equations (Chequer et al., 2018):

The mass balance equation accounting for suspended, attached, and strained particles is:

$$\frac{\partial}{\partial t}(\phi c + \sigma_a + \sigma_s) + \alpha U \frac{\partial c}{\partial x} = 0, \tag{3}$$

where c and σ_s are the suspended and strained particle concentration respectively, t is time, ϕ is the porosity, α is the drift delay factor, and x is the linear coordinate along the core length.

The rate of irreversible particle straining is assumed to be proportional to the advective flux of suspended particles:

$$\frac{\partial \sigma_s}{\partial t} = \lambda c \alpha U, \tag{4}$$

where λ is the filtration coefficient.

The solute transport equation is:

$$\phi \frac{\partial \gamma}{\partial t} + U \frac{\partial \gamma}{\partial x} = 0. \tag{5}$$

A modified form of Darcy's equation is used to account for the permeability damage due to strained particles:

$$U = -\frac{k_I}{\mu(1 + \beta \sigma_s)} \frac{\partial p}{\partial x}, \tag{6}$$

where k_I is the initial permeability, μ is the fluid viscosity, β is the formation damage coefficient, and p is the fluid pressure.

The initial conditions for the system of equations include the salinity of the in situ fluid, γ_I, the injection of a particle free solution, the absence of strained particles, and the assumption that the initial attached particle concentration is equal to the critical retention function

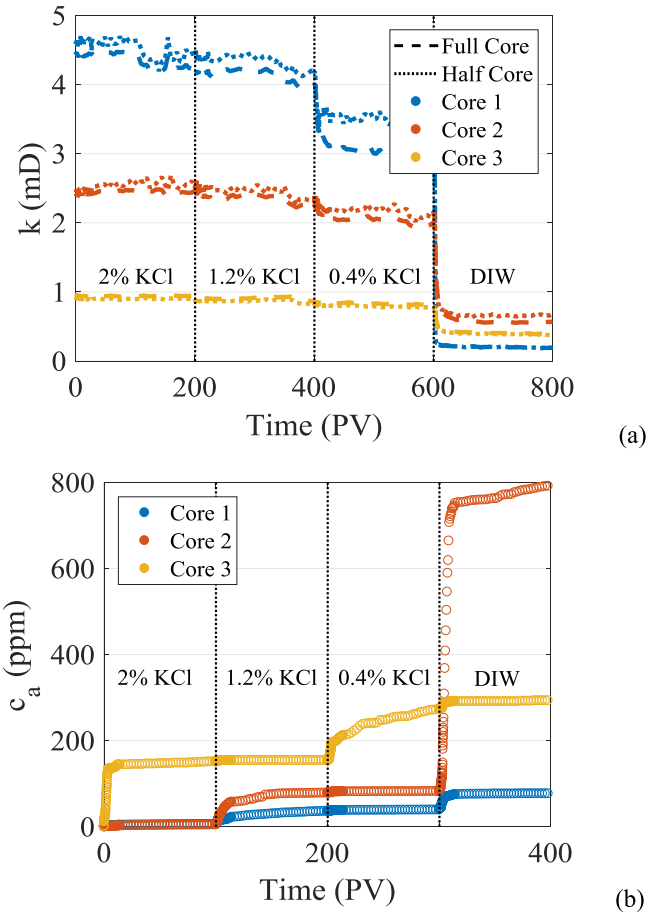

Fig. 8. Coreflooding data for all three cores: (a) permeability decline due to salinity change; (b) accumulated breakthrough particle concentration.

corresponding to the in situ fluid salinity:

$$t = 0: \quad \gamma = \gamma_I, \quad c = 0, \quad \sigma_s = 0, \quad \sigma_a = \sigma_{cr}(\gamma_I). \tag{7}$$

The inlet boundary conditions for a particle free solution with a given salinity, γ_J, are:

$$x = 0: \quad \gamma = \gamma_J, \quad c = 0. \tag{8}$$

Salinity change from γ_I to γ_J yields a release of particles governed by the critical retention function. The total detached particle concentration, $\Delta\sigma_{cr}$, is:

$$\Delta\sigma_{cr} = \sigma_{cr}(\gamma_I) - \sigma_{cr}(\gamma_J). \tag{9}$$

The system of equations (2)–(6) can be expressed in dimensionless form by introducing the following dimensionless parameters and variables:

$$t_D = \frac{Ut}{\phi L}, \quad x_D = \frac{x}{L}, \quad C = \frac{c}{\Delta\sigma_{cr}}, \quad S_a = \frac{\sigma_a}{\phi\Delta\sigma_{cr}},$$
$$S_s = \frac{\sigma_s}{\phi\Delta\sigma_{cr}}, \quad \Lambda = \lambda L, \quad p_D = \frac{pk_I}{U\mu L}, \tag{10}$$

where L is the core length.

With the substitution of (2) into (3), the system of equations becomes:

$$\frac{\partial}{\partial t_D}(C + S_{cr}(\gamma) + S_s) + \alpha\frac{\partial C}{\partial x_D} = 0, \tag{11}$$

$$\frac{\partial S_s}{\partial t_D} = \alpha\Lambda C, \tag{12}$$

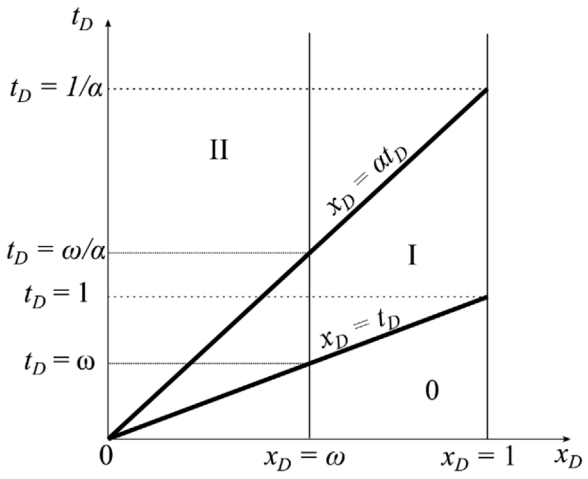

Fig. 9. Concentration fronts in (x_D, t_D)-plane during low-salinity coreflooding with fines migration.

$$\frac{\partial\gamma}{\partial t_D} + \frac{\partial\gamma}{\partial x_D} = 0, \tag{13}$$

$$1 = -\frac{1}{1 + \phi\beta\Delta\sigma_{cr}S_s}\frac{\partial p_D}{\partial x_D}. \tag{14}$$

The governing system of equations (11)-(14) subject to initial (7) and boundary conditions (8) determines four unknowns: suspended, and strained particle concentrations, salinity, and pressure. Details of the exact solution derivation are published in Chequer et al. (2018). The resulting exact solution is divided into three regions, as shown in Fig. 9, separated by the fluid front ($x_D = t_D$), and the suspended particle front, ($x_D = \alpha t_D$). Region 0 is ahead of the injected solution front, Region I is between the injected solution front and the suspended particle front, and Region II is behind the suspended particle front.

The model contains the following empirical coefficients: the drift delay factor, α, the filtration coefficient, Λ, the formation damage coefficient, β, and the total detached particle concentration, $\Delta\sigma_{cr}$. Fundamental relations for these unknowns based on other core properties are not available, therefore these constants must be determined by treating laboratory data.

4.3. Treatment of three point pressure measurements

The laboratory pressure measurements allow us to calculate the differential pressure between the inlet ($x_D = 0$) and some intermediate point in the core ($x_D = \omega$), where $0 < \omega \leq 1$. For three-point pressure measurements, pressure drops are calculated from pressure measurements between the inlet and half core ($\omega = 0.027/L$), and between the inlet and outlet ($\omega = 1$). These two sets of laboratory pressure drop data can be transformed into impedance, $J_\omega^L(t_D)$, by:

$$J_\omega^L(t_D) = \frac{[p(0, t_D) - p(\omega, t_D)]U(0)}{U(t_D)[p(0,0) - p(\omega, 0)]}. \tag{15}$$

Under the condition of constant injection rate, the impedance can be calculated from Eq. (14), which is used to fit the dimensionless pressure drop given in Eq. (15):

$$J_\omega^M(t_D) = p_D(0, t_D) - p_D(\omega, t_D) = 1 + \phi\beta\Delta\sigma_{cr}\int_0^\omega S_s(x_D, t_D)dx_D. \tag{16}$$

The breakthrough suspended particle concentration measured from the laboratory experiment, expressed as the accumulated breakthrough concentration (C_a^L), can be calculated from the model as per:

Table 3
Exact solution for impedance at a point along the core (J_ω^M, where $0 < \omega \leq 1$) and dimensionless accumulated breakthrough concentration (C_a^M) in regions 0 ($T < \omega$), I ($\omega < T < \omega/\alpha$) and II ($T > \omega/\alpha$) derived by Chequer et al. (2018).

	Region	Exact Solution
J_ω^M	0	$1 + \frac{\beta\Delta\sigma_{cr}}{\omega}\left[T + \frac{1}{\alpha\Lambda}(\exp(-\alpha\Lambda T) - 1)\right]$
	I	$1 + \frac{\beta\Delta\sigma_{cr}}{\omega}\left[\omega + \frac{1}{\alpha\Lambda}\left(\exp(-\alpha\Lambda T) + (\alpha - 1)\exp\left(\frac{\alpha\Lambda(\omega - T)}{1-\alpha}\right) - \alpha\right)\right]$
	II	$1 + \frac{\beta\Delta\sigma_{cr}}{\omega}\left[\omega + \frac{1}{\Lambda}(\exp(-\Lambda\omega) - 1)\right]$
C_a^M	0	0
	I	$\frac{\Delta\sigma_{cr}}{\phi\Lambda}\left[1 - \exp\left(\frac{\alpha\Lambda(1-T)}{1-\alpha}\right)\right]$
	II	$\frac{\Delta\sigma_{cr}}{\phi\Lambda}[1 - \exp(-\Lambda)]$

$$C_a^M(1, t_D) = \alpha\int_0^{t_D} C(1, y)dy. \quad (17)$$

The final form for the impedance and accumulated breakthrough concentration of the mathematical model given by Chequer et al. (2018) are presented in Table 3.

5. Matching the laboratory data by mathematical model

The current section presents the methodology and results of tuning the mathematical model for fines migration to the laboratory coreflooding results.

5.1. Tuning methodology

The data obtained from the laboratory study ($J_1^L(t_D)$, $J_\omega^L(t_D)$, and $C_a^L(t_D)$) can be used to tune the parameters of the mathematical model presented in Section 4. While the laboratory procedure outlined in this paper facilitates fitting with all three data sets, additional fitting was performed using only a subset of these data sets to determine whether a less rigorous laboratory procedure would have significant adverse effects on the model parameters.

Three sets of model tuning were performed using different techniques: fitting technique A used all three sets of data ($J_1^L(t_D)$, $J_\omega^L(t_D)$, and $C_a^L(t_D)$), fitting technique B utilised only the impedance data ($J_1^L(t_D)$ and $J_\omega^L(t_D)$), and fitting technique C used the full core impedance and accumulated breakthrough concentration ($J_1^L(t_D)$ and $C_a^L(t_D)$).

Even prior to fitting, an immediate disadvantage of fitting technique B is apparent. Of the four tuning parameters, the formation damage coefficient, β, and total detached particle concentration, $\Delta\sigma_{cr}$, appear in the impedance formulae (see Table 3) only as their product, $\beta\Delta\sigma_{cr}$. Therefore the use of only impedance data prevents these two parameters from being identified separately. This issue is absent for fitting techniques A and C as they both make use of the accumulated breakthrough concentration to evaluate $\Delta\sigma_{cr}$. As such, fitting technique B will be limited to tuning only 3 parameters (namely, α, Λ, $\beta\Delta\sigma_{cr}$).

A genetic algorithm, implemented in the software MATLAB 2017a, was used to obtain the fitting parameters.

5.2. Tuning results

The tuned values of the model coefficients for three cores are given in Table 4. The matching results for the full core impedance, half core impedance, and accumulated breakthrough concentration are shown all three cores in Figs. 10–12. In Figs. 10(a), 11(a) and 12(a), green and blue dots correspond to impedance data measured across the full core and half core. Green dots in Figs. 10(b), 11(b) and 12(b) correspond to the accumulated breakthrough concentration. Continuous, dashed, and dash-dot curves correspond to the model predictions, based on fitting techniques A, B, and C, respectively.

Table 4
Tuning results from coreflooding data.

Technique	Core	Salinity (% KCl)	α	Λ	β	$\Delta\sigma_{cr}$	$\beta\Delta\sigma_{cr}$
A	1	0.4	0.0076	12.13	98,097	3.14E-06	0.308
		0	0.0057	40.72	87,859	1.65E-04	14.5
	2	0.4	0.0039	72.14	10,078	2.04E-05	0.206
		0	0.014	5.64	9672	3.36E-04	3.25
	3	0.4	0.0017	36.45	64	7.04E-04	0.045
		0	0.0016	68.85	22,698	4.50E-05	1.02
B	1	0.4	0.022	6.06	–	–	0.311
		0	0.0047	50	–	–	14.2
	2	0.4	0.036	9.64	–	–	0.225
		0	0.012	5.50	–	–	3.13
	3	0.4	0.0050	23.53	–	–	0.041
		0	0.0093	14.23	–	–	1.03
C	1	0.4	0.0021	52.05	254,717	1.57E-06	0.400
		0	0.0036	67.46	605,795	3.09E-05	18.7
	2	0.4	0.013	57.94	87,931	1.63E-06	0.143
		0	0.012	6.11	70,522	4.80E-05	3.38
	3	0.4	0.0074	1.72	13,527	6.93E-06	0.094
		0	0.0047	23.02	633,396	1.81E-06	1.14

The values of the coefficient of determination, R^2, are used to demonstrate the quality of fitting (Kvålseth, 1985):

$$R^2 = 1 - \sum (y^L - y^M)^2 / \sum (y^L - y_m)^2, \quad (18)$$

where y^L is the laboratory data, y^M is the fitted model value and y_m is the arithmetic mean of the collected laboratory data. Figs. 10–12 contain the coefficients of determination for overall impedance, R_{J1}^2, half core impedance, $R_{J\omega}^2$, and accumulated concentration, R_{Ca}^2.

During the high salinity injection cycles, i.e. 2% KCl and 1.2% KCl, permeability reduction for all three cores was negligible. Therefore, the model fitting exercise was not conducted for these salinities.

The fitting results for the DIW injection are good for all three cores, with R^2 values higher than 0.88, 0.86, and 0.87, for the J_1, J_ω and C_a data, respectively. A stronger deviation between the experimental data and model is noted for all three cores during the 0.4% injection. This is attributed to relatively small amount of damage and concentration of produced particles. The exception is in Core 3, where a large number of particles were produced, but the non-exponential shape of the accumulated breakthrough curve resulted in a poor fit.

The tuned values of the model parameters – drift delay factor α, filtration coefficient Λ, formation damage coefficient β, detached fines concentration $\Delta\sigma_{cr}$ – are of the same order of magnitude as those obtained from matching previous laboratory tests (Chequer et al., 2018; Russell et al., 2018; Yang et al., 2018). While of similar magnitude, the values of Λ and β obtained in this study are higher than those reported in literature. This is likely due to the low permeability of the cores used in this study.

5.3. Sensitivity study

The results from investigating the effects of fitting parameters to full core and half core impedances are presented in Fig. 13. Fitting parameter values from Core 2 DIW using fitting technique A were used as the base case, which is shown in orange. Fig. 13(a) reveals that as the drift delay factor, α, increases, the time required for both half core and full core impedances to reach stabilisation reduces. In fact, complete stabilisation of the impedance occurs at $t_D = \omega/\alpha$ and $t_D = 1/\alpha$ for the half and full core, respectively (Chequer et al., 2018). However, α does not affect the magnitude of the stabilised impedances as it does not alternate the particle trajectory.

Fig. 13(b) shows the effects of the dimensionless filtration coefficient, Λ, which is the inverse of the distance travelled by a suspended particle before it is captured. As Λ increases, the stabilisation time decreases and the magnitude of the stabilised impedance increases. The

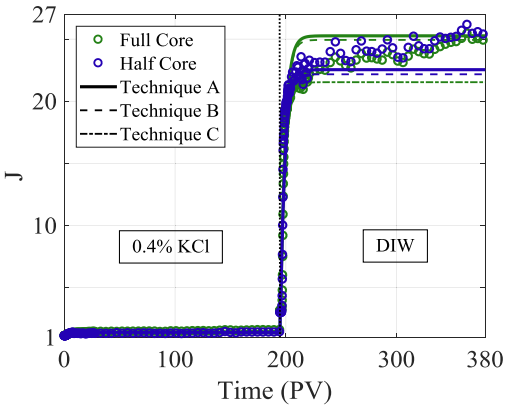

Technique	A	B	C
0.4%KCl	$R^2_{J1} = 0.78$	$R^2_{J1} = 0.9$	$R^2_{J1} = 0.93$
0.4%KCl	$R^2_{J\omega} = 0.33$	$R^2_{J\omega} = 0.79$	-
DIW	$R^2_{J1} = 0.88$	$R^2_{J1} = 0.89$	$R^2_{J1} = 0.89$
DIW	$R^2_{J\omega} = 0.88$	$R^2_{J\omega} = 0.86$	-

(a)

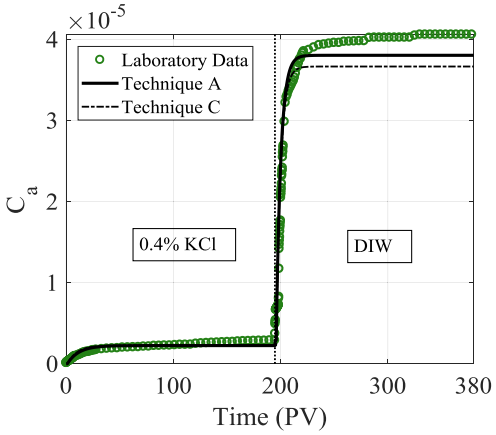

Technique	A	C
0.4%KCl	$R^2_{C_a} = 0.91$	$R^2_{C_a} = 0.87$
DIW	$R^2_{C_a} = 0.9$	$R^2_{C_a} = 0.89$

(b)

Fig. 10. Comparison between the fines migration models and experimental results for Core 1: (a) impedance across the full core, J_1, (green) and half core, J_ω, (blue); (b) accumulated breakthrough concentration, C_a.

shorter stabilisation time follows from the notion that particles are captured very quickly after detachment, and the higher impedance is a consequence of a smaller fraction of the detached particles reaching the core outlet. For low values of Λ, fewer particles are strained close to the core inlet. For large Λ, particles are likely to be captured closer to where they detach and produce a more uniform strained concentration profile. When the strained particle concentration is more uniform, the half core and full core impedances becomes closer, as demonstrated in Fig. 13(b). In the case of very high Λ, the two data sets would appear identical, and the three independent data sets (J_1^L, J_ω^L and C_a^L) would be reduced to two (J_1^L and C_a^L).

Fig. 13(c) illustrates the impact of the formation damage factor, $\beta\Delta\sigma_{cr}$, on the impedance. As $\beta\Delta\sigma_{cr}$ increases, the level of formation damage is higher, therefore the impedance increases. Another observation is that as $\beta\Delta\sigma_{cr}$ decreases, the difference between half core and full core impedance decreases. The effects of small $\beta\Delta\sigma_{cr}$ would be similar to large Λ, reducing the number of independent data sets by one.

In all of the sensitivity figures, a common trend is observed, wherein the half core impedance initially grows faster than the full core, then a transition occurs where the full core impedance exceeds the half core.

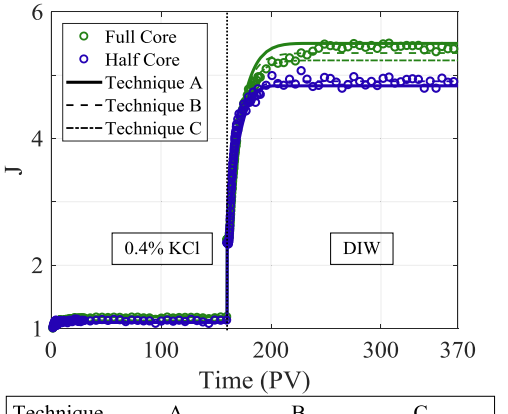

Technique	A	B	C
0.4%KCl	$R^2_{J1} = 0.66$	$R^2_{J1} = 0.66$	$R^2_{J1} = 0.69$
0.4%KCl	$R^2_{J\omega} = 0.39$	$R^2_{J\omega} = 0.39$	-
DIW	$R^2_{J1} = 0.98$	$R^2_{J1} = 0.98$	$R^2_{J1} = 0.98$
DIW	$R^2_{J\omega} = 0.95$	$R^2_{J\omega} = 0.96$	-

(a)

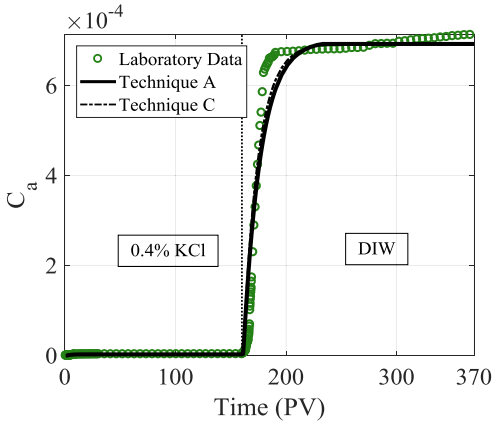

Technique	A	C
0.4%KCl	$R^2_{C_a} = 0.83$	$R^2_{C_a} = 0.47$
DIW	$R^2_{C_a} = 0.93$	$R^2_{C_a} = 0.91$

(b)

Fig. 11. Comparison between the fines migration models and experimental results for Core 2: (a) impedance across the full core, J_1, (green) and half core, J_ω, (blue); (b) accumulated breakthrough concentration, C_a.

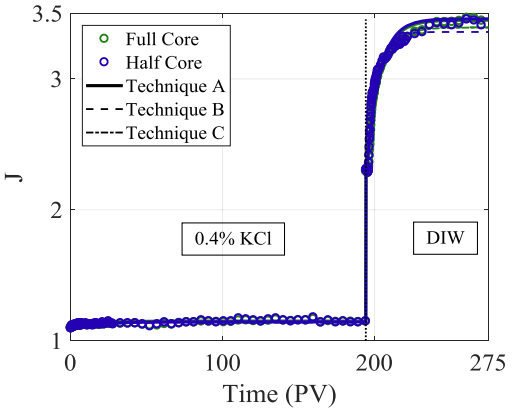

Technique	A	B	C
0.4%KCl	$R^2_{J1} = 0.65$	$R^2_{J1} = 0.64$	$R^2_{J1} = 0.55$
0.4%KCl	$R^2_{J\omega} = 0.39$	$R^2_{J\omega} = 0.49$	-
DIW	$R^2_{J1} = 0.96$	$R^2_{J1} = 0.97$	$R^2_{J1} = 0.95$
DIW	$R^2_{J\omega} = 0.94$	$R^2_{J\omega} = 0.96$	-

(a)

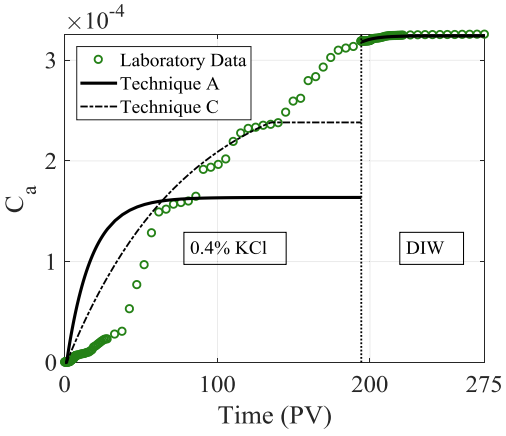

Technique	A	C
0.4%KCl	$R^2_{C_a} = 0.58$	$R^2_{C_a} = 0.91$
DIW	$R^2_{C_a} = 0.86$	$R^2_{C_a} = 0.87$

(b)

Fig. 12. Comparison between the fines migration models and experimental results for Core 3: (a) impedance across the full core, J_1, (green) and half core, J_ω, (blue); (b) accumulated breakthrough concentration, C_a.

Particle detachment, and hence straining, only occurs behind the injected salinity front, and thus during the early stages of injection, straining is more vigorous in the first half of the core. Despite this, the stabilised strained particle concentration will always monotonically increase with time across the core length. Compared to the full core impedance, the half core impedance only accounts for the incremental pressure increase for the first 2.7 cm damage in the core. Therefore the half core impedance will stabilise at a value less than or equal to the full core impedance.

6. Formation damage during fracturing

In this section, a mathematical model is derived to express the extent of formation damage caused by fines migration during fracture leak-off.

6.1. Assumptions

The main assumptions for the skin factor derivation are as following:

- Constant $\Delta\sigma_{cr}$ when upscaling from the core scale to the reservoir scale
- During the leak-off period, which is significantly shorter than the production period, a linear flow regime from the fracture into the formation is established
- The leak-off rate is constant throughout the fracturing period
- The hydraulic resistance inside the fracture is significantly lower than that for flow of leak-off fluid in the reservoir, i.e. pressure and rate along the fracture are uniformly distributed

6.2. Derivation of skin factor

Suppose there is a fractured vertical gas or oil well with well radius, r_w, located in the centre of a circular drainage area with radius, r_e. Due to fracturing fluid leak-off, there exists a damaged zone, with depth, B, where low-salinity induced fines migration has occurred. The total pressure drop from $r = 0$ to $r = r_e$ is the sum of the pressure drop within the damaged zone and undamaged reservoir:

$$\Delta p(t) = \int_0^{r_e} (-\nabla p)dl = \int_0^{B} (-\nabla p)dl + \int_B^{r_e} (-\nabla p)dl. \tag{19}$$

Assuming the leak-off period is short, and an infinite conductivity fracture is achieved, the fracturing fluid leak-off occurs under a formation linear regime in the damaged zone. This allows for the calculation of the pressure drop in the damaged zone using the modified Darcy's equation (6). Rearranging and substituting Eq. (6) into (19) gives:

$$\Delta p(t) = \frac{\mu\beta}{k_I}\int_0^{B} U\sigma_s(x,t)dx + \int_0^{r_e} (-\nabla p)_I dl. \tag{20}$$

The first integral in Eq. (20) expresses the pressure drop increase due to formation damage. The second integral is the initial pressure drop between the well and the drainage boundary, which can be found in terms of the initial productivity index (PI_I):

$$\int_0^{r_e} (-\nabla p)_I dl = \Delta p_I = \frac{q}{PI_I}. \tag{21}$$

In the particular case of a short fracture with length significantly smaller than the drainage radius, by the derivation of Barenblatt et al. (1989), the pressure drop in an undamaged reservoir with a fracture of half length, x_f, is equivalent to the pressure drop in a reservoir with wellbore radius, $r_w = x_f/2$. Let the pressure drop from the centre of the well ($r = 0$) to the wellbore ($r = x_f/2$) be negligible, then by Eq. (20) we have:

$$\Delta p(t) = \frac{\mu\beta}{k_I}\int_0^{B} U\sigma_s(x,t)dx + \frac{q\mu}{2\pi h k_I}\int_{x_f/2}^{r_e} \frac{1}{r}dr. \tag{22}$$

With the assumption of constant fracturing fluid leak-off rate and evenly distributed flow across the fracture face, the fracturing fluid velocity in the damaged zone is:

$$U = \frac{q}{4x_f h}. \tag{23}$$

Substituting Eq. (23) into Eq. (22) and integrating the resulting equation, the total pressure drop across the reservoir is:

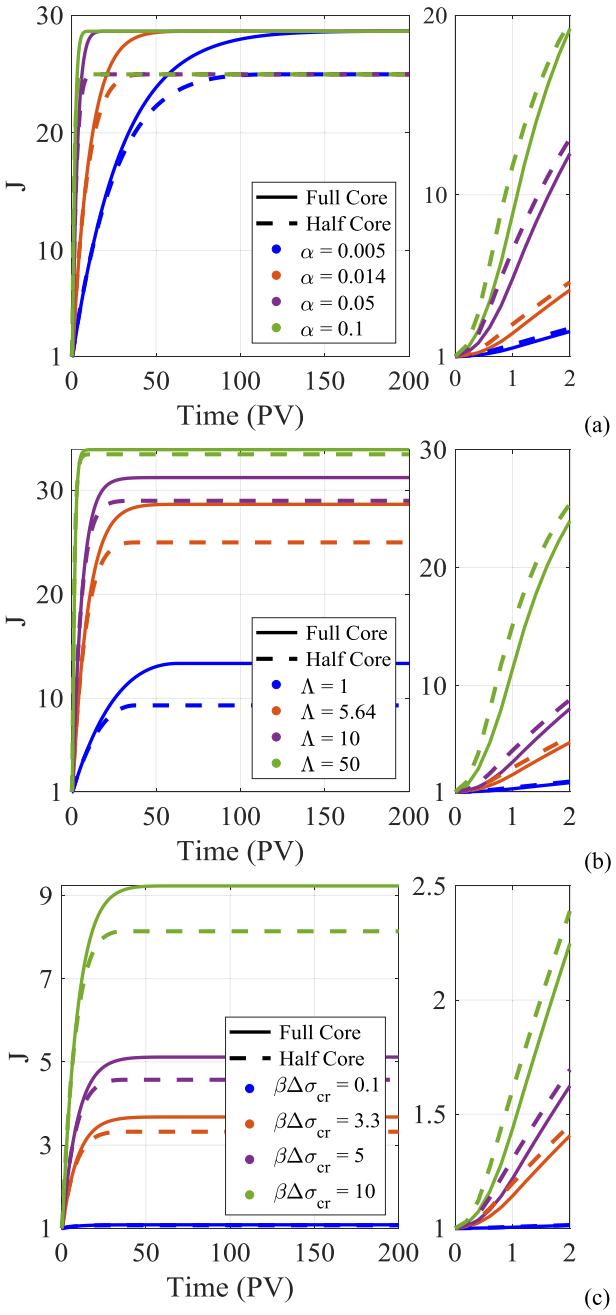

Fig. 13. Fitting parameter sensitivity analysis for the delayed particle detachment model using Core 2 DIW as base case (orange): (a) drift delay factor, α; (b) dimensionless filtration coefficient, Λ; (c) formation damage factor, $\beta\Delta\sigma_{cr}$.

$$\Delta p(t) = \frac{q\mu}{2\pi k_1 h}\left[\ln\left(\frac{r_e}{r_w}\right) + \ln\left(\frac{2r_w}{x_f}\right) + \frac{\beta\pi}{2x_f}\int_0^B \sigma_s(x,\, t)dx\right]. \tag{24}$$

The steady state inflow equation accounting for skin given by Dake (1998) is:

$$\Delta p(t) = \frac{q\mu}{2\pi k_1 h}\left[\ln\left(\frac{r_e}{r_w}\right) + s_T\right]. \tag{25}$$

Comparing Eq. (24) to Eq. (25), the total skin factor, s_T, due to low-salinity induced fines migration in a fractured well has two components:

$$s_F = \ln\left(\frac{2r_w}{x_f}\right), \tag{26}$$

$$s_{FM} = \frac{\pi\beta}{2x_f}\int_0^B \sigma_s(x,\, t)dx, \tag{27}$$

where s_F and s_{FM} correspond to the skin due to the fracture and fines migration, respectively.

To evaluate the strained particle concentration integral in Eq. (27), we introduce field scale dimensionless parameters:

$$t_{wD} = \frac{Ut}{\phi B},\quad x_{wD} = \frac{x}{B},\quad \Lambda_w = \lambda B. \tag{28}$$

Substituting the field scale dimensionless parameters in (28) and dimensionless form of strained particle concentration in (10) into Eq. (27) gives:

$$s_{FM} = \frac{\pi\phi\beta\Delta\sigma_{cr}}{2x_f}B\int_0^1 S_s(x_{wD},\, t_{wD})dx_{wD}. \tag{29}$$

With the assumption of constant permeability in the damaged zone, the formula for skin factor (29) reduces to the classical Cinco-Ley & Samaniego skin definition (Cinco-Ley and Samaniego, 1977).

By definition, the injected solution will reach the damaged depth, B, after the injection of one pore volume. From this, we can write B, as the ratio of the injected volume to the pore cross sectional area of the fracture:

$$B = \frac{V(1-E)}{4\phi x_f h_f}, \tag{30}$$

where V is the total fracturing fluid volume pumped into the reservoir, E is the fluid efficiency defined as the ratio of the injected volume which remains in the fracture, and h_f is the fracture height.

The final expression for the skin factor can be found by rearranging and substituting the impedance expression in Eq. (16) into Eq. (29), and then evaluating Eq. (29) at $t_{wD} = 1$:

$$s_{FM} = \frac{\pi V(1-E)}{8x_f^2 h_f}[J_1(1) - 1]. \tag{31}$$

Eqs. (11-14) for fines migration contain characteristic length $1/\Lambda$, so the solution (16) is not self-similar, i.e. it cannot be expressed via a dimensionless group containing x_D and t_D. For example, the 1D solution for displacement of oil by water is self-similar depending on the dimensionless group $\phi x/Ut$ (the Buckley-Leverett solution, see Dake (1998) and Barenblatt et al. (1989)). In this case, the solution at point $(x_D,\, t_D)$ is the same as in points $(ax_D,\, at_D)$ for any $a > 0$. It allows for a direct recalculation of pressure drop across core with length L, to another with length L_1. The solution for S_s, shown in Table 3, is non-self-similar, therefore a direct pressure drop recalculation for another core length is impossible. Hence, the presented recalculation method consists of first determining the model constants from the laboratory measurements and then recalculating S_s for the large scale using the exact solution shown in Table 3. The dimensionless filtration coefficient at the reservoir scale is:

$$\Lambda_w = \lambda\frac{B}{L}. \tag{32}$$

6.3. Skin factor estimation

From the explicit expression (31), it can be seen that the skin factor can be evaluated with known fracture and formation properties (i.e. h_f, x_f, V, and E) as well as the fines migration parameters (i.e. α, Λ, and $\beta\Delta\sigma_{cr}$) to calculate the impedance, J_1. The fines migration parameters and rock porosity are determined from the laboratory testing, and the total injected volume, V, is known from fracturing design. The remaining uncertain parameters are the fracture half length, x_f, fracture height, h_f, and fluid efficiency, E. To rigorously evaluate the skin factor, we used a probabilistic approach to determine the likelihood of the skin factor being significant. Each of the three uncertain parameters was

Table 5
Fracture parameter sensitivity range.

	Fracture Half Length (ft)	Fracture Height (ft)	Fluid Efficiency
Min	50	30	0.3
Max	300	100	0.6

Table 6
Probabilistic skin evaluated from the tuning results.

Fitting Technique	Core	Salinity (% KCl)	Skin > 0.1
A	1	0.4	0.004
		0	0.88
	2	0.4	0.002
		0	0.45
	3	0.4	0
		0	0.071
B	1	0.4	0.004
		0	0.88
	2	0.4	0.0028
		0	0.44
	3	0.4	0
		0	0.071
C	1	0.4	0.008
		0	0.92
	2	0.4	0
		0	0.47
	3	0.4	0
		0	0.087

assigned a uniform probabilistic distribution with upper and lower bounds (given in Table 5) determined from analogue studies for x_f and h_f, and from typical values reported in the literature for E (Britt et al., 1994). Monte Carlo simulation was used in conjunction with Eq. (31) to determine the probabilistic distribution for the skin factor.

For this study, a skin factor of 0.1 was chosen as a threshold, above which preventative measures, such as increasing the salt concentration of the fracturing fluid, should be taken. The probability of the skin exceeding 0.1 for 0.4% KCl injection (the approximate salinity for the proposed fracturing fluid) is less than 0.008 for all three cores evaluated by the three fitting techniques, as shown in Table 6. While the minimum probability of the skin factor exceeding 0.1 in DIW injection by the three fitting techniques is 0.88, 0.44, and 0.071 for Core 1, 2 and 3, respectively.

The calculated cumulative distribution functions (CDFs) for the skin factor, presented in Fig. 14, allow comparing the results for the different fitting techniques. Skin factor estimations from techniques A and B are closely matching, yet significant deviations are observed in 0.4% KCl injections for all three cores for technique C. However, technique C is not consistently overestimating nor underestimating compared to the other two techniques. For DIW injections, Core 2 and 3 have consistent skin factor estimations across the three fitting techniques, while a slight overestimation occurred in Core 1 for fitting technique C.

7. Discussion

7.1. Neglecting additional formation damage mechanisms

Besides fines migration, there are many other formation damage mechanisms prevalent in petroleum reservoirs. The methodology presented in this work has, however, assumed that all permeability decline measured in the laboratory study was due to low salinity water induced fines migration. The combination of effluent suspended particle concentration and the before/after SEM study provides direct evidence of fines migration. The occurrence of deep bed filtration due to injected particles is highly unlikely due to strict filtration (up to 0.2 μm) of all injected solutions. While clay swelling would be a likely candidate for a low-salinity dependent formation damage mechanism, the absence of any swelling clays in the XRD study for all three cores allows neglecting this mechanism. Thus, while fines migration has been observed directly, all other formation damage mechanisms can be neglected and thus the assumption used in the methodology is valid.

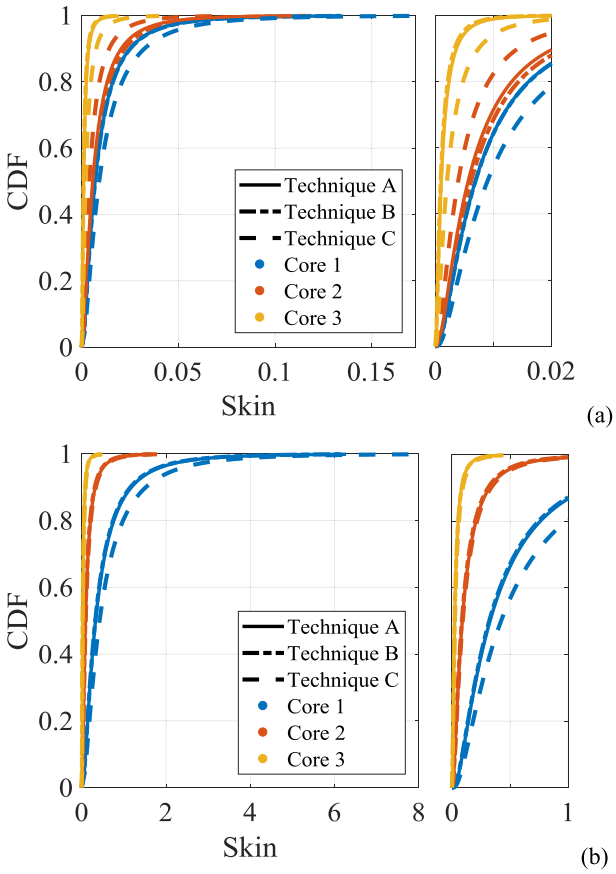

Fig. 14. Probabilistic evaluation of skin due to fines migration: (a) 0.4% KCl injection; (b) DIW injection.

7.2. Fines migration for low permeable, high-clay-content cores

Permeability decline is associated with fines production at the core outlet, as shown by the laboratory results shown in Fig. 8. Significant fines production occurred during the DIW injection cycle for Core 1 and 2 with a moderate amount of fines produced during the 1.2% KCl injection. However, for Core 3 most of the produced fines were collected during the injection of 2% KCl and 0.4% KCl.

It is possible that this difference is a result of the mineral dickite being present in Core 3 rather than the disordered kaolinite present in Cores 1 and 2. While both minerals have similar compositions, they vary in crystal structure (Wilson, 2013), which could give rise to a difference in the electrostatic force holding the particles to the surface. The origin of the differences between the rocks cannot be accurately determined and could be a result of varying sedimentation and diagenetic histories of the rocks.

Based on the XRD results provided in Table 2, Core 1 had the lowest clay content, while Core 3 had the highest clay content. Yet, the permeability decline in Core 1 is much more significant than that observed in Core 3. This demonstrates that the total clay content is not a good predictor for permeability reduction due to low salinity coreflooding.

It has been suggested that low-permeability rocks should be more susceptible to fines migration due to smaller pore throats, which increase the probability of straining (Civan, 2015; Tiab and Donaldson, 2004). Yet despite the low permeability and moderate clay content of

the three cores in this study, all cores demonstrated only a moderate permeability decline in response to low-salinity water. This is in contrast with studies performed on other sandstone cores with higher permeability and lower clay contents (Khilar et al., 1983; Mungan, 1965; Chequer et al., 2018), which exhibited a much greater extent of permeability decline when injected with DIW. Furthermore, Russell et al. (2017) investigated the effects of clay contents (primarily kaolinite) on permeability through a series of laboratory studies on artificial cores. It was found that permeability reduction was negligible for the 0% kaolinite core as injection fluid salinity decreased. While small damage was observed below a kaolinite content threshold, above this threshold, no clear trend between kaolinite content and total permeability decline was found. This suggests that additional factors other than permeability and clay content are required to predict the extent of fines migration.

7.3. Formation damage due to different migrating minerals

Different clay particles (kaolinite, illite, and chlorite) and silica can have different impact on permeability damage, i.e. filtration and formation damage coefficients are different for different minerals. While measurements of mineralogy have been made in this study, a more focussed investigation would be required to make clear conclusions on the impact of individual minerals. A systematic study could be performed using artificial cores with engineered rock compositions. A comparison between formation damage in cores with single and multiple migrating minerals can lead to aggregation formulae for permeability damage in multi-mineral rocks. Regarding natural reservoir cores, measurements of individual mineral concentrations initially in the rock and in the effluent during corefloods can result in critical retention functions and filtration coefficients for all involved minerals.

7.4. Linear flow in damaged zone

The mathematical derivation of skin in a fractured well due to fines migration was presented based on the assumption of linear flow from the fracture into the formation. Flow patterns in hydraulically fractured wells begin with a very short period of fracture linear flow (linear flow within the fracture), then transition to either formation linear flow (linear flow from the fracture into the formation) for infinite-conductivity fractures, or bilinear flow (both fracture linear and formation linear flow) for finite-conductivity fractures (Lee et al., 2003). The pressure gradient along the fracture is insignificant compared to the pressure gradient from the fracture to the formation, especially in tight formations. In addition, the leak-off period is short, therefore formation linear flow is most likely to occur, which supports the assumption of linear flow from the fracture to the formation.

7.5. Comparison of fitting techniques

Laboratory tests designed to study formation damage due to suspended particles in the injected solution have combined measurements of breakthrough fines concentrations with three-point-pressure measurements across the core (Bedrikovetsky et al., 2001; Vaz et al., 2016, 2017), while previous studies of fines migration have measured breakthrough curves and pressure drop across the overall core only (Russell et al., 2018; Yang et al., 2018). In the current work, 3-point pressure measurements have been performed. The tuning of laboratory data has been done with different techniques, each utilizing different combinations of laboratory data. As discussed in Section 5, the quality of fitting was similar for the different techniques. The tuned laboratory parameters, and consequently the distributions for skin factor, are similar for all three models. Hence it appears as though the choice of which data to measure during laboratory tests comes down to convenience.

The measurement of the pressure drop across the core is typically much cheaper, quicker, and easier to perform remotely compared to measuring the breakthrough suspended concentration. The measurement of pressure drop is typically done through automatic data acquisition software. In order to obtain accumulated breakthrough concentration, manual processing of the effluent samples collected by the sampling collector using a particle counter is required. Thus fitting technique B is more convenient as it does not require the breakthrough suspended particle concentration.

As discussed in Section 4, the 1D solution for linear flow, shown in Table 3, depends on four independent model parameters α, Λ, β, and $\Delta\sigma_{cr}$. Full characterisation of the fines-migration system includes determination of those four parameters. However, the analytical expression for impedance contains only the product $\beta\Delta\sigma_{cr}$ (so-called formation damage factor). Therefore, the sole use of impedance data is only appropriate where the formation damage factor and total detached particle concentration do not need to be identified separately. The model used in the current work is one such case, as the flow field in the up-scaled model is linear, and the total detached concentration was assumed to be the same for the core and reservoir. In the context of this proposed model, neglecting the breakthrough suspended particle concentration still provides reliable estimates of skin during fracture fluid leak-off. For more complex flow fields, or in situations where the extent of particle detachment changes during upscaling, the critical retention function would need to be constructed. Doing this would require the detached concentration, $\Delta\sigma_{cr}$, from multiple injection stages and thus knowing only the product $\beta\Delta\sigma_{cr}$ would be insufficient.

7.6. Upscaling fitting parameters from core to field

A mathematical property of the solution for fines migration is that it is not self-similar (Chequer et al., 2018), meaning that the solution cannot be transferred from one scale to another simply by rescaling the linear coordinate. As a consequence, there is no direct recalculation of permeability damage in the reservoir from the laboratory measurements. As such, the procedure of the coreflood-based formation damage prediction includes matching the coreflooding data by the mathematical model, tuning the model coefficients, and predicting the incremental pressure drop across the leak-off zone using the up-scaled model.

It is interesting to note that even in the cases where significant damage was observed in the laboratory test, the calculated skin probability distribution still predicts a high likelihood that formation damage due to fines migration will be insignificant. This follows from the fact that the laboratory tests were run until the entire core permeability had stabilised, whereas in the up-scaled model, the leak-off volume from the fracture into the formation is fixed, and most of the damaged zone ($x \leq B$) will not reach the stabilised permeability observed in the laboratory, with permeability at B equal to that of the undamaged reservoir.

The varying degrees of stabilisation and the non-uniform distribution of permeability even at stabilisation emphasize the importance of rigorous mathematical modelling when upscaling laboratory results to the field-scale. Simply using the permeability damage ratio to predict skin during leak-off would drastically overestimate the impact of fines migration on well productivity.

The following steps should be taken to predict the skin factor due to leak-off fluid for a hydraulically fractured well using the laboratory coreflood data. From the coreflood experiment, we can obtain the dimensionless fitting parameter values, α, β, $\Delta\sigma_{cr}$, and Λ. Parameters α, β, and $\Delta\sigma_{cr}$ are assumed to be independent of scale. By using the dimensionless variables (28) and recalculating the dimensionless filtration coefficient from Eq. (32), we can use the same equations to calculate impedance that were used to tune the laboratory data, given in Table 4. Incorporating the rock and fracture properties with the evaluated impedance, the skin factor can be predicted using Eq. (31).

7.7. Fines migration in oil and gas recovery

Fines migration occurs during gas production from coal beds, yielding significant permeability decline and environmental problems due to coal-fines production (Bai et al., 2015; Guo et al., 2015, 2016; Huang et al., 2017, 2018). The difference between the fines migration due to fracture-fluid leak-off, discussed in the current paper, and fines during the production of coal-bed methane (CBM), is that the main fines detaching factor in CBMs is the reservoir stress, which can significantly increase during dewatering and gas desorption.

Other fines-detaching factors are capillary force exerting from interface menisci on the attached clays, which occurs during waterflooding and numerous EOR processes (Farajzadeh et al., 2008, 2009, 2016; Feng et al., 2016; Huang et al., 2018; Othman et al., 2018; Zeinijahromi et al., 2016), and high temperature during steam injection (Rosenbrand et al., 2014; Schembre and Kovscek, 2005).

The present work discusses single-phase flow. However, the conditions close to oil and gas production would require the presence of residual phase (Sarkar and Sharma, 1990). In this case, creating residual gas or oil in the cores requires the tests described in Section 2 to start with primary drainage by gas or oil, then followed by water injection. Accounting for turbulent flows occurring near the wellbores of gas wells, the flow velocity in the tests must be enhanced by 1–2 orders of magnitude. The model (11–14) assumes incompressible flow; gas compressibility can be accounted for by considering pressure-dependent density. Another assumption is dispersion-free fines migration; laboratory tests in short cores require including diffusion term in right hand side of mass balance equation (Eq. (11)).

Fines mobilisation and migration with consequent permeability damage during drilling fluid invasion into the formation is similar to that during fracturing fluid leak-off; the mathematical models are almost the same (Li and Prigiobbe, 2018; Mikhailov et al., 2018).

Fines migration during oil and gas production can be decreased by injection of nanofluids (Assef et al., 2014; Bera and Belhaj, 2016; Habibi et al., 2012; Yuan and Moghanloo, 2018; Yuan et al., 2015, 2016). Nanoparticles can attract clay fines and silica grains simultaneously, yielding sticking of clays to rock surface and preventing clay-fine mobilisation (Yuan and Moghanloo, 2018; Yuan et al., 2016).

The laboratory-based analytical model (11–14) allows for field-scale predictions by using a quasi 3D stream-line model (Bedrikovetsky, 2013). This model assumes that stream lines are immobile during fines migration. For close flow patterns, a mobility alteration up to 20 times still yields high accuracy of stream-line modelling.

8. Conclusions

The laboratory study and analytical modelling of fines migration caused by fracturing fluid leak-off allows making the following conclusions:

1. SEM imaging of inlet core cross section along with SEM-EDX analysis of produced solids and the close matching of the laboratory data by the analytical model composed a direct evidence of fines migration as a formation damage mechanism. The absence of smectite group clays from the XRD study enabled us to exclude formation damage due to clay swelling.
2. The laboratory study showed that all three cores are susceptible to fines migration during low salinity water injection. Permeability reduced by 36.5%, 17.6% and 14.4% for 0.4% KCl injection from initial permeability, and 95.7%, 76.0% and 58.3% for DIW injection from initial permeability for Cores 1, 2 and 3, respectively.
3. Despite the observed permeability reduction and moderate clay content of the three cores, skin due to low salinity induced fines migration is small. The probability of skin exceeding 0.1 is less than 0.008 for 0.4% KCl injection. For DIW injection, the probability of skin exceeding 0.1 for Cores 1, 2 and 3 are 0.88, 0.44, and 0.071, respectively.
4. Tuning the model for fines migration with only pressure drop data only allows determining the product $\beta\Delta\sigma_{cr}$, while the addition of outlet concentration data allows the two variables to be determined separately. Therefore, while sufficient in some circumstances, multiple pressure drop measurements across the core cannot substitute measurements of fines breakthrough concentration.
5. Fitting parameter sensitivity analysis shows that for large Λ values, the half core impedance approaches the full core impedance. As large Λ value means high probability of fines capture, the strained fines concentration reaches equilibrium closer to the core inlet. Therefore the same impedance data is observed at half and full core, which results in the reduction of the number of independent data sets.

Acknowledgements

The authors would like to thank Dr. Abbas Zeinijahromi for his strong support during our laboratory studies. Many thanks are due to Emily Walker and Antreas Florentzou (University of Adelaide) for contribution to the laboratory work. Tony Hall (University of Adelaide) is gratefully acknowledged for contribution to the XRD analysis. The authors are grateful to Dr. Jonathan Rudd (Santos Ltd) for useful discussions and support of this study. Many thanks are due to David H. Levin (Murphy, NC, USA) who provided professional English-language editing of this article.

Nomenclature

A	Cross-sectional flow area, m^2
B	Damage depth, m
c	Suspended particle concentration
C	Dimensionless suspended particle concentration
C_a	Dimensionless accumulated breakthrough particle concentration
E	Fluid efficiency
F_d	Drag force, N
F_e	Electrostatic force, N
h	Formation height, m
h_f	Fracture height, m
J_ω	Impedance
k	Permeability, m^2
l	Lever arm ratio
l_d	Drag force lever arm, m
l_n	Electrostatic force lever arm, m
L	Core length, m
p	Fluid pressure, Pa
PI	Productivity index
q	Volumetric flow rate, m^3s^{-1}
r_e	Reservoir radius, m
$< r_p >$	Mean pore radius, m
$< r_s >$	Mean particle radius, m
r_w	Wellbore radius, m
s	Total skin
s_F	Skin due to hydraulic fracture
s_{FM}	Skin due to fines migration
S_a	Dimensionless attached particle concentration
S_s	Dimensionless strained particle concentration
t	Time, s
t_D	Dimensionless time
U	Flow velocity, ms^{-1}
V	Total injected fracturing fluid volume, m^3
x	Linear coordinate, m
x_D	Dimensionless linear coordinate
x_f	Fracture half length, m

Greek letters

α	Drift delay factor
β	Formation damage coefficient
γ	Fluid salinity
λ	Filtration coefficient, m^{-1}
Λ	Dimensionless filtration coefficient
μ	Fluid viscosity, $kg.m^{-1}.s^{-1}$
σ_a	Attached particle concentration
$\sigma_{cr}(\gamma,U)$	Critical retention function
$\Delta\sigma_{cr}$	Total detached particle concentration due to salinity difference
σ_s	Strained particle concentration
ϕ	Porosity
ω	Dimensionless location along the core

Subscript

D	Dimensionless
I	Initial condition
J	Injected condition
w	Field scale

Superscript

L	Laboratory data
M	Fitted model value

References

Akhmetgareev, V., Khisamov, R., 2015. 40 Years of low-salinity waterflooding in Pervomaiskoye field, Russia: incremental oil. In: SPE Paper 174182 Presented at the SPE European Formation Damage Conference and Exhibition. Society of Petroleum Engineers, Budapest, Hungary 3-5 June 2015.

Assef, Y., Arab, D., Pourafshary, P., 2014. Application of nanofluid to control fines migration to improve the performance of low salinity water flooding and alkaline flooding. J. Petrol. Sci. Eng. 124 (-), 331–340.

Badalyan, A., Carageorgos, T., Bedrikovetsky, P., You, Z., Zeinijahromi, A., Aji, K., 2012. Critical analysis of uncertainties during particle filtration. Rev. Sci. Instrum. 83 (9), 095106.

Bai, T., Chen, Z., Aminossadati, S.M., Pan, Z., Liu, J., Li, L., 2015. Characterization of coal fines generation: a micro-scale investigation. J. Nat. Gas Sci. Eng. 27 (-), 862–875.

Barenblatt, G.I., Entov, V.M., Ryzhik, V.M., 1989. Theory of Fluid Flows through Natural Rocks. Springer, Amsterdam, The Netherlands.

Bedrikovetsky, P., 2013. Mathematical Theory of Oil and Gas Recovery (With Applications to Ex-USSR Oil and Gas Fields). Springer Science & Business Media, London.

Bedrikovetsky, P., Marchesin, D., Shecaira, F., Souza, A., Milanez, P., Rezende, E., 2001. Characterisation of deep bed filtration system from laboratory pressure drop measurements. J. Petrol. Sci. Eng. 32 (-), 167–177.

Bedrikovetsky, P., Siqueira, F.D., Furtado, C.A., Souza, A.L.S., 2010. Modified particle detachment model for colloidal transport in porous media. Transport Porous Media 86 (2), 353–383.

Bera, A., Belhaj, H., 2016. Application of nanotechnology by means of nanoparticles and nanodispersions in oil recovery-A comprehensive review. J. Nat. Gas Sci. Eng. 34 (-), 1284–1309.

Bradford, S.A., Torkzaban, S., Shapiro, A., 2013. A theoretical analysis of colloid attachment and straining in chemically heterogeneous porous media. Langmuir 29 (23), 6944–6952.

Britt, L., Hager, C., Thompson, J., 1994. Hydraulic fracturing in a naturally fractured reservoir. In: SPE Paper 28717 Presented at the International Petroleum Conference and Exhibition of Mexico. Society of Petroleum Engineers, Veracruz, Mexico 10-13 October 1994.

Byrne, M.T., Waggoner, S.M., 2009. Fines migration in a high temperature gas reservoir-laboratory simulation and implications for completion design. In: SPE Paper 121897 Presented at the 8th European Formation Damage Conference. Society of Petroleum Engineers, Scheveningen, The Netherlands 27-29 May 2009.

Chequer, L., Vaz, A., Bedrikovetsky, P., 2018. Injectivity decline during low-salinity waterflooding due to fines migration. J. Petrol. Sci. Eng. 165 (-), 1054–1072.

Cinco-Ley, H., Samaniego, F., 1977. Effect of wellbore storage and damage on the transient pressure behaviour of vertically fractured wells. In: SPE Paper 6752 Presented at the SPE Annual Fall Technical Conference and Exhibition. Society of Petroleum Engineers, Denver, Colorado 9-12 Oct 1977.

Civan, F., 2015. Reservoir Formation Damage, 3rd. Gulf Professional Publishing, , Huston, TX.

Dake, L.P., 1998. Fundamentals of Reservoir Engineering, 17th. Elsevier, Amsterdam.

Derjaguin, B., Landau, L., 1941. Theory of the stability of strongly charged lyophobic sols and of the adhesion of strongly charged particles in solution of electrolytes. Acta Physicochim: USSR 14 (-), 633–662.

Elimelech, M., Gregory, J., Jia, X., 2013. Particle Deposition and Aggregation: Measurement, Modelling and Simulation. Butterworth-Heinemann.

Farajzadeh, R., Bedrikovetsky, P., Lotfollahi, M., Lake, L., 2016. Simultaneous sorption and mechanical entrapment during polymer flow through porous media. Water Resour. Res. 52 (3), 2279–2298.

Farajzadeh, R., Krastev, R., Zitha, P.L., 2008. Foam film permeability: theory and experiment. Adv. Colloid Interface Sci. 137 (1), 27–44.

Farajzadeh, R., Zitha, P.L., Bruining, J., 2009. Enhanced mass transfer of CO2 into water: experiment and modeling. Ind. Eng. Chem. Res. 48 (13), 6423–6431.

Feng, Q., Chen, H., Wang, X., Wang, S., Wang, Z., Yang, Y., Bing, S., 2016. Well control optimization considering formation damage caused by suspended particles in injected water. J. Nat. Gas Sci. Eng. 35 (-), 21–32.

Guo, Z., Hussain, F., Cinar, Y., 2015. Permeability variation associated with fines production from anthracite coal during water injection. Int. J. Coal Geol. 147 (-), 46–57.

Guo, Z., Hussain, F., Cinar, Y., 2016. Physical and analytical modelling of permeability damage in bituminous coal caused by fines migration during water production. J. Nat. Gas Sci. Eng. 35 (-), 331–346.

Habibi, A., Ahmadi, M., Pourafshary, P., Al-Wahaibi, Y., 2012. Reduction of fines migration by nanofluids injection: an experimental study. SPE J. 18 (02), 309–318.

Huang, F., Kang, Y., You, L., Li, X., You, Z., 2018. Massive fines detachment induced by moving gas-water interfaces during early stage two-phase flow in coalbed methane reservoirs. Fuel 222, 193–206.

Huang, F., Kang, Y., You, Z., You, L., Xu, C., 2017. Critical conditions for massive fines detachment induced by single-phase flow in coalbed methane reservoirs: modeling and experiments. Energy Fuel. 31 (7), 6782–6793.

Khilar, K.C., Fogler, H.S., 1998. Migrations of Fines in Porous Media. Springer Science & Business Media.

Khilar, K.C., Fogler, H.S., Ahluwalia, J.S., 1983. Sandstone water sensitivity Existence of a critical rate of salinity decrease for particle capture. Chem. Eng. Sci. 38 (5), 789–800.

Kvålseth, T.O., 1985. Cautionary note about R2. Am. Statistician 39 (4), 279–285.

Lagasca, J.R.P., Kovscek, A.R., 2014. Fines migration and compaction in diatomaceous rocks. J. Petrol. Sci. Eng. 122 (-), 108–118.

Lake, L., 1989. Enhanced Oil Recovery. Prentice Hall, Upper Saddle River, New Jersy.

Lee, J., Rollins, J.B., Spivey, J.P., 2003. Pressure Transient Testing. Society of Petroleum Engineers, Richardson, TX.

Li, Q., Prigiobbe, V., 2018. Numerical simulations of the migration of fine particles through porous media. Transport Porous Media 122 (3), 745–759.

Mikhailov, D., Zhvick, V., Ryzhikov, N., Shako, V., 2018. Modeling of rock permeability damage and repairing dynamics due to invasion and removal of particulate from drilling fluids. Transport Porous Media 121 (1), 37–67.

Morrow, N., Buckley, J., 2011. Improved oil recovery by low-salinity waterflooding. J. Petrol. Technol. 63 (05), 106–112.

Mungan, N., 1965. Permeability reduction through changes in pH and salinity. J. Petrol. Technol. 17 (12), 1449–1453.

Oliveira, M.A., Vaz, A.S.L., Siqueira, F.D., Yang, Y., You, Z., Bedrikovetsky, P., 2014. Slow migration of mobilised fines during flow in reservoir rocks: laboratory study. J. Petrol. Sci. Eng. 122 (-), 534–541.

Othman, F., Yu, M., Kamali, F., Hussain, F., 2018. Fines migration during supercritical CO 2 injection in sandstone. J. Nat. Gas Sci. Eng. 56 (-), 344–357.

Qiao, C., Han, J., Huang, T.T., 2016. Compositional modeling of nanoparticle-reduced-fine-migration. J. Nat. Gas Sci. Eng. 35 (-), 1–10.

Rosenbrand, E., Haugwitz, C., Jacobsen, P.S.M., Kjøller, C., Fabricius, I.L., 2014. The effect of hot water injection on sandstone permeability. Geothermics 50 (-), 155–166.

Russell, T., Chequer, L., Borazjani, S., You, Z., Zeinijahromi, A., Bedrikovetsky, P., 2018. Formation damage by fines migration. In: Formation Damage during Improved Oil Recovery. Springer, Singapore.

Russell, T., Pham, D., Neishaboor, M.T., Badalyan, A., Behr, A., Genolet, L., Kowollik, P., Zeinijahromi, A., Bedrikovetsky, P., 2017. Effects of kaolinite in rocks on fines migration. J. Nat. Gas Sci. Eng. 45 (-), 243–255.

Sarkar, A.K., Sharma, M.M., 1990. Fines migration in two-phase flow. J. Petrol. Technol. 42 (05), 646–652.

Schembre, J., Kovscek, A., 2005. Mechanism of formation damage at elevated temperature. J. Energy Resour. Technol. 127 (3), 171–180.

Song, W., Kovscek, A.R., 2016. Direct visualization of pore-scale fines migration and formation damage during low-salinity waterflooding. J. Nat. Gas Sci. Eng. 34 (-), 1276–1283.

Tiab, D., Donaldson, E., 2004. Petrophysics, 2nd. Gulf Professional Publishing.

van Oort, E., Van Velzen, J., Leerlooijer, K., 1993. Impairment by suspended solids invasion: testing and prediction. SPE Prod. Facil. 8 (03), 178–184.

Vaz, A., Bedrikovetsky, P., Fernandes, P.D., Badalyan, A., Carageorgos, T., 2017. Determining model parameters for non-linear deep-bed filtration using laboratory pressure measurements. J. Petrol. Sci. Eng. 151 (-), 421–433.

Vaz, A., Maffra, D., Carageorgos, T., Bedrikovetsky, P., 2016. Characterisation of formation damage during reactive flows in porous media. J. Nat. Gas Sci. Eng. 34 (-), 1422–1433.

Verwey, E.J.W., Overbeek, J.T.G., 1948. Theory of the Stability of Lyophobic Colloids. Elsevier Publishing, New York.

Wilson, M.J., 2013. Rock-forming Minerals, 2nd. Geological Society, London.

Yang, Y., Siqueira, F.D., Vaz, A., Badalyan, A., You, Z., Zeinijahromi, A., Carageorgos, T., Bedrikovetsky, P., 2018. Fines Migration in Aquifers and Oilfields: Laboratory and Mathematical Modelling. *Flow and Transport in Subsurface Environment*. Springer, Singapore.

Yang, Y., Siqueira, F.D., Vaz, A.S., You, Z., Bedrikovetsky, P., 2016. Slow migration of detached fine particles over rock surface in porous media. J. Nat. Gas Sci. Eng. 34 (-), 1159–1173.

Yuan, B., Moghanloo, R.G., 2018. Nanofluid pre-treatment, an effective strategy to

improve the performance of low-salinity waterflooding. J. Petrol. Sci. Eng. 165 (-), 978–991.
Yuan, B., Moghanloo, R.G., Zheng, D., 2016. Analytical evaluation of nanoparticle application to mitigate fines migration in porous media. SPE J. 21 (06), 2317–2332.
Yuan, B., Su, Y., Moghanloo, R.G., Rui, Z., Wang, W., Shang, Y., 2015. A new analytical multi-linear solution for gas flow toward fractured horizontal wells with different fracture intensity. J. Nat. Gas Sci. Eng. 23 (-), 227–238.
Zeinijahromi, A., Farajzadeh, R., Bruining, J.H., Bedrikovetsky, P., 2016. Effect of fines migration on oil–water relative permeability during two-phase flow in porous media. Fuel 176, 222–236.

6. 3D effects in two-phase steady-state tests

Yang, S., Hemmati, N., Russell, T., Zeinijahromi, A., Borazjani, S., Behr, A., Genolet, L. and Bedrikovetsky, P.

Journal of Petroleum Science and Engineering, p.109533

Statement of Authorship

Title of Paper	3D effects in two-phase steady-state tests
Publication Status	☑ Published ☐ Accepted for Publication ☐ Submitted for Publication ☐ Unpublished and Unsubmitted w ork w ritten in manuscript style
Publication Details	Yang, S., Hemmati, N., Russell, T., Zeinijahromi, A., Borazjani, S., Behr, A., Genolet, L. and Bedrikovetsky, P., 2022. 3D effects in two-phase steady-state tests. Journal of Petroleum Science and Engineering, 208, p.109533.

Principal Author

Name of Principal Author (Candidate)	Shuyan Yang		
Contribution to the Paper	Developed 3D models, performed scenario investigation, result analysis, and inverse modelling, prepared manuscript		
Overall percentage (%)	60%		
Certification:	This paper reports on original research I conducted during the period of my Higher Degree by Research candidature and is not subject to any obligations or contractual agreements with a third party that would constrain its inclusion in this thesis. I am the primary author of this paper.		
Signature		Date	13/11/2021

Co-Author Contributions

By signing the Statement of Authorship, each author certifies that:

i. the candidate's stated contribution to the publication is accurate (as detailed above);

ii. permission is granted for the candidate in include the publication in the thesis; and

iii. the sum of all co-author contributions is equal to 100% less the candidate's stated contribution.

Name of Co-Author	Nassim Hemmati		
Contribution to the Paper	Performed laboratory experiments		
Signature		Date	13/11/2021

Name of Co-Author	Thomas Russell		
Contribution to the Paper	Technical discussions, result analysis, manuscript preparation		
Signature		Date	13/11/2021

Name of Co-Author	Abbas Zeinijahromi
Contribution to the Paper	Laboratory procedure development, technical discussions
Signature	Date 15/11/21

Name of Co-Author	Sara Borazjani
Contribution to the Paper	Technical discussions, inverse modelling development, manuscript revision
Signature	Date 14/11/2021

Name of Co-Author	Aron Behr
Contribution to the Paper	Technical discussions and problem formulation
Signature	Date 11/11/21

Name of Co-Author	Luis Genolet
Contribution to the Paper	Technical discussions and problem formulation
Signature	Date 11/11/21

Name of Co-Author	Pavel Bedrikovetsky
Contribution to the Paper	Problem formulation, technical discussions, supervision of the project, manuscript revision
Signature	Date 11/11/21

Journal of Petroleum Science and Engineering 208 (2022) 109533

Contents lists available at ScienceDirect

Journal of Petroleum Science and Engineering

journal homepage: www.elsevier.com/locate/petrol

3D effects in two-phase steady-state tests

Shuyan Yang [a], Nassim Hemmati [a], Thomas Russell [a], Abbas Zeinijahromi [a], Sara Borazjani [a], Aron Behr [b], Luis Genolet [b], Pavel Bedrikovetsky [a,*]

[a] University of Adelaide, Adelaide, SA, 5000, Australia
[b] Wintershall Holding GmbH, Kassel, Germany

ARTICLE INFO

Keywords:
Steady state test
Capillary pressure
Relative permeability
3D effects
Core simulation
Laboratory coreflood

ABSTRACT

This study analyses three-dimensional (3D) effects during steady-state tests in short cores, primarily used to determine relative permeability (K_r) and capillary pressure (P_c). Here we concentrate on steady-state transition tests (SSTTs), which allows simultaneous determination of K_r and P_c from the steady-state data and the transition data measured between the steady states. Comparison between three- and one-dimensional (1D) modelling in short cores shows a significant difference in measured water-cut and pressure-drop data. This difference has been observed for cores with different inlet distributor geometries, aspect ratios, and anisotropy. Despite the influence of 3D flow effects on measurement data, the agreement between K_r and P_c as obtained from the 3D and 1D models is close. This phenomenon of conservative inverse-solution results has been demonstrated for different inlet distributor geometries. The Spiral distributor exhibits lower 3D flow effects and more accurate determination of relative permeability and capillary pressure from SSTT tests.

1. Introduction

Two-phase flow in porous media occurs in almost every petroleum development project. The main model functions for two-phase transport are relative phase permeability and capillary pressure (Barenblatt et al., 1989; Lake et al., 2014). Reliable determination of these functions from laboratory tests is a critical component of field-scale engineering.

The Welge-JBN method determines the fractional flow function from measurements of effluent water-cut, and total mobility from measurements of pressure drop across the core (Johnson et al., 1959; Jones and Roszelle, 1978; Welge, 1952). Combining these functions allows determining the relative phase permeabilities ($K_{rw}(S_w)$ and $K_{ro}(S_w)$). Measurements are performed during continuous water injection, i.e. this method is unsteady-state. The method is restricted by the assumption that capillary pressure is negligible compared to the pressure drop across the core (Bedrikovetsky, 2013; Lake et al., 2014). It is possible to include the capillary pressure in the equations for two phase flow, and the resulting equation has been solved numerically (Chen et al., 2016; Maas et al., 2011; Wang and Masalmeh, 2019), or using asymptotic analytical models (Hussain et al., 2012). However, if the capillary pressure $P_c(S_w)$ is treated as an unknown function alongside $K_{rw}(S_w)$ and $K_{ro}(S_w)$ then the set of unknowns cannot be uniquely determined from the two sets of measurements. In this case, the capillary pressure must be determined from other tests, such as the porous plate or centrifuge methods (McPhee et al., 2015). Then, the relative permeability can be determined by inverse modelling, minimising the difference between the model and measured data.

A shortcoming of these procedures is that the tests determining K_r and P_c involve different sequences of saturation. The relative phase permeability and capillary pressure are history-dependent; hysteretic phenomena are highly pronounced for two-phase flow in porous media (Braun and Holland, 1995; Lake et al., 2014). Therefore, the relative permeability and capillary pressure must be determined from processes that follow the same sequence of rock-saturation. Another shortcoming originates from the ill-posed inverse problem of determining relative phase permeability from water-cut and pressure-drop measurements for a known capillary-pressure function (Krause and Benson, 2015; Kuo and Benson, 2015; Rabinovich, 2017; Rabinovich et al., 2016; Reed and Maas, 2018; Wang and Masalmeh, 2019).

During steady-state tests (SSTs), the commingled injections of the two phases are performed at increasing piecewise constant water-cuts F_n, $n = 1, 2, \ldots, N$ (Fig. 1). In the case where the capillary pressure is negligibly small and can be neglected, the stabilised pressure measurements (Fig. 1b) ΔP_n, corresponding to water-cut F_n, allow determining relative phase permeability directly from the modified Darcy's law for each phase. If the capillary pressure has the same order of magnitude as

* Corresponding author.
E-mail addresses: pavel.russia@gmail.com, pavel.bedrikovetski@adelaide.edu.au (P. Bedrikovetsky).

https://doi.org/10.1016/j.petrol.2021.109533
Received 27 August 2021; Received in revised form 16 September 2021; Accepted 17 September 2021
Available online 20 September 2021

the pressure drop, $P_c(S_w)$ must be determined from independent measurements, as with the unsteady state tests outlined previously. Thus, the steady-state tests also suffer from the hysteretic nature of the system, and the ill-posed nature of the inverse problem.

A potential remedy for these shortcomings is to complement the water cut and pressure drop measurements with additional data. One such source of information is X-ray profiles measured at steady states for all water cuts (Reed and Maas, 2018, 2019; Wang and Masalmeh, 2019). The only shortcoming that remains in this method is ill-posed inverse problem for the determination of relative phase permeability and capillary pressure from stabilised pressure drop measurements and X-ray profiles.

To obtain an extra information from a steady state test and simultaneously determine the relative phase permeability and capillary pressure, the injections at every fractional flow can be repeated at different injection rates (Virnovsky et al., 1995; Virnovsky et al., 1998). However, this method results in a significant increase in the total time of the test.

By combining the steady state data with effluent water cut and pressure drop during the transient periods between them (the steady-state-transition test, SSTT), the relative phase permeability and capillary pressure can be simultaneous and uniquely determined. This has been demonstrated for oil-wet (Borazjani et al., 2021a) and water wet rocks (Borazjani et al., 2021b). The method uses an analytical model for steady-states and numerical solution for transition periods. The pressure drop and water-cut histories measured during the transitional periods are approximated by smooth type curves, obtained during the "preliminary" mathematical modelling. An inverse solver treats the approximated type curves. These procedures regularise the ill-posed inverse problem (Tikhonov et al., 2013).

3D flows during steady-state and continuous-injection tests allows for averaging (upscaling) that simplifies the test data treatment and inverse solutions (Kuo and Benson, 2015; Rabinovich et al., 2015, 2016; Shapiro, 2021). Relative permeability can be calculated from micro-scale imaging using various visualisation techniques (Hussain et al., 2014; Zou et al., 2018). Yet, those methods do not substitute the necessity for simultaneous determination of K_r and P_c from corefloods.

Pressure drop across the core is proportional to its length L, while the capillary pressure is independent of L. Therefore, the cases where the capillary pressure has the same order of magnitude as the pressure drop are typical for short cores. Usually, cores in the petroleum industry have lengths not significantly greater than their diameter: typical values are 0.05–0.07 m and 0.038 m, respectively. In order to inject the two phases simultaneously without prior mixing, while maintaining a uniform fluid distribution over the core surface, grooves are etched into the inlet distributor (Figs. 2a and 2b), (Gupta and Maloney, 2015, 2019; Gupta et al., 2016). These factors determine the 3D nature of simultaneous transport of immiscible phases in SSTT and their significant differences from 1D flows. However, the inverse solutions to determine relative phase permeability and capillary pressure during SSTT are based on the 1D Buckley-Leverett equations (Reed and Maas, 2018, 2019).

Yet a study of the impact of 3D flow effects on the determination of relative phase permeabilities and capillary pressure from SSTs and SSTTs is not available.

This paper fills the gap. We conducted 3D numerical modelling of steady-state saturation distributions during commingled injections of water and oil in short cores. The significant difference in saturation distributions along and across the core between 3D and 1D models have been observed. However, the difference between the inverse solutions for relative phase permeability and capillary pressure for 3D and 1D is significantly lower. We conducted steady-state-transition test in the laboratory with 11 injected water fractions, also showing good agreement between relative phase permeability as obtained from 1D and 3D data, while the "measured" data on water-cut and pressure-drop differ significantly. 3D modelling was also performed for half moon (Fig. 2c and 2d) and spiral (Fig. 2e) geometries of inlet distributors of injected oil and water; the Spiral distributor exhibits significantly lower 3D effects and provides more accurate determination of relative phase permeability and capillary pressure from SSTT data.

The structure of the manuscript is as follows. Section 2 presents the set-up for 3D coreflood model and validates it by comparison with 1D modelling. Section 3 analyses 3D flows with different inlet distributor geometries and the effects of core aspect ratio and anisotropy. Section 4 uses SSTT measured data generated by the 3D model to determine relative phase permeability and capillary pressure, and compares them with 1D results. Section 5 presents the laboratory study and matches the laboratory results by the 3D and 1D models. Section 6 discusses the laboratory SSTT procedures, the effects of different distributor

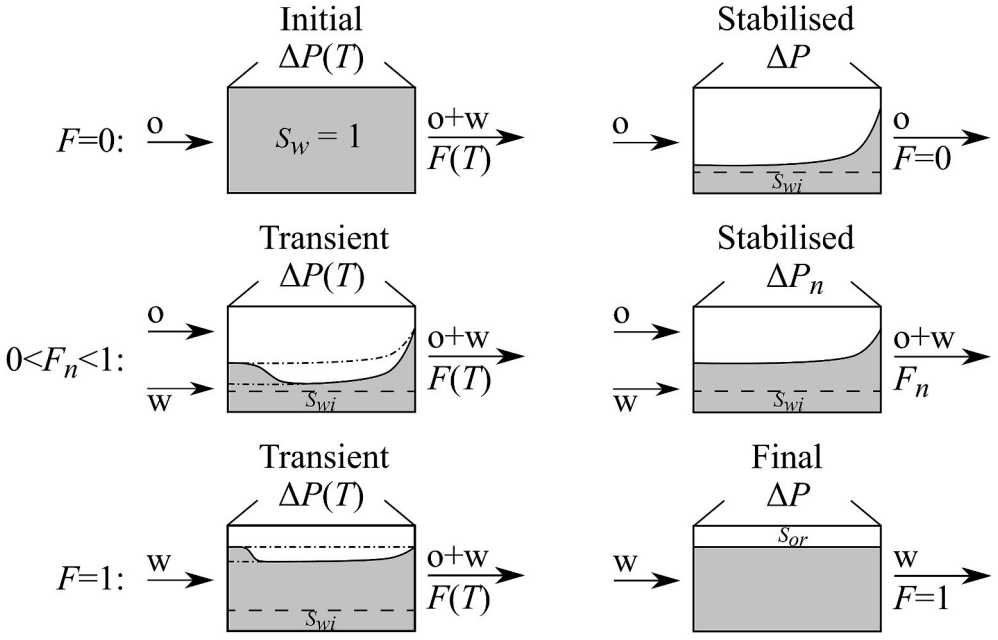

Fig. 1. Schematic of steady-state-transient coreflood tests (SSTT) for different water fractions F measuring pressure drop ΔP across the core and water production at the outlet during: (a) transient states and (b) steady states.

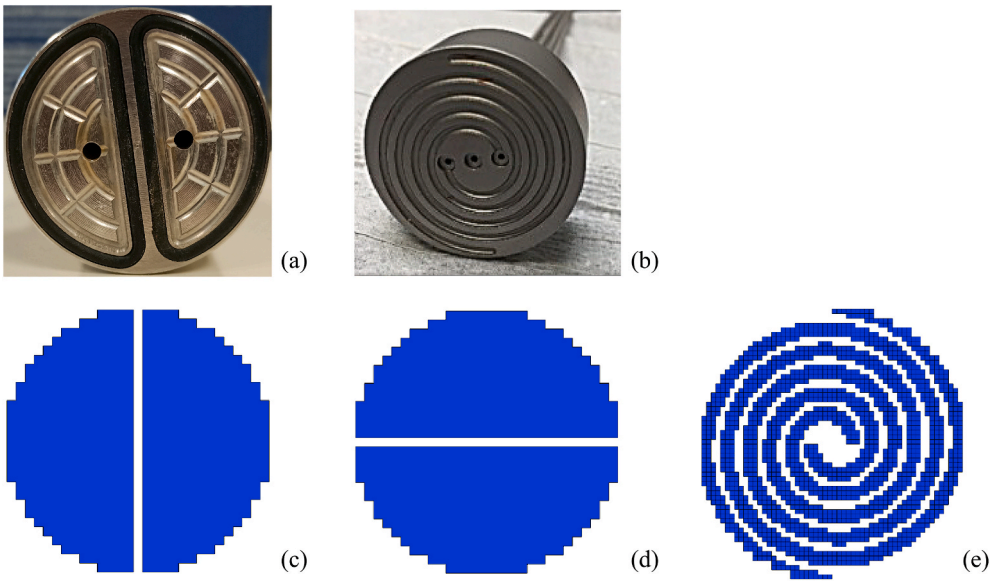

Fig. 2. Inlet distributors with different geometry used in the experiments and 3D simulations: (a) Half-moon distributor, (b) elastomer Spiral distributor, (c) Half-moon distributor positioned left-right (HM LR), (d) Half-moon distributor positioned top-bottom (HM TB), and (e) Spiral distributor. Image b) was taken from Gupta et al. (2016).

geometries on 3D and 1D modelling, adequacy of 3D modelling in core-flooding, and the extensions of the method. Section 7 concludes the work.

2. 3D model of steady-state transient test (SSTT)

This section outlines the construction of the 3D numerical model using the reservoir simulation software CMG STARS and validates the 3D model by comparing the results with the solution to the 1D equations of two-phase flow under the conditions of a SSTT.

2.1. Model set-up

CMG STARS is a simulator for three-phase multi-component modelling of fluid flow in porous media with the capability to account for thermal, steam, and other advanced processes (CMG, 2016). CMG STARS allows for modelling on both field and laboratory scales. The adaptive implicit option in CMG STARS performs calculations either by a fully implicit scheme or the IMPES (implicit pressure, explicit saturation) scheme depending on the throughput or degree of change in primary variables (e.g. pressure, saturation, etc). The adaptive change in calculation scheme is designed to minimise computational cost without sacrificing accuracy.

The core was modelled in CMG STARS using the rectangular Cartesian system (Figs. 3a and 4). There are 32 grid blocks in the *I*-direction (i.e. along the core) with block sizes in this direction (ΔI) logarithmically increasing from the inlet to 1 cm into the core and logarithmically decreasing from 1 cm from the outlet to the outlet of the core. The remaining blocks in the *I*-direction have a constant length of 9.4×10^{-3} m. This distribution of block sizes in the *I*-direction allows for the capture of inlet and outlet end-effects while reducing the computational cost of the simulation. The core cross-section was modelled with 29 blocks in the *J*-direction (i.e. across the core face) and 29 blocks in the *K*-direction (i.e. vertically down from the top of the core). The grid dimensions in each of these two directions is a constant 1.31×10^{-3} m.

In a SSTT, two phases (e.g. oil and water) are injected simultaneously into a core. The two phases must remain isolated prior to entering the core in order to obtain individual inlet phase pressures (Gupta et al., 2016). In order to approximate the flow as 1D, it is important that the two phases are fully mixed and distributed over the entire inlet cross-section. This is achieved by the use of a distributor positioned against the inlet face of the core. A distributor contains a number of grooves designed to create multiple points of entry for the fluid into the core (Figs. 2a and 2b). Careful design of the distributor allows fluid phase separation while maximising phase mixing within the core. In this study, two distributors were modelled in CMG STARS, namely Half-moon and Spiral, shown in Figs. 2a and 2b respectively (Gupta et al., 2016). Geometries of the Half-moon and Spiral distributors were measured, drawn as shapes, and discretised into a set of two-dimensional grid blocks in MATLAB. For the Half-moon case, the *AMALGAMATE function in CMG STARS was used to combine the set of grid blocks in each half moon into a single block, to ensure uniform distribution of each phase into the core. Two half moon configurations were used as a left-right alignment (HM LR), shown in Fig. 2c, and a top-bottom alignment (HM TB), shown in Fig. 2d. Alignment of the half moons is speculated to be important in the presence of gravity and permeability anisotropy. In order to more accurately capture the shape of the Spiral distributor, the *RG function in CMG STARS was used to refine the grid blocks (see Fig. 2e). The isolation of the two phases in a distributor was achieved by assigning a value of zero to permeability and porosity to grid blocks within regions between the distributor grooves, allowing them to act as seals. In addition to the inclusion of an inlet distributor, an outlet distributor was included in all modelling. The outlet distributor was positioned adjacent to the outlet of the core and connected to a "producer", which consisted of the amalgamation of all the active grid blocks into one block across the entire core face. The purpose of an outlet distributor was to ensure that the cross-sectional saturation distribution at the outlet of the core is uniform. The width of the distributors in the model was equal to the width of the grooves of the distributors, which was 3.5×10^{-3} m. The distributors were modelled with relative permeabilities and porosity of unity, zero capillary pressure, and permeability of 100,000 mD (9.87×10^{-11} m^2 in SI units) given that the pressure drop within the distributor is assumed to be zero.

A total of 11 injection stages were simulated with a total injection rate of 2 ml/min (3.33×10^{-8} m^3/s in SI units). 178 pore volumes injected (PVI) was simulated for every stage except the first and last, which were run with 17,800 PVI, to ensure fluid saturations and pressures had reached stabilisation. Table 1 shows the water fraction (*F*), i.e. the ratio of water to total injection rate, for each stage. The order of the injection stages follows the injection procedure used in this study. The

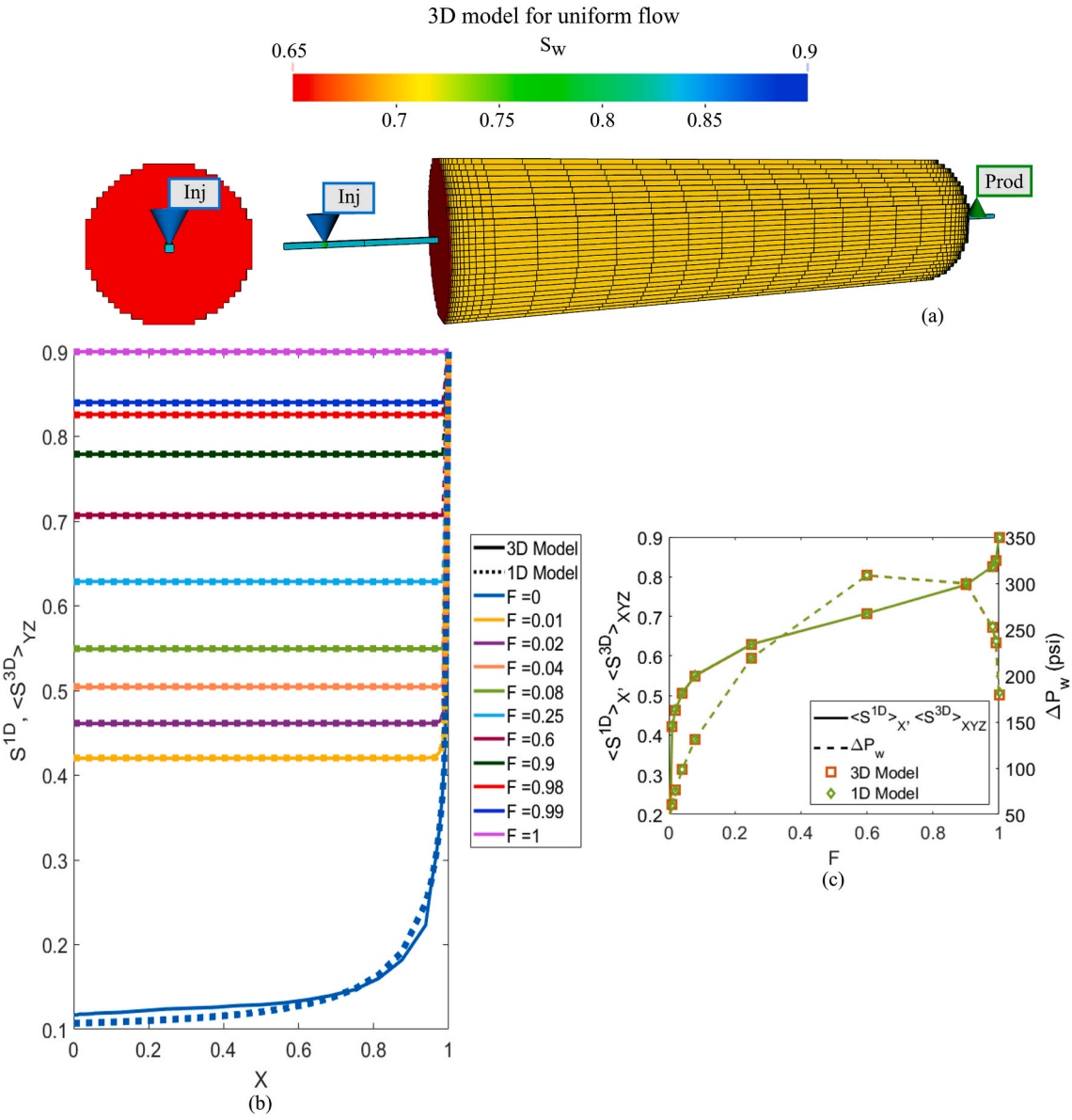

Fig. 3. Comparison between steady-state measurements for 1D and 3D with uniform boundary conditions for each injected water fraction F: (a) 3D simulation set-up with uniform boundary conditions at dimensionless time $T = 178$ PVI for $F = 0.6$, (b) stabilised average water saturation across the core comparison between the 1D model S^{1D} and the 3D model $<S^{3D}>_{YZ}$, and (c) stabilised average water saturation of the core for the 1D model $<S^{1D}>_X$ and the 3D model $<S^{3D}>_{XYZ}$ and stabilised pressure drop of water across the core ΔP_w.

fully water-wet core was initially fully saturated with water, with an initial pressure of 300 psi (2.07×10^6 Pa in SI units) and a temperature of 25 °C, corresponding to the back pressure and laboratory temperature applied in a SSTT. Other rock and fluid properties are shown in Table 2. The Corey model was used for the relative permeability of water, K_{rw}:

$$K_{rw}(S_w) = K_{rw|sor}\left(\frac{S_w - S_{wi}}{1 - S_{or} - S_{wi}}\right)^n, \tag{1}$$

and the relative permeability of oil, K_{ro}:

$$K_{ro}(S_w) = K_{ro|swi}\left(1 - \frac{S_w - S_{wi}}{1 - S_{or} - S_{wi}}\right)^m, \tag{2}$$

where $K_{rw|sor}$ is the relative permeability of water at residual oil saturation, $K_{ro|swi}$ is the relative permeability of oil at initial water saturation, S_w, S_{wi}, and S_{or} are the water saturation, initial water saturation, and residual oil saturation, respectively, n and m are Corey exponents.

The formula used for capillary pressure is:

$$P_c(S_w) = P_d\left(\frac{S_w - S_{wi}}{1 - S_{or} - S_{wi}}\right)^{-1/\lambda}, \tag{3}$$

where P_d is the displacement pressure and λ is the pore-size distribution index.

Values of the parameters used in the simulations are shown in Table 3.

2.2. 1-D equations for steady-state-transition coreflood tests

In order to evaluate any 3D effects, first we consider fully 1D flow. Two-phase flow in porous media is described by the following system of partial differential equations (Borazjani et al., 2021a):

$$\frac{\partial S_w}{\partial T} + \frac{\partial f(S_w)}{\partial X} = \varepsilon\frac{\partial^2 \Psi(s)}{\partial X^2}, \Psi'(s) = -K_{ro}(S_w)f(S_w)J'(S_w), \tag{4}$$

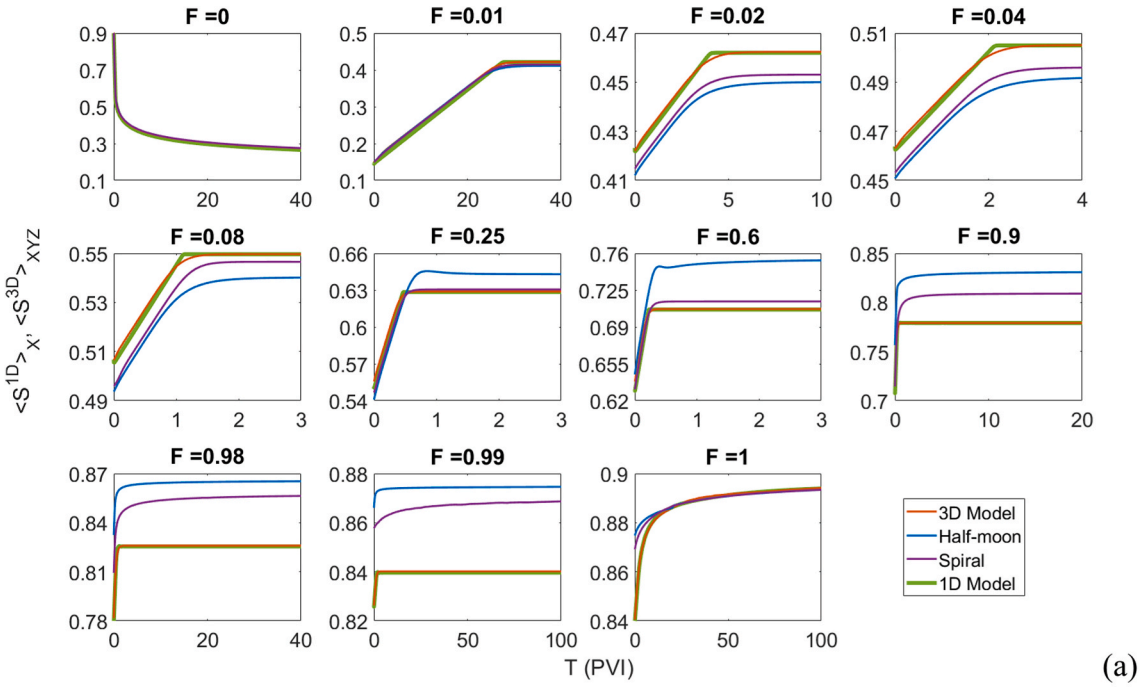

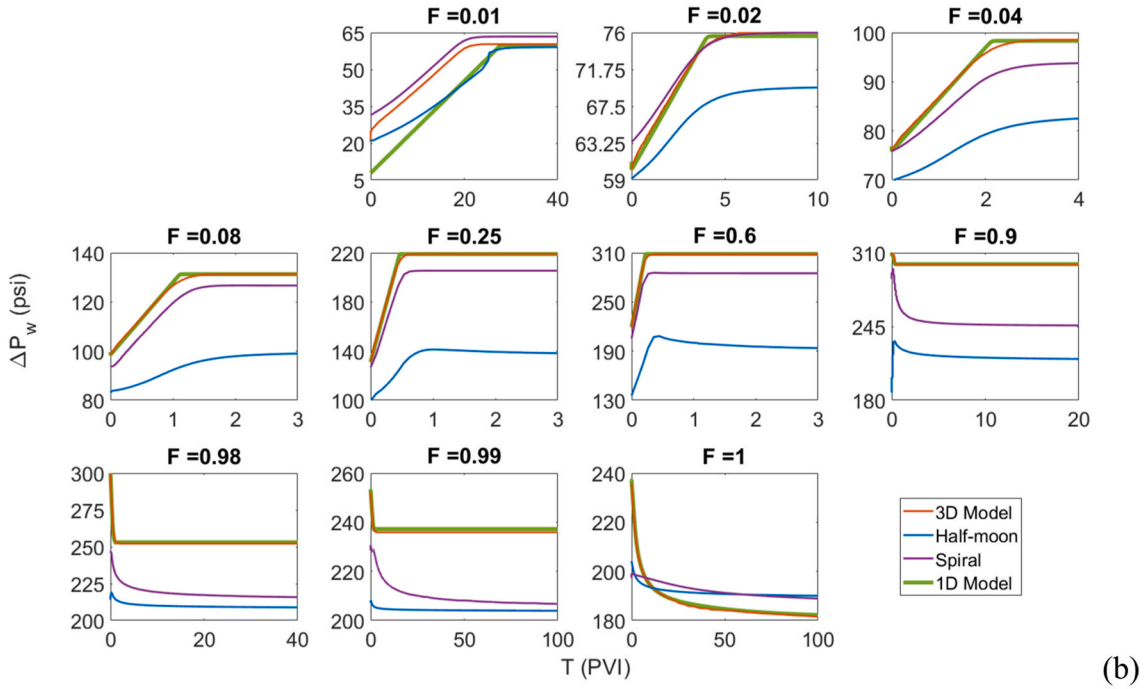

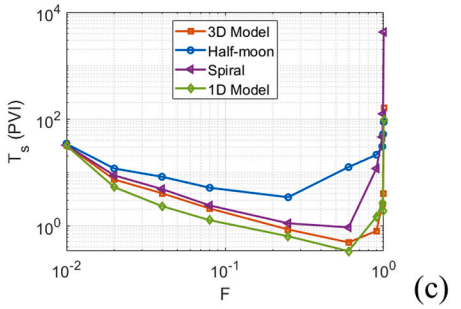

Fig. 4. Transient data and dimensionless stabilisation time T_s comparison for the different models for each injected water fraction F: (a) average water saturation of the core for the 1D model $<S^{1D}>_X$ and the 3D simulations $<S^{3D}>_{XYZ}$, (b) pressure drop of water across the core ΔP_w, and (c) dimensionless stabilisation time T_s for. 3D model, Half-moon, and Spiral correspond to 3D simulations with uniform boundary conditions, the Half-moon distributor, and the Spiral distributor, respectively.

Table 1
Injection stages and the corresponding water fractions F during steady-state-transient coreflood test injections.

Stage #	1	2	3	4	5	6	7	8	9	10	11
F	0	0.01	0.02	0.04	0.08	0.25	0.6	0.9	0.98	0.99	1

Table 2
Rock and fluid properties used in the simulation.

	Isotropic core	Anisotropic core	Distributor
Rock properties			
Diameter (m)	0.038	0.038	0.038
Length (m)	0.15	0.15	3.5×10^{-3}
Permeability – Horizontal (m^2) [mD]	5.92×10^{-14} [60]	5.92×10^{-14} [60]	9.87×10^{-11} [10^5]
Permeability – Vertical (m^2) [mD]	5.92×10^{-14} [60]	5.92×10^{-15} [6]	9.87×10^{-11} [10^5]
Porosity	0.19	0.19	1
	Oil	**Water**	
Fluid properties			
Viscosity (Pa.s)	0.0011	0.001	
Density (kg/m^3)	763.5	1000	

Table 3
Relative permeabilities and capillary pressure parameters used in CMG STARS simulations.

	$K_{rw\|sor}$	$K_{ro\|swi}$	λ	P_d (psi)	S_{wi}	S_{or}	n	m
Values	0.06	0.65	2.3	3.28	0.1	0.1	3.9	2.4

$$\frac{\partial \overline{P}_w}{\partial X} = \left(-1 - \varepsilon K_{ro}(S_w)\frac{\partial J}{\partial X} \right) \left(\frac{K_{rw}(S_w)\mu_o}{\mu_w} + K_{ro}(S_w) \right)^{-1}, \tag{5}$$

where the dimensionless parameters and variables are:

$$X = \frac{x}{L}, T = \frac{Ut}{\phi L}, \overline{P}_w = \frac{K}{UL\mu_o}P_w, \varepsilon = \frac{\sqrt{K\phi}\sigma\cos\theta}{UL\mu_o}. \tag{6}$$

and the fractional flow function, f, is:

$$f(S_w) = \left(1 + \frac{\mu_w K_{ro}(S_w)}{K_{rw}(S_w)\mu_o} \right)^{-1}. \tag{7}$$

Here, J is the Leverett J-function, L is the length of the core, U is the Darcy's velocity, K is the absolute permeability, ϕ is the porosity, θ is the contact angle, σ is the oil/water interfacial tension, μ is the viscosity. Subscripts w and o represent water and oil, respectively.

The boundary conditions are:

$$X = 0: \ f(S_w) + \varepsilon \frac{\partial (K_{ro}(S_w) f(S_w) J^{`}(S_w))}{\partial X} = F_{n+1}, \tag{8}$$

$$X = 1: \ J(S_w) = 0 \tag{9}$$

and the initial condition is:

$$T = 0: \ \frac{1-X}{\varepsilon} = \int_{S_w}^{S_w(J=0)} \frac{K_{ro}(s) f(s) J^{`}(s)}{F - f(s)} ds \tag{10}$$

The initial condition (10) for the transient period during the injection with water fraction $F = F_{n+1}$ corresponds to steady state (stabilised) profiles after the injection with $F = F_n$. The steady-state saturation profiles, $S_w(X)$, at each injected fraction are obtained by the integration of the right-hand side of Eq. (4) with respect to S_w, see Fig. 3b for $S_w(X)$ profiles. The stabilised pressure drop of water is calculated from the given $S_w(X)$ from Eq. (4) for steady-state profile $F = F_n$ by integration of Eq. (5) in X.

Borazjani et al. (2021a) and Borazjani et al. (2021b) used the Matlab PDE function, `pdepe`, to solve Eqs. (4) and (5) subject to the boundary and initial conditions (8–10) numerically to obtain the transient saturation profiles $S_w(X,T)$ between two consequent steady-state profiles. This solution is referred to as the '1D model'. Further in the text, we refer to the water saturation determined from the 1D model as S^{1D}.

For the purposes of comparing the models, we introduce the following average water saturations: $<S^{3D}(X,T)>_{YZ}$ representing the 3D saturation averaged over each cross-section, and $<S^{1D}(T)>_X$ and $<S^{3D}(T)>_{XYZ}$ representing the saturation averaged over the entire core for the 1D and 3D models respectively. The expressions for each saturation are as follows:

$$<S^{3D}(X,T)>_{YZ} = \iint_{Y^2+Z^2\le 1} S^{3D}(X,Y,Z,T)dYdZ, \tag{11a}$$

$$<S^{1D}(T)>_X = \int_0^1 S^{1D}(X,T)dX, \tag{11b}$$

$$<S^{3D}(T)>_{XYZ} = \int_0^1 <S^{3D}(X,T)>_{YZ} dX. \tag{11c}$$

where the dimensionless parameters X, and T are defined in (6), and Y and Z are the two coordinates perpendicular to the flow direction, defined as zero on the central axis of the core and normalised by the core radius such that $Y, Z \in (-1,1)$.

2.3. Numerical validation

A 3D core initially fully saturated with water, with isotropic properties, and a single injector were constructed in CMG STARS. The purpose of this simulation is to validate that under the total mixing of the phases, the simulation results match the 1D model presented in Section 2.2. To this end, the injector was connected to a distributor consisting of one amalgamated block to ensure a uniform injection into the inlet core cross section, as shown in Fig. 3a. For different injection stages, a mixture of oil and water was injected, with the fluid ratio determined by F. The same rock and fluid properties as well as simulation conditions described in Section 2.1. were used.

Fig. 3b shows the average water saturations along the core at stabilisation for the 3D model $<S^{3D}>_{YZ}$ and the 1D model S^{1D}, for the eleven F-values. In the 3D model, uniform boundary conditions over the inlet cross-section have been used. The two different schemes (i.e. the 1D model and the 3D simulation) show high agreement, with the exception of a slight deviation in the saturation profiles for $F = 0$. As the injection period for $F = 0$ was significantly higher than 1 PVI (17,800 PVIs), this deviation cannot be attributed to not reaching steady state. The 1D model exhibits a capillary end effect, which is captured by the 3D simulation. We note that while the 1D model predicts $S^{1D} = 1\text{-}S_{or} = 0.9$ at $X = 1$, the saturation in the final grid core cross section is slightly lower, due to the finite size of the grid blocks in the I-direction (i.e., along the core).

Fig. 3c shows the stabilised average water saturation of the core $<S^{1D}>_X$ for the 1D model and $<S^{3D}>_{XYZ}$ for the 3D model and the stabilised pressure drop of water across the core ΔP_w for each F obtained from 3D model and the 1D model. The values of $<S^{1D}>_X$ and $<S^{3D}>_{XYZ}$, as well as ΔP_w obtained from the two models match closely.

Fig. 4 compares the transient data obtained from the 1D and 3D

models. The thick blue line is from the 1D model and the orange line is from the 3D model. Fig. 4a compares the average core saturations, $<S^{1D}>_X$ and $<S^{3D}>_{XYZ}$, Fig. 4b shows ΔP_w obtained from the two models, and Fig. 4c presents the dimensionless stabilisation time T_s for the different F values. We define the dimensionless stabilisation time, T_s, as the time where both the average core saturation and pressure drop of water are within 1% of their respective stabilised values. As with the steady-state data, the transient data from the 3D model also shows a close match to the 1D model.

The strong match between the 3D and the 1D model for average saturations and ΔP_w for both stabilised and transient data shows that the numerical simulation is sufficiently accurate to capture the characteristics of the flow, which validates the 3D numerical model.

3. Results of 3D modelling

In this Section, we discuss the results obtained from the 3D modelling. In particular, the effects of the different inlet distributor geometries, aspect ratios, permeability anisotropy on fluid mixing, as well as transient data and stabilisation time are investigated.

3.1. Comparison between different distributor geometries

Three sets of 3D, steady-state tests using different inlet distributor geometries for an isotropic core were simulated in CMG STARS. The simulation set up and conditions are described in Section 2.1. Figs. 5a, 5b, and 5c present the simulation results for the following distributor geometries: Half-moon Left-Right (HM LR), Half-moon Top-Bottom (HM TB), and Spiral, respectively. This figure shows how fluid saturations are distributed along the core following stabilisation. The simulation results are taken at $T = 178$ PVI for $F = 0.6$. This figure also demonstrates that for all distributors, the desired goal of uniform fluid saturations in each cross-section has not been achieved. Further discussions of this incomplete mixing will be presented below.

Fig. 6 shows the cross-sectional stabilised water saturation distribution at dimensionless core length, X, of 0.998, which was the location of the grid blocks adjacent to the core outlet grid blocks. Figs. 6a, d, and 6g show the saturation distribution for the HM LR simulation at $F = 0.25$, $F = 0.6$, and $F = 0.9$, respectively. Figs. 6b, 6e, and 6h show the results for the HM TB at the same F values, while Figs. 6c, 6f, and 6i show the results for the Spiral simulation. These figures show that at stabilisation, the cross-sectional saturations of water are not uniform and are dependent on the type of distributor used at the inlet. A well-defined oil-

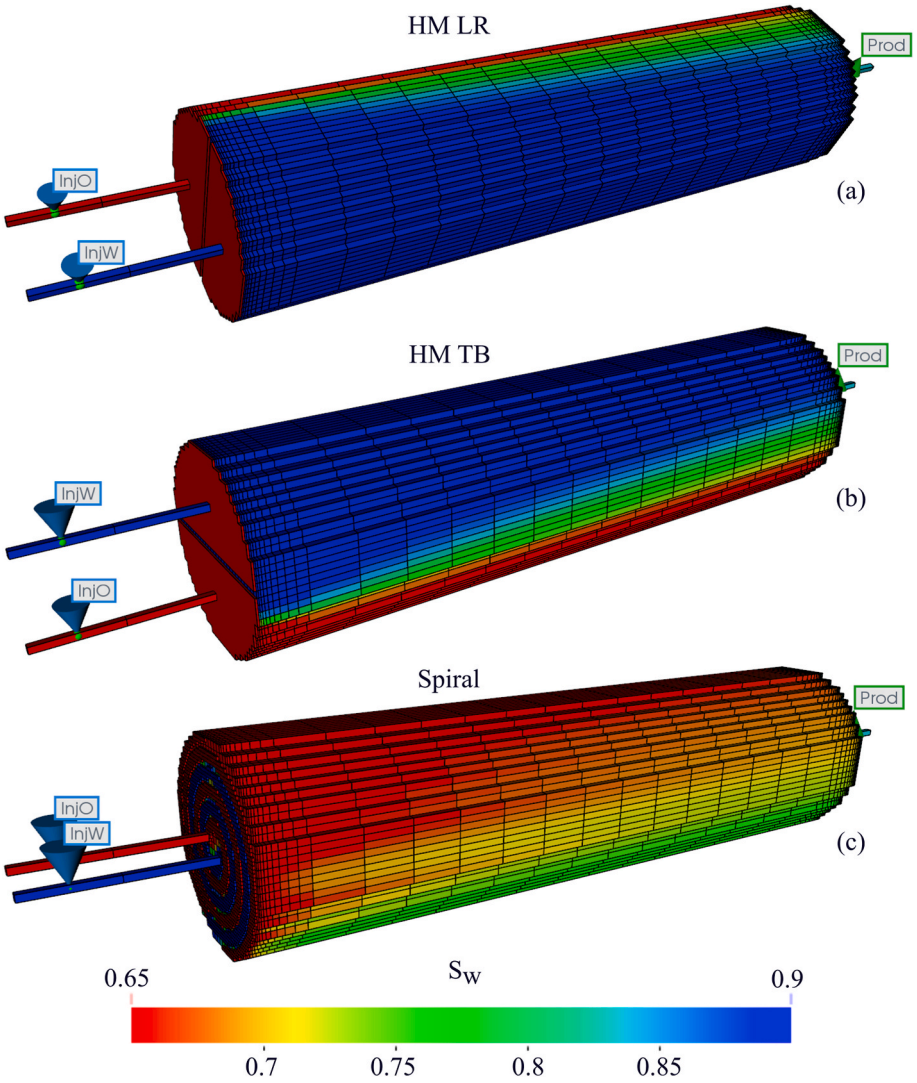

Fig. 5. CMG STARS 3D simulation models for the different inlet distributors: (a) Half-moon distributor with half moons positioned left-right (HM LR), (b) Half-moon distributor with half moons positioned top-bottom (HM TB), (c) Spiral distributor. All simulations are shown at dimensionless time $T = 178$ PVI for injected water fraction $F = 0.6$.

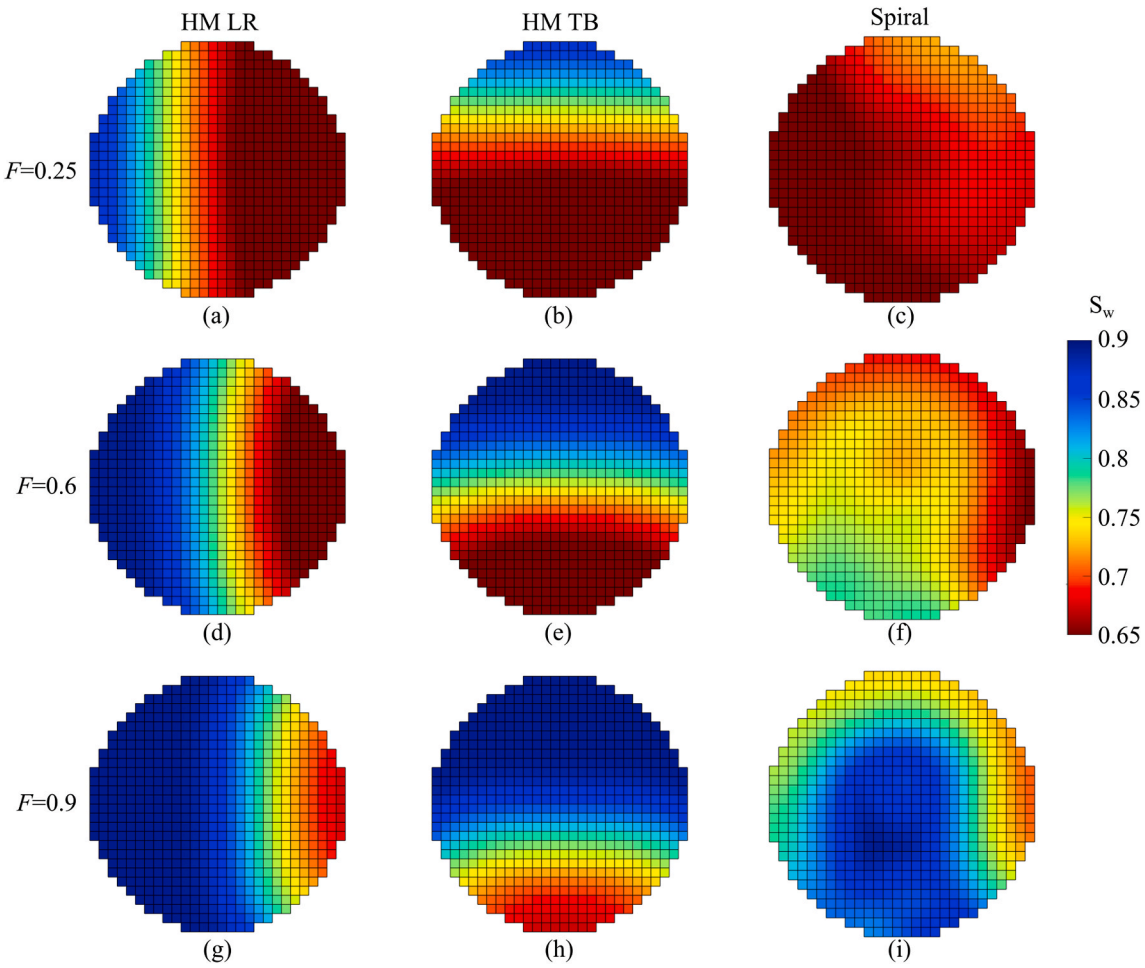

Fig. 6. Cross-sections of the 3D simulations of an isotropic core showing water saturations at $X = 0.998$ near to outlet: (a) Half-moon distributor with half moons positioned left-right (HM LR) for water fraction $F = 0.25$, (b) Half-moon distributor with half moons positioned top-bottom (HM TB) for $F = 0.25$, and (c) Spiral distributor for $F = 0.25$. For $F = 0.6$, the cross-sectional images for HM LR, HM TB, and Spiral are shown in (d), (e), and (f), respectively. The cross sections for HM LR, HM TB, and Spiral for $F = 0.9$ are shown in (g), (h), and (i), respectively.

water mixing zone is apparent for both Half-moon distributors, which has been observed for all injection stages. A mixing zone is less well-defined when the Spiral distributor was used, in part due to the greater degree of mixing.

As demonstrated in Section 2.3, when an oil-water mixture is injected across the entire inlet cross-section, guaranteeing mixing, the 3D simulation reproduces the saturation profiles predicted by the 1D model. Below, we illustrate the differences between steady-state saturation profiles calculated by the 1D model and the 3D simulations using inlet distributors described in Section 2.1 in an attempt to quantify the effects of incomplete mixing on fluid saturations and pressures.

Fig. 7 shows the results from 3D simulations and the comparison to the 1D model. Fig. 7a shows $<S^{3D}>_{YZ}$ along the core obtained for all F shown in Table 1 from the HM LR, HM TB, and Spiral simulations, as well as S^{1D} for the 1D model. $<S^{3D}>_{YZ}$ profiles obtained from simulations using the HM LR and HM TB simulations were identical, indicating that the effect of gravity on fluid mixing was negligible. The dimensionless parameter that reflects the ratio between the buoyancy and pressure gradient is

$$\frac{K\Delta\rho g}{U\mu}\frac{2r}{L}, \tag{12}$$

where g is the gravitational acceleration and r is the core radius.

Using the test velocity $U = 2.94\times10^{-5}$ m/s and the properties in Table 2, the buoyancy and pressure gradient ratio is 0.00118 for water and 0.00106 for oil, both of which are significantly smaller than one, indicating the dominance of pressure over buoyancy. This explains why the positions of the two injection points (LR and TB) does not affect the average saturation and pressure drop curves. As a result, we will not distinguish between the two Half-moon cases and refer to them collectively as Half-moon.

Aided by the non-uniform grid dimensions along the core, both the Half-moon and Spiral cases were able to exhibit a capillary end effect that closely matches that of the 1D model. Despite the significant inlet effect observed in the 3D simulations, there is a general tendency of the saturation profiles towards the horizontal profile predicted by the 1D model. This suggests that despite the separation of the two phases at the inlet, fluid mixing within the core tends the system towards flow that resembles 1D two-phase flow. While the Spiral distributor for most injections exhibits a higher inlet effect, generally the Spiral distributor provided a closer match the 1D model compared to the Half-moon. At and above $F = 0.9$, $<S^{3D}>_{YZ} = 0.78$ for the Spiral case or $F = 0.6$, $<S^{3D}>_{YZ} = 0.71$ for the Half-moon case, significant deviations can be observed between the simulations and the 1D model. Here, in addition to substantial inlet effects, there is no longer a clear asymptotic tendency of the simulations towards the uniform saturation predicted by the 1D model. This can be explained by the transition from stable to unstable displacement marked by a water mobility ratio, $M_w=(K_{rw}/\mu_w)/(K_{ro}/\mu_o)$ greater than one, resulting in high water saturation flow channels that inhibit fluid mixing.

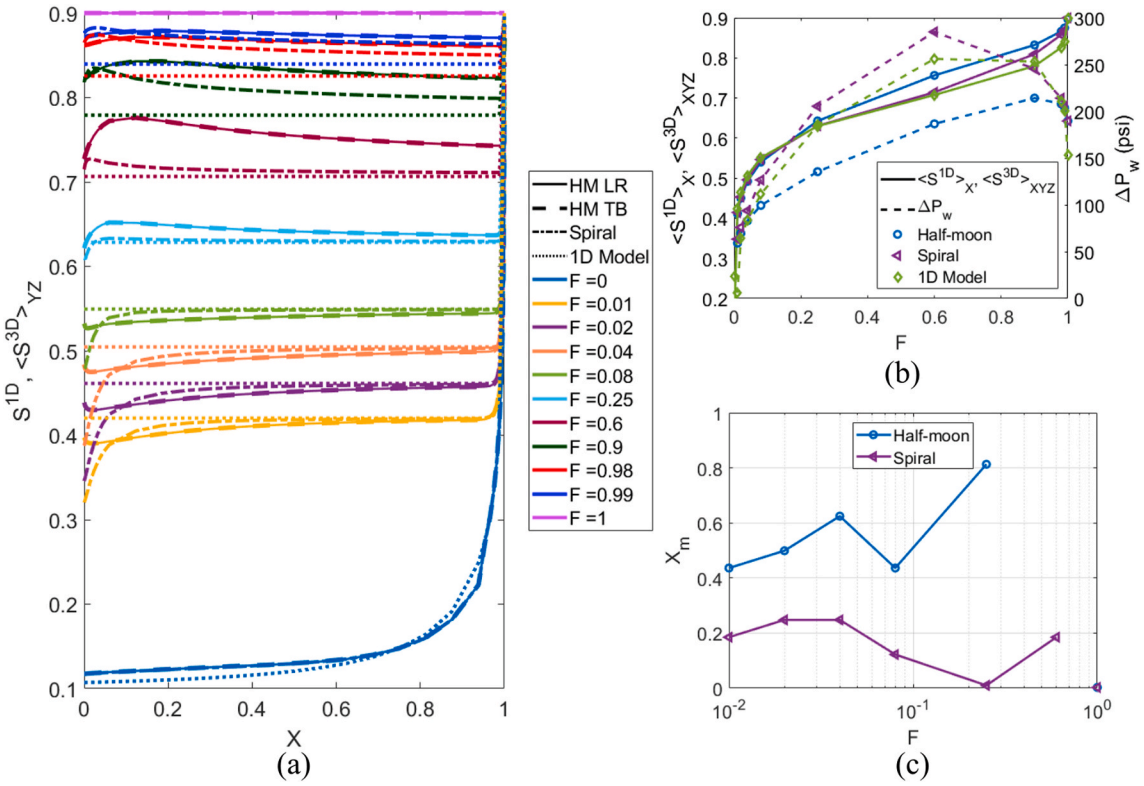

Fig. 7. Comparison between steady-state measurements for 1D and 3D with different distributor geometries for an isotropic core for each injected water fraction F: (a) stabilised average water saturation across the core comparison between the 1D model S^{1D} and the different inlet distributors $<S^{3D}>_{YZ}$, (b) stabilised average water saturation of the core for the 1D model $<S^{1D}>_X$ and the 3D model $<S^{3D}>_{XYZ}$ and stabilised pressure drop of water across the core ΔP_w, and (c) dimensionless mixing length X_m. HM LR, HM TB, and Spiral are the 3D simulations using the Half-moon distributor with half moons positioned left-right, the Half-moon distributor with half moons positioned top-bottom, and the Spiral distributor, respectively.

Fig. 7b shows the stabilised $<S^{3D}>_{XYZ}$ and the stabilised ΔP_w at each F for the Half-moon and Spiral simulations and the stabilised $<S^{1D}>_X$ and the stabilised ΔP_w for the 1D model. In this figure, both $<S^{3D}>_{XYZ}$ and ΔP_w obtained from the Spiral simulation were closer matched to the 1D model than those obtained from the Half-moon simulation, illustrating further that the Spiral distributor provided better fluid mixing than the Half-moon distributor. The average absolute deviation ($= \sum_i |\omega_{i,sim} - \omega_{i,1D}|$, where ω = stabilised water saturation of the core and stabilised pressure drop of water) was 0.0126 for the Spiral case and 0.0224 for the Half-moon case.

As discussed earlier, the $<S^{3D}>_{YZ}$ profiles derived from the 3D simulations exhibit inlet effects which dissipate after some distance from the core inlet, resulting in good agreement between the 3D simulation and 1D model. To this end, we introduce the mixing length, defined as the distance from the inlet beyond which the 3D simulation saturation profile lies within 1% of that predicted by the 1D model. Fig. 7c presents the dimensionless mixing length (X_m) in both the Half-moon and Spiral simulations for each F. In cases where the simulation and 1D model profiles never converge, a mixing length cannot be defined. In the Half-moon simulation, values of X_m were able to be determined for $F < 0.6$, while in the Spiral simulation, values of X_m were able to be determined for $F < 0.9$. Where the mixing length can be defined, the Spiral distributor exhibited smaller values, demonstrating agreement with the 1D model for a greater fraction of the core length.

3.2. Effects of aspect ratio

In addition to the investigation on the effects of inlet distributor geometries on fluid flow, the effects of aspect ratio (α) were also investigated, where α is the ratio of the core length to the diameter. While the core diameter remained the same as shown in Table 2, simulations of cores with length 0.05 and 0.1 m were performed in addition to the 0.15 m core presented in the previous section. The aspect ratios for the core lengths 0.05, 0.1, and 0.15 m were 1.3, 2.6, and 3.9, respectively. The simulation set-up and conditions remained the same as described in Section 2.1.

Figs. 8a and 8b shows the effect of aspect ratio on $<S^{3D}>_{YZ}$ profiles for the Half-moon and Spiral simulations, respectively. In both figures, $<S^{3D}>_{YZ}$ profiles obtained from the higher α are extensions from the lower α (except for the outlet end effect) and the overall match to the 1D model improved with increasing α. This showed that increasing α reduced the effect of 3D fluid flow. Beyond variations in the first 0.02 m of the core, all profiles tend monotonically towards the horizontal profile predicted by the 1D model. Given that the inlet effects are independent of aspect ratio, the longer cores will naturally approximate the 1D model better, as the converged section of the saturation profile becomes a larger fraction of the entire profile. While convergence is roughly monotonic towards the 1D model, as noted before, for high F, convergence does not appear to be towards the correct horizontal asymptote. This issue, previously attributed to unstable displacement, is unlikely to be resolved with higher aspect ratios.

While the inlet end effects are different for the Spiral and Half-moon simulations, consideration of different aspect ratios has not changed the conclusion that the Spiral distributor produces better mixing.

Figs. 8c and 8d presents the $<S^{3D}>_{XYZ}$ and $\Delta P_w/L$ for each α and $<S^{1D}>_X$ from the 1D model for the Half-moon and Spiral simulations, respectively, where $\Delta P_w/L$ is the pressure drop of water normalised by the core length. Generally, the figures show that increasing the aspect ratio increases the agreement with the 1D model, with the exception of ΔP_w at high F for the Spiral distributor. While decreasing the aspect ratio reduces the agreement with the 1D model for both distributors, doing so

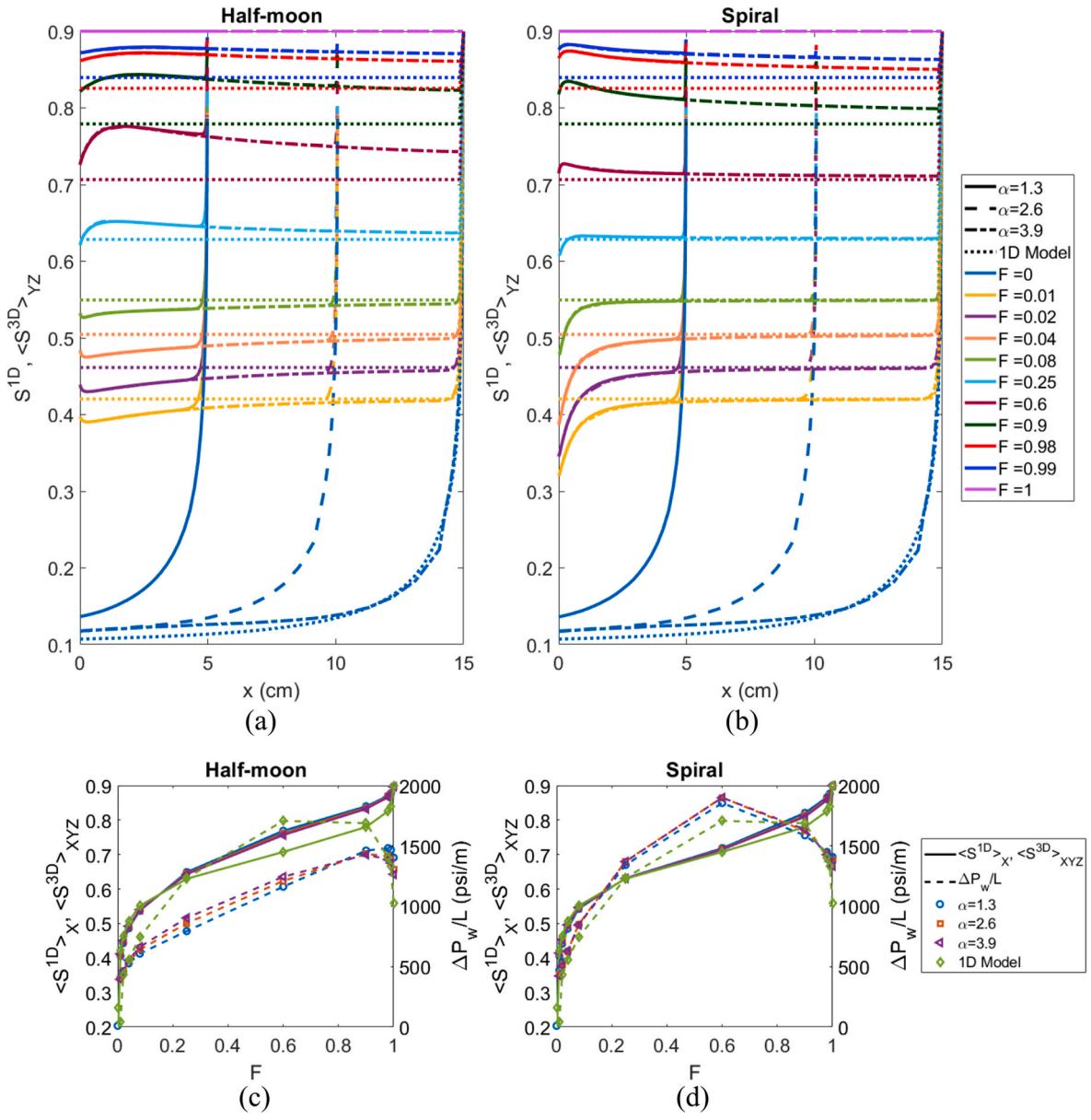

Fig. 8. Comparison between steady-state measurements for 1D and 3D with different aspect ratios α for an isotropic core for each injected water fraction F: (a) and (b) stabilised average water saturation across the core for the 1D model S^{1D} and the 3D simulations $<S^{3D}>_{YZ}$ using the Half-moon and Spiral distributor, respectively, (c) and (d) stabilised average water saturation of the core for the 1D model $<S^{1D}>_X$ and the 3D simulations $<S^{3D}>_{XYZ}$ and stabilised pressure drop of water across the core ΔP_w using the Half-moon and Spiral distributor, respectively.

has a greater effect on the Half-moon simulation. Regardless of aspect ratio, the Spiral distributor still exhibits greater agreement with the 1D model. The differences between the 3D simulations at different aspect ratios is relatively insignificant compared to the differences between the simulations and the 1D model.

3.3. Effects of anisotropy

Due to its prevalence in natural reservoir rocks, the effect of permeability anisotropy on fluid mixing has also been studied. The directional dependence of permeability, or permeability anisotropy, arises most commonly in sedimentary rocks due to the presence of thin horizontal layers of low-permeability sediments. We approximate this phenomenon by reducing the vertical permeability to one tenth of the horizontal permeability, as shown in Table 2. All other simulation set-up and conditions remain the same as described in Section 2.1.

Fig. 9 shows the stabilised water saturation distribution for the anisotropic case at $X = 0.998$, which was the location of the grid blocks adjacent to the core outlet grid blocks.

As with the isotropic case, Figs. 9a, 9d, and 9g show the saturation distribution for the HM LR simulation at $F = 0.25$, $F = 0.6$, and $F = 0.9$, respectively. Figs. 9b, 9e, and 9h show the results for the HM TB at the same F values, while Figs. 9c, 9f, and 9i show the results for the Spiral simulation. Compared to the results for the isotropic case presented in Fig. 6, the degree of mixing has been reduced for all distributors as a result of the reduced vertical permeability. The effect is most prominent in the HM TB case, where the mixing zone is now significantly smaller than in the HM LR case. For the Spiral case, the concentric profiles seen in the isotropic case (Fig. 6) are now disjointed, with separate low saturation ganglia now present.

Fig. 10a shows $<S^{3D}>_{YZ}$ along the core for the anisotropic case using the HM LR, HM TB, and Spiral simulations, as well as S^{1D} from the 1D model. Similar to the $<S^{3D}>_{YZ}$ profiles for the isotropic core, the 3D simulated results exhibit both inlet and outlet effects. Unlike in the

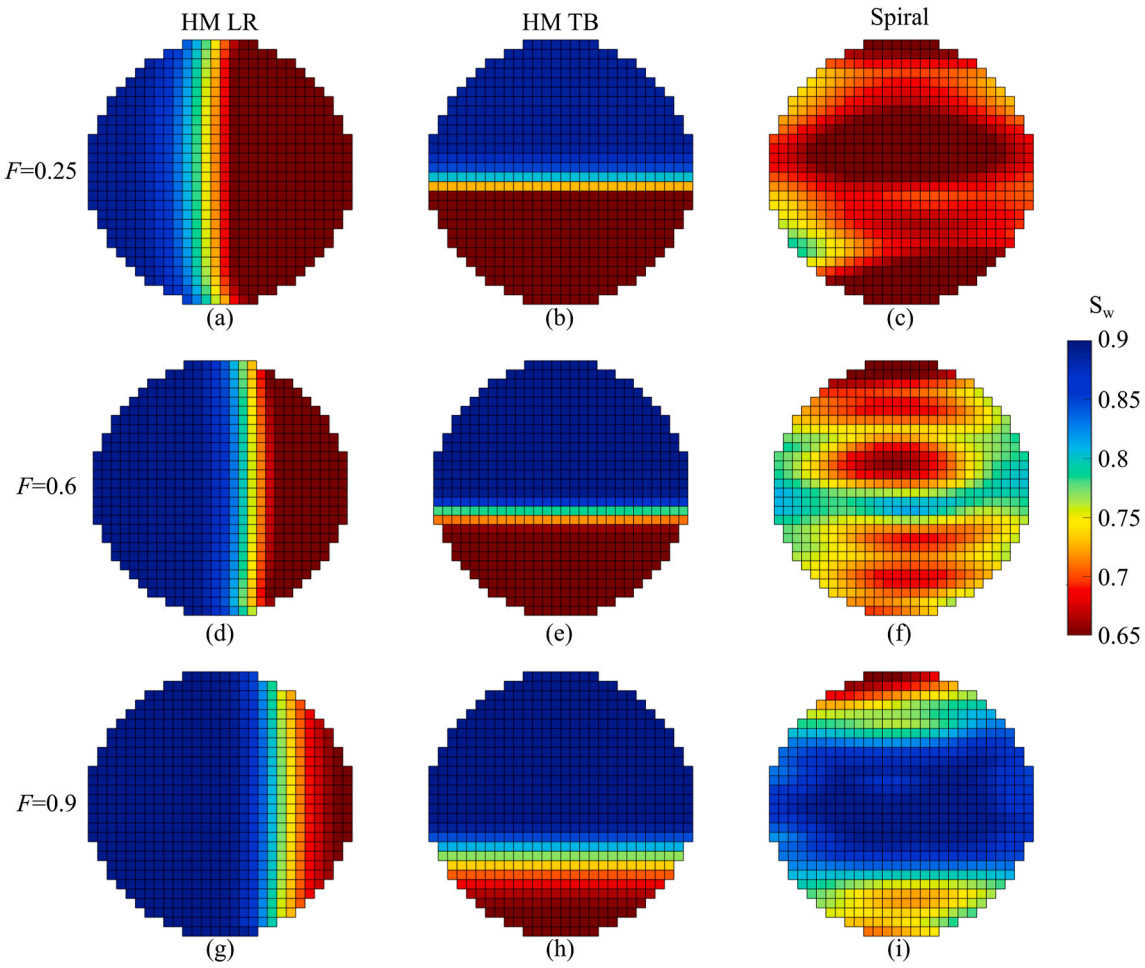

Fig. 9. Cross-sections of the 3D simulations of an anisotropic core showing water saturations at $X = 0.998$ near to outlet: (a) Half-moon distributor with half moons positioned left-right (HM LR) for water fraction $F = 0.25$, (b) Half-moon distributor with half moons positioned top-bottom (HM TB) for $F = 0.25$, and (c) Spiral distributor for $F = 0.25$. For $F = 0.6$, the cross-sectional images for HM LR, HM TB, and Spiral are shown in (d), (e), and (f), respectively. The cross sections for HM LR, HM TB, and Spiral for $F = 0.9$ are shown in (g), (h), and (i), respectively.

isotropic case, the HM LR and HM TB now exhibit significant differences in the saturation profiles. While all distributors demonstrate a worse match to the 1D model than in the isotropic case, the HM TB now differs substantially, with asymptotic tendency that is rarely in line with the profiles predicted by the 1D model. Where the half moons are aligned such that water is injected above oil (HM TB), the reduction in vertical permeability significantly inhibits the vertical cross-flow between the two fluids, inhibiting mixing. As the horizontal permeability was unchanged, the effect on the HM LR case was less severe. In the isotropic case, the Spiral case exhibited a more significant inlet effect which dissipated faster with flow distance compared to the Half-moon case. When permeability anisotropy is present, the spiral inlet effects are even more pronounced and extend further into the core as a result of the reduction in mixing. Beyond the first few injection stages, the Spiral distributor $<S^{3D}>_{YZ}$ profile still appears to match the 1D profile better than the Half-moon distributor.

Fig. 10b presents the $<S^{3D}>_{XYZ}$ and ΔP_w at each F for the HM LR, HM TB, and Spiral simulations, as well as $<S^{1D}>_X$ for the 1D model. $<S^{3D}>_{XYZ}$ values from the Spiral simulation matched to the 1D model better than the Half-moon simulations at high fractional flows ($0.04 \leq F \leq 0.9$). At lower fractional flows ($F \leq 0.02$), the significant inlet effects in the Spiral simulation result in the HM LR simulation demonstrating a better fit to the 1D model. Above $F = 0.9$, all simulations exhibit poor agreement with the 1D model. The results from HM LR simulation were better matched to the 1D model than the results from HM TB simulation.

Fig. 10c shows the mixing length, X_m, at each F for the three simulations. Using the same 1% dissimilarity threshold as in Section 3.1, no mixing lengths could be defined for the HM TB simulation, except for the final injection stage, $F = 1$. Both the HM LR and Spiral simulations demonstrated longer mixing lengths when anisotropy was accounted for. Although generally the Spiral distributor exhibited a lower mixing length than the HM LR, it was more significantly affected by the reduction in vertical permeability, to the extent that it almost didn't fully converge at low F. This explains why blue line is located below the yellow line in Fig. 10c. This is likely due to the necessity for both horizontal and vertical flow for mixing when using the Spiral distributor.

3.4. Transient data and stabilisation time

In the previous sections we focussed on measurements taken following the stabilisation of each injection stage, as these are the measurements used to derive rock-fluid properties. Recent studies have presented the use of transient data before stabilisation to improve the determination of relative permeability and capillary pressure curves (Borazjani et al., 2021a, 2021b). Thus in Fig. 4a we present the transient data for $<S^{3D}>_{XYZ}$ and $<S^{1D}>_X$ from the 3D simulations and 1D model, respectively, and in Fig. 4b, we present the transient data for ΔP_w. For $F = 0$, there was no water injection, therefore, ΔP_w was not shown in Fig. 4b. While the stabilised saturation values provided a good match for most values of F, the transient profiles showed greater disagreement

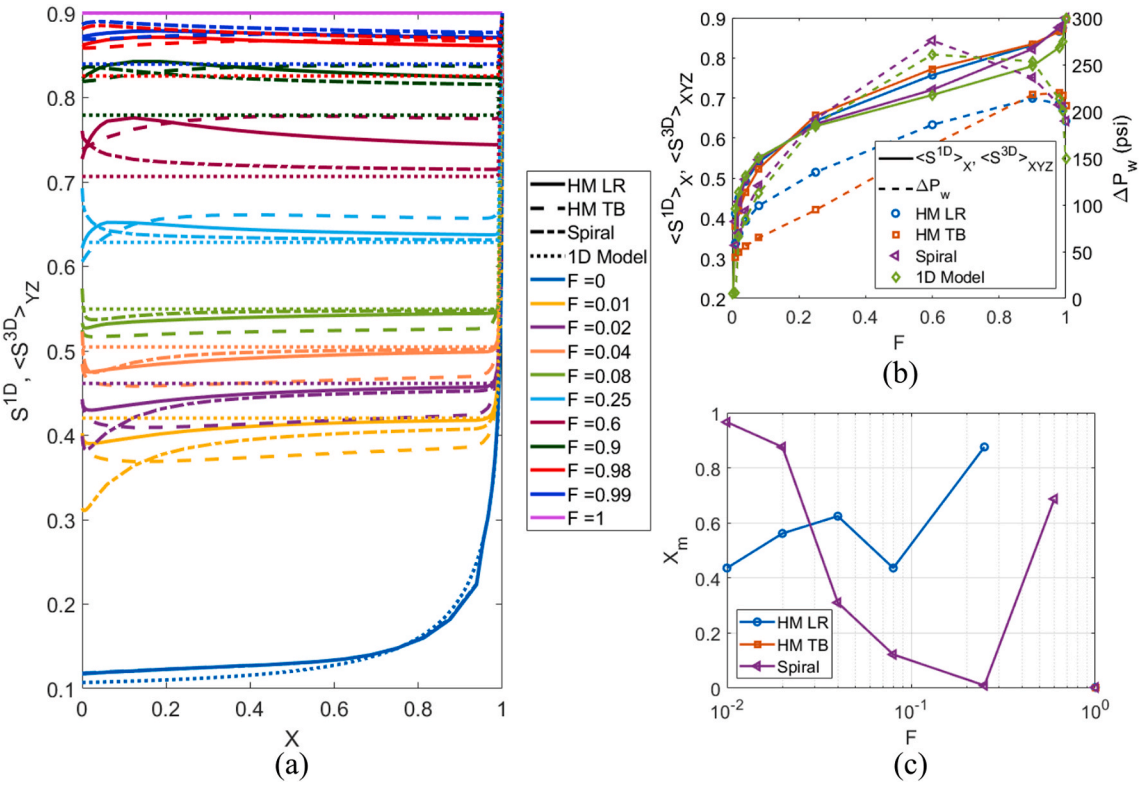

Fig. 10. Comparison between steady-state measurements for 1D and 3D with different distributor geometries for an anisotropic core for each injected water fraction F: (a) stabilised average water saturation across the core comparison between the 1D model S^{1D} and the different inlet distributors $<S^{3D}>_{YZ}$, (b) stabilised average water saturation of the core for the 1D model $<S^{1D}>_X$ and the 3D model $<S^{3D}>_{XYZ}$ and stabilised pressure drop of water across the core ΔP_w, and (c) dimensionless mixing length X_m for each water fraction F. HM LR, HM TB, and Spiral are the 3D simulations using the Half-moon distributor with half moons positioned left-right, the Half-moon distributor with half moons positioned top-bottom, and the Spiral distributor, respectively.

between the 3D simulations and the 1D model. Therefore, the 3D mixing effects contribute not only to the system at stabilisation, but also the duration and nature of stabilisation. At larger fractional flows, the Spiral and Half-moon simulations clearly show a more elongated transient profile, demonstrating a longer stabilisation time.

Fig. 4c shows the dimensionless stabilisation time for the different F values by the different models. The time required to reach stabilisation in 3D modelling was higher than the time required for the 1D model. Furthermore, the comparison between T_s for the Half-moon and Spiral simulations demonstrates that better mixing reduces the stabilisation time. In all models, the final injection stages, i.e. for $F = 1$, required the longest time to reach stabilisation.

4. Inverse algorithm for 3D models

In this section, we describe the inverse algorithm used to simultaneously determine relative permeability and capillary pressure using the steady-state and transient data obtained from the 3D simulation models, and compare them to the input relative permeability and capillary pressure.

4.1. Methodology

While the effects of 3D flow have been characterised thus far by their effects on 1D flow measurements such as saturation profiles and pressure drop, what remains unclear is whether the 3D incomplete mixing effects impact the derivation of rock-fluid properties by way of inverse modelling. To this end, we treat the 1D measurement data obtained from the 3D simulations and compare the results of the inverse modelling to the inputs used in the simulations. The hypothesis is that if 3D effects do not affect the inverse problem, then the output rock properties ought to be the same as those used as input. The $<S^{3D}>_{XYZ}$ and ΔP_w obtained from the 3D steady-state simulations using the Half-moon and Spiral distributor for the isotropic case were used for the inverse calculation study. See Section 3.1 for the details of these simulations. These results were treated as the 'experimental data' used to determine relative permeability of water K_{rw} and oil K_{ro}, collectively noted as K_r, and capillary pressure P_c.

A detailed procedure for simultaneously determining K_r and P_c in a water-wet rock through inverse modelling can be found in the work by (Borazjani et al., 2021a). Below we provide a brief description of the workflow.

In the particular case of using Eqs. (1)-(3) for relative permeability and capillary pressure, inverse modelling involves the tuning of eight independent constants: $K_{rw|sor}$, $K_{ro|swi}$, λ, P_d, S_{wi}, S_{or}, n, and m. As the core in the simulation was water-wet, S_{or} can be determined directly from the stabilised $<S^{3D}>_{XYZ}$ during the water injection stage (i.e. $F = 1$), i.e., $S_{or} = 1 - <S^{3D}>_{XYZ}$.

The remaining model parameters (namely, $K_{rw|sor}$, $K_{ro|swi}$, λ, P_d, S_{wi}, n, and m) are determined from the SSTT data of $<S^{3D}>_{XYZ}$ and ΔP_w.

Using the transient $<S^{3D}>_{XYZ}$ and ΔP_w data from each injection stage along with the model parameters obtained from the steady-state data as the initial guess, a numerical optimisation was performed to minimise the difference between the transient $<S^{3D}>_{XYZ}$ and ΔP_w predicted by the model and the simulated transient data. Upon the completion of the optimisation study, a set of K_r and P_c for the saturation interval corresponding to that injection stage was obtained.

A complete set of K_r and P_c was obtained by combining the segments from the optimisation of the injection stages. The combined set of results were then fitted with a single, continuous curve using a single set of model parameters that represents the properties of the core.

4.2. Results

Fig. 11 shows the results from the inverse calculations using the simulated data. The corresponding model parameters and the coefficients of determination (R^2), Eq. (13), are presented in Table 4.

$$R^2 = 1 - \sum (y_d - y_m)^2 \Big/ \sum \left(y_d - y_{d,mean}\right)^2, \quad (13)$$

where y_d is the 'experimental data' from the simulations, y_m is the fitted model value, and $y_{d,mean}$ is the arithmetic mean of the 'experimental data'.

Figs. 11a and 11b presents the K_r and P_c curves, respectively, from the Half-moon simulation. Figs. 11c and 11d are the K_r and P_c curves, respectively, from the Spiral simulation. The colourful segments shown in both the K_r and P_c plots were obtained by inverse calculations of the results from each injection stage. The red dotted lines were obtained by fitting the colourful segments by adjusting the model parameters and are the final result for the K_r and P_c derived from the simulation data. The black solid lines were the input K_r and P_c used in the simulation.

The inversely calculated K_r curves from both the Half-moon and Spiral simulations were good matches to the input K_r curves, as shown in Figs. 11a and 11c. The R^2 values in Table 4 show the Spiral simulation had a slightly better match to the input results than the Half-moon simulation. For both distributors, the fitted S_{wi} values were higher than the input value. While this has little effect on the shape of the K_r curves, it means that the derived curves do not cover the entire saturation range explored during the simulations. The effect of this

Table 4
Model parameters and coefficient of determination R^2 for relative permeabilities and capillary pressure obtained by the inverse algorithm.

	Half-moon	Spiral
$K_{rw\|sor}$	0.074	0.067
$K_{ro\|swi}$	0.58	0.55
λ	2.51	2.46
P_d (psi)	3.85	3.34
S_{wi}	0.13	0.14
S_{or}	0.1	0.1
n	3.80	3.81
m	2.41	2.40
$R^2(K_{rw})$	0.92	0.98
$R^2(K_{ro})$	0.99	0.99
$R^2(P_c)$	0.12	0.55

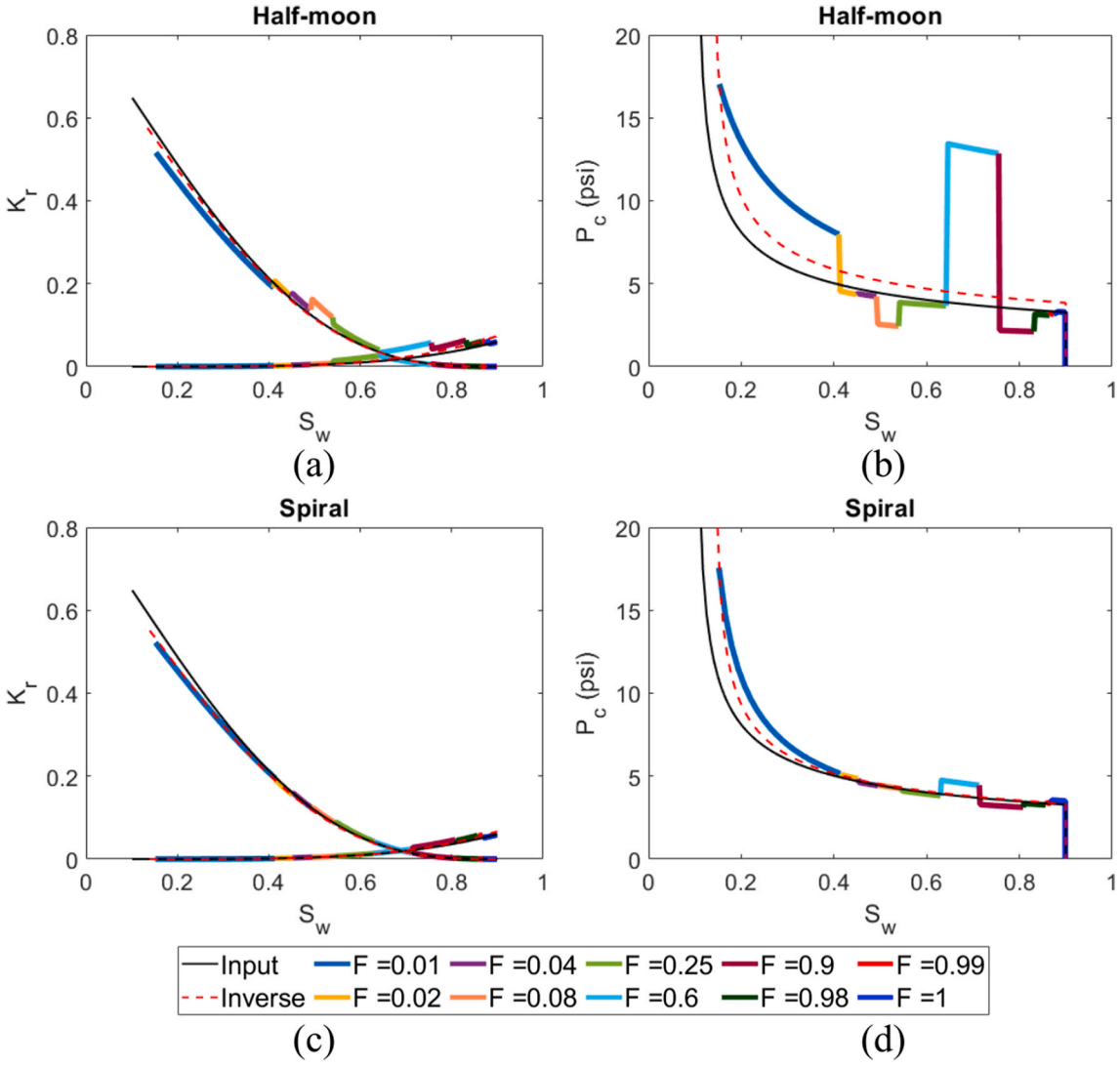

Fig. 11. Inverse modelling of 3D simulation data: (a) and (b) relative permeability K_r and capillary pressure P_c obtained from the Half-moon simulation, respectively, (c) and (d) relative permeability K_r and capillary pressure P_c obtained from the Spiral simulation, respectively. The black solid lines are the simulation input curves, the red dotted lines are derived from fitting the simulation data, and the coloured segments are the inverse solutions obtained from each water fraction F injected. (For interpretation of the references to colour in this figure legend, the reader is referred to the Web version of this article.)

parameter is more significant in the P_c curve, where significant deviation at low saturations is observed for both distributors. The high value of P_d explains the consistent deviation between the derived and input curves for the Half-moon distributor. This deviation is largely a result of the erroneously large capillary pressure predicted during $F = 0.6$ injection stage. For both K_r and P_c, the curves derived from the Spiral simulation exhibit greater continuity than those derived from the Half-moon simulation. Overall, the inverse solutions obtained from the Spiral simulation provided a better match to the input K_r and P_c than the Half-moon simulation.

5. Comparison with laboratory data

In this section we present the SSTT conducted as part of this study, conduct 3D numerical simulation using the experimentally derived rock properties, and obtain relative permeability and capillary pressure through the inverse algorithm from the simulation results.

5.1. Laboratory study

The SSTT used a Berea Sister Gray sandstone core with SOLTROL® 130 Isoparaffin Solvent from Chevron Phillips Chemical as the injected oil phase, and synthetic brine, composed of Milli-Q deionized water (filtrated through a 0.22 μm) and 0.6 M of sodium chloride (laboratory grade, purity 99.7%), as the injected water phase. Rock and fluid properties are shown in Table 5. The temperature, flow rate, confining pressure, and outlet pressure were maintained at 22 °C ± 0.5 °C, 1 ml/min (1.67×10^{-8} m^3/s), 1000 psi (6.90×10^6 Pa), and 300 psi (2.07×10^6 Pa), respectively.

The saturation of the core was conducted by first placing the core under vacuum for 24 hours, then exposing the core to the synthetic brine to achieve 100% saturation. The porosity was determined by the weight difference between the dry and brine saturated core, and the permeability was measured by injecting the brine through undamaged core. In the sequence of performing primary drainage and primary imbibition, each for 50 PVIs of the brine, the irreducible water saturation, S_{wi}, and the residual oil saturation, S_{or}, were determined. Then secondary drainage was performed to minimise the effect of hysteresis. Lastly, secondary imbibition was conducted for the steady-state test with stepwise increase in the injection of brine fractions using a Half-moon distributor positioned top-bottom (HM TB) as shown in Fig. 2d.

A total of 9 injection stages were performed for this test. The brine fraction (F) for the stages were 0.01, 0.03, 0.05, 0.15, 0.50, 0.85, 0.95, 0.97, 1.00. A sensitivity study was performed on the optimum number of injection stages which concluded that the improvement in matching is insignificant beyond 8 stages. For $F = 0$ and $F = 0.5$, the 1D model was used to determine corresponding $<S^{1D}>_X$. The interval between two $<S^{1D}>_X$ values was divided into four equal steps and the corresponding F at each step was selected (i.e. $F = 0$, 0.05, 0.15, and 0.5). For the F interval between 0.5 and 1, the symmetric values were chosen (i.e. $F =$ 0.85, 0.95, and 1). As the transition period is higher at very low and very high F, the transient behaviour at these fractions is more reliable, therefore $F = 0.03$ and its symmetric value $F = 0.97$ were also included.

Table 5
Rock and fluid properties used in the laboratory study.

	Isotropic Core
Rock Properties	
Diameter (m)	0.0376
Length (m)	0.05
Permeability (m^2) [mD]	1.63×10^{-14} [16.47]
Porosity	0.18
Fluid Properties	
Oil viscosity (Pa.s)	0.0011
Water viscosity (Pa.s)	0.001
Oil density (kg/m^3)	763.5
Water density (kg/m^3)	1020

During the test, the differential pressure between the inlet and outlet in each phase was measured in real-time. The laboratory setup is shown in Fig. 12. When the measured differential pressure stabilised during the injection of a given F, the injection would continue for another 10 PVIs before beginning injection with the next F to ensure steady-state condition was achieved. The average saturation of water within the core for each F was measured by sampling the produced fluid. The combination of differential pressure and average core saturations were used to simultaneously predict K_r and P_c.

5.2. Determining K_r and P_c by treating 1D and 3D data using the inverse algorithm

In Section 4, synthetic relative permeability and capillary pressure curves were used in a 3D simulator to assess whether the 3D effects influenced the determination of such curves via inverse modelling. In this section, we perform the same procedure using laboratory data. The K_r and P_c curves used in the simulation are those determined by performing inverse modelling on the laboratory data. Using these curves as input for a 3D simulation will allow determining whether the 3D effects significantly alter the measurement data ($<S^{3D}>_{XYZ}$, ΔP_w) and whether these differences affect the ability to accurately derive the desired rock-fluid properties (K_r and P_c).

A 3D steady-state simulation was performed using a Half-moon distributor, as described in Section 2.1, for an isotropic core with rock and fluid properties as per the laboratory test, shown in Table 6. The Half-moon distributor in the simulation was positioned top-bottom the same as the laboratory set up. From the 3D simulation results, inverse modelling was performed to determine K_r and P_c. The procedure for inverse calculation is the same as that presented in Section 4.1. For comparison purposes, we include the output of the 1D model using the K_r and P_c curves derived from the inverse modelling of the laboratory data. The comparison between the laboratory data, 3D simulation, and 1D model is shown in Fig. 13.

Fig. 13a presents the stabilised average core saturation and the stabilised water pressure drop for each injection stage obtained from the laboratory test (shown in blue), the 3D simulation (shown in orange), and the 1D model (shown in blue). The discrepancies between the laboratory data and modelling is more significant for both $<S^{1D}>_X$ from the 1D modelling and $<S^{3D}>_{XYZ}$ from the 3D modelling than in the ΔP_w measurements. The ΔP_w obtained from the 1D model matched well to the measured ΔP_w from the laboratory test.

Fig. 13b shows the time required for each injection stage to reach stabilisation. The 1D model provided a closer match to the stabilisation time measured in the laboratory study than the 3D simulation. As before, the 3D simulation requires significantly longer time for each injection stage to stabilise.

Figs. 13c and d compare the simulation input K_r and P_c, which were obtained through the inverse modelling of the laboratory data, with the inversely calculated K_r and P_c from the simulation output. Despite the significant difference in stabilised saturations and pressures, and stabilisation time, the relative permeability and capillary pressure curves derived from the 3D simulation data match reasonably well to those derived from the laboratory data. The fitted parameters are shown in Table 6.

6. Discussion

In this work we have illustrated the 3D effects present during SSTT by way of numerical simulation. The results presented in Section 3 show that measurable parameters such as saturation profiles, average saturations and pressures, and stabilisation times are significantly impacted by 3D effects, depending greatly on the inlet distributor, aspect ratio, and permeability anisotropy. In Sections 4 and 5, we investigated what impacts these 3D effects might have on inverse modelling of SSTT. The

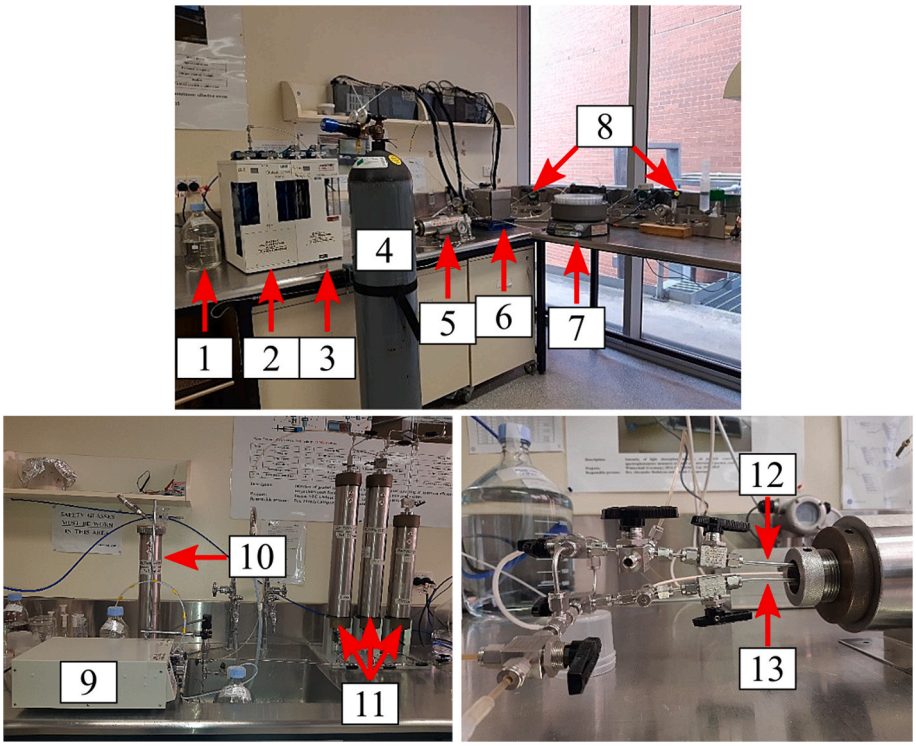

Fig. 12. Steady-state transient test (SSTT) experimental setup: (1) brine tank, (2) brine injection pump, (3) oil injection pump, (4) overburden pressure cylinder, (5) cardholder, (6) back-pressure regulator, (7) sampling carousel, (8) differential pressure transmitters, (9) pump, (10) refilling cylinder, (11) transfer vessels, (12) brine injection line, and (13) oil injection line.

Table 6
Model parameters and coefficient of determination R^2 obtained from inverse algorithm of results from laboratory experiment and 3D model with Half-moon distributor.

	Laboratory	3D model
$K_{rw\|sor}$	0.03	0.03
$K_{ro\|swi}$	0.71	0.98
λ	1.74	1.45
P_d (psi)	5.07	4.73
S_{wi}	0.24	0.18
S_{or}	0.26	0.26
n	1.58	4.38
m	2.16	2.24
$R^2(K_{rw})$	–	0.58
$R^2(K_{ro})$	–	0.98
$R^2(P_c)$	–	0.75

results showed that depending on the magnitude and nature of the 3D effects, arising due to incomplete mixing, the extraction of relative permeabilities and capillary pressure from 1D data can be affected.

6.1. Consequences for laboratory design

While 3D effects have been made clear in this study, any practitioner performing laboratory tests will naturally be unaware of the magnitude and impact of such effects. The results of this work can be used to provide suggestions to minimise any errors introduced by incomplete mixing. Firstly, as shown in Sections 3.1, when using the common Half-moon distributor, the alignment of the two distributor sections can be important. For the studied fluids, gravitational segregation, or gravity-assisted mixing were insignificant. For two-phase or even three-phase studies with significant density differences between the injected fluids (such as during natural gas production), gravity may play a larger role, and injection of the heavier fluid into the top half of the core may assist mixing. Such effects were not observed in this study due to the densities of the two fluids being too similar. However, the alignment of the two Half-moons was significant when permeability anisotropy was introduced. To this end, maximisation of fluid mixing is achieved when the half moons are aligned such that fluid transfer between the two half moons is aligned with the direction of highest permeability. In practice, many cores exhibit lower vertical permeability due to horizontal bed layering, and as such the half moons should be aligned to the left and right of each other. A study of incomplete mixing in the presence of strong gravitational mixing and permeability anisotropy would be informative for gas production and gas storage studies.

Another recommendation that follows from this study is that the Spiral distributor will create a greater degree of mixing than the Half-moons. These results cannot be stated generally however, and experiments with different rock and fluid properties may observe different outcomes. Generally, the notion that creating a larger fluid-fluid interface in the distributor creates a greater degree of mixing is supported by this study. Further investigation could lead to the optimal design of an inlet distributor so long as the physical limitations of the grooves and sealing components on the distributor are not compromised.

Lastly, the study demonstrated that laboratory tests ought to be performed on sufficiently long cores to prevent adverse effects from 3D mixing. Core lengths are typically limited due to core availability. A quantitative criterion for the core length is not presented in this work. Such a criterion must be dependent on the rock and fluid properties, distributor geometry, as well as the criteria used to define a successful experiment. In Section 4, we demonstrated that varying degrees of mixing can result in differing success in extracting the correct relative permeability and capillary pressure functions. The emergence of non-uniqueness problems, or unsatisfactory degrees of uncertainty in inverse modelling could be used to describe the 'success' of an experiment. This relies on the view that experiments are being run purely to extract these rock properties. Tests run to derive other properties, or tests run for entirely different reasons, might construct other definitions of success.

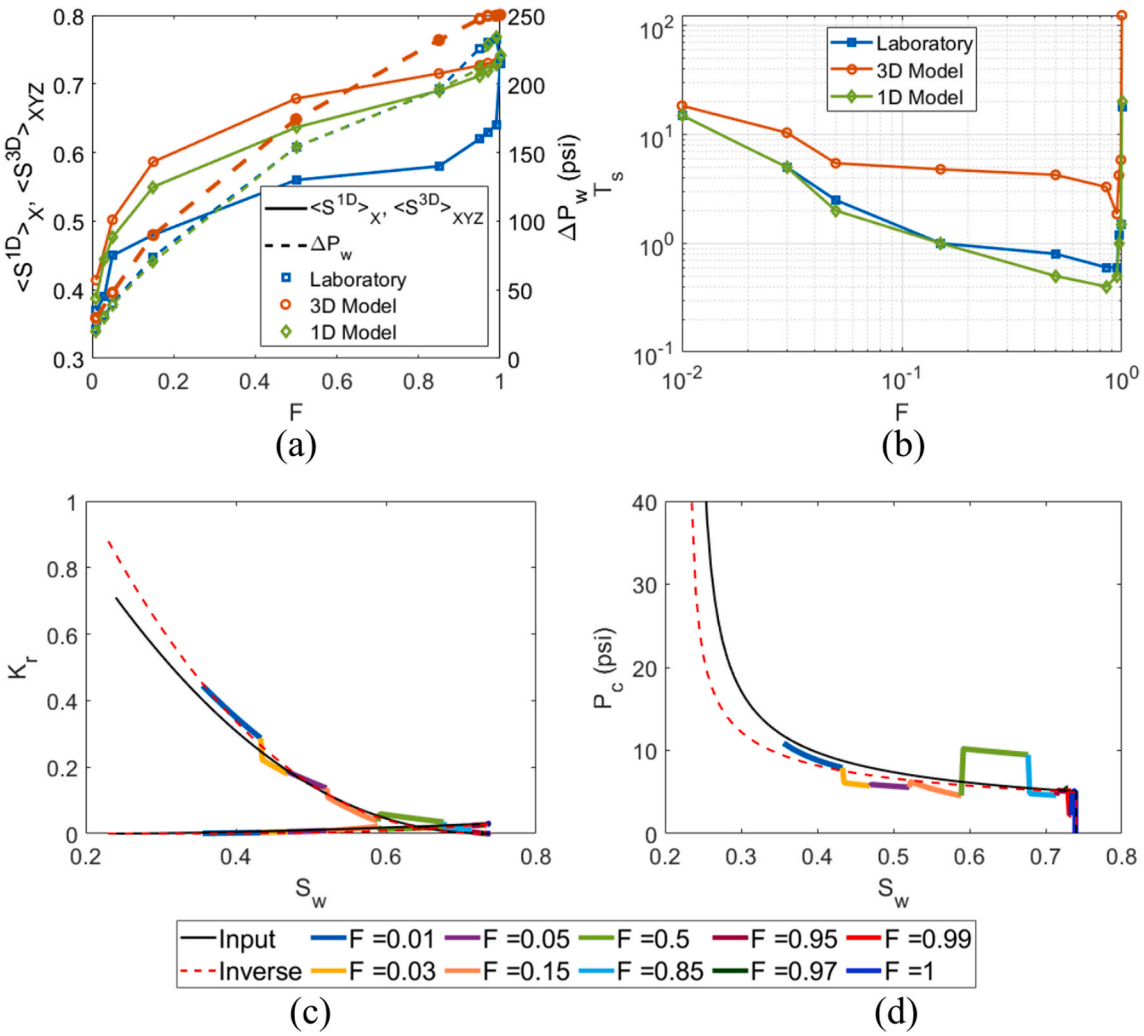

Fig. 13. Comparison between laboratory and modelling results: (a) stabilised average water saturation of the core for the 1D model $<S^{1D}>_X$ and the 3D model $<S^{3D}>_{XYZ}$ and pressure drop of water across the core ΔP_w for each water fraction F injected, (b) stabilisation time T_s for each F injected, (c) and (d) relative permeability K_r and capillary pressure P_c obtained from fitting the 3D model data, respectively. The black solid lines are the simulation input curves from fitting the laboratory data, the red dotted lines are derived from fitting the simulation data, and the coloured segments are the inverse solutions obtained from each injection stage. (For interpretation of the references to colour in this figure legend, the reader is referred to the Web version of this article.)

The longer is the core, the lower is the capillary-viscous ratio ε (Rapoport-Leas number), given by Eq. (6). This number expresses the impact of capillary pressure into solutions of the forward and inverse problems (4–10), i.e. relative permeability can be determined from steady-state data for $\varepsilon \ll 1$. For the laboratory test presented in section five, $\varepsilon = 2.0$, i.e. the application of SSTT method that accounts for capillary pressure is essential.

Regarding the numerical experiments, presented in section two, $\varepsilon = 0.65$. The corresponding saturation profiles exhibit end effect, and the profiles for 1D and 3D highly match (Fig. 3b). However, the capillary-viscous ratio is not small enough to disregard P_c. The first-order asymptotic expansion accounting for capillary pressure, developed by Hussain et al. (2012), is valid for ε that does not exceed 0.3–0.5, i.e. the explicit asymptotic expressions are not valid for $\varepsilon = 0.65$ (Al-Sarihi et al., 2020).

6.2. On the forward and inverse problems

In Section 3, we focussed on the 'forward problem', where rock and fluid properties are known, and measurements, such as the saturation profile, stabilised pressure drop, etc., are calculated. In Sections 4 and 5, we presented results for the 'inverse problem', where these measurements are used to derive the rock properties. As is shown in Fig. 7b, while the 3D simulation and 1D model present vastly different results for the forward problem, Fig. 11 shows that performing inverse modelling on the outputs produces similar relative permeability and capillary pressure curves. There are two hypotheses to explain this phenomenon. Firstly, it is possible that the stability, or sensitivity to perturbation, of the forward and inverse problems differs greatly. This is a function only of the 1D model for two-phase flow. Secondly, it is possible that certain changes induced in the measurements by the 3D effects have no impact on the inverse problem. It is shown in Fig. 11 that in certain cases, where incomplete mixing is more severe, the inverse problem is also affected. The question of what changes to the forward problem will affect the inverse problem is dependent on the nature of the equations for two-phase flow and is beyond the scope of this study.

Similar phenomenon of more conservative inverse solution than the forward solution was observed by Hussain et al. (2012) and Al-Sarihi et al. (2020), with respect to small capillary pressure during continuous displacement of oil by water. The fact of more conservative inverse solution (calculated relative permeability and capillary pressure) than the forward solution (measured or predicted by modelling pressure-drop and water-cut) supports using SSTT in short cores.

6.3. Adequacy of 3D modelling of two-phase flow in coreflooding

The boundary conditions in the 3D model reflect full occupation of the grooves by the respective phases, i.e. that the injection actually occurs according to the geometry of the inlet piece. However, Berg (2021) observed that fluids were indeed continuous in the respective part of the inlet, but not such that each fluid filled their full share of the groove structure. These observations were made by imaging the inlet piece and also by 3D micro-CT in-situ during the experiment. In that sense, it is not a given that the injection actually occurs to the same extent as the designed geometry would suggest, and what the 3D numerical model assumes.

The assumption of complete segregation of the fluids within the inlet distributor also leads to visible effects of the distributor geometry on the 3D saturation distribution. Indeed, Figs. 6b and 6e and 6h show the segregated flow at the core outlets with transition zones determined by capillary imbibition; this flux structure is supported by the negligible values of the gravity-capillary ratio given by Eq. (12). However, several experimental works have measured the 3D saturation distribution during corefloods and did not find evidence of such substantial segregation of the injected fluids (Berg et al., 2013; Berg and Ott, 2012). The authors of these studies demonstrated how segregation resulting from heterogeneity and fingering instabilities is diminished by capillary pressure. More complex simulations of the distributions of fluids within the distributor may resolve the observed differences between the numerical simulations and experiments.

Another aspect of the adequacy of the 3D modelling is the ability to accurately derive the correct rock properties by way of inverse modelling. The results in this work show that the observed 3D mixing effects do not greatly inhibit the inverse modelling. Recent studies of inverse modelling of two-phase coreflooding data using Bayesian inversion (Berg et al., 2021; Valdez et al., 2020, 2021) highlighted the importance of the form of relative permeabilities and capillary pressure. Therefore, a complete and general investigation of the adequacy of the 3D simulations in this study ought to cover a range of these functions (e.g. LET, Brooks-Corey) and resolve questions around parameter uncertainty ranges and uniqueness.

6.4. Extensions of the method

SST and SSTT techniques can be applied for two-phase multicomponent flows, which are typical for enhanced oil recovery (Bedrikovetsky et al., 2009; Borazjani et al., 2019; Farajzadeh et al., 2013, 2017; Hao et al., 2019; Hussain et al., 2013; Lake et al., 2014; Rabinovich et al., 2015, 2019; Sorop et al., 2015). In the case of partly miscible flooding, two equilibrium phases must be co-injected. The mixture of the injected and reservoir fluid separates into immiscible phases before the test, and no interface mass transfer occurs during the commingled injections. In particular, wet CO_2 and saturated by CO_2 water must be used to determine K_r and P_c by SSTT (Zhang et al., 2020).

In the case of low-salinity waterflooding, the breakthrough ion concentrations are measured during SSTT. This adds adsorption isotherms of ions to the list of determined functions (K_r and P_c) from the SSTT data (Borazjani et al., 2017). SSTT method can be applied to sequential drainage and imbibition, to recover the hysteretic effects on K_r and P_c (Plohr et al., 2001; Schaerer et al., 2006).

However, relative permeability and capillary pressure are function not only of saturation, but also of the equilibrium component concentrations; so different combinations of the injected and reservoir fluid must be used in SSTs or SSTTs to cover the concentration-dependencies.

The theory of two-phase flow in porous media accounting for moving interface menisci results in a description of relative permeability different to that given by Eqs. 4 and 5 (Shapiro, 2015, 2016, 2018). The formulation for steady-state coreflood tests and the experimental protocol must be changed accordingly.

7. Conclusions

In this study 3D numerical simulations of two-phase steady-state transient test (SSTT) for different inlet distributor geometries, aspect ratios, and permeability anisotropy were performed. Relative permeability and capillary pressure curves were simultaneously determined using an inverse algorithm from the simulated results, and compared to the 'true' and experimental relative permeability and capillary pressure curves. The results of these analyses allow making the following conclusions:

1. Accounting for the 3D effects of flow results in incomplete mixing, an inlet effect on the saturation profile, and longer stabilisation times. 3D simulations exhibit longer times until fluid saturations stabilise than 1D. The more incomplete is the mixing, the longer the stabilisation time.
2. Injection of the two phases into different areas of the distributor results in non-uniform fluid saturations in cross-sections throughout the core, which reflects the geometry of the distributor. This effect is more significant when the core exhibits anisotropic permeability.
3. At the typical aspect ratios for reservoir cores, gravity effects are negligible, so 3D modelling data for left-right and top-bottom Half-moon distributors are almost the same.
4. The relative permeability and capillary pressure curves derived from fitting the 3D simulation data differed from the simulation inputs for the Half-moon distributor, but good agreement was achieved when using the Spiral distributor. A Spiral distributor provides a closer agreement between 1D and 3D modelling than a Half-moon distributor in both isotropic and anisotropic cores, yielding to more precise determination of relative permeability and capillary pressure drop SSTT data.
5. Increasing core length from 0.05 m to 0.15 m enhances mixing in isotropic cores.
6. When the vertical permeability is lower than the horizontal permeability, vertical mixing is inhibited, so injecting the two phases into the left and right halves of the core (left-right half moons) results in greater mixing than injecting into the top and bottom halves despite the effects of gravitational mixing.
7. Introducing permeability anisotropy reduces mixing in all cases.
8. Cross-section images in 3D are very different from 1D.
9. Numerical 3D simulation was conducted using inversely fitted laboratory relative permeability and capillary pressure curves. Despite the differences observed in the 3D simulated and laboratory stabilised average water saturation and pressure drop of water across the core, relative permeability and capillary pressure curves obtained by inversely solving the 3D simulation results are good match to the laboratory curves.
10. More conservative inverse SSTT solution than the forward solution supports the use of SSTT for determination of relative permeability and capillary pressure.

Credit author statement

Shuyan Yang: numerical modelling, formulation of conclusions, writing. Nassim Hemmati: laboratory study, Thomas Russell: discussion of results, formulation of conclusions, writing and editing. Abbas Zeinijahromi: formulating the laboratory study protocol. Sara Borazjani: development of numerical algorithm, editing. Aron Behr: formulation of numerical study and result analysis. Luis Genolet: formulation of laboratory study and result analysis. Pavel Bedrikovetsky: methodology and supervision.

Declaration of competing interest

The authors declare that they have no known competing financial

interests or personal relationships that could have appeared to influence the work reported in this paper.

Acknowledgements

Dr. A. Badalyan was extremely helpful in organising and discussing the laboratory study. This work was motivated by encouraging communications with Drs. J. Maas (Consultant, EOR, SCAL, Geothermal) and S. Berg (Shell); their contribution is gratefully acknowledged. PB gratefully remembers his teachers in petroleum engineering Profs K. Basniev, S. Zakirov and A. Kurbanov (Gubkin Russian State University of Oil and Gas).

Nomenclature

A	Cross-sectional area, m^2
A_r	Aspect ratio, -
CC	Geometric factor in CMG STARS, -
f	Fraction flow function, -
F	Water fraction, -
g	Gravitational acceleration, m/s^2
h	Depth, m
J	Leverett *J*-function, -
K	Absolute permeability, m^2
K_r	Relative permeability, -
$K_{ro\|swi}$	Relative permeability of oil at initial water saturation, -
$K_{rw\|sor}$	Relative permeability of water at residual oil saturation, -
L	Core length, m
m	Corey exponent, -
n	Corey exponent, -
P_c	Capillary pressure, Pa
P_d	Displacement pressure, Pa
P	Pressure, Pa
P^-	Dimensionless pressure, -
q_k	Sink/source flux, m^3/s
r	Radius, m
R^2	Coefficient of determination, -
$<S^{1D}>_X$	Water saturation from the 1D model averaged over the entire core, -
$<S^{3D}>_{YZ}$	Water saturation from the 3D simulation averaged over a given cross-section of the core, -
$<S^{3D}>_{XYZ}$	Water saturation from the 3D simulation averaged over the entire core, -
S_{or}	Residual oil saturation, -
S_{wi}	Initial water saturation, -
S_w	Water saturation, -
t	Time, s
T	Dimensionless time, -
T_s	Dimensionless stabilisation time, -
T_w	Water transmissibility, -
U	Darcy's velocity, m/s
V_f	Total fluid volume, m^3
x	Linear coordinate, m
X	Dimensionless linear coordinate, -
X_m	Dimensionless mixing length, -
y_d	Experimental data
$y_{d,mean}$	Arithmetic mean of the experimental data
$y^{\neg}{}_m$	Fitted model data

Greek letters

Δ	Difference
ε	Capillary-viscous ratio, -
θ	Contact angle, -
Φ	Potential, m^2/s
λ	Pore size distribution index, -
μ	Viscosity, Pa.s
ρ	Density, kg/m^3
σ	Oil/water interfacial tension, mN/m
ϕ	Porosity, -

Subscripts

e	Reservoir
eff	Effective

o	Oil phase
T	Total
w	Water phase

Appendix A. Equations used in CMG STARS

In this Appendix we present the equations solved by CMG STARS to derive fluid saturations, pressures, etc. Only equations relevant to the simulations used in this study are included.

First, we present the mass conservation equation for water:

$$\frac{\partial}{\partial t}V_f\rho_w S_w = \sum_{k=1}^{n_f} T_w\rho_w\Delta\Phi_w + \rho_w q_{wk}, \tag{A.1}$$

where t is the time, V_f is the total fluid volume, ρ_w is the water density, S_w is the water density, T_w is the water transmissibility, Φ_w is the water potential, and q_{wk} is the sink/source flux. The first term on the right-hand-side accounts for flux, and the potential gradient $\Delta\Phi_w$ is calculated for all n_f neighbouring grid-blocks. In this simulation study, the second term on the right-hand side is only present in grid-blocks with a connecting well.

The conservation equation for oil is:

$$\frac{\partial}{\partial t}V_f\rho_o S_o = \sum_{k=1}^{n_f} T_o\rho_o\Delta\Phi_o + \rho_o q_{ok}, \tag{A.2}$$

where ρ_o, S_o, T_o, and Φ_o are the density, saturation, transmissibility, and flow potential for oil, respectively.

The transmissibility for component j is defined as:

$$T_j = \left(\frac{A}{l}\right)^{eff}\frac{K_{rj}}{\mu_j}K^{eff},\ j = w, o. \tag{A.3}$$

where A is the cross-sectional area to flow (between adjacent grid-blocks), l is the distance between grid-block centres, K_{rj} is the relative permeability of component j, μ_j is the viscosity of component j, and K is the absolute permeability. The superscript *eff*, short for effective, refers to the process of calculating properties at the interface between two grid-blocks to calculate flow between them. The effective permeability is an area weighted average of the permeabilities of the two grid-blocks. Relative permeability, viscosity, and density are taken from the phase upstream region.

The fluid potential for phase j is defined as:

$$\Phi_j = P_j - \rho_j g h, j = w, o. \tag{A.4}$$

The boundary conditions equate to constraining fluid movement on the outer boundary of the core.

The equation describing the well flow terms is:

$$q_{jk} = I_k\left(P_{wfk} - P_k\right)\frac{K_{rj}}{\mu_j}, \tag{A.5}$$

where P_{wfk} is the well flowing pressure in layer k of the well completion, P_k is the reservoir pressure in block k, and

$$I_k = \frac{2\pi h K f_h f_w}{\ln\left(\frac{r_e}{r_w}\right) + s}, \tag{A.6}$$

where h is the layer thickness, K is the absolute permeability normal to the wellbore direction, f_h is the layer thickness factor (accounting for partial completion, $f_h = 1$ in this study), f_w is the well fraction ($f_w = 1$ for wells in the centre of grid blocks, as in this study), r_w is the wellbore radius, s is the skin factor and r_e is the effective wellbore radius, given by:

$$r_e = CC\sqrt{\frac{\Delta x^2 + \Delta y^2}{f\pi}}, \tag{A.7}$$

where CC is a geometrical factor (equal to 0.235 for a well in an edge block, as in this study), and Δx and Δy are the block dimensions in the plane perpendicular to the wellbore.

For injection wells, the fluid properties are taken from the wellbore conditions, while in production wells they are taken from the connected grid-block.

In this study, all injection wells are rate controlled in order to achieve fixed injection rates. For the 3D simulation with uniform inlet boundary conditions, the rate is given by:

$$q_{inj} = q_w + q_o = Fq_T + (1 - F)q_T. \tag{A.8}$$

For the other simulations, there were two injectors, one for each of the two phases, with rates determined by the fractional flow, F:

$$q_{inj,w} = Fq_T, \tag{A.9}$$

$$q_{inj,o} = (1 - F_n) q_T. \tag{A.10}$$

For these wells, the well flowing pressure is calculated as per Eq. (A.5).

The single production well at the core outlet is controlled by bottom-hole pressure. This value is maintained at the backpressure used in laboratory studies (see Section 5). The production rate is calculated in CMG STARS by Eq. (A.5).

The initial conditions of the experiment are:

$$T = 0 : S_w = 1 - S_{or}, P = P_e, \tag{A.11}$$

where P_e is the reservoir pressure.

Appendix B. Supplementary data

Supplementary data to this article can be found online at https://doi.org/10.1016/j.petrol.2021.109533.

References

!"count(.//sb:host[1]//child::*//sb:date)">Al-Sarihi, A., You, Z., Behr, A., Genolet, L., Kowollik, P., Zeinijahromi, A., Bedrikovetsky, P., . Admissible parameters for two-phase coreflood and Welge–JBN method. Transport Porous Media 131, 831–871.

Barenblatt, G.I., Entov, V.M., Ryzhik, V.M., 1989. Theory of Fluid Flows through Natural Rocks.

Bedrikovetsky, P., 2013. Mathematical Theory of Oil and Gas Recovery: with Applications to Ex-USSR Oil and Gas Fields. Springer Science & Business Media.

Bedrikovetsky, P.G., Mackay, E.J., Silva, R.M., Patricio, F.M., Rosário, F.F., 2009. Produced water re-injection with seawater treated by sulphate reduction plant: injectivity decline, analytical model. J. Petrol. Sci. Eng. 68, 19–28.

Berg, S., 2021. RE: Observations in 3D Two-phase Coreflood Experiments.

Berg, S., Oedai, S., Ott, H., 2013. Displacement and mass transfer between saturated and unsaturated CO2–brine systems in sandstone. Int. J. Greenh. Gas Contr. 12, 478–492.

Berg, S., Ott, H., 2012. Stability of CO2–brine immiscible displacement. Int. J. Greenh. Gas Contr. 11, 188–203.

Berg, S., Unsal, E., Dijk, H., 2021. Sensitivity and uncertainty analysis for parameterization of multiphase flow models. Transport in Porous Media, pp. 1–31.

Borazjani, S., Behr, A., Genolet, L., Kowollik, P., Bedrikovetsky, P., 2019. Ion-exchange inverse problem for low-salinity coreflooding. Transport Porous Media 128, 571–611.

Borazjani, S., Behr, A., Genolet, L., Van Der Net, A., Bedrikovetsky, P., 2017. Effects of fines migration on low-salinity waterflooding: analytical modelling. Transport Porous Media 116, 213–249.

Borazjani, S., Hemmati, N., Behr, A., Genolet, L., Mahani, H., Zeinijahromi, A., Bedrikovetsky, P., 2021a. Determining water-oil relative permeability and capillary pressure from steady-state coreflood tests. J. Petrol. Sci. Eng. 205, 108810.

Borazjani, S., Hemmati, N., Behr, A., Genolet, L., Mahani, H., Zeinijahromi, A., Bedrikovetsky, P., 2021b. Simultaneous determination of gas–water relative permeability and capillary pressure from steady-state corefloods. J. Hydrol. 598, 126355.

Braun, E., Holland, R., 1995. Relative permeability hysteresis: laboratory measurements and a conceptual model. SPE Reservoir Eng. 10, 222–228.

Chen, X., Kianinejad, A., Dicarlo, D.A., 2016. An extended JBN method of determining unsteady-state two-phase relative permeability. Water Resour. Res. 52, 8374–8383.

CMG, 2016. Stars User Guide: Advanced Processes & Thermal Reservoir Simulator. Computer Modelling Group, Calgary, Alberta Canada.

Farajzadeh, R., Ameri, A., Faber, M.J., Van Batenburg, D.W., Boersma, D.M., Bruining, J., 2013. Effect of continuous, trapped, and flowing gas on performance of alkaline surfactant polymer ASP flooding. In: SPE Enhanced Oil Recovery Conference. OnePetro.

Farajzadeh, R., Guo, H., Van Winden, J., Bruining, J., 2017. Cation exchange in the presence of oil in porous media. ACS Earth Space Chem. 1, 101–112.

Gupta, R., Maloney, D., 2015. Applications of the intercept method to correct steady-state relative permeability for capillary end-effects. Int. Symp. Soc. Core Anal. Held St. John's Nfld. Labrador Can. 16–21.

Gupta, R., Maloney, D., Laverick, D., Longoria, R., Poore, L., Spitzenberger, J., 2016. A novel laboratory method for determining capillary pressure and wettability while measuring steady state relative permeability. In: International Symposium of the Society of Core Analysts. Snowmass, Colorado.

Gupta, R., Maloney, D.R., 2019. Intercept method—a novel technique to correct steady-state relative permeability data for capillary end effects. SPE Reservoir Eval. Eng. 19, 316–330.

Hao, J., Mohammadkhani, S., Shahverdi, H., Esfahany, M.N., Shapiro, A., 2019. Mechanisms of smart waterflooding in carbonate oil reservoirs-A review. J. Petrol. Sci. Eng. 179, 276–291.

Hussain, F., Cinar, Y., Bedrikovetsky, P., 2012. A semi-analytical model for two phase immiscible flow in porous media honouring capillary pressure. Transport Porous Media 92, 187–212.

Hussain, F., Pinczewski, W.V., Cinar, Y., Arns, J.-Y., Arns, C., Turner, M., 2014. Computation of relative permeability from imaged fluid distributions at the pore scale. Transport Porous Media 104, 91–107.

Hussain, F., Zeinijahromi, A., Bedrikovetsky, P., Badalyan, A., Carageorgos, T., Cinar, Y., 2013. An experimental study of improved oil recovery through fines-assisted waterflooding. J. Petrol. Sci. Eng. 109, 187–197.

Johnson, E., Bossler, D., Bossler, V., 1959. Calculation of relative permeability from displacement experiments. Trans. AIME 216, 370–372.

Jones, S., Roszelle, W., 1978. Graphical techniques for determining relative permeability from displacement experiments. J. Petrol. Technol. 30, 807–817.

Krause, M.H., Benson, S.M., 2015. Accurate determination of characteristic relative permeability curves. Adv. Water Resour. 83, 376–388.

Kuo, C.-W., Benson, S.M., 2015. Numerical and analytical study of effects of small scale heterogeneity on CO2/brine multiphase flow system in horizontal corefloods. Adv. Water Resour. 79, 1–17.

Lake, L.W., Johns, R., Rossen, B., Pope, G.A., 2014. Fundamentals of Enhanced Oil Recovery. Richardson, TX, Society of Petroleum Engineers.

Maas, J.G., Flemisch, B., Hebing, A., 2011. Open source simulator DuMux available for SCAL data interpretation. In: International Symposium of the Society of Core Analysts. Austin, Texas.

Mcphee, C., Reed, J., Zubizarreta, I., 2015. Core Analysis: a Best Practice Guide. Elsevier.

Plohr, B., Marchesin, D., Bedrikovetsky, P., Krause, P., 2001. Modeling hysteresis in porous media flow via relaxation. Comput. Geosci. 5, 225–256.

Rabinovich, A., 2017. Estimation of sub-core permeability statistical properties from coreflooding data. Adv. Water Resour. 108, 113–124.

Rabinovich, A., Anto-Darkwah, E., Mishra, A., 2019. Determining characteristic relative permeability from coreflooding experiments: a simplified model approach. Water Resour. Res. 55, 8666–8690.

Rabinovich, A., Itthisawatpan, K., Durlofsky, L.J., 2015. Upscaling of CO2 injection into brine with capillary heterogeneity effects. J. Petrol. Sci. Eng. 134, 60–75.

Rabinovich, A., Li, B., Durlofsky, L.J., 2016. Analytical approximations for effective relative permeability in the capillary limit. Water Resour. Res. 52, 7645–7667.

Reed, J., Maas, J., 2018. Review of the intercept method for relative permeability correction using a variety of case study data. In: The International Symposium of the Society of Core Analysts.

Reed, J., Maas, J., 2019. Review of the intercept method for relative permeability correction a variety of case study data. Petrophys. SPWLA J. Format. Eval. Reserv. Descr. 60, 283–296.

Schaerer, C.E., Marchesin, D., Sarkis, M., Bedrikovetsky, P., 2006. Permeability hysteresis in gravity counterflow segregation. SIAM J. Appl. Math. 66, 1512–1532.

Shapiro, A.A., 2015. Two-phase immiscible flows in porous media: the Mesocopic Maxwell–Stefan approach. Transport Porous Media 107, 335–363.

Shapiro, A.A., 2016. Mechanics of the separating surface for a two-phase co-current flow in a porous medium. Transport Porous Media 112, 489–517.

Shapiro, A.A., 2018. A three-dimensional model of two-phase flows in a porous medium accounting for motion of the liquid–liquid interface. Transport Porous Media 122, 713–744.

Shapiro, A.A., 2021. Continuous upscaling and averaging. Chem. Eng. Sci. 234, 116454.

Sorop, T.G., Masalmeh, S.K., Suijkerbuijk, B.M., Van Der Linde, H.A., Mahani, H., Brussee, N.J., Marcelis, F.A., Coorn, A., 2015. Relative Permeability Measurements to Quantify the Low Salinity Flooding Effect at Field Scale. Abu Dhabi International Petroleum Exhibition and Conference, OnePetro.

Tikhonov, A.N., Goncharsky, A., Stepanov, V., Yagola, A.G., 2013. Numerical Methods for the Solution of Ill-Posed Problems. Springer Science & Business Media.

Valdez, A.R., Rocha, B.M., Chapiro, G., Dos Santos, R.W., 2020. Uncertainty quantification and sensitivity analysis for relative permeability models of two-phase flow in porous media. J. Petrol. Sci. Eng. 192, 107297.

Valdez, A.R., Rocha, B.M., Da Fonseca Facanha, J.M., De Souza, A.V.O., Perez-Gramatges, A., Chapiro, G., Dos Santos, R.W., 2021. Foam-assisted water–gas flow parameters: from core-flood experiment to uncertainty quantification and sensitivity analysis. Transport in Porous Media, pp. 1–21.

Virnovsky, G., Guo, Y., Skjaeveland, S.M., 1995. Relative permeability and capillary pressure concurrently determined from steady-state flow experiments. In: IOR 1995-8th European Symposium on Improved Oil Recovery. European Association of Geoscientists & Engineers cp-107-00007.

Virnovsky, G., Vatne, K., Skjaeveland, S., Lohne, A., 1998. Implementation of multirate technique to measure relative permeabilities accounting for capillary effects. SPE Annual Technical Conference and Exhibition, OnePetro.

Wang, Y., Masalmeh, S.K., 2019. Obtaining high quality scale data: combining different measurement techniques, saturation monitoring, numerical interpretation and continuous monitoring of experimental data. In: E3S Web of Conferences. EDP Sciences, p. 2007.
Welge, H.J., 1952. A simplified method for computing oil recovery by gas or water drive. J. Petrol. Technol. 4, 91–98.
Zhang, X., Ge, J., Kamali, F., Othman, F., Wang, Y., Le-Hussain, F., 2020. Wettability of sandstone rocks and their mineral components during CO2 injection in aquifers: implications for fines migration. J. Nat. Gas Sci. Eng. 73, 103050.
Zou, S., Hussain, F., Arns, J., Guo, Z., Arns, C.H., 2018. Computation of relative permeability from in-situ imaged fluid distributions at the pore scale. SPE J. 23, 737–749.

7. Laboratory validation of a steady-state-transition test for determining relative permeability and capillary pressure

Hemmati, N., Borazjani, S., **Yang, S.**, Badalyan, A., Genolet, L., Behr, A., Zeinijahromi, A., and Bedrikovetsky, P.

Fuel, 321, 123940.

Statement of Authorship

Title of Paper	Laboratory validation of steady-state-transient test to determine relative permeability and capillary pressure
Publication Status	☑ Published ☐ Accepted for Publication ☐ Submitted for Publication ☐ Unpublished and Unsubmitted work written in manuscript style
Publication Details	Hemmati, N., Borazjani, S., Yang, S., Badalyan, A., Genolet, L., Behr, A., Zeinijahromi, A., and Bedrikovetsky, P. (2022). Laboratory validation of steady-state-transient test to determine relative permeability and capillary pressure. Fuel, 321, 123940.

Principal Author

Name of Principal Author (Candidate)	Shuyan Yang		
Contribution to the Paper	Developed 3D models, performed scenario investigation, result analysis, inverse modelling of the 3D results		
Overall percentage (%)	40%		
Certification:	This paper reports on original research I conducted during the period of my Higher Degree by Research candidature and is not subject to any obligations or contractual agreements with a third party that would constrain its inclusion in this thesis. I am the primary author of this paper.		
Signature		Date	07/05/2022

Co-Author Contributions

By signing the Statement of Authorship, each author certifies that:

i. the candidate's stated contribution to the publication is accurate (as detailed above);

ii. permission is granted for the candidate in include the publication in the thesis; and

iii. the sum of all co-author contributions is equal to 100% less the candidate's stated contribution.

Name of Co-Author	Nassim Hemmati		
Contribution to the Paper	Performed laboratory experiments, data treatment and interpretation, inverse modelling of the laboratory results		
Signature		Date	09.05.2022

Name of Co-Author	Sara Borazjani		
Contribution to the Paper	Development of inverse modelling, technical discussion, manuscript preparation		
Signature		Date	10.05.2022

Name of Co-Author	Abbas Zeinijahromi
Contribution to the Paper	Laboratory procedure development, performed laboratory tests. technical discussions
Signature	Date 10/05/2022

Name of Co-Author	Aron Behr
Contribution to the Paper	Technical discussions, laboratory experiment design and problem formulation
Signature	Date 12/05/2022

Name of Co-Author	Luis Genolet
Contribution to the Paper	Technical discussions, laboratory experiment design and problem formulation
Signature	Date 13/05/2022

Name of Co-Author	Alex Badalyan
Contribution to the Paper	Technical discussions, Laboratory procedure development, performed laboratory tests
Signature	Date 12.05.2022

Name of Co-Author	Pavel Bedrikovetsky
Contribution to the Paper	Problem formulation, technical discussions, supervision of the project, manuscript preparation
Signature	Date 09/05/2022

Fuel 321 (2022) 123940

Contents lists available at ScienceDirect

Fuel

journal homepage: www.elsevier.com/locate/fuel

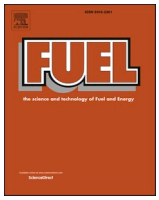

Full Length Article

Laboratory validation of steady-state-transient test to determine relative permeability and capillary pressure

N. Hemmati [a], S. Borazjani [a], S. Yang [a], A. Badalyan [a], L. Genolet [b], A. Behr [b], A. Zeinijahromi [a], P. Bedrikovetsky [a]

[a] University of Adelaide, Adelaide, SA 5000, Australia
[b] Wintershall Holding GmbH, Kassel, Germany

ARTICLE INFO

Keywords:
Water–gas flow
Relative permeability
Capillary pressure
Steady-state method
Transient data
Special core analysis

ABSTRACT

The work aims at the laboratory validation and practical implementation of the steady-state-transient method for simultaneous determination of relative permeability K_r and capillary pressure P_c, which uses steady-state data along with the transient data between the steady states. A new methodology for preliminary choice of K_r and P_c and the detailed test modelling yields planning and design of the steady-state-transient test SSTT – the definition of admissible flow rate, number of steady states and injected water fractions, frequency and volumes of the effluent samples. The test-parameter choice is based on the newly derived theoretical criteria for validity of the model for two-phase flow in porous media, and the operational criteria for the accuracy of the measurements. The preliminary modelling also allows determining the type curves for transient pressure-drop histories, which are used to approximate the measured data and input the inverse solver. Two laboratory SSTTs with inlet half-moon and concentric-circle distributors are carried out. The agreement between the matched-modelling and experimental data for pressure-drop is significantly higher than for average saturation for both tests. The agreement for the test with the concentric-circle distributor is significantly closer than that of the half-moon distributor. This is explained by non-uniform saturation distributions in core cross-sections due to 3D flow, which is more pronounced in the case of half-moon distributor.

1. Introduction

Two-phase transport in porous media occurs during numerous technological processes in the energy sector. The incomplete list consists of oil and gas production, including waterflooding [1,2] and enhanced oil recovery methods [3–6], petroleum production from tight formations and shales [7–9], in-situ storage of natural gas, CO_2 and hydrogen [10,11], pressure depletion in unconventional gas and oil fields, geothermal projects [12], and gas production from coal beds [13–16]. Relative phase permeability (K_r) and capillary pressure (P_c) are the main model functions that determine two-phase flow and fuel recovery using the above-mentioned technologies. Therefore, the K_r and P_c functions are the main input into the mathematical models for the energy-recovery technologies from natural subterranean reservoirs [17,18].

Those three functions are empirical and must be determined from the laboratory corefloods. The methods of laboratory determination have been under intensive investigation since the early 50th and are covered by a vast literature. Below we present a brief description of those studies with the final focus on the simultaneous determination of K_r and P_c from steady-state coreflooding, which is the final goal of the present work. However, numerous recent works report the physics phenomena that are not covered by the classical theory with K_r and P_c functions, given by Eqs. (A1) and (A2) [19–24], including several hysteretic effects [25–27].

'Welge' and JBN methods determine relative phase permeability from the continuous displacement of oil by water [28,29]. Two saturation functions of relative phase permeability $k_{rw}(s)$ and $k_{ro}(s)$ are determined by explicit formulae using the histories of water-cut at the core effluent and pressure-drop across the core. The method assumes negligible capillary pressure compared with pressure-drop across the core, which is a significant limitation on the core length. Additional measurements of the component concentrations during two-phase multicomponent corefloods allows determining adsorption or ion-exchange functions [30,31].

The alternative to the Welge-JBN method to account for capillary pressure is history matching of the coreflood data [32]. Yet, this method requires a known capillary pressure curve $p_c(s)$, which must be determined from porous-plate, electrical resistivity or centrifuge methods

E-mail address: pavel@asp.adelaide.edu.au (P. Bedrikovetsky).

https://doi.org/10.1016/j.fuel.2022.123940
Received 21 December 2021; Received in revised form 8 March 2022; Accepted 20 March 2022
Available online 1 April 2022

Nomenclature

English letters

A	Core cross-sectional area, L^2
D	Core diameter, L
f_{min}	The minimum measured fractional flow value
F_n	Water fraction during n^{th} SSTT injection
J	Leverett function
k	Absolute permeability, L^2
k_{rw}	Water relative permeability
k_{ro}	Oil relative permeability
k_{rowi}	Endpoint relative permeability of oil
k_{rwor}	Endpoint relative permeability of water
l	Average distance between low permeable inclusions or a distance between microlayers in laminas, L
L	Core length, L
L_m	Minimum admissible core length
m	Corey's exponent for the oil phase
m_t	Total effluent mass
n	Corey's exponent for water phase
N_{min}	minimum number of samples
p	Pressure, $ML^{-1}T^{-2}$
p_c	Capillary pressure, $ML^{-1}T^{-2}$
P_d	Entry pressure for the non-wetting fluid
p_D	Dimensionless pressure
p_{min}	Half-scale pressure measured by the laboratory pressure transmitters
R	Core radius, L
R^2	Coefficient of determination
s	Saturation
S_{or}	Residual oil saturation
S_{wi}	Irreducible water saturation
S_{av}	Average water saturation
S_{in}	Saturation at the core inlet
t	Time, T
t_D	Dimensionless time in PVIs
T	Normalized dimensionless time in each transition interval
T_s	Stabilization time in PVIs
u_w	Water injection flow rate, LT^{-1}
u_o	Oil injection flow rate, LT^{-1}
u_c	Uncertainty of measurements
U	Total injection flow rate, LT^{-1}
U_m	Maximum admissible flow rate
V_I	Cumulative injected water volume, L^3
V_P	Cumulative produced water volume, L^3
V_{min}	The half-scale volume of the sampling burette, L^3
x	Length coordinate, L
x_D	Dimensionless length coordinate

Greek letters

ε	Capillary-viscous ratio
ε_τ	Non-equilibrium kinetics ratio
ε_g	Gravity-viscous ratio
ε_p	Pressure measurement precision ratio
ε_s	Sampling frequency ratio
ε_w	Sampling volume ratio
θ	Contact angle
λ	Brooks-Corey parameter
μ	Viscosity, $ML^{-1}T^{-1}$
σ	Oil/water interfacial tension, MT^{-2}
ρ	Phase density, ML^{-3}
τ	Delay time
ϕ	Porosity
Ψ'	Saturation-diffusion coefficient

Subscript

o	Oil
TC	Type curve
w	Water

Superscript

i	Initial of a period between steady states
e	End of a period between steady states

Abbreviations

K_r	Relative permeability
P_c	Capillary pressure
SS	Steady-state

using sister cores, where the rock saturation scenarios are different than those during coreflooding [15,33,34]. However, the discrepancies between the history-dependent functions $p_c(s)$ as determined by separate measurements, and those realized during the coreflood, is the shortcoming of the history-matching-based determination of K_r and P_c.

The asymptotic solution for waterflooding with small capillary pressure can significantly accelerate the matching procedure for determining K_r functions from the water-cut and pressure-drop histories [35]. However, the inconsistency problem of separate P_c curve determination from the sister cores remains.

Steady-state test (SST) accounts for capillary pressure and, contrary to the Welge-JBN method, is applied in short cores [34,36]. This method also requires separately acquired knowledge of $p_c(s)$ with the consequent difficulties.

One way around is repeating SS procedures under at least three alternate velocities [37–40]. The SS data obtained at significantly different high and low rates allow for determining K_r and P_c curves. The "capillary-pressure-free" relative permeability is calculated by extrapolation to "infinite" flow velocity.

Another way around is using steady-state saturation profiles obtained by X-ray measurements [41–44] or computational tomography [45]. The full core scanning is repeated for all SSs. Tuning of K_r and P_c curves is achieved by simultaneous matching SS data and saturation profiles.

Using the transient data on pressure-drop between sequential steady states along with the routine SS data allows for simultaneous determination of relative phase permeability and capillary pressure. This so-called steady-state-transient test (SSTT) is developed for gas displacement by water in water-wet cores [46] and for the displacement of oil by water in oil-wet cores [47]. The method validation in those works is based on steady-state saturation profiles; the measurements involve X-ray equipment on top of the routine coreflooding rig.

Whereas the algorithm and computational method for calculating the Kr and Pc functions from SSTT data is well established, a critical gap exists due to the absence of laboratory validation and practical implementation of SSTT. To the best of our knowledge, the measurements of water-cut during the transition periods between steady states, which are necessary for SSTT validation, haven't been presented in the literature. The laboratory study of the effect of inlet distributors on the SS coreflood results and uniformity of two-phase saturation in the core is unavailable. Besides, there is no experimental SSTT protocol for choosing flow rate, sample volumes and frequencies. Therefore, the laboratory validation of the SSTT method using coreflood data alone is not available.

The present work designs the sequence of quasi-steady-state and continuous imbibition injections that includes SSTT test and provides the data for its validation. A new preliminary/predictive modelling

methodology that includes the theoretical and operations criteria for the test parameters, allows calculating the optimal test parameters, including flow rate, a necessary range for pressure transducers, sampling frequency, number of measurements during transient periods, and stabilization periods. Two sets of displacements with half-moon and concentric-circle inlet distributors indicate higher accuracy of the second option due to lower impacts of three-dimensional (3D) flows effects. The matched and predicted pressure-drop data across the core exhibit close agreement with the laboratory data, while the accuracy of average saturation prediction is lower. The matching in the test with concentric-circle inlet distributor is significantly closer than that for half-moon distributor, which is explained by significant 3D flow effects in the case of half-moon distributor. A 3D reservoir simulation of SSTT confirms this explanation for both distributors with different geometries.

The structure of the text is as follows. Section 2 presents the laboratory setup and the experimental study methodology. Section 3 plans and designs SSTT using theoretical and operational criteria and preliminary modelling based on Berea sandstones' typical K_r and P_c curves. Section 4 presents the experimental results of two SSTTs. Section 5 explains the inverse solution and creation of the solver input. Section 6 shows the match between model and experimental data for the 1st and 2nd tests. Section 7 presents a 3D reservoir simulation with different inlet distributors and analyses the 3D effects. Discussion of the results and conclusions in Sections 8 and 9 conclude the paper.

2. Laboratory study

This section presents properties of rock, oil, and water (2.1), a brief description of laboratory setup (2.2), and a detailed listing of laboratory proceedings according to the experimental protocol (2.3).

2.1. Rocks and fluids

Mineral content characterization of Berea Sister Gray sandstone core was performed by quantitative X-ray diffraction (XRD) analysis. This was conducted by a Bruker D8 ADVANCE Powder X-ray Diffractometer with a Cu-radiation source. Data were processed using Bruker DIFFRAC. EVA software and Crystallography Open Database reference patterns for identifying mineral phases. The quantification was carried out using TOPAZ-profile fitting-based software.

The following mineral composition was obtained: quartz 95.67 %, muscovite-2 M1 1.72 %, kaolinite 1.39 %, calcite 0.95 %, and albite 0.26 %. Table 1 presents the rock and fluid properties.

A non-polar mineral oil (SOLTROL® 130 isoparaffin solvent, Chevron Phillips, USA) with a mixture of C12-C14 azoalkanes was used as a model oil. 0.6 M NaCl solution was used as the synthetic formation brine.

2.2. Laboratory setup

Fig. 1 shows the general view of the laboratory setup. The experimental and modelling study compares two tests that use half-moon and concentric-circle inlet distributors (Fig. 1b and 1c, respectively). The schematic for the setup is presented in Fig. 2. High-pressure piston pumps 8 and 10 separately inject water and oil from different containers into the core. In the 1st test, the inlet distributor has a half-moon form; the effluent water-cut is determined by visualization using the sampling carousel (33) (Fig. 2). The 2nd test uses the concentric-circle inlet distributor; water-cut is measured using the weighting method [34].

Table 1
Rock and fluid properties in the 1st and 2nd tests.

Parameter	Unit	1st Test	2nd Test
k	mD	16.47	33.55
L	cm	5.00	5.03
D	cm	3.73	3.76
U	mL/min	1.00	1.00
μ_o	cP	1.11	1.11
μ_w	cP	1.00	1.00
ρ_o	g/cm^3	0.76	0.76
ρ_w	g/cm^3	1.02	1.02
σ	N/m	0.03	0.03
ϕ	%	18.4	18.6

2.3. Study methodology

Fig. 3 presents the sequence of core saturation. The preparation stage includes initial water saturation of the core under vacuum. To check for clay destabilisation by the synthetic formation brine, the brine was flown prior to primary drainage with 6 different rates increasing from 1 ml/min to 10 ml/min. The permeability fluctuated from 34 md to 40 md without any tendency of decreasing as rate increases, allowing neglecting the formation damage due to clay destabilisation Then follow primary drainage (D1), primary imbibition (I1), and secondary drainage (D2), Fig. 3a. The laboratory protocol aims at complete steady-state coreflooding with measurements of the transient data (Fig. 3b) followed by continuous water injection for validation purposes only (Fig. 3c). Quasi-steady-state injections with piecewise-constant increasing injected water fractions $F_1,F_2…F_n,F_{n+1}$ include the measurements of transitional and stabilized values of water-cut at the effluent and pressure-drop across the core. The steady-state stage follows by tertiary drainage of the core by oil (D3) and continuous water injection (I3), Fig. 3c.

To model waterflooding in an oilfield, K_r and P_c must be measured in primary imbibition mode. Here, to validate the proposed SSTT protocol and the developed inverse solver, the steady-state stage is performed in secondary imbibition mode, to avoid capillary hysteresis for K_r and P_c during the steady-state and the following continuous tertiary-imbibition injection. In particular, the average saturation and relative permeability for oil before secondary imbibition and tertiary imbibition are compared, to validate the hysteresis-free hypothesis for the processes I2 and I3 (Fig. 3b and c).

After continuous waterflood in the 1st test, core at S_{or} was placed into an oil environment in the Amott cell to check for spontaneous drainage and, consequently, for rock wettability. Spontaneous water imbibition in Amott test has been performed for 3rd sister core: connate water saturation has been achieved by evaporation technique, then the core was saturated by oil, and placed into aqueous environment [48].

3. Planning and design of laboratory SSTT

Preliminary mathematical modelling precedes the laboratory test to plan and design the test, i.e., predict the measured data, select the optimal test parameters, and approximate the raw measured data. Section 3.1 includes a description of theoretical criteria to fulfil the assumptions of the mathematical model during the tests and the operational criteria to assure the necessary accuracy of the measurements. Section 3.2 describes the selection of injected water fractions F_1, $F_2…F_n$ during steady states to evenly cover the overall saturation intervals $[S_{in},1\text{-}S_{or}]$ for determining K_r and P_c values. Section 3.3 shows the determination of the type curves for the measured data by predictive mathematical modelling.

3.1. Meeting the theoretical and operational criteria during the test

This work uses the traditional Rapoport-Leas model for two-phase flow in porous media. Eq. (A5) is mass balance for water. Eq. (A6) is the momentum balance for two-phase flow and rock (Lake et al. 2014). Eq. (A5) subject to the initial (A10) and boundary conditions (A8) and (A9) solves for unknown saturation $s(x_D,t_D)$ during continuous or piecewise constant imbibition. Tertiary imbibition corresponds to $F_{n+1} = 1$ in boundary condition (A8). The SSTT uses a piecewise constant

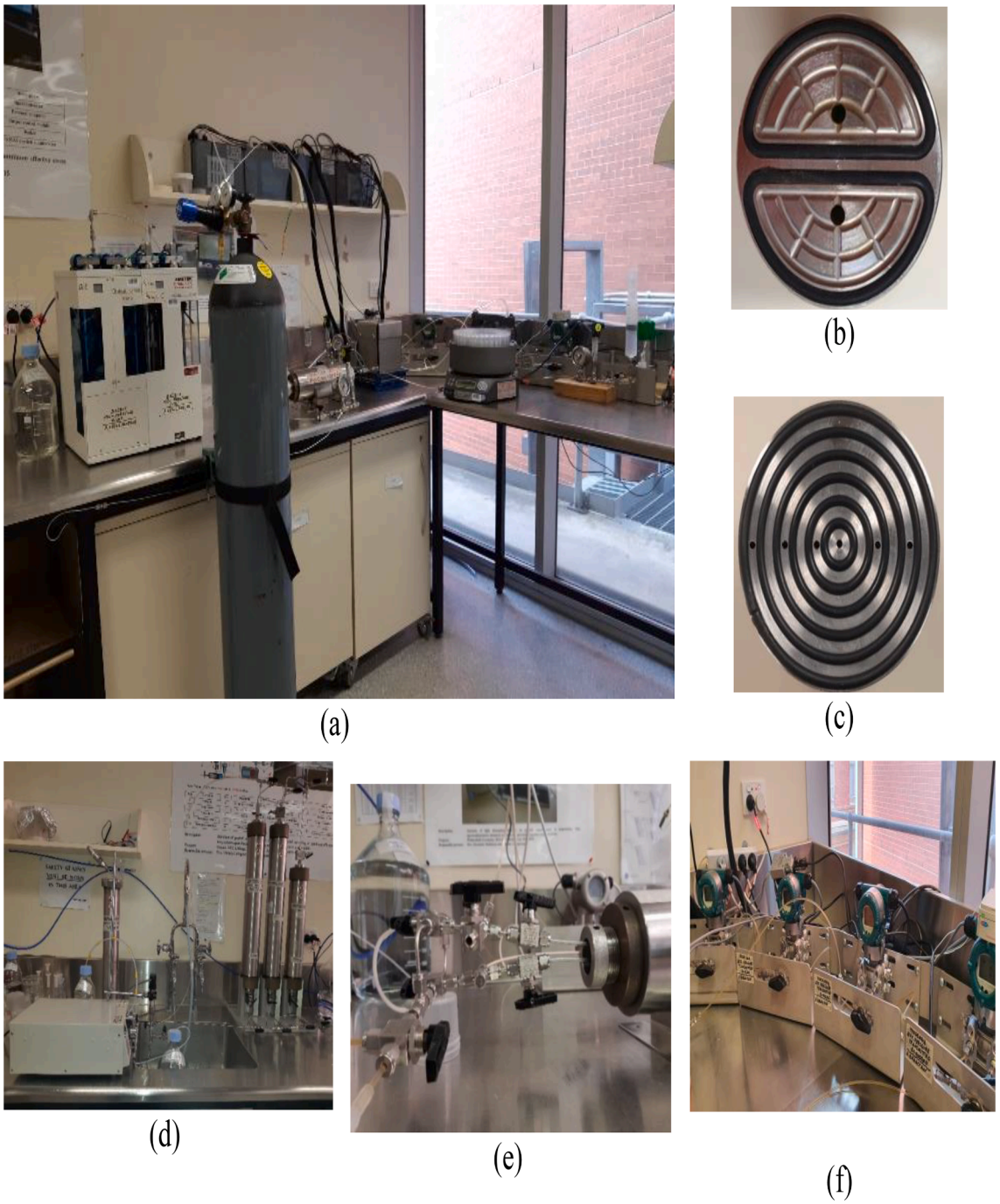

Fig. 1. Laboratory setup for steady-state-transition test (SSTT): (a) overall view of the setup; (b) face of the inlet half-moon distributor; (c) face of the inlet concentric-circle distributor; (d) oil refilling system; (e) inlet pressure-measurement point of water (top line) and oil (bottom line); (f) differential pressure transmitters to measure pressure drops in oil and water at different ranges.

injected water fraction $0 < F_1 < F_2 \ldots < F_{n+1}$. For a known saturation distribution $s(x_D,t_D)$, pressure in either of the phases can be found by integrating the pressure gradient with respect to x_D in Eq. (A6). The detailed formulation for the Rapoport-Leas equations (A1) and (A2) and boundary conditions (A8) and (A9) can be found in Barenblatt et al. [49] and Lake et al. [18].

The methodology to determine working velocity U, the minimum core length that fulfils the theoretical and operational criteria, sampling volumes and frequency is presented by Al-Sarihi et al. [50] for continuous water injection. In this SSTT study, the capillary pressure is accounted for, so the criterion of small capillary-viscous ratio is irrelevant. The other criteria values below correspond to the 1st test (Fig. 4a and b), which slightly differs from the admissible values for the 2nd test (Fig. 4c and d).

The capillary number N_c doesn't exceed 10^{-6} [18], yielding a maximum flow rate U_m.

$$N_c = \frac{U\mu_w}{\sigma} < 10^{-6}, \quad U_m = 10^{-6}\frac{\sigma}{\mu_w} = 3 \times 10^{-5}\ m/s \tag{1}$$

as calculated using the values from Table 1. Here, U, μ_w, and σ are the total injection flow rate, water viscosity, and oil/water interfacial tension, respectively.

A small gravity-viscous number ε_g expresses the assumption of

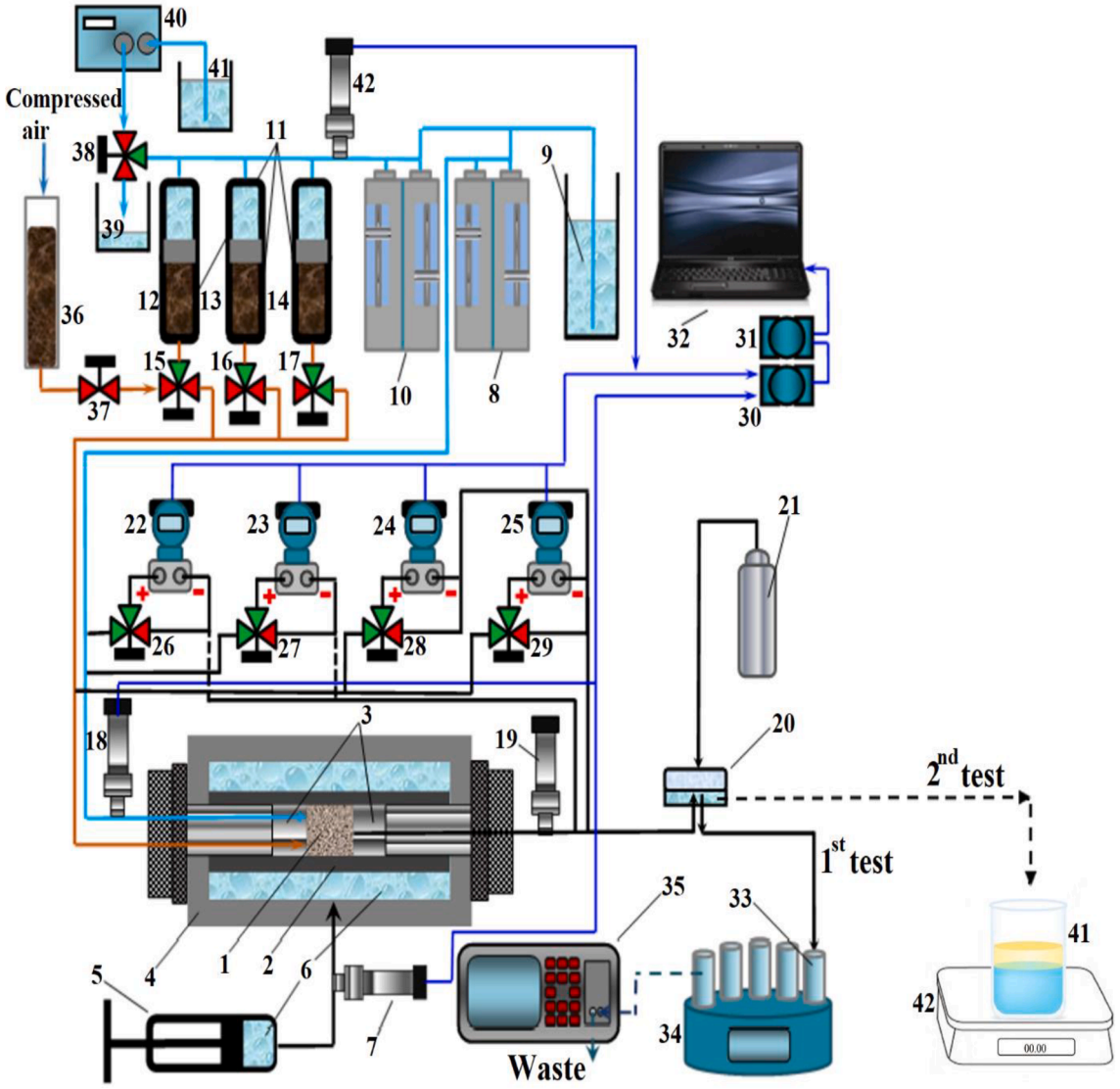

Fig. 2. Schematic of the setup for steady-state-transition test: (1) core plug; (2) Viton sleeve; (3) flow distributor; (4) high-pressure coreholder; (5) manual overburden pressure generator; (6) distilled water; (7, 18, 19, 42) absolute pressure transmitter; (8, 10, 40) high-pressure piston pump (QUIZIX, Prep-36); (9, 41) NaCl solution; (11, 36) oil; (12–14) high-pressure transfer vessels; (15–17, 26–29, 38) three-port valve; (20) back-pressure regulator; (21) compressed air cylinder; (22–25) differential pressure transducer; (30) data acquisition module; (31) signal conditioning module; (32) personal computer; (33) effluent sampling tubes; (34) sampling carousel; (35) PAMAS particle counter/sizer; (37) two-way valve; (39) waste; (41) sampling bottle; (42) balance.

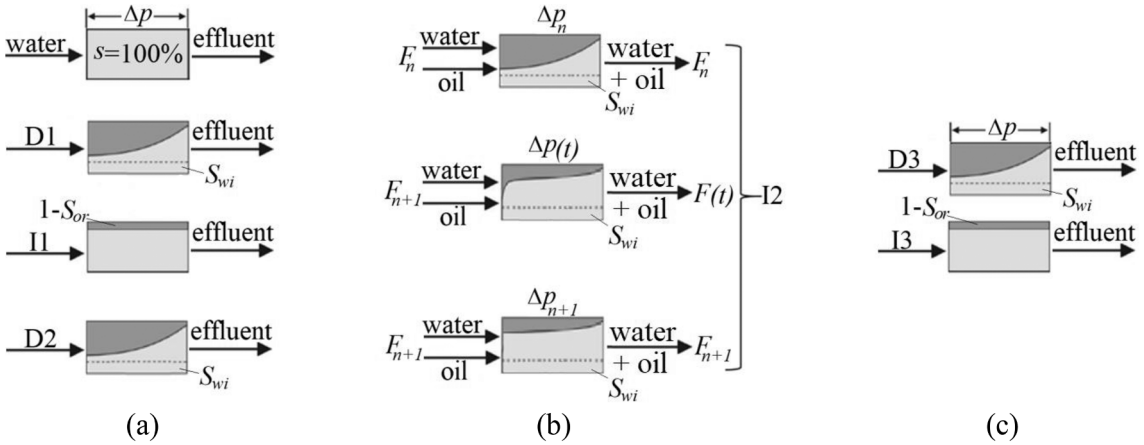

Fig. 3. Schematic description of the laboratory procedure: (a) core initialization with primary drainage D1; primary imbibition I1 and secondary drainage D2; (b) SSTT with injected water fraction F_n, n = 1,2…in secondary imbibition mode; c) unsteady-state test with tertiary drainage D3 and imbibition I3.

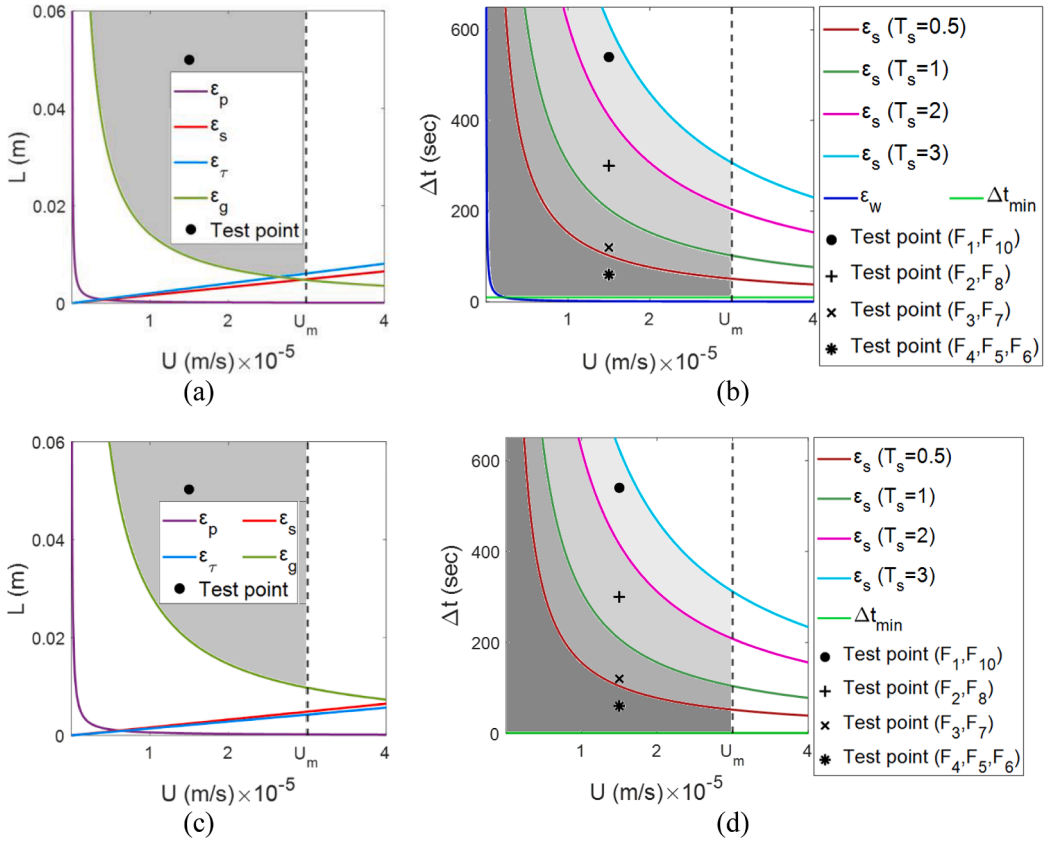

Fig. 4. Admissible areas for SSTT accounting for restrictions on pressure measurements (ε_p), gravity-viscous ratio (ε_g), number of samples (ε_s), capillary non-equilibrium (ε_τ), sample volume (ε_w), and maximum flow rate U_m: (a) for the 1st test in the plane velocity–core length (U, L); (b) for the 1st test in the plane velocity–sampling period (U, Δt); (c) for the 2nd test in the plane velocity–core length (U, L); (d) for the 2nd test in the plane velocity–sampling period (U, Δt).

negligible gravity segregation in the core during the test. Here, the small-threshold value is taken as 0.01:

$$\varepsilon_g = \frac{2(\rho_w-\rho_o)gRkk_{rowi}}{UL\mu_o} < 0.01 \Rightarrow LU > \frac{2(\rho_w-\rho_o)gRkk_{rowi}}{0.01\mu_o} = 1.4\times10^{-7}\, m^2/s \quad (2)$$

where ρ_w is the water phase density, ρ_o is the oil phase density, g is the gravitational force, R is the core radius, k is the absolute permeability, k_{rowi} is the endpoint relative permeability of oil, L is the core length, and μ_o is oil viscosity. The N_c and ε_g -limitations (1) and (2) yield a grey domain in Fig. 4a, located above the green parabola and to the left of the dashed line.

Considering the maximum right-hand side of inequality (2) and the maximum admissible velocity U_m, defined by the capillary number criterion (1), the minimum admissible core length L_m is obtained by intersecting the green parabola with straight-line $U = U_m$:

$$L_m = \frac{2(\rho_w-\rho_o)gRk}{0.01\mu_o U_m} = \frac{200(\rho_w-\rho_o)gRk}{\mu_o U_m} = 0.0047\ m \quad (3)$$

The injected water advances via the paths with higher permeability at the micro scale, followed by cross-section imbibition from the fingers into unswept areas. Also, the advanced water bypasses low-permeable inclusions; imbibition into the inclusions occurs with delay behind the displacement front. These processes occur until establishment of the uniform saturation in a cross section. Despite these effects at the sub-core scale are three dimensional, the assumption of relaxation of "instant" K_r and P_c curves to those determined by the capillary equilibrium, allows for 1D description. Appendix B presents the Barenblatt's 1D model for non-equilibrium two-phase flow in porous media, given by Eqs. (B1)-(B3) [49,51]. The mathematical model (A5) and (A6) to determine K_r and P_c is one-dimensional. A theoretical admissibility criterion that guarantees capillary equilibrium is negligible relaxation time τ due to transversal imbibition in each core cross-section as compared with the time of 1 PVI [49]. The typical relaxation time is calculated from the dispersivity size of the rock and the non-linear capillary-diffusion flux:

$$\tau = \frac{l^2\mu_o}{\sigma}\sqrt{\phi/k} \quad (4)$$

where l is the average distance between low permeable inclusions or a distance between microscale laminas in the core, and ϕ is porosity. For homogeneous Berea cores, we took $l = 0.01$ m [49]. The corresponding admissible area in Fig. 4a is located above the straight blue line.

$$\varepsilon_\tau = \frac{U}{L}\frac{l^2\mu_o}{\sqrt{k\phi}} < 0.01, \quad \frac{L}{U} > 202.4\, s \quad (5)$$

The admissible flow velocity must be high enough to allow the pressure-drop across the core to be significantly higher than the pressure measurement accuracy. So, the admissible area in Fig. 4a is located above the purple parabola corresponding to the pressure measurement accuracy ε_p:

$$\varepsilon_p = \frac{\Delta p}{p_{min}} \gg 1, U = \frac{k\lambda(s)\Delta p}{\mu_o} \gg \frac{k\lambda_{min}p_{min}}{\mu_o}, UL \gg \frac{k\lambda_{min}p_{min}}{\mu_o} = 2.95\times10^{-9}\, m^2/S \quad (6)$$

where $\lambda(s)$ is the total mobility of the two-phase flow, and p_{min} is the half-scale in pressure transducer; (p_{min} = 200 Pa for the 1st and 2nd tests). The λ_{min} value is calculated using the coefficients presented in

Table 1 and the second column (base case) of Table 2.

The minimum time Δt_{min} between the samples, when one burette replaces another one, is determined from the maximum carousel angular velocity. For our setup (Figs. 1 and 2), $\Delta t_{min} = 10$ s. So, the restriction for the time interval between the samples is.

$$\Delta t \geqslant \Delta t_{min} = 10 \ s \tag{7}$$

The admissible area in Fig. 4b, given by inequality (7), lies above the horizontal green line. For the 2nd test, due to the use of the weighting method, the time interval between two subsequent samples is chosen at a significantly lower value: $\Delta t_{min} = 1$ s.

During the transition periods between steady states, the measurements must reproduce the type curves given by formulae (C3) and (C4). We need to define such number of measurements that a smooth curve passing by the transient measurement points and two SS points reflect type curves. The type curves for transient pressure-drop have either exponential- or S-shape. Therefore, we set the minimum number of samples $N_{min} = 3$. So, the volume injected during the transition time T_s must exceed the sample volume more than three times, which is another test criterion called sampling frequency ratio ε_s.

$$\varepsilon_s = \frac{T_s \pi R^2 L \phi}{U \pi R^2 \Delta t} > N_{min} = 3, \ \frac{T_s \pi R^2 L \phi}{U \pi R^2} > \Delta t N_{min} \Rightarrow \frac{L}{U} > \frac{\Delta t_{min} N_{min}}{T_s \phi} = 163.04 \ s \tag{8}$$

For the 1st and 2nd tests, the corresponding admissible areas lie in the plane (U,L) above the red lines (Fig. 4a and 4c, respectively).

$$\varepsilon_s = \frac{T_s \pi R^2 L \phi}{U \pi R^2 \Delta t} > N_{min} = 3, \ \frac{T_s \pi R^2 L \phi}{N_{min} \pi R^2} > U \Delta t \Rightarrow U \Delta t < \frac{T_s L \phi}{N_{min}} = 0.0031 \ m \tag{9}$$

For T_s = 0.5, 1.0, 2.0, and 3.0 PVI and L = 0.05 m, the above inequality defines the admissible areas in the plane $(U,\Delta t)$ below the blue, pink, green, and red hyperbolae, respectively. Fig. 4b and d correspond to the 1st and 2nd tests. Four dots in these figures are located inside the respective admissible areas and can be used for the tests with those T_s values. The positions of the four dots in the plane (U, L) coincide (Fig. 4a, c).

Now let us define the minimum measurable volume for each phase. This volume is equal to $f_{min} V_{min}$, where V_{min} is the half-scale for volume in the burette, and f_{min} is the corresponding minimum of the phase fraction which can be visualized. The volume produced during the time Δt must exceed the visualized volume for each phase:

$$\varepsilon_w = \frac{U \pi R^2 \Delta t}{f_{min} V_{min}} > 1 \ \Rightarrow \ U \Delta t > \frac{f_{min} V_{min}}{\pi R^2} = 4.57 \times 10^{-5} \ m \tag{10}$$

The sampling volume ratio ε_w, given by inequality (10), defines the admissible area above the blue parabola in the plane $(U,\Delta t)$, Fig. 4b.

The calculations (1)-(10) refer to the 1st test, where carousel sampling and the visualization method is used for water-cut measurements. The parameters for the 2nd test, where effluent water-cut is measured by weighting method, are calculated using Eqs. (1)-(9); here, the sampling volume ratio restriction is waved.

Table 2
Corey relative permeability and capillary pressure parameters obtained by the inverse solver.

Parameter	Base	1st Test	2nd Test
ε	1.97	1.97	2.81
S_{or}	0.15	0.26	0.23
k_{rwor}	0.1	0.03	0.04
k_{rowi}	0.75	0.71	0.87
S_{wi}	0.15	0.24	0.24
λ	2.3	1.54	1.84
P_d (psi)	3.2	5.07	1.64
n	2.2	1.58	2.62
m	2.8	2.16	1.31
$R^2_{\Delta p}$	–	0.99	0.99
R^2_{Sav}	–	0.88	0.98

3.2. Preliminary modelling for selection of injected water fractions

Let us select the number of steady states with corresponding injected water fractions F_n for SSTT. At the core scale, the fractional flow curve has S-shape, and derivative in the inflection point highly exceeds the derivative near the two endpoint saturations. Thus, the frequencies of injected water fractions are significantly higher at F_n close to zero or unity than for the intermediate values.

The methodology and corresponding calculations to choose the values F_n are given in Fig. 5. Fig. 5a shows the K_r and P_c curves chosen in advance for the 1st coreflood for the Berea sandstone described in Section 2. The corresponding Corey values are given in the second column of Table 2.

Fig. 5c presents steady-state profiles as calculated for the SSTT for ten values of the injected water fractions. While the inlet saturation does not exceed the connate water value S_{wi} after the primary drainage, even for lower imbibition value $F_n = 0.01$, S_{in} highly exceeds S_{wi}. Fig. 5b also shows a high increase of inlet saturation with injected water fraction increase near $F_n = 0$ and $F_n = 1$. However, the minimum and maximum values for injected water fractions are limited by the accuracy of water-cut measurements. These are other limitations for planned F_n values. Yet, the F_n values selected in Fig. 5c result in even covering of the saturation interval by S_{in} values.

3.3. Determining type curves by preliminary modelling

Pressure-drop transient data for the 1st and 2nd tests are presented in Figs. 8 and 9, respectively. The data scattering can cause instability of the curves K_r and P_c determined by the inverse solver and non-uniqueness of the minimum of deviation, given by Eq. (C5). Ill-posed inverse problems of the determination of K_r and P_c curves and the ways of their regularization are presented in the literature [20,21,52]. Here we find the type curves and use them to approximate the experimental data for further treatment by an inverse solver.

Eqs. (A5) and (A6) for two-phase flow of immiscible incompressible fluids subject to initial and boundary conditions (A8)-(A10) are solved numerically to predict the results of SSTT. The "base" values of the K_r and P_c constants typical for Berea sandstones are given in the second column of Table 2. The numerical data shows that pressure-drop histories have an S-shape for low values of the injected water fractions (black curves in Fig. 8a–d and 9–g) and an exponential curve for high injected-water fractions (black curves in Fig. 8e–j and 9–j). Formulae (C1)-(C4) represent S-shape and exponential curves.

4. Experimental results

In order to check the hypothesis of water-wetness of the cores 1 and 2, the third sister core was saturated by oil under connate water saturation. Then the core was placed in the Amott cell in a water environment. An intensive spontaneous imbibition has been observed immediately. The saturation stabilized at $1\text{-}S_{or} = 0.74$, which is approximately equal to S_{or} values given in the second and third lines of Table 2. This allows concluding that the sister core is water-wet. After the 1st test, when saturation was equal to $1\text{-}S_{or}$, the core has been placed in the Amott cell in an oleic environment. Spontaneous oil imbibition hasn't been observed, which also supports the statement of the core water-wetness in 1st and 2nd tests.

The results of SSTTs are presented in Fig. 6a and b. Pressure drop in oil Δp_o was used for matching the data for low fractions of injected water, F < 0.5. At F > 0.5, pressure drop in water Δp_w was used for matching the data. Pressure-drops for water and oil across the core for the 1st test are given by blue and red dots, respectively (Fig. 6a). In the 2nd test, the pressure-drops for water and oil across the core almost

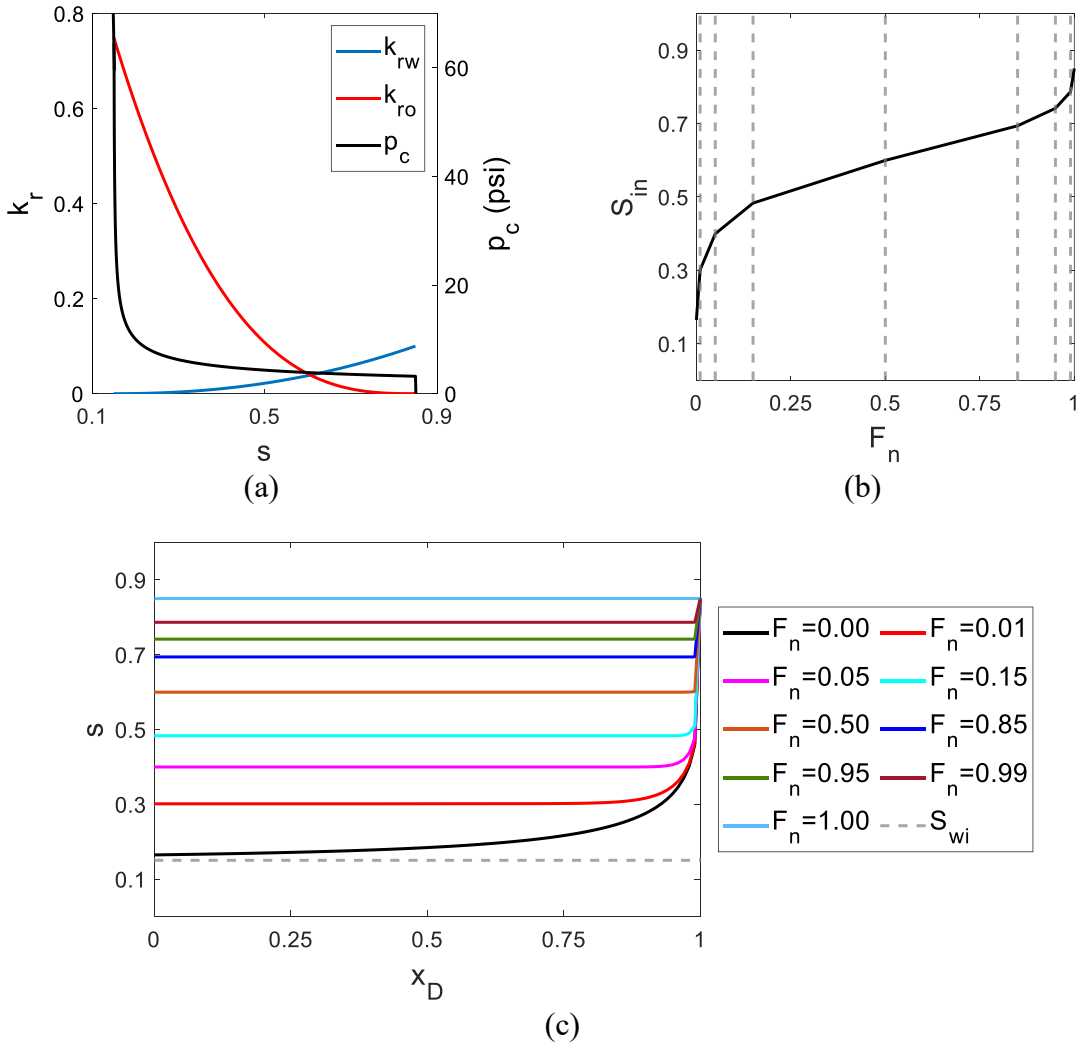

Fig. 5. Determination of the number of steady-states and injected water fractions for SSTT: (a) preliminary estimates of relative permeability K_r and capillary pressure P_c for 1st test with half-moon distributor in Berea sandstone; (b) inlet saturation *vs* injected water fractions F_n; (c) steady-state saturation profiles.

coincide and are given by black dots. Fig. 6b shows average water saturation versus time as obtained by integrating the water-cut values with respect to time. Blue and black dots correspond to the 1st and 2nd tests, respectively.

Fig. 6b presents error bars for the 1st test. Due to the high precision of pressure-drop measurement (0.04% of full-scale measurement of the differential-pressure transducers), the error bars in Fig. 6a are neglected. The error bars for visualization measurements of water-cut in the 1st test are significant (blue vertical bars in Fig. 6b), while the error bars for the weighting method are negligible and not shown. The analysis of uncertainties in SSTTs can be found in works [46,47].

To check the hypothesis of equivalence of two-phase flows during secondary imbibition (I2) and tertiary imbibition (I3), we compared the states of two phases before those processes. The average water saturations before I2 and I3 were 0.3174 and 0.3197, receptively. The relative permeability for oil before I2 and I3 were 0.6223 and 0.6105, receptively. High agreement allows neglecting the hysteresis for K_r and P_c curves between I2 and I3.

Fig. 6c shows pressure-drop across the core in water and average saturation for the 1st test during the tertiary imbibition (black and blue dots, respectively). Fig. 6d presents the results of tertiary imbibition for the 2nd test.

5. The inverse solver

This section describes the traditional mathematical model for two-phase flow containing K_r and P_c (Appendix A) and the inverse solution algorithm and its numerical implementation to determine K_r and P_c from SS and transient data. The preliminary mathematical modelling analyzes pressure-drop data during SS and transient stages, allowing the formulation of type curves (Appendix C). The rough data of the direct measurements are interpolated by the type curve, allowing for a significant decrease in data scattering (Section 5.1). Section 5.2 briefly describes the inverse solver that uses the steady-state and transient data. This solver uses water-cut and pressure-drop across the core during the steady states and pressure-drop across the core during transient stages.

Fig. 7 presents the results of inverse problem solutions for K_r and P_c of the 1st and 2nd tests. The results of interpolation of the preliminary modelling data by the type curves are presented in Tables 3 and 4. Figs. 8 and 9 show pressure-drop across the core during each transient stage for the 1st and 2nd test, respectively. The coefficients for K_r and P_c obtained by the inverse solver for both tests are given in Table 2. Fig. 10 shows the schematic for the inverse algorithm. The comparative analysis of both tests is given in Fig. 11.

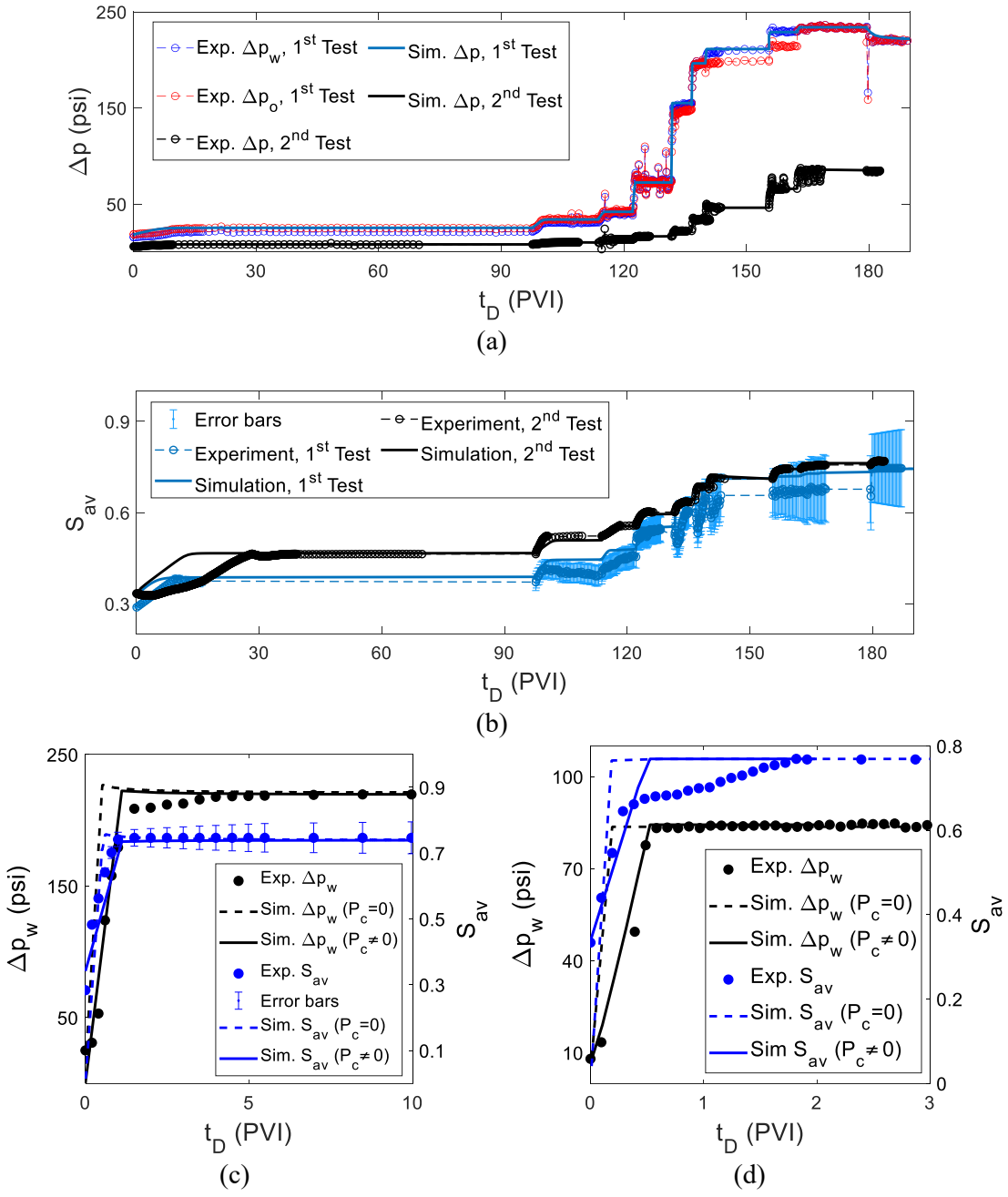

Fig. 6. Measured laboratory data and their matching during 1st (half-moon distributor) and 2nd (concentric-circle distributor) tests: (a) pressure drops Δp in water and oil across the core during SSTT; (b) average water saturation S_{av} during SSTT; (c) pressure drop and average water saturation during continuous water injection using half-moon distributor; (d) pressure drop and average water saturation during continuous water injection using concentric-circle distributor.

5.1. *Interpolation of pressure-drop data by type curves*

The initial K_r and P_c for preliminary modelling are taken in the Corey form; the coefficients for prediction of the 1st test are given in the second column in Table 2. Since sister cores are used in all tests, the K_r and P_c curves obtained from the 1st test are used for preliminary modelling of the 2nd test (third column in Table 2). The initial-boundary problem (A5)-(A10) is solved numerically. The injected water fractions F_n have been chosen during the preliminary modelling (Section 3.2); the results for the 1st test are given in Fig. 5. Eq. (A10) shows that the steady state for the n^{th} stage is an initial condition for injection with water fraction F_{n+1}, i.e., for $n+1th$ stage. The problem is solved numerically using the PDEPE function in MATLAB software. Inlet condition at $x_D = 0$ (A8) defines the third Neuman's type boundary conditions; the details can be found in works [46,47]. We use 500 areal grids for $x_D \in [0,1]$; the time step of the numerical scheme is selected automatically from the stability conditions. The inverse solver results for the pressure-drop data of the 1st and 2nd tests are shown in Fig. 6a by continuous blue and black lines, respectively. Zoom for each stage of the 1st and 2nd tests are shown in Figs. 8 and 9.

Figs. 8 and 9 show that the transient pressure-drop curves have S-shape for low values of the injected water fraction ($F_n < 0.5$). For large water fractions starting from 0.5, the pressure-drop curves are exponential. Formulae for S-shape and exponential curves are given by equations (C3) and (C4), respectively. These formulae use normalized transition time between zero and stabilization time $T_s = t^e_D - t^i_D$ and normalized pressure-drops given by Eq. (C2).

The preliminary K_r and P_c curves for the 1st test are marked as

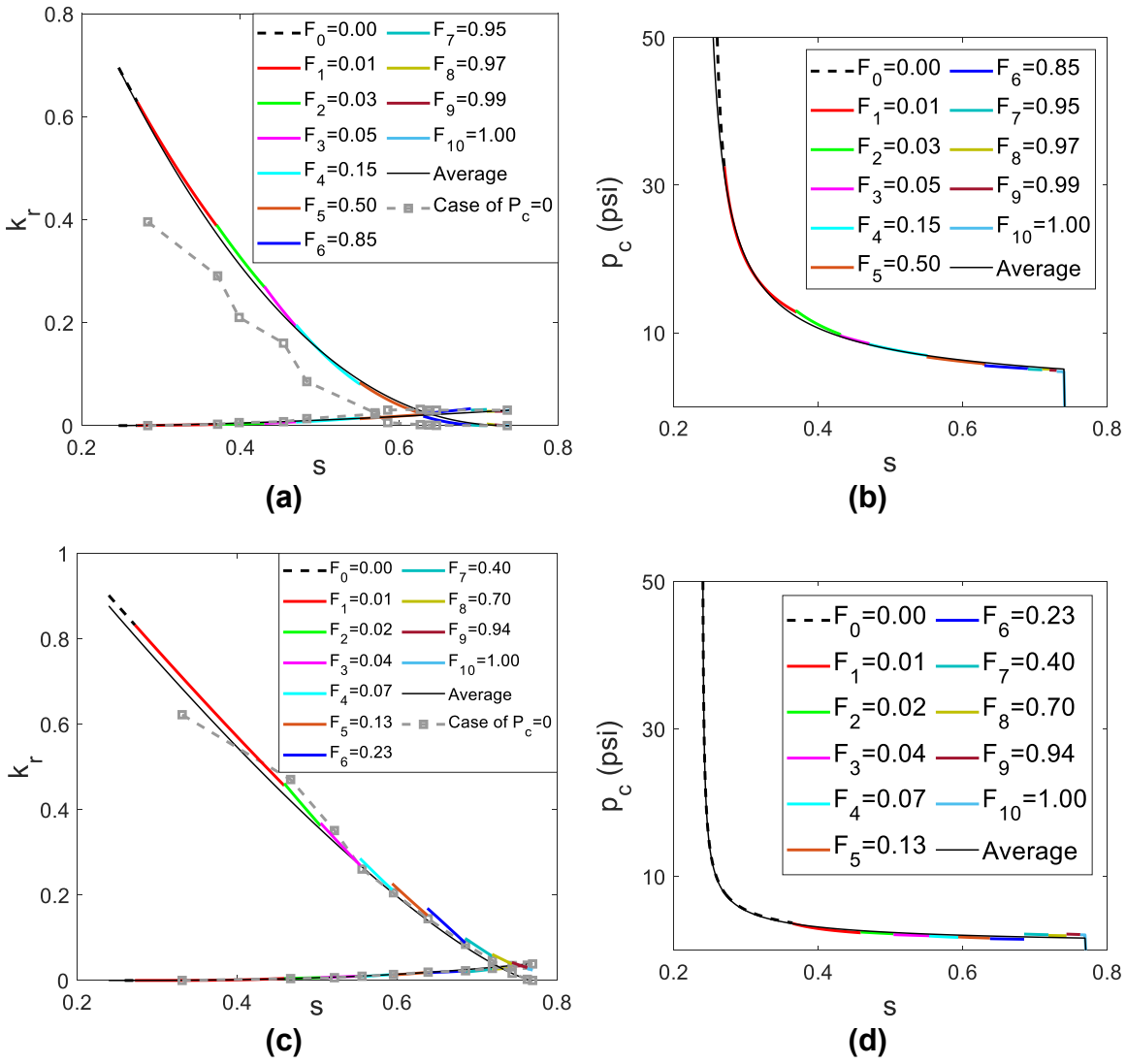

Fig. 7. Treatment of the experimental data using the iterative inverse algorithm: (a) relative permeability obtained from the 1st test (half-moon distributor) data; (b) capillary pressure obtained from the 1st test data; (c) relative permeability obtained from the 2nd test (concentric-circle distributor) data; (d) capillary pressure obtained from the 2nd test data.

''base'' in Table 2. The preliminary curves for the 2nd test are the result of the inverse solution of the 1st test. Fig. 11a and b show the ''base'' curves and those calculated from the 1st test data, which significantly differs from each other. Despite this difference, the type curves for both tests are the same, as could be observed from Figs. 8 and 9. The results of interpolation for S-shape and exponential curves are given in Tables 3 and 4. Figs. 8 and 9 show that type curve interpolations of the measured data significantly decrease the scattering.

5.2. Inverse solution

The SS saturation profile is uniform during water injection in water-wet core at $F_n = 1$. So, the two Corey constants S_{or} and k_{rwor} are determined from the last SSTT step. The other six coefficients – k_{rowi}, S_{wi}, λ, P_d, n, and m – are determined by the iterative algorithm minimizing deviation G between the modelling and interpolated experimental data given by Eq. (C5). The detailed description of the inverse solver can be found in works [46,47]. Fig. 10 presents the algorithm. The algorithm starts at $F_n = 1$, moving to *n-1,n-2,…1*. At each transition period between two subsequent SSs, the K_r functions are determined from the SS data, assuming the preliminary curve for P_c. It allows determining K_r values by matching with the measured transient data; stabilized values correspond to the best match. Then, the stage with lower F_n is matched (Fig. 7). The inverse solver determines K_r and P_c curves for saturation intervals between two subsequent SS steps. The intervals expand by decreasing the injected water fraction from one to zero, which results in delivering K_r and P_c over the saturation intervals from 1-S_{or} to S_{in}.

6. Validation of the results

Section 6.1 presents the results of matching steady-state data and the transient pressure-drop data from the inverse solver. Average saturation during transition periods, as obtained by the tuned model, are given in Section 6.2. Section 6.3 presents the predictive results for pressure-drop and average saturation for continuous injection in the tertiary imbibition mode.

6.1. Matching SS and transient pressure-drop data

The mathematical model, described in Appendix A, contains three curves $k_{rw}(s)$, $k_{ro}(s)$, and $p_c(s)$. The inverse solver (Section 5) allows determining them from the SS average saturation data and the SS and

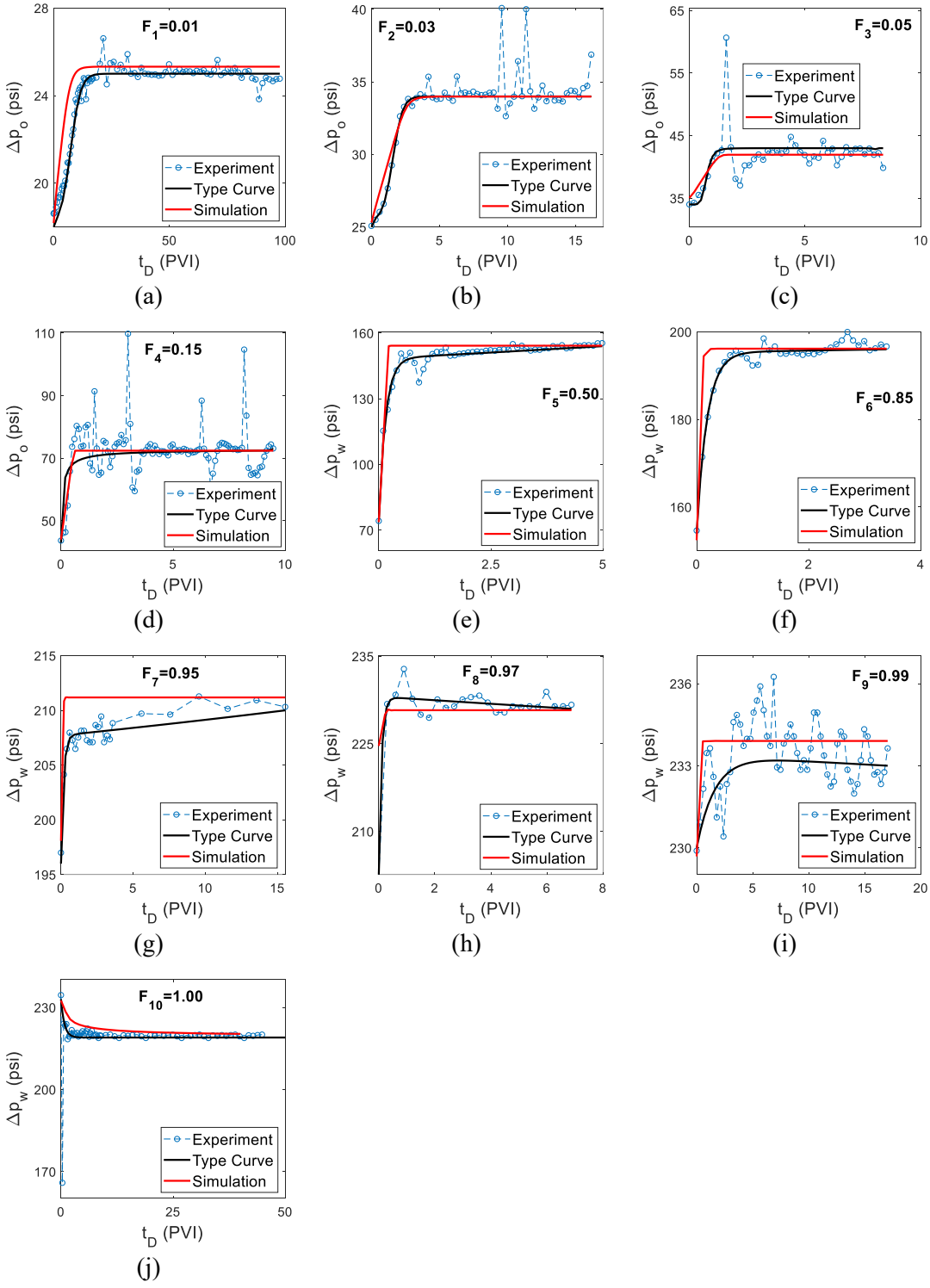

Fig. 8. Matching the pressure drop data from the 1st test: (a), (b)…(j) correspond to transient behaviour with injected water fractions $F_1 = 0.01$, $F_2 = 0.03 \ldots F_{10} = 1.0$, respectively.

transient pressure-drops. The results are presented in Fig. 6a and 7 for both tests. Table 2 shows the tuned eight model parameters – six Corey coefficients for K_r and two parameters for P_c. In Fig. 6a, the modelling pressure-drop curves form central curves for the clouds of the experimental points for both tests.

Figs. 8 and 9 show pressure-drop curves for all transition periods between the steady states for the 1st and 2nd tests, respectively. The matched pressure-drop (red curves) fit close to the black type curves, which approximate the measured data (blue points). The coefficient of determination $R^2_{\Delta p}$ for pressure-drop in both tests is equal to 0.99 (Table 2, line 11), i.e., the agreement between the matched and experimental data is very high.

The deviation minimization applied in the inverse solver is conditional; the determined K_r and P_c fix the SS conditions. This explains the ideal fit of SS data for both tests (Fig. 11c and d).

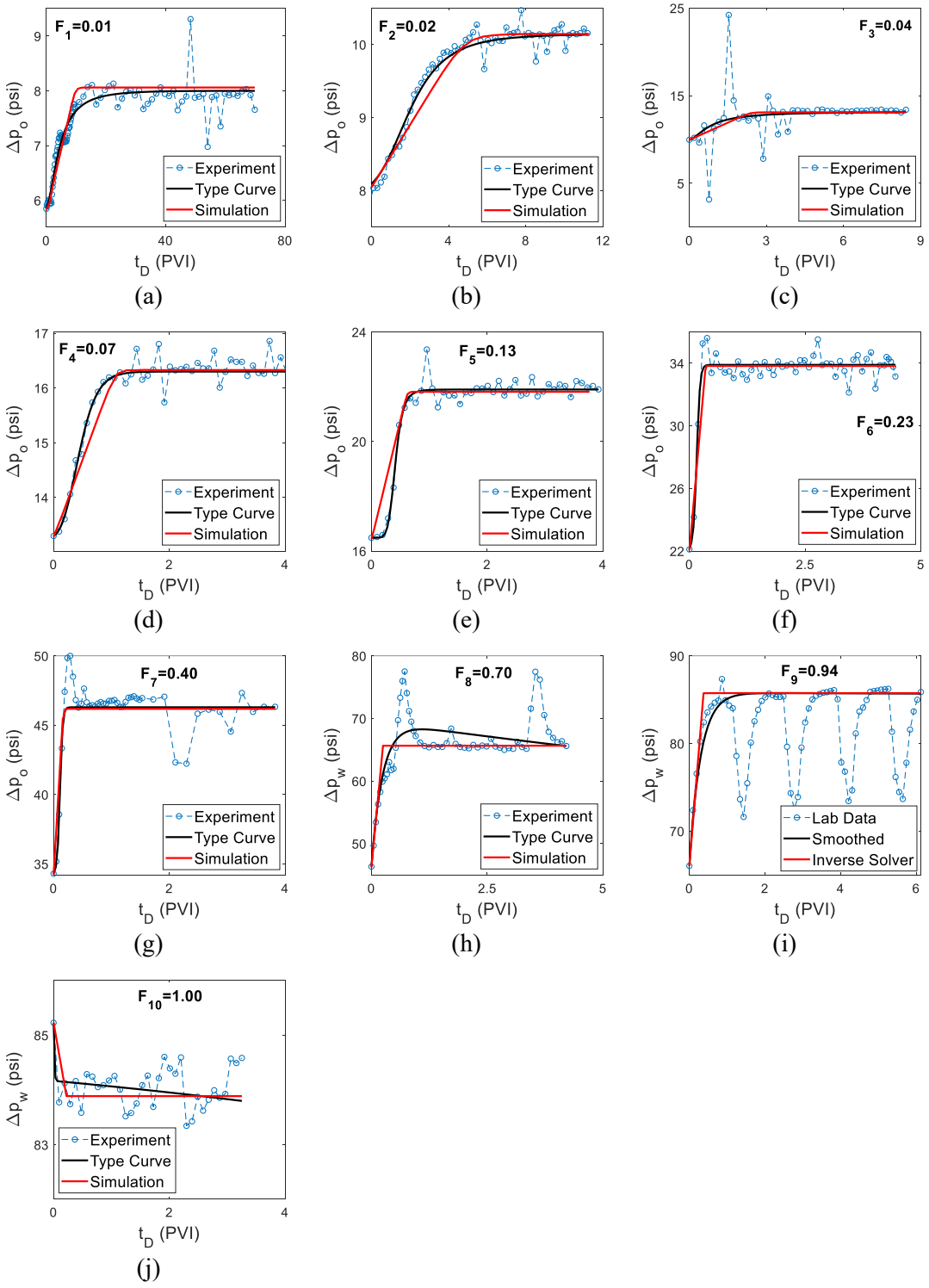

Fig. 9. Matching the pressure drop data from the 2nd test: (a), (b)…(j) correspond to transient behaviour with injected water fractions $F_1 = 0.01$, $F_2 = 0.02$…$F_{10} = 1.0$, respectively.

6.2. Fitting SS and transient average saturation data

The results of the comparison between the modelling and measured transient average-saturation data are presented in Fig. 6b. The simulation data are within the error bars, which validates the results. Yet, the coefficient of determination for saturation R^2_{Sav} (Line 12 in Table 2) is lower than that for pressure-drop (Line 11 in Table 2), especially for the 1st test. Similar to pressure-drop data, the prediction of saturation during the 2nd test is better than that for the 1st test.

The conditional optimization based on the coincidence of the modelling and SS data (Section 5) provides an ideal fit between the modelling and SS data in Fig. 11c and d.

Fig. 11e shows the dependency of the stabilization time T_s on the injected water fraction. U-form of the stabilization curve $T_s(F)$ is typical for water-wet cores [46]. For the 1st and 2nd tests, this agrees with the Amott test data for the third sister core. Close agreement of the

Table 3
Parameters *a*, *b*, and *c* for normalized measured pressure-drop matched by S–shape function of normalized time *T*.

	F_n	*a*	*b*	*c*	R^2
1st Test	0.01	0.1041	40.57	17.97	0.9752
	0.03	0.5712	43.89	307.6	0.9981
	0.05	6.492	−3.645	1.117e-7	0.9622
	0.15	0.8074	3.224e-4	0.0188	0.9535
2nd Test	0.01	1.590	2.527	0.01366	0.9315
	0.02	4.184	6.592e-6	6.279e-3	0.9856
	0.04	1.595	6.403e-4	0.02532	0.9603
	0.07	1.318	13.49	0.2288	0.9958
	0.13	6.100	1.969	1.359e-6	0.9813
	0.23	0.001	121.7	83.59	0.9626
	0.40	0.010	164.3	120.96	0.8517

Table 4
Parameters *d* and *e* for normalized experimental pressure-drop matched parameters by the exponential function of normalized time *T*.

	F_n	*d*	*e*	R^2
1st test	0.50	−33.1	0.07385	0.9827
	0.85	0.01647	−18.22	0.9975
	0.95	−90.91	0.1789	0.9426
	0.97	−70.06	−0.07085	0.8765
	0.99	−10.6	−0.1267	0.9201
	1.00	11.39	−65.59	0.9761
2nd test	0.70	−17.61	−0.19	0.9410
	0.94	−20.52	−0.0055	0.9242
	1.00	−290.3	0.2967	0.8776

stabilization curves in the figure also validates SSTT.

The end-point values obtained in the current study (third and fourth columns in Table 2) belong to their typical intervals for Berea cores [18–21].

6.3. Prediction of continuous water injection

Fig. 6c and d show predictions of pressure-drop (black curves) and average saturation (blue curves) during tertiary imbibition, using K_r and P_c as obtained from SSTT during the 1st and 2nd tests, respectively. The coefficients of determination for pressure-drop and average saturation for the 1st test are 0.93 and 0.90, respectively. For the 2nd test, they are 0.99 and 0.75. Like in SSTTs, the agreement between the experimental data and fully predictive modelling is significantly better for pressure-drop than average water saturation.

7. Comparative 3D modelling for two tests

The SSTT coreflood was modelled by CMG STARS using the rectangular Cartesian system. There are 32 grid blocks in the x-direction (i. e. along the core). The block size Δx logarithmically increases from the inlet in 1 cm interval and logarithmically decreases in 1 cm interval up to the outlet. The remaining blocks in the x-direction in the bulk of the core have a constant length of 9.4×10^{-3} m. This allows capturing inlet and outlet boundary conditions under a relatively coarse grid. The core cross-section was modelled with 29 blocks in the y-direction (i.e. across the core face) and 29 blocks in the z-direction (i.e. vertically down from the top of the core). The grid dimensions in each of these two directions is a constant 1.31×10^{-3} m.

The SSTT data matching and prediction show the higher agreement between the experimental and modelling data for the 2nd test than for the 1st test. We explain is as follows: concentric-circle distributor in the 2nd test has lower 3D-flow effects and provides higher areal sweep than with in the 1st test with half-moon distributor (Fig. 1c and b).

To verify this hypothesis, we undertook 3D modelling of corefloods with both geometries of the inlet grooves of the distributors for the case that corresponds to tests 1 and 2 (Fig. 12). The simulation study methodology is the same as that presented by Yang et al. [53]: 3D modelling mimics the "measured" data of pressure-drop and average saturation (Fig. 12a and 12b, respectively), which are then treated by the inverse solver presented in Section 5. The results are presented in Fig. 12f and g. For both K_r and P_c curves, the deviation from the base input dotted curve is smaller for the concentric-circle case (dashed curve) than for the half-moon case (solid curve).

3D areal saturation distributions over the core when using half-moon and concentric-circle distributor are shown in Fig. 12d and 12c,

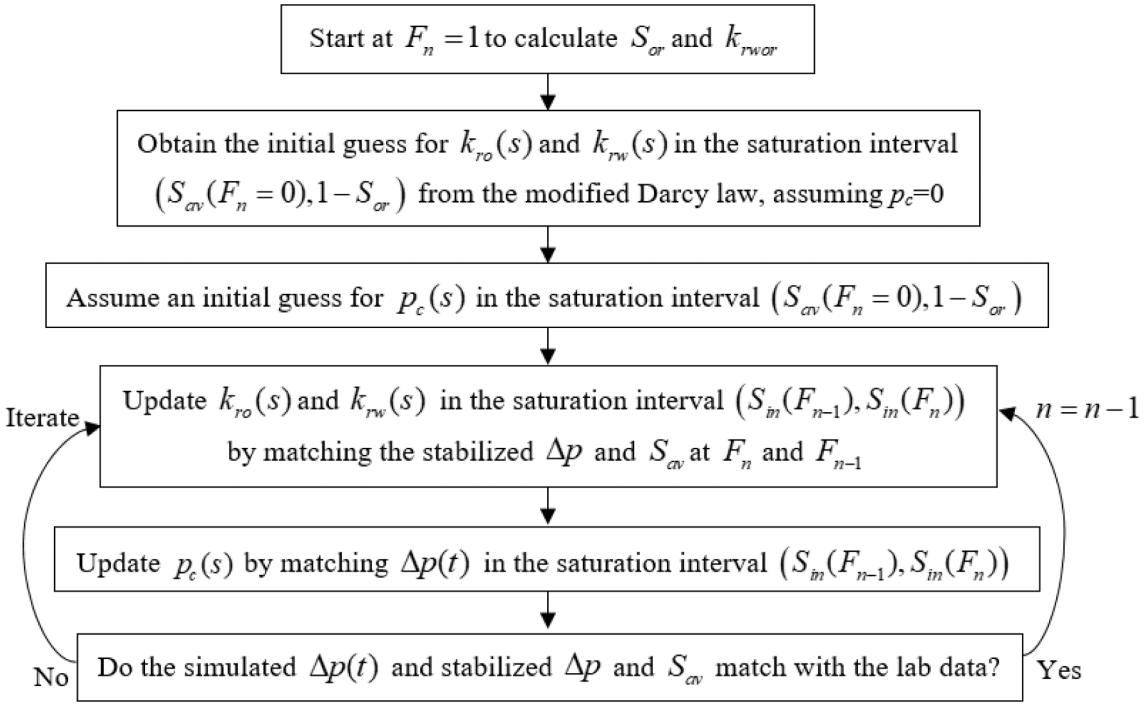

Fig. 10. The algorithm for the inverse solver.

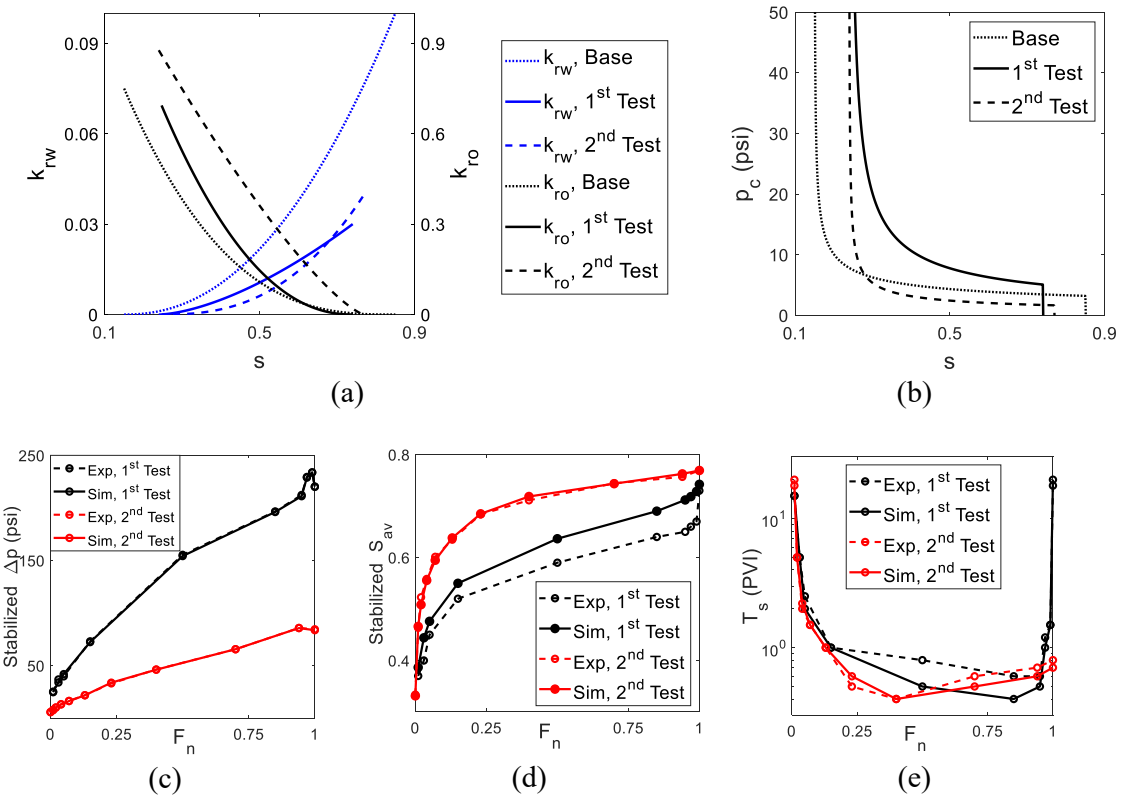

Fig. 11. Comparing the results of 1st and 2nd tests: (a) relative permeability K_r curves; (b) capillary pressure P_c curves; (c) stabilized pressure-drop Δp data versus injected water fraction; (d) stabilized average saturation S_{av} versus injected water fraction; (e) stabilization time T_s versus injected water fraction.

respectively. Fig. 12c exhibits a significantly higher areal sweep than Fig. 12d. The same conclusion can be drawn from Fig. 12e. 3D effects at the outlet core cross-section at half-moon test are significantly higher than for the concentric-circle case. The areal distributions of saturation in the cross-sections are more uniform in the case of concentric-circle distributor for all values of injected water fraction. Table 5 shows that both standard deviation for saturation (*SD* in columns 3 and 6) and coefficient of variation (C_v in columns 4 and 7) are lower for core with the concentric-circle distributor than those for the half-moon case.

The above inverse-solution data explain higher matching and prediction precisions for the 2nd test than for the 1st test by 3D effects of inlet flux distributors with different geometries of the grooves.

8. Summary and discussion

This work aims at the laboratory validation and practical implementation of steady-state-transient tests (SSTT), where the transient data between the steady states are used for simultaneous determination of relative permeability K_r and capillary pressure P_c. The previous works [46,47] regularized and solved the corresponding inverse problem. Hence, the remaining gap was practical SSTT feasibility, including uncertainty of the measurements using the routine laboratory equipment, K_r and P_c determination accuracy, and the experimental protocol.

The 1st test uses a half-moon distributor at the core inlet and visualization method for water-cut measurement at the effluent, while the 2nd test uses a concentric-circle distributor and weighting method for the effluent water-cut measurement, allowing studying the effect of inlet distributors on the SS coreflood results and uniformity of two-phase saturation in the core. Previously, higher sweep and more uniform saturation distribution in core cross-sections in the test with concentric-circle inlet distributor were proved by 3D reservoir simulation [53].

For water-wet cores, the inverse problem for determining K_r and P_c requires SS data for pressure-drop and water-cut, as well as the transient data of pressure-drop only. The transient water-cut data are used for the method validation.

This study also includes post-SSTT drainage with further continuous water injection to obtain additional information for SSTT method validation. SSTT is performed in secondary imbibition mode to avoid capillary hysteresis between secondary imbibition and tertiary imbibition. The following continuous water injection corresponds to tertiary imbibition.

Type curves to adjust the lab data To regularize the inverse problem of determining K_r and P_c from the SS and transient data, the raw data of pressure-drop across the core are approximated by the type curves. Then, the type curves are matched by the mathematical model for steady-state and transient waterfloods. The type curves are determined by multiple preliminary simulations, using so-called "base" K_r and P_c curves. Using type curves allows smoothing the raw measured data and significantly decreases their scattering.

In this study, the typical Corey-Brooks curves for Berea sandstones with similar permeability and porosity are used for the 1st core. Since the two tests are conducted on sister cores, the K_r and P_c curves obtained from the 1st test are used as the base curves for the 2nd test. The type curves are confirmed using the tuned curves obtained from the SSTT data – they have the same type.

The base K_r and P_c curves used in the preliminary modelling of both tests significantly differ from those obtained from the SSTT data. However, the type curves for transient pressure-drop and average saturation remain the same, which validates the type-curve method.

The experimental pressure drop in Figs. 8 and 9 have some spikes and sudden changes. This behaviour has been observed in many lab coreflood studies [44–46]. The problem of unusual behaviour of the pressure drop can be resolved in two ways. The first one is the theoretical understanding of the phenomena, like it is attempted in works [19–24],

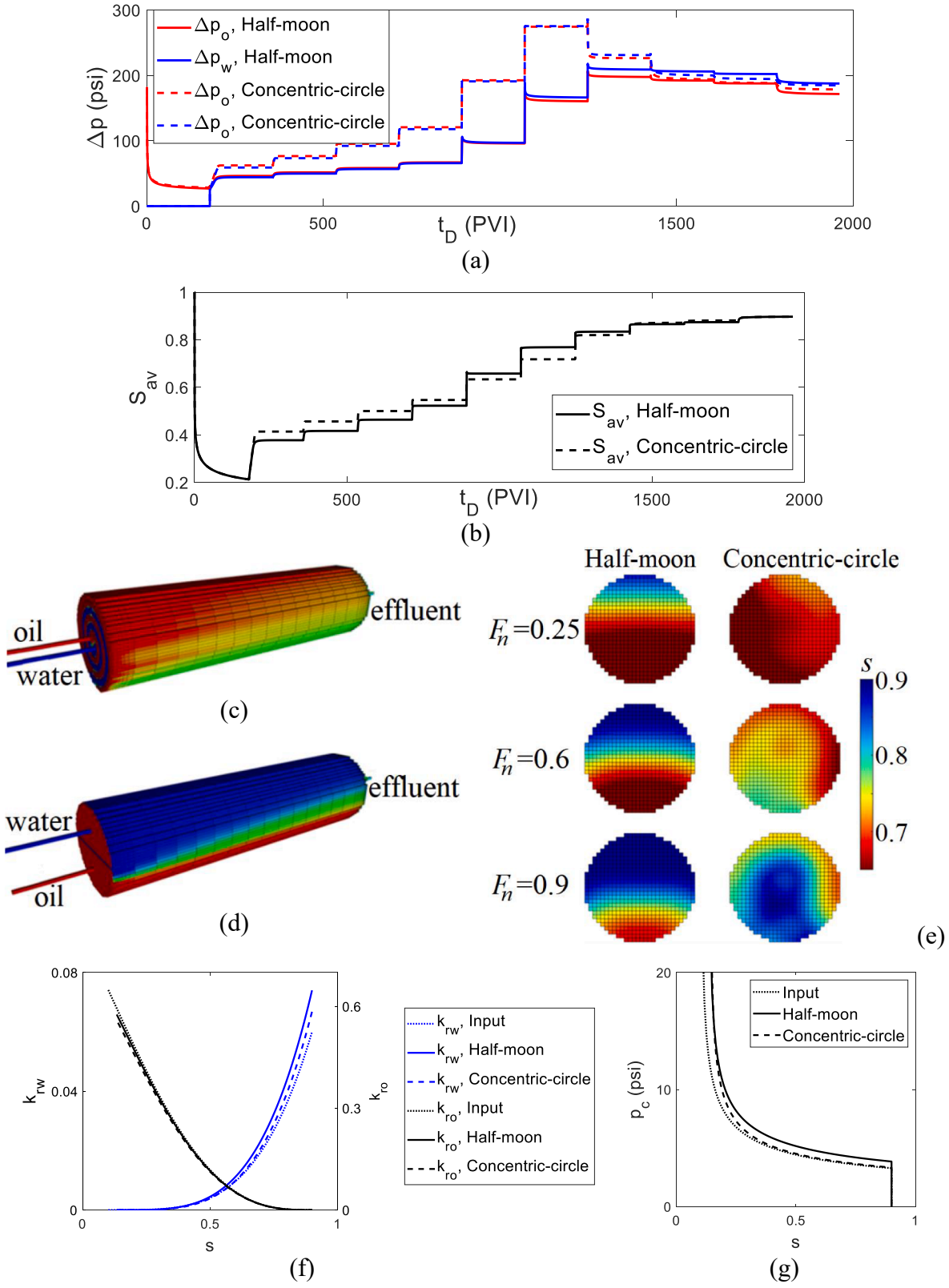

Fig. 12. 3D reservoir simulation for 1st and 2nd SSTTs: (a) pressure drop across the core; (b) average saturation; (c) 3D saturation distribution in the core with concentric-circle distributor; (d) 3D saturation distribution in the core with half-moon distributor; (e) areal saturation distributions at the core outlet for three injected-water fractions; (f) relative permeability curves; (g) capillary pressure curves.

Table 5
Coefficient of variation for the stabilized saturation profile in 3D simulation.

F_n	Half-moon			Concentric-circle		
	Mean	*SD*	C_v	Mean	*SD*	C_v
0.25	0.6851	0.0915	0.133557	0.6659	0.0301	0.045202
0.60	0.7623	0.1027	0.134724	0.7256	0.0343	0.047271
0.90	0.8295	0.074	0.08921	0.8052	0.0525	0.065201

and its implementation in the mathematical model. Another way is treatment of the lab data to deliver Kr and Pc curves for reservoir simulation. Currently, reservoir simulators use 3D governing equations (A1-A3), so the lab data must be interpreted in framework of this model. The type curves (C3, C4) solve this problem. They provide an approximate projection of the lab data onto the domain of the solutions of governing system (A5, A6). Then, the inverse solver makes this projection exact.

Pressure drop fluctuations after the stabilisation time in Fig. 8c, 8d, 8i, 9 h, 9i, and 9j are attributed to slug flow downstream the core in the connecting tubes. The outlet water and oil fluxes via the pore ensemble transforms to the stable slug flow in the tubes. This does affect the upstream flow in porous media. Using the type curves that approximate those raw data allows eliminating those art effects.

Planning and design of the lab tests We use the dimensionless criteria for admissible test parameters to plan and design the SSTTs, i.e., to determine an optimal velocity and timing between the samples and minimum acceptable core length. The theoretical criteria comprise capillary, gravity-viscous, and non-equilibrium numbers that are given by Eqs. (1, 2, 5); their smallness provide Kr and Pc independence of velocity, no gravity segregation, and equilibrium Kr and Pc during CCTT, respectively. Comparing with continuous waterflood and Welge-JBN method, SSTT accounts for end effect, so the capillary-viscous number is not used [35,50]. The operational criteria are given by Eqs. (6–8, 10); they provide the required accuracy of pressure and volume measurements, sample collection, and number of samples during the transitional periods.

The preliminary mathematical modelling, based on type curves, allows determining the pressure-drop and average saturation type curves, which smoothes the raw measured data and significantly decreases their scattering. The preliminary modelling also estimates the transition periods between the SSs, enabling planning of the test: prediction of the transient durations, determining the sampling frequencies and volumes, selecting the necessary pressure transducers during SSTT, and checking the operational criteria.

The number of stages and the corresponding injected water fractions F_n are determined to evenly cover the saturation range from S_{in} to 1-S_{or} by the measurements. The results show that most stages must use low water-cut values below 0.1 and above 0.9, and only three injections must be performed with intermediate water-cut values. This is explained by the smaller slope of fractional flow curves at low and high F_n values.

The SSTT method provides K_r and P_c in the saturation range [S_{in},1-S_{or}], where the inlet saturation exceeds the connate water saturation, $S_{in} > S_{wi}$. The difference between S_{in} and S_{wi} can be decreased by increasing flow velocity and core length, i.e., reducing the capillary-pressure effects.

Using pressure drops in phases for matching Several papers report the backflow during steady-state tests, where one phase enters the grooves connected to the pump injecting another phase; the flow lines path in the inner of the rock [37–40]. We assume that at low fractions of the injected water, pressure drop in oil is higher than in water by the value that exceeds the capillary pressure, so it is likely that oil enters the water grooves; this perturbs pressure in water. In this case, we use pressure drop in oil for the data matching. Otherwise, at high fractions of injected water, the difference in pressures in oil and water is less than capillary pressure, so water invasion in oil grooves is likely, and we use the pressure drop in water for matching. We observed that inlet pressure in water exceeds that in oil at $F > 0.5$, so $F = 0.5$ was used for switching from Δp_o to Δp_w in the matching.

The above method must be supported by mathematical modelling of two-phase flow in connections, grooves, and in the porous media adjacent to the core inlet, which is outside the scope of the present work. Understanding the pressure drop behaviour versus pore volume injected at two-phase steady-state flows still remains a key challenge.

Comparison between the half-moon and concentric-circle distributors Matching quality of SS pressure-drop and average water saturation data and transient pressure-drop data by the mathematical model for the 1st test is reasonable; the same corresponds to prediction quality of transient average saturation. However, the matching and prediction quality for the 2nd test is significantly better than the 1st test. This is explained by the higher accuracy of the weighting method and better sweep efficiency of the concentric-circle distributor, both used in the 2nd test. 3D reservoir simulation confirms the statement of better sweep efficiency of the core using the concentric-circle distributor rather than in the half-moon case.

To have laboratory confirmation of the 3D- and lower sweep hypothesis, after the final stage with $F_n = 1$, we injected water in oil connection only. At the 1st test that uses half-moon distributor, some additional oil was recovered. No additional oil was observed after the same procedure for the core with concentrate grooves at 2nd test. This indicates the lower degree of uniformity of saturations in the core at the 1st test.

The accuracy of matching of the SS data and transient pressure-drop data is significantly higher than that for predicting the transient average saturation data. Berg et al. [20,21] presented several explanations in this regard in terms of unstable effluent water-cut due to pore-scale phenomena: spontaneous snap-off, counterflow imbibition in small pores, hysteretic phenomena, etc. The mathematical model used for matching is a traditional Rapoport-Leas model for two-phase flow in porous media. The previous studies [46,47] show that the inverse algorithm is stable with respect to small 1D perturbations of the measured data. The algorithm is also stable with respect to 3D perturbations [53].

The algorithm determines K_r and P_c from SS pressure-drop data, SS average saturation data, stabilisation (transient) time, and transient pressure-drop data. The number of degrees of freedom (dimension) of the experimental data array at each F_n is the total of two SS values for saturation, two SS values for pressure-drop, stabilisation time, and two–three parameters for transient pressure-drop (three for S-shape curves and two for exponential curves, given by Eqs. (C3) and (C4), respectively). So, the number of degrees of freedom of SSTT measurements is either 7 or 8.

The model for two-phase flow of incompressible fluids contains 8 parameters, presented in Eqs. (A12)-(A14). Two constants – S_{or} and k_{rwor} – are determined from the last SSTT stage with $F_n = 1$, leaving 6 unknown Corey-Brooks parameters to be determined by the inverse solver. So, the number of model parameters does not exceed the number of degrees of freedom of the measured data array. Therefore, the close agreement between the measured data and the matched modelling results validates the SSTT method.

The current laboratory study provides the transient average saturation data as predictive values to validate the two-phase flow model under test conditions. We also measure pressure-drop and average saturation during tertiary imbibition, which is predictive and can be used to validate the model. The accuracy of matched SS and transient pressure-drop data is significantly better than average saturation. Moreover, the predictive pressure-drop during tertiary imbibition agrees with the model considerably better than the saturation data.

K_r and P_c curves in Fig. 7 correspond to the saturation intervals obtained from different intervals between subsequent steady states by the inverse solver. The intervals of different pieces in K_r and P_c curves, matched from different SSTT stages, are found to be located on the same smooth curves. This validates the algorithm proposed.

The preliminary modelling delivers the curve “stabilisation time T_s

versus injected water fraction F_n", Fig. 11e. For water-wet rocks, the curve has U-shape [46,47]. So, we approximated the lab data for $T_s = T_s(F_n)$ by U-turn shape curve. The approximated values are used for transient data treatment by Eqs C(3) and C(4). The plot for Ts-curve obtained by inverse solver for both tests has U-shape, as it is shown in Fig. 11e. This also validates the SSTT method.

To check for uniqueness of the match to the experimental data and possibility of multiple local minima, we perturbed 6 model parameters for the 2nd test, obtained by the inverse solver and presented in Table 2. We perturbed the parameters one-by-one by plus-minus 10%. For all 12 runs, the algorithm converts to the same non-perturbed model parameters with coefficient of determination 0.99 (Table 2). This indicates the unique deviation minimum for the matching.

However, perturbation runs around an optimal point cannot substitute a rigorous mathematical investigation, which is out of the scope of the present work.

For 12 runs, the coefficient of determination between the lab data and matched data vary from 0.960 to 0.968, while those between the lab data and type curves vary from 0.973 to 0.986. This shows the appropriate choice of power-law and exponential type curves for approximation of the lab data.

Extensions and applications Recent papers by Schlüter et al. [54], Armstrong et al. [19], Rabinovich et al. [55,56], Standnes et al. [23], Berg et al. [20,21], Sun et al. [24], and Anderson et al. [33] propose several physics effects during two-phase waterflood, which the classical Rapoport-Leas model (A1, A2) does not capture. The deviations between the predicted and measured data of transient average saturation during SSTT and average saturation and pressure-drop during continuous tertiary imbibition, obtained in the present work, can be used to quantify the non-equilibrium and hysteretic effects. The non-equilibrium effects can be evaluated by the Barenblatt's delay model [49,51]. Two-phase flow equations with scanning K_r and P_c curves allows estimating the hysteretic phenomena [27,57].

The present work uses the Brooks-Corey model for K_r and P_c, given by Eqs (A12)-(A14). Yet, real data often do not fit this model [20,58]. The alternative LET model can provide better fit [20,21]. Yet, this model contains four more constants than the Brooks-Corey model, which requires more test information and, consequently, some additional measurements during SSTTs. Pressure measurement in an intermediate core point (so-called 3-point-pressure method) can provide an additional experimental information from SSTT sufficient to determine all constants in more advanced models for K_r and P_c [59,60].

The forward problem for the transient flows between the sequential steady states from F_n to F_{n+1} is obtained by the numerical solution of system (A1) and (A2) with initial condition (A10) and boundary condition (A8). Yet, an industrial implementation of SSTT can enjoy two simplifications of the inverse solver. First, the difference between the injected water fractions in two sequential stages is small, so that F_n-$F_{n+1} \ll 1$. The transition from F_n to F_{n+1} occurs between two steady states. Fig. 5c shows small change of the saturation profiles during the transitions, that is the difference in saturation profiles given by Eq. (A11) is significantly lower than one. It allows for linearization of governing system (A1, A2), where the coefficients depend on steady-state profiles (A11). Finite difference solutions of linearized PDEs are significantly simpler than those for the non-linear equations.

Another approach can be an analytical modelling. The initial-boundary value problem (A8, A10) for the linearized Eq. (A1) can be solved by the Sturm-Liouville method, which provides the explicit formulae for $s(x_D,t_D)$. The details can be found in the books [61,62].

In the most wide-spread mixed-wet case of the large oil-wet pores, where the capillary pressure is negative at high saturations, the formula for Pc has two additional parameters [33]. So, it is necessary to tune 8 parameters by the deviation minimisation algorithm, while for exponential transient pressure curves, which are typical for high water-cut values, the number of degrees of freedom of the steady-state data and transitional pressure-drop data is 7. Therefore, the model parameters cannot be uniquely determined from the measured data. One way around is using the transient average saturation data. Another way is some more measurements performed during SSTT. The so-called 3-point-pressure method, where the pressure drop is measured across the overall core and its section [23,33]. Another method is multi-rate injection that provides pressure drops and average saturations for two / three different flow velocities [36,40].

The theory of two-phase flow in porous media transformed by Shapiro [63–65] that reflects the menisci movements and their interaction with both phases is an example of the extension to the traditional theory (A5) and (A6), which can be tuned by SSTT. Here, the SS and transient data for pressure drop and average saturation, which is excessive for matching the traditional model, can be used to determine a higher number of the empirical model functions. Additional pressure measurements in an intermediate core point provide extra data for the model tuning [60].

Using two phases in thermodynamic equilibrium for coreflooding allows extension of SSTT for partly-miscible displacement processes (EOR flows, CO_2 storage) [3,4,18,58,66].

9. Conclusions

The laboratory and mathematical modelling of two-phase coreflood SSTTs allow drawing the following conclusions.

The admissibility criteria determine selection of the flow rate, the sampling number and volumes, and the minimum core length for SSTTs. The three theoretical criteria guarantee that two-phase flow fulfils the assumptions of the classical Rapoport-Leas model during the test. The four operational criteria provide the required accuracy of pressure and sample volume measurements, and the sample number and volume. The close match between the mathematical model and the experimental data, measured according to the established experimental protocol, proves the efficiency of using the theoretical and operational accessibility criteria to plan and design the laboratory SSTTs.

The higher matching and predictive accuracy for the test with concentric-circle inlet distributor and determination of the outlet water-cut by weighting method than for the test with half-moon distributor and visual determination of the outlet water-cut) is explained by higher areal sweep of the core due to use of concentric-circle inlet distributor and significantly higher accuracy of weighting than visualization method.

The accuracy of transient pressure-drop matching, with R^2 equal 0.99 for both tests, is higher than the accuracy of average saturation prediction (0.88 and 0.98 for the 1st and 2nd test, respectively). Yet, the matched modelling lines for both pressure-drop and saturation are located within the respective error bars in both tests, which allows claiming high match for both tests.

High agreement between the measured data and their type curve approximation and close match between the raw measured data and the modelling predictions observed in both tests prove the efficiency of the type-curve procedure.

Despite the "base" K_r and P_c functions significantly differ from those obtained from the SSTT data by the inverse solver for both tests, the same type curves have been obtained. This also validates the type-curve procedure.

Different saturation intervals of K_r and P_c obtained by the inverse solver for different saturation intervals, which correspond to different Fn-stages, are located on the same curves with high accuracy for both tests, which validates the SSTT method too.

Uniqueness of the local minimum for the matching must be checked for each lab case. In this study, perturbation of each tuned model parameter yields higher coefficient of determination than that for tuned values, and all perturbed solutions tend to the same limit.

CRediT authorship contribution statement

N. Hemmati: Software, Methodology. **S. Borazjani:** Investigation, Methodology. **S. Yang:** Validation, Methodology. **A. Badalyan:** Methodology. **L. Genolet:** Validation, Writing – review & editing. **A. Behr:** Validation, Investigation, Writing – review & editing. **A. Zeinijahromi:** Validation, Writing – review & editing. **P. Bedrikovetsky:** Methodology, Supervision.

Declaration of Competing Interest

The authors declare that they have no known competing financial interests or personal relationships that could have appeared to influence the work reported in this paper.

Acknowledgements

This work was motivated by encouraging communications with Dr. J Maas (Consultant, EOR, SCAL, Geothermal); his contribution is gratefully acknowledged. PB is highly grateful to his mentors Profs M. Lurie, K. Basniev, V. Maron, and A. Kurbanov (Moscow Gubkin Oil-Gas University) for thorough and fruitful discussions on two-phase flows during two centuries.

Appendix A. . Governing equations for two-phase transport of immiscible fluids

One-dimensional (1D) two-phase transport of two immiscible incompressible phases in porous media is described by a system of two partial differential equations, which express the mass balance of water and extended Darcy's law for two-phase flux [18,49].

$$\phi\ \frac{\partial s}{\partial t}+U\frac{\partial f(s)}{\partial x}\ =\ -\frac{\sqrt{k\phi}\sigma cos\,\theta}{\mu_o}\ \frac{\partial}{\partial x}\left(f\,k_{ro}(s)\ \frac{\partial J(s)}{\partial x}\right) \tag{A1}$$

$$U=\ -k\left(\frac{k_{rw}(s)}{\mu_w}+\frac{k_{ro}(s)}{\mu_o}\right)\ \frac{\partial p_w}{\partial x}-\frac{k\,k_{ro}(s)}{\sqrt{k/\phi}\mu_o}\ \frac{\partial\left(\sigma cos\,\theta J(s)\right)}{\partial x} \tag{A2}$$

where s is the water saturation, t is the time, x is the linear coordinate, J is the Leverett function, θ is the contact angle, $k_{rw}(s)$ and $k_{ro}(s)$ are the relative permeabilities for water and oil, respectively, p_w is the pressure in water, and $f(s)$ is the fractional flow function:

$$f(s)=\left(1+\frac{\mu_w k_{ro}(s)}{k_{rw}(s)\mu_o}\right)^{-1} \tag{A3}$$

Introducing the dimensionless parameters below.

$$x_D=\frac{x}{L},\ t_D=\frac{Ut}{\phi L},\ P_o=\frac{k}{UL\mu_o}p_o,\ P_w=\frac{k}{UL\mu_o}p_w,\ \varepsilon=\frac{\sqrt{k\phi}\sigma cos\theta}{UL\mu_o} \tag{A4}$$

transforms Eqs. (A1)-(A2) to the following form.

$$\frac{\partial s}{\partial t_D}+\frac{\partial f(s)}{\partial x_D}=\varepsilon\frac{\partial^2\psi(s)}{\partial x_D^2} \tag{A5}$$

$$\frac{\partial\,P_w}{\partial\,x_D}\ =\ \left(-1-\ \varepsilon\ k_{ro}(s)\frac{\partial J}{\partial\,x_D}\right)\left(\frac{k_{rw}(s)\mu_o}{\mu_w}+k_{ro}\right)^{-1} \tag{A6}$$

where ε is the capillary-viscous ratio, and $\psi'(s)$ is the nonlinear pressure-diffusion coefficient:

$$\psi/(s)=\ -k_{ro}(s)f(s)J/(s) \tag{A7}$$

Mass balance in Eq. (A5) shows that water flux consists of two components – driven by the pressure gradient (on the left-hand side) and by the capillary pressure gradient (on the right-hand side). Inlet boundary condition for injection of two-phase flux with water fraction F_{n+1} fixes inlet flux is.

$$x_D=0:\ \ f(s)-\varepsilon\frac{\partial\psi(s)}{\partial x_D}=F_{n+1} \tag{A8}$$

Outlet boundary condition corresponds to equality of phase pressures.

$$x_D=1:\ \ J(s)=0 \tag{A9}$$

Initial condition for transient flow during the injection of two-phase fluid with injected water fraction F_{n+1} is the stabilized saturation distribution after the injection with water fraction F_n is.

$$t_D=0:\ \ f(s)-\varepsilon\frac{\partial\psi(s)}{\partial x_D}=F_n \tag{A10}$$

Under SS conditions, when saturation doesn't change with respect to time, the expression for saturation is SS solution of Eq. (A5):

$$\frac{1-x_D}{\varepsilon}=\int_s^{1-S_{or}}\frac{k_{ro}f(s)J/(s)ds}{F_n-f(s)} \tag{A11}$$

Eq. (A5) subject to the initial and boundary conditions (A8)-(A10) fully determines the transient saturation behaviour $s(x_D,t_D)$ during the sequence of injections with water fraction $F_1,F_2\ldots F_n$, including the stabilized saturation distributions $s(x_D, F_k)$. Momentum balance equation (A6) separates from Eq. (A5) – unknown pressure $P_w(x_D,t_D)$ is determined from Eq. (A6) by integration in x_D for known solution of initial-boundary problem (A5), (A8),

(A9), and (A11) – $s(x_D,t_D)$.

We consider Corey formula to describe K_r of oil and water.

$$k_{ro}(s) = k_{rowi}(1-S)^m, \quad S = \frac{s - S_{wi}}{1 - S_{wi} - S_{or}} \tag{A12}$$

$$k_{rw}(s) = k_{rwor}S^n, \tag{A13}$$

and Brooks-Corey model for P_c.

$$p_c(s) = \begin{cases} P_d S^{-1/\lambda} & 0 < S < 0.99 \\ 10P_d(0.99)^{-1/\lambda}\sqrt{1-S} & 0.99 < S < 1 \end{cases}, \tag{A14}$$

Here, P_d is the entry pressure for the non-wetting fluid (oil), λ is the Brooks-Corey parameter, S_{wi} and S_{or} are endpoint saturations for oil and water, respectively, k_{rowi} and k_{rwor} are endpoint relative phase permeability for oil and water, m and n are powers.

The first line of Eq. (14) shows that the Brooks-Corey capillary pressure is equal to P_d at residual oil saturation. However, phase pressures are continuous along the streamlines upon crossing the core outlet, so the capillary pressure is continuous too. Downstream, the capillary pressure under the low-dispersivity flow, is negligible comparing with that in porous media. Therefore, the capillary pressure upstream the core outlet is zero, which contradicts to the first line in Eq. (14). The second line in Eq. (14) provides the fall of P_c from P_d to zero, resolving the contradiction. The second line in Eq. (A14) fulfils the condition of $p_c(s) = 0$ at the core outlet. Here we extrapolate the capillary pressure curve in the normalized saturation S interval of [0.99, 1.0] by the square root of oil saturation, which significantly simplifies the calculations. With the smoothing interval [1-δ,1] tending to zero ($\delta \to 0$), the solution of systems (A5) and (A6) tends to the solution with the capillary pressure curve that tends to the threshold P_d value as saturation s tends to 1-S_{or}.

Appendix B. . Non-equilibrium two-phase flow in porous media

The fundamental saturation dependencies of K_r and P_c, used in the mathematical model (A1, A2), are based on the conditions of capillary equilibrium of two-phase fluid in porous media. The capillary equilibrium conditions can be breached during the corefloods with high rates in short cores, when the capillary two-phase system of immiscible fluids relaxes toward the equilibrium conditions. Barenblatt et al. [49] decompose two-phase flow into the equilibrium displacement in the core-flow direction and cross-sectional pore-scale imbibition that homogenises the saturation distribution across the core. This decomposition corresponds to K_r and P_c being functions of non-equilibrium saturation η which delays in reaching the actual saturation by the time τ [49,51]. The governing system (A1, A2) becomes:

$$\frac{\partial s}{\partial t_D} + \frac{\partial f(\eta)}{\partial x_D} = \varepsilon \frac{\partial^2 \psi(\eta)}{\partial x_D^2} \tag{B1}$$

$$\frac{\partial P_w}{\partial x_D} = -\left(1 + \varepsilon k_{ro}(\eta)\frac{\partial J(\eta)}{\partial x_D}\right)\left(\frac{k_{rw}(\eta)\mu_o}{\mu_w} + k_{ro}(\eta)\right) \tag{B2}$$

$$\varepsilon_\tau \frac{\partial s}{\partial t_D} = \eta - s \tag{B3}$$

where the relaxation time τ is a typical period of the imbibition into low-permeable inclusion with size l, given by Eq. (4), and the relaxation number ε_t is given by Eq. (5). As it follows from Eq. (5), the non-equilibrium effects vanish at low flow rate in long cores, where $\varepsilon_\tau \ll 1$.

Appendix C. . Inverse solver

The measured data presented in Fig. 6a and b show that the transient pressure-drop Δp can be matched by exponential functions. Here, we normalize these data to vary in interval of [0, 1]:

$$T \to \frac{t_D - t_D^i}{t_D^e - t_D^i} \tag{C1}$$

$$\Delta P \to \frac{\Delta p(t_D) - \Delta p(t_D^i)}{\Delta p(t_D^e) - \Delta p(t_D^i)} \tag{C2}$$

where t_D^i and t_D^e are the beginning and end of transition process with 98% of confidence interval.

Figs. 8 and 9 show that the transient pressure-drop curves have S-shape for low water fractions of injected water ($F_n < 0.5$) and exponential form for high injected water fraction ($F_n > 0.5$). The formulae for the S-shape curve and exponential curve are (C3) and (C4), respectively:

$$\Delta P(T) = \frac{T^a}{T^a + c(1-T)^b} \tag{C3}$$

$$\Delta P(T) = \frac{exp(dT) - exp(eT)}{exp(d) - exp(e)} \tag{C4}$$

Further in the current work, we use Eqs. (C3) and (C4) to approximate the raw measured data on transient pressure-drop (Section 5.1), and use those approximations to determine K_r and P_c by the inverse solver (Section 5.2 and Fig. 10).

Figs. 8 and 9 show that either S-shape or exponential curves can closely approximate the pressure-drop histories. Tables 3 and 4 present the tuned

parameters a, b, and c for S-shape, and d and e for exponential curves, respectively. The coefficient of determination R^2(last columns in Tables 3 and 4) show the close agreement between the type curves and transient pressure-drop-data.

The inverse method minimizes the difference between S_{av} from the modelling and the measured during steady states, and also the difference between Δp from the modelling and the ones obtained by fitting type curves on the measured pressure-drop Δp_{TC}:

$$min(G(t_D, k_{rw}, k_{ro}, p_c))$$

$$G = \frac{\int_{t_D^i}^{t_D^e} (\Delta p(y) - \Delta p_{TC}(y))^2 dy}{\int_{t_D^i}^{t_D^e} (\Delta \bar{p}_{TC}(y) - \Delta p_{TC}(y))^2 dy} + \frac{\left(S_{av}(t_D^i) - S_{av_{lab}}(t_D^i)\right)^2}{\left(\frac{S_{av_{lab}}(t_D^i) + S_{av_{lab}}(t_D^e)}{2} - S_{av_{lab}}(t_D^i)\right)^2} + \frac{\left(S_{av}(t_D^e) - S_{av_{lab}}(t_D^e)\right)^2}{\left(\frac{S_{av_{lab}}(t_D^i) + S_{av_{lab}}(t_D^e)}{2} - S_{av_{lab}}(t_D^e)\right)^2} \quad \text{(C5)}$$

We use ''fminsearch'' optimization function provided in MATLAB. The function ''fminsearch'' finds the minimum of constrained nonlinear multivariable function and determines the constants k_{rowi}, S_{wi}, λ, P_d, n, and m. The ''fminsearch'' needs an initial first-iteration guess of the variables for the iterative minimization procedure. The initial guess in this study is obtained from SS data on the pressure-drops and rates for each phase, ignoring the capillary pressure.

References

[1] Li Y, Li H, Chen S, Mbia E, Wang Ke, Ren H. Capillarity characters measurement and effects analysis in different permeability formations during waterflooding. Fuel 2017;194:129–43.

[2] Torabi F, Mosavat N, Zarivnyy O. Predicting heavy oil/water relative permeability using modified Corey-based correlations. Fuel 2016;163:196–204.

[3] Farajzadeh R, Ameri A, Faber MJ, Van Batenburg DW, Boersma DM, Bruining J. Effect of Continuous, Trapped, and Flowing Gas on Performance of Alkaline Surfactant Polymer ASP Flooding. In: SPE Enhanced Oil Recovery Conference. 2013:SPE-165238-MS.

[4] Farajzadeh R, Guo H, van Winden J, Bruining J. Cation Exchange in the Presence of Oil in Porous Media. ACS Earth Space Chem 2017;1(2):101–12.

[5] Yuan B, Moghanloo RG. Analytical model of well injectivity improvement using nanofluid preflush. Fuel 2017;202:380–94.

[6] Yuan B, Moghanloo RG. Analytical modeling nanoparticles-fines reactive transport in porous media saturated with mobile immiscible fluids. AIChE J 2019;65(10). https://doi.org/10.1002/aic.v65.1010.1002/aic.16702.

[7] Ojha SP, Misra S, Tinni A, Sondergeld C, Rai C. Relative permeability estimates for Wolfcamp and Eagle Ford shale samples from oil, gas and condensate windows using adsorption-desorption measurements. Fuel 2017;208:52–64.

[8] Xu C, Yang X, Liu C, Kang Y, Bai Y, You Z. Dynamic fracture width prediction for lost circulation control and formation damage prevention in ultra-deep fractured tight reservoir. Fuel 2022;307:121770. https://doi.org/10.1016/j.fuel.2021.121770.

[9] Zhang Y, Song C, Yang D. A damped iterative EnKF method to estimate relative permeability and capillary pressure for tight formations from displacement experiments. Fuel 2016;167:306–15.

[10] Kuo C-W, Benson SM. Numerical and analytical study of effects of small scale heterogeneity on CO2/brine multiphase flow system in horizontal corefloods. Adv Water Resour 2015;79:1–17.

[11] Perrin J-C, Krause M, Kuo C-W, Miljkovic L, Charoba E, Benson SM. Core-scale experimental study of relative permeability properties of CO2 and brine in reservoir rocks. Energy Procedia 2009;1(1):3515–22.

[12] Yuan B, Wood DA. A holistic review of geosystem damage during unconventional oil, gas and geothermal energy recovery. Fuel 2018;227:99–110.

[13] Bai T, Chen Z, Aminossadati SM, Li L, Liu J, Lu H. Dimensional analysis and prediction of coal fines generation under two-phase flow conditions. Fuel 2017;194:460–79.

[14] Durucan S, Ahsan M, Shi J-Q, Syed A, Korre A. Two phase relative permeabilities for gas and water in selected European coals. Fuel 2014;134:226–36.

[15] Shaw D, Mostaghimi P, Armstrong RT. The dynamic behaviour of coal relative permeability curves. Fuel 2019;253:293–304.

[16] Zhu S, Du Z, Li C, You Z, Peng X, Jiang H, et al. Effects of numerical dispersion on pressure diffusion in CBM reservoirs. Fuel 2019;251:534–42.

[17] Aziz K, Settari A. Petroleum Reservoir Simulation. London: Applied Science Publishers; 1979.

[18] Lake LW, Johns R, Rossen B, Pope GA. Fundamentals of enhanced oil recovery. TX: Society of Petroleum Engineers Richardson; 2014.

[19] Armstrong RT, McClure JE, Berrill MA, Rücker M, Schlüter S, Berg S. Beyond Darcy's law: The role of phase topology and ganglion dynamics for two-fluid flow. Phys Rev E 2016;94(4):043113.

[20] Berg S, Unsal E, Dijk H. Non-uniqueness and uncertainty quantification of relative permeability measurements by inverse modelling. Comput Geotech 2021;132:103964. https://doi.org/10.1016/j.compgeo.2020.103964.

[21] Berg S, Unsal E, Dijk H. Sensitivity and uncertainty analysis for parameterization of multiphase flow models. Transp Porous Media 2021;140(1):27–57.

[22] Liu Z, Herring A, Arns C, Berg S, Armstrong RT. Pore-scale characterization of two-phase flow using integral geometry. Transp Porous Media 2017;118(1):99–117.

[23] Standnes DC, Andersen PØ, Papatzacos P, Skjæveland SM. Interpretation of 1-D Counter-Current Spontaneous Imbibition Processes Using Microscopic Diffusion Theory and a Modified Buckley-Leverett Approach. Energy Fuels 2020;34(5):5868–83.

[24] Sun C, McClure J, Berg S, Mostaghimi P, Armstrong RT. Universal description of wetting on multiscale surfaces using integral geometry. J Colloid Interface Sci 2022;608:2330–8.

[25] Aghabozorgi S, Sohrabi M. Generalised model for simulation of two-and three-phase cycle-dependent hysteresis in sandstones. Fuel 2022;310:122328. https://doi.org/10.1016/j.fuel.2021.122328.

[26] McClure JE, Berg S, Armstrong RT. Capillary fluctuations and energy dynamics for flow in porous media. Phys Fluids 2021;33(8):083323. https://doi.org/10.1063/5.0057428.

[27] Schaerer CE, Marchesin D, Sarkis M, Bedrikovetsky P. Permeability hysteresis in gravity counterflow segregation. SIAM J Appl Math 2006;66(5):1512–32.

[28] Johnson EF, Bossler DP, Bossler VON. Calculation of Relative Permeability from Displacement Experiments. Trans AIME 1959;216(01):370–2.

[29] Jones SC, Roszelle WO. Graphical Techniques for Determining Relative Permeability From Displacement Experiments. J Petrol Technol 1978;30(05):807–17.

[30] Borazjani S, Behr A, Genolet L, Kowollik P, Bedrikovetsky P. Ion-exchange inverse problem for low-salinity coreflooding. Transp Porous Media 2019;128(2):571–611.

[31] Zeinijahromi A, Farajzadeh R, (Hans) Bruining J, Bedrikovetsky P. Effect of fines migration on oil–water relative permeability during two-phase flow in porous media. Fuel 2016;176:222–36.

[32] Maas JG, Flemisch B, Hebing A. Open source simulator DuMux available for SCAL data interpretation. SCA 2011;8:2011.

[33] Andersen PØ, Skjæveland SM, Standnes DC. An Analytical Model for Analysis of Capillary Pressure Measurements by Centrifuge. Petrophys-SPWLA J Formation Eval Reservoir Description 2017;58(04):366–75.

[34] McPhee C, Reed J, Zubizarreta I. Core analysis: a best practice guide. Elsevier; 2015.

[35] Hussain F, Cinar Y, Bedrikovetsky P. A semi-analytical model for two phase immiscible flow in porous media honouring capillary pressure. Transp Porous Media 2012;92(1):187–212.

[36] Andersen PØ, Zhou Y. Steady state relative permeability experiments with capillary end effects: Analytical solutions including derivation of the intercept method. J Petrol Sci Eng 2020;192:107249. https://doi.org/10.1016/j.petrol.2020.107249.

[37] Gupta R, Maloney D. Intercept Method—A Novel Technique To Correct Steady-State Relative Permeability Data for Capillary End Effects. SPE Reservoir Eval Eng 2014;19(02):316–30.

[38] Gupta R, Maloney D. Applications of the intercept method to correct steady-state relative permeability for capillary end-effects. International Symposium of the Society of Core Analysts held in St. John's Newfoundland and Labrador Canada 2015:16–21.

[39] Virnovsky GA, Relative GY. Permeability and Capillary Pressure Concurrently Determined from Steady-State Flow Experiments 1995.

[40] Virnovsky GA, Vatne KO, SkjaeveLand SM, Lohne A. Implementation of Multirate Technique to Measure Relative Permeabilities Accounting. In: SPE Annual Technical Conference and Exhibition. 1998:SPE-49321-MS.

[41] Alhammadi AM, Gao Y, Akai T, Blunt MJ, Bijeljic B. Pore-scale X-ray imaging with measurement of relative permeability, capillary pressure and oil recovery in a mixed-wet micro-porous carbonate reservoir rock. Fuel 2020;268:117018. https://doi.org/10.1016/j.fuel.2020.117018.

[42] Kianinejad A, Chen X, DiCarlo DA. Direct measurement of relative permeability in rocks from unsteady-state saturation profiles. Adv Water Resour 2016;94:1–10.

[43] Reed J, Maas J. Review of the intercept method for relative permeability correction using a variety of case study data. The International Symposium of the Society of Core Analysts. 2018.
[44] Reed J, Maas J. Review of the intercept method for relative permeability correction a variety of case study data. Petrophys-SPWLA J Formation Eval Reservoir Description 2019;60(2):283–6.
[45] Zhao H, Hu J, Wang J, Zhang Y. A comprehensive model for calculating relative permeability based on spontaneous imbibition and CT scanning measurement. Fuel 2019;247:287–93.
[46] Borazjani S, Hemmati N, Behr A, Genolet L, Mahani H, Zeinijahromi A, et al. Simultaneous determination of gas–water relative permeability and capillary pressure from steady-state corefloods. J Hydrol 2021;598:126355. https://doi.org/10.1016/j.jhydrol.2021.126355.
[47] Borazjani S, Hemmati N, Behr A, Genolet L, Mahani H, Zeinijahromi A, et al. Determining water-oil relative permeability and capillary pressure from steady-state coreflood tests. J Petrol Sci Eng 2021;205:108810. https://doi.org/10.1016/j.petrol.2021.108810.
[48] Springer N, Korsbech U, Aage H. Resistivity index measurement without the porous plate: A desaturation technique based on evaporation produces uniform water saturation profiles and more reliable results for tight North Sea chalk. France: International Symposium of the Society of Core Analysts Pau; 2003. p. 21–4.
[49] Barenblatt GI, Entov VM, Ryzhik VM. Theory of fluid flows through natural rocks. Kluwer Academic; 1991.
[50] Al-Sarihi A, You Z, Behr A, Genolet L, Kowollik P, Zeinijahromi A, et al. Admissible parameters for two-phase coreflood and Welge–JBN method. Transp Porous Media 2020;131(3):831–71.
[51] Silin D, Patzek T. On Barenblatt's model of spontaneous countercurrent imbibition. Transp Porous Media 2004;54(3):297–322.
[52] Palatnik B, Førland E. An Application of the Regression Technique to Generate Pseudo Relative Permeability Functions and Upscale Multiphase Flow Models. In: ECMOR V-5th European Conference on the Mathematics of Oil Recovery. European Association of Geoscientists & Engineers; 1996:cp-101-00035.
[53] Yang S, Hemmati N, Russell T, Zeinijahromi A, Borazjani S, Behr A, et al. 3D effects in two-phase steady-state tests. J Petrol Sci Eng 2022;208:109533. https://doi.org/10.1016/j.petrol.2021.109533.
[54] Schlüter S, Berg S, Rücker M, Armstrong RT, Vogel H-J, Hilfer R, et al. Pore-scale displacement mechanisms as a source of hysteresis for two-phase flow in porous media. Water Resour Res 2016;52(3):2194–205.
[55] Rabinovich A. Estimation of sub-core permeability statistical properties from coreflooding data. Adv Water Resour 2017;108:113–24.
[56] Rabinovich A. Analytical Corrections to Core Relative Permeability for Low-Flow-Rate Simulation. SPE J 2018;23(05):1851–65.
[57] Bedrikovetsky P, Marchesin D, Ballin P. Mathematical Theory for Two Phase Displacement with Hysteresis (With application to WAG injection). In: ECMOR V-5th European Conference on the Mathematics of Oil Recovery. European Association of Geoscientists & Engineers; 1996:cp-101-00006.
[58] Kamali F, Hussain F. Field-scale simulation of CO2 enhanced oil recovery and storage through SWAG injection using laboratory estimated relative permeabilities. J Petrol Sci Eng 2017;156:396–407.
[59] Bedrikovetsky P, Tran P, Van den Broek WMGT, Marchesin D, Rezende E, Siqueira A, et al. Damage Characterization of Deep Bed Filtration from Pressure Measurements. In: International Symposium and Exhibition on Formation Damage Control. 2002:SPE-73788-MS.
[60] Vaz A, Bedrikovetsky P, Fernandes PD, Badalyan A, Carageorgos T. Determining model parameters for non-linear deep-bed filtration using laboratory pressure measurements. J Petrol Sci Eng 2017;151:421–33.
[61] Kolmogorov AN. Fomin SVe. Elements of the theory of functions and functional analysis: Courier Corporation; 1957.
[62] Polyanin A, Nazaikinskii V. Handbook of linear partial differentialequations for engineers and scientists, BocaRaton. London: CRC Press; 2016.
[63] Shapiro AA. Two-phase immiscible flows in porous media: The Mesocopic Maxwell-Stefan approach. Transp Porous Media 2015;107(2):335–63.
[64] Shapiro AA. Mechanics of the separating surface for a two-phase co-current flow in a porous medium. Transp Porous Media 2016;112(2):489–517.
[65] Shapiro AA. A three-dimensional model of two-phase flows in a porous medium accounting for motion of the liquid–liquid interface. Transp Porous Media 2018;122(3):713–44.
[66] Ajoma E, Saira, Sungkachart T, Ge J, Le-Hussain F. Water-saturated CO2 injection to improve oil recovery and CO2 storage. Appl Energy 2020;266:114853.

8. Analytical modelling of the water block phenomenon in hydraulically fractured wells

Naik S, **Yang, S.**, Woolley M, Bedrikovetsky P.

Journal of Natural Gas Science and Engineering, 67, pp. 56-70

Statement of Authorship

Title of Paper	Analytical modelling of the water block phenomenon in hydraulically fractured wells
Publication Status	☑ Published ☐ Accepted for Publication ☐ Submitted for Publication ☐ Unpublished and Unsubmitted work written in manuscript style
Publication Details	Naik, S., Yang, S., Woolley, M. and Bedrikovetsky, P., 2019. Analytical modelling of the water block phenomenon in hydraulically fractured wells. Journal of Natural Gas Science and Engineering, 67, pp.56-70.

Principal Author

Name of Principal Author	Saurabh Naik		
Contribution to the Paper	Numerical analysis, manuscript preparation		
Signature		Date	11/11/21

Co-Author Contributions

By signing the Statement of Authorship, each author certifies that:

i. the candidate's stated contribution to the publication is accurate (as detailed above);

ii. permission is granted for the candidate in include the publication in the thesis; and

iii. the sum of all co-author contributions is equal to 100% less the candidate's stated contribution.

Name of Co-Author (Candidate)	Shuyan Yang		
Contribution to the Paper	Helped with the development of the model, production data analysis and fitting, manuscript preparation		
Overall percentage (%)	40%		
Certification:	This paper reports on original research I conducted during the period of my Higher Degree by Research candidature and is not subject to any obligations or contractual agreements with a third party that would constrain its inclusion in this thesis. I am the primary author of this paper.		
Signature		Date	13/11/2021

Name of Co-Author	Matthew Woolley		
Contribution to the Paper	Problem formulation, technical discussions, supervision of the project		
Signature		Date	11/11/21

Name of Co-Author	Pavel Bedrikovetsky		
Contribution to the Paper	Problem formulation, technical discussions, supervision of the project		
Signature		Date	11/11/21

Journal of Natural Gas Science and Engineering 67 (2019) 56–70

Contents lists available at ScienceDirect

Journal of Natural Gas Science and Engineering

journal homepage: www.elsevier.com/locate/jngse

Analytical modelling of the water block phenomenon in hydraulically fractured wells

S. Naik[a], S. Yang[a], M. Woolley[b], P. Bedrikovetsky[a,*]

[a] The University of Adelaide, South Australia, Australia
[b] Santos Ltd, Adelaide, South Australia, Australia

ARTICLE INFO

Keywords:
Water blocking
Fractured well
Formation damage
Analytical model
End effect
Gas production

ABSTRACT

Hydraulic fracturing is a key technology which has enhanced the economic viability of the unconventional low permeability reservoirs by increasing their productivity. However, the high capillary forces associated with low permeability reservoirs can trap water near to the fracture face and impair the production of gas or oil. This phenomenon is commonly referred to as water block. In order to estimate how water blocking impairs well productivity, the model for well inflow performance must account for two phases, gas compressibility, gas-water capillary pressure, wettability, inertial flows, and pressure-dependent gas viscosity. In this paper, we derive an exact solution for the inflow performance of a fractured gas well during non-inertial flow. For inertial flow, an approximate analytical solution is obtained using the streamline method. The solutions account for immobile water, gas compressibility, gas-water capillary pressure, wettability, inertial flows, and pressure-dependent gas viscosity. A sensitivity analysis shows the essential role played by the Leverett *J* function, the relative permeability curves and the ratio between the capillary, viscous and inertial forces. The derived solutions are applied in a case study to determine that water block is a likely contributor to skin.

1. Introduction

Improving inflow performance is important in order to achieve commerciality of tight reservoirs, and one of the most common techniques to achieve this is hydraulic fracturing (Economides and Nolte, 1989; Yuan and Wood, 2015; Yuan et al., 2015).

For water-wet or mixed-wet rocks, the low capillary pressures in the hydraulic fracture result in high water saturations at the fracture face (Barenblatt et al., 1989; Jiang and Younis, 2016; Civan, 2015). This high water saturation creates a significant hydraulic resistance against flow of gas or oil. This phenomenon is referred to as water block, and is more problematic in tight reservoirs, where the capillary pressures in the rock is significantly higher than the fracture.

The extent of water block in a hydraulically fractured well is influenced by the compressibility of the gas, the flow convergence near to the well fracture and capillary, viscous and inertial forces. The inflow performance of the well can be calculated using numerical or analytical modelling.

Analytical models provide explicit or implicit formulae for skin. If compared with numerical models, this allows for significantly faster sensitivity studies and determination of model parameters from field data. Analytical models for oil or gas production permit clearer interpretation of the production history. As a result there have been many efforts to derive analytical solutions in different areas of reservoir and production engineering (Economides and Nolte, 1989; Bedrikovetsky, 2013; Lake et al., 2014; Huang et al., 2018).

Analytical solutions for one-dimensional (1D) flows accounting for two phase flows, gas compressibility, and capillary pressure have been published (Naik et al., 2015, 2018). However, for fractured wells the exact solution for 1D flow only corresponds to just the initial stage of production (Lee, 1982; Dake, 2013). When the pressure transient propagates far from the fracture, the deviation of the pressure distribution given by the linear flow model becomes significant due to curvilinear streamlines and singular flow near to the fracture tips.

Despite the high occurrence of water block in fractured wells in low permeability reservoirs (Bazin et al., 2010; Bahrami et al., 2011), the analytical solutions for fractured gas wells accounting for water block are not available. The present paper fills the gap.

The governing system of equations for gas-water flow with immobile water is well established. It consists of the mass balance equation for the gas phase, the momentum balance equation accounting for two phases (Darcy-Forchheimer's law), the equation for capillary pressure between the water and gas phase and the equation of state for gas (Dake, 2013; Towler, 2002).

* Corresponding author.
E-mail address: pavel@asp.adelaide.edu.au (P. Bedrikovetsky).

https://doi.org/10.1016/j.jngse.2019.04.018
Received 18 March 2019; Received in revised form 11 April 2019; Accepted 18 April 2019
Available online 24 April 2019
1875-5100/

The exact solutions for single-phase flow into fractured wells have been derived by reducing the governing system of equations to the Laplace equation (Bear, 2013). Similarly for two phase flow, we reduce the governing system of equations accounting for the gas and the immobile water to the Laplace equation, allowing for an exact solution. The exact formula for water block skin is then derived. The approximate solution accounting for inertial effects under high velocities near the fracture is obtained using the streamline method. The comparison of the solution with the numerical solution shows high accuracy of the approximate analytical solution. A sensitivity analysis determines that the most sensitive parameter affecting the skin is the pore size distribution index. The analytical models are used in a case study to determine if water block is a reasonable explanation for the increase of skin.

The text has the following structure. Section 2 derives the exact solution for the gas inflow performance with water blocking assuming Darcy's law. To validate the model proposed, Section 3 compares the analytical model to a numerical reservoir simulator. Section 4 develops a streamline method for gas flow accounting for capillary end-effects and the Darcy-Forchheimer law, and validates the analytical model numerically. Section 5 compares the plane parallel and radial flow solution to the analytical model derived. Section 6 performs a sensitivity study for the inflow performance accounting for non-inertial effects with respect to the modified capillary number and the dimensionless Forchheimer number. Section 7 provides the simplified analytical model for incompressible fluid, which corresponds to oil production. Section 8 applies the derived analytical models to a case study. Section 9 discusses the applications and the limitations of the models derived. Section 10 concludes the paper.

2. Derivation of gas inflow into a hydraulic fracture with immobile water

This section formulates assumptions for the model, presents basic equations and derives the exact solution for flow towards a fracture.

2.1. Assumptions of the model

Consider a vertical well which produces from a circular reservoir. The position of the well is given in Fig. 1. The reservoir has constant thickness and is isotropic and homogenous. The reservoir temperature is constant.

The well is hydraulically fractured. The fracture penetrates the entire thickness of the reservoir. This eliminates flow in the vertical direction. The pressure drop between the fracture tip and the wellbore is significantly smaller than the pressure drop between the reservoir and the wellbore. Therefore, the fracture is assumed to have infinite conductivity. The fracture half-length is less than half of the drainage radius.

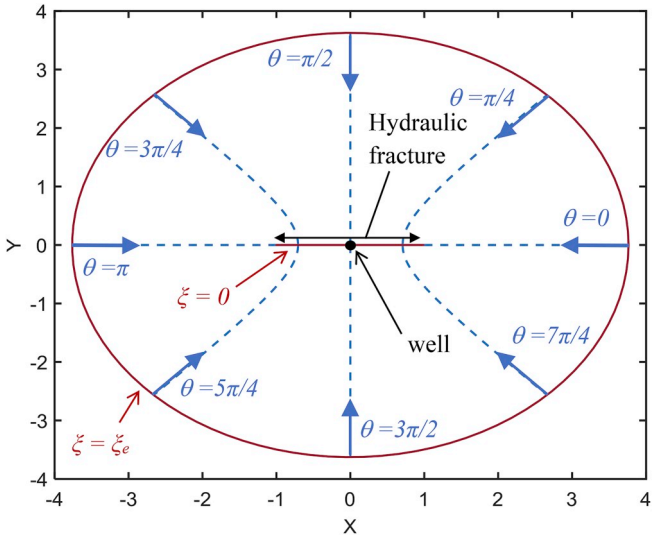

Fig. 1. Schematic of the elliptic coordinates used for the inflow performance model of a hydraulically fractured well.

Gas is produced under steady state and follows Darcy's law. There is no water production, however water is present in the reservoir.

2.2. Derivation of basic equations

The governing system for steady state gas flow with trapped water in a low-permeability porous medium consists of the mass balance equation for gas, Darcy's law for gas flow with Klinkenberg slip effects and the capillary pressure equation with constant water pressure:

$$\nabla \cdot u = 0 \tag{1}$$

$$\nabla p_g = u B_g(p_g) \frac{\mu_g(p_g)}{k k_{rg}(s) k_{kg}(p_g)} \tag{2}$$

$$p_g(s) = \frac{\sigma}{\sqrt{k/\phi}} J(s) + p_w \tag{3}$$

where u is the velocity at surface conditions, p is the pressure, B is the formation volume factor, k is the permeability, k_{rg} is the relative permeability to gas, s is the water saturation, k_{kg} is the Klinkenberg coefficient, μ is the viscosity, σ is the interfacial tension, ϕ is the porosity and J is the Leverett J function. The subscripts g and w represent gas and water at reservoir conditions, respectively.

The formation volume factor for gas, B_g, is defined as:

$$B_g(p_g) = \frac{p_{sc} z(p_g) T}{p_g z_{sc} T_{sc}} \tag{4}$$

where z is the compressibility factor, T is the temperature, and the subscript sc indicates surface conditions. The Klinkenberg coefficient k_{kg} (Jones and Owens, 1980) is defined as:

$$k_{kg}(p_g) = 1 + b/p_g, \quad b = 0.9735 k^{-0.33} \tag{5}$$

where b is an empirical constant. Since the fracture has infinite conductivity, the gas pressure is equal to the flowing bottom-hole pressure p_{wf} throughout the fracture. As the water is immobile, the water pressure is constant and can be evaluated from the bottom-hole flowing pressure:

$$p_w = p_{wf} - \frac{\sigma}{\sqrt{k/\phi}} J(s_{wf}) \tag{6}$$

where s_{wf} is the water saturation at the fracture face. The pore radius and permeability inside the hydraulic fracture are substantially higher than in the reservoir. As a result, the capillary pressure inside the fracture is negligible compared to the capillary pressure in the reservoir. The continuity in capillary pressure between the fracture and the reservoir rock causes the capillary pressure inside the reservoir rock to approach zero at the fracture face (Van Duijn et al., 1995). This means that for water wet cases, $s_{wf} = 1 - s_{gr}$, where s_{gr} is residual gas saturation. For gas wet cases $s_{wf} = s_{wirr}$, where s_{wirr} is the irreducible water saturation. For any other wettability, s_{wf} can be found from solving the equation $P_c(s_{wf}) = 0$. Let us define the potential Φ as:

$$\Phi(s) = \sigma \sqrt{k\phi} \int_{s_{wf}}^{s} \frac{k_{kg}(p_g(s))}{B_g(p_g(s))} \frac{k_{rg}(s) J'(s)}{\mu_g(p_g(s))} ds \tag{7}$$

This potential given by Eq. (7) satisfies the following equation:

$$\nabla \cdot u = \nabla^2 \Phi \tag{8}$$

2.3. Boundary conditions

Consider a set of Cartesian coordinates (x,y) such that the coordinate x is parallel to the hydraulic fracture and the coordinate y is perpendicular to the hydraulic fracture. The well is located at the origin of the axes (0,0). As $s = s_{wf}$ at the hydraulic fracture, the potential Φ is equal to zero at the hydraulic fracture. Therefore the inner boundary condition for potential is:

$$y = 0, -x_f < x < x_f: \Phi = 0 \tag{9}$$

where x_f is the fracture half-length. The outer boundary condition for potential is:

$$y^2 + x^2 = r_e^2: \Phi = \Phi(s_e) \tag{10}$$

where r_e is the drainage radius and s_e is the water saturation at the drainage radius which satisfies the following condition:

$$p_g(s_e) = p_e \tag{11}$$

where p_e is the pressure at the drainage radius. The function $p_g(s)$ is given by Eq. (3).

2.4. Flow equations under the streamline method

Prats (1961) and Hale and Evers (1981) used elliptic coordinates to describe the flow of fluid from a reservoir to a hydraulically fractured vertical well. The elliptic coordinates (ξ,θ) are defined by:

$$x(\xi, \theta) = x_f \cosh\xi \cos\theta$$
$$y(\xi, \theta) = x_f \sinh\xi \sin\theta \tag{12}$$

The dimensionless Cartesian coordinates can be obtained by dividing Eq. (12) by fracture half-length:

$$X = x/x_f$$
$$Y = y/x_f \tag{13}$$

The relationship between the dimensionless Cartesian coordinates and the elliptic coordinates is presented in Fig. 1. The gradient for potential under the new set of curvilinear coordinates is expressed as (Tang, 2007):

$$\nabla\Phi = \frac{\hat{e}_\xi}{h_\xi}\frac{\partial\Phi}{\partial\xi} + \frac{\hat{e}_\theta}{h_\theta}\frac{\partial\Phi}{\partial\theta} \tag{14}$$

where $\hat{e}_\xi$ and $\hat{e}_\theta$ are the unit vectors in direction ξ and θ respectively. The scale factors h_ξ and h_θ are:

$$h_\xi = \sqrt{\left(\frac{\partial x}{\partial\xi}\right)^2 + \left(\frac{\partial y}{\partial\xi}\right)^2}$$
$$h_\theta = \sqrt{\left(\frac{\partial x}{\partial\theta}\right)^2 + \left(\frac{\partial y}{\partial\theta}\right)^2} \tag{15}$$

The substitution of Eq. (12) into Eq. (15) results in:

$$h_\xi = h_\theta = x_f\sqrt{\sinh^2\xi + \sin^2\theta} \tag{16}$$

Let us assume that there is no flow in the θ direction. This gives the following equation:

$$u_\theta = 0, \frac{\partial\Phi}{\partial\theta} = 0 \tag{17}$$

The substitution of Eq. (16) and Eq. (17) into Eq. (14) results in:

$$\nabla\Phi = \frac{\hat{e}_\xi}{h_\xi}\frac{\partial\Phi}{\partial\xi} \tag{18}$$

2.5. Solution for potential

Using Eqs. (2) and (3) and the definition of the potential Eq. (7) we arrive at:

$$u = \nabla\Phi \tag{19}$$

From the substitution of Eqs. (16)–(18) into Eq. (19) we arrive at:

$$u_\xi = \frac{1}{x_f\sqrt{\sinh^2\xi + \sin^2\theta}}\frac{d\Phi}{d\xi} \tag{20}$$

where u_ξ is the velocity in direction ξ. The flow rate into the fracture is determined by integrating the normal component of velocity over any closed path around the fracture. If we choose an iso-potential line as the path to integrate on, the normal component of velocity will be u_ξ. The equation for gas flow rate is:

$$q_g = h\int_0^{2\pi} u_\xi\frac{\partial a}{\partial\theta}d\theta \tag{21}$$

where h is the formation height and a is the arc length. The arc length is defined as:

$$a = \int\sqrt{\left(\frac{\partial x}{\partial\theta}\right)^2 + \left(\frac{\partial y}{\partial\theta}\right)^2}d\theta \tag{22}$$

From the substitution of Eq. (12) into Eq. (22), we obtain:

$$\frac{\partial a}{\partial\theta} = x_f\sqrt{\sinh^2\xi + \sin^2\theta} \tag{23}$$

The substitution of Eq. (20) and Eq. (23) into Eq. (21) gives us the following equation for gas flow rate:

$$q_g = 2\pi h\frac{d\Phi}{d\xi} \tag{24}$$

The inner boundary condition (Eq. (9)) under the elliptic coordinates is:

$$\xi = 0: s = s_{wf}, \Phi = 0 \tag{25}$$

An important characteristic of the elliptic coordinates in Eq. (12) is that at large ξ ($\xi \gg 2$) they begin to resemble cylindrical coordinates with radius r (where $r = x_f\sinh\xi = x_f\cosh\xi$). A circular reservoir with boundary radius $r = r_e$ can be approximated by an elliptic reservoir with boundary $\xi_e = \ln(2r_e/x_f)$, as long as $r_e > > 2x_f$. Therefore, the outer boundary condition under elliptic coordinates is:

$$\xi = \xi_e = \ln(2r_e/x_f): \Phi = \Phi(s_e) \tag{26}$$

Finally, the solution for the potential is:

$$\Phi = \frac{\Phi(s_e)}{\xi_e}\xi \tag{27}$$

2.6. Analytical model for inflow performance

Substituting Eq. (3) into Eq. (24) and applying the chain rule to the resultant gives us:

$$q_g = 2\pi kh\frac{k_{kg}(p_g(s))}{B_g(p_g(s))}\frac{k_{rg}(s)}{\mu_g(p_g(s))}\frac{dp_g}{d\xi} \tag{28}$$

The definition of pseudo pressure ψ for reservoirs with Klinkenberg slip effects is:

$$\psi(p) = 2\int_0^p \frac{k_{kg}(p_g)p_g}{z(p_g)\mu_g(p_g)}dp_g \tag{29}$$

The substitution of Eq. (29) into Eq. (28) allows us to arrive at the inflow performance equation:

$$q_g = \pi kh\frac{z_{sc}T_{sc}}{p_{sc}T}\left[\frac{\psi(p_e) - \psi(p_{wf})}{\ln(r_e/r_w) + S_f + S_{wb}}\right] \tag{30}$$

where S_f is the skin for hydraulic fracture and S_{wb} is the skin for water block. They are expressed as:

$$S_f = \ln(2r_w/x_f) \tag{31}$$

$$S_{wb} = \int_0^{\xi_e} \left[\frac{1}{k_{rg}(s(\xi))} - 1 \right] d\xi \tag{32}$$

The saturation profile required for Eq. (32) can be found implicitly from applying the chain rule to Eq. (28):

$$\xi = \frac{1}{N_{mca}} \int_{s_{wf}}^{s(\xi)} \frac{k_{kg}(p_g(s))}{B_g(p_g(s))} \frac{\mu_g(p_{wf})}{\mu_g(p_g(s))} k_{rg}(s) J'(s) ds \tag{33}$$

where N_{mca} is the modified capillary number:

$$N_{mca} = \frac{q_g \mu_g(p_{wf})}{2\pi\sigma h \sqrt{k\phi}} \tag{34}$$

The modified capillary number is the ratio between the viscous and capillary forces on the pore scale (Barenblatt et al., 1989).

3. Comparison between the analytical model and the numerical reservoir simulator

This section formulates the input empirical model functions into the exact solution and validates the analytical model by comparison with a numerical reservoir simulator.

3.1. Forms of the relative permeability and capillary pressure curves

Any form of the Leverett J function and relative permeability can be used in the presented model. The Brooks-Corey capillary pressure model (Brooks and Corey, 1964) is applied in this study for the Leverett J function. The two parameters which define this model are the pore size distribution index λ and the dimensionless capillary entry pressure C. The Leverett J function has the form:

$$J(s) = C s_n(s)^{-\frac{1}{\lambda}} \tag{35}$$

where s_n is the normalised water saturation. It is expressed as:

$$s_n(s) = \frac{s - s_{wirr}}{1 - s_{gr} - s_{wirr}} \tag{36}$$

The Brooks-Corey-Mualem model (Mualem, 1976) for relative permeability is used in this paper and is defined as:

$$k_{rg}(s) = (1 - s_n(s))^{\eta} \left(1 - s_n(s)^{2+\frac{2}{\lambda}} \right) \tag{37}$$

where η is the tortuosity coefficient.

3.2. Numerical validation of the exact solution

The proposed analytical model was tested against the black oil reservoir simulator IMEX. The simulated reservoir contains a single hydraulically fractured production well in the centre. Input data for the simulated reservoir and the well is given in Table 1. The properties for the gas were generated with the Petroleum Experts' software PROSPER.

Table 1
Input data for validation test against reservoir simulator.

Parameter	Value
k (mD)	100
A (m^2)	1.225×10^5
x_f (m)	22.5
h (m)	6
ϕ	0.1
λ	1.5
η	2
σ (N/m)	0.05

Table 2
Gas composition.

Component	Mole precent
C_1	54.8
C_2	11.86
C_3	3.62
i-C_4	0.52
n-C_4	1.03
i-C_5	0.42
n-C_5	0.51
C_6	0.99
C_7	1.38
C_8+	0.93
CO_2	23.52
N_2	0.42

Table 3
Properties of component C_8+.

Parameter	Value
Critical Temperature (K)	594.6
Critical Pressure (MPa)	2.29
Acentric factor	0.4435

The compressibility factor was determined from the Peng and Robinson equation of state and the viscosity was determined from the Lohrenz, Bray and Clark gas viscosity correlation. The composition of the gas used is given in Table 2 and the combined properties of the larger components C_8+ is given in Table 3.

The model in the reservoir simulator has the following differences from the proposed model: the shape of the reservoir in the simulator is square instead of circular (the existence of a hydraulic fracture restricts the numerical model in IMEX to a Cartesian coordinate system), and the simulator does not have an infinite conductivity fracture. To accommodate the shape factor difference, the size of the reservoir is made much larger than the half-length of the fracture. To approximate an infinitely conductive fracture, the fracture in the simulator is given a permeability of 5000 Darcy and a width of 0.02 m.

Gas injectors are placed across the boundary of the reservoir. The total injection rate is the same as the production rate. The reservoir has an initial reservoir pressure of 13 MPa and water saturation of 0.1. The simulation is run until the bottom-hole pressure of the production well stabilizes and steady state is reached.

A total of 12 scenarios were investigated: 4 different values for production rate against 3 different values for dimensionless entry pressure C. The production rates q_g were 0.58, 0.81, 1.04 and 1.27 m^3/s. The modified capillary numbers N_{mca} for the given rates were 2.66×10^6, 3.72×10^6, 4.78×10^6 and 5.85×10^6, respectively. The values for C were 0.0375, 0.075 and 0.15.

The saturation profile for the proposed model is given by Eq. (33). The pressure for the model is given be Eq. (3) and the dimensionless pressure is given by:

$$P_g = \frac{\sqrt{k/\phi}}{\sigma} p_g \tag{38}$$

Fig. 2 shows the comparison between the saturation profiles and the dimensionless pressure profiles calculated by the proposed model and the reservoir simulator for the scenario where $C = 0.15$ and $N_{mca} = 4.78 \times 10^6$. The average coefficient of determination (R^2) for the saturation profiles is 0.94 and for the dimensionless pressure profiles is 0.99. The high water saturation at the fracture face causes a dramatic increase in pressure gradient close to the wellbore.

The bottom hole flowing pressure p_{wf} and the average reservoir pressure $\overline{p}$ from the numerical reservoir simulator allow us to calculate water block skin from the following equation (Ahmed and McKinney,

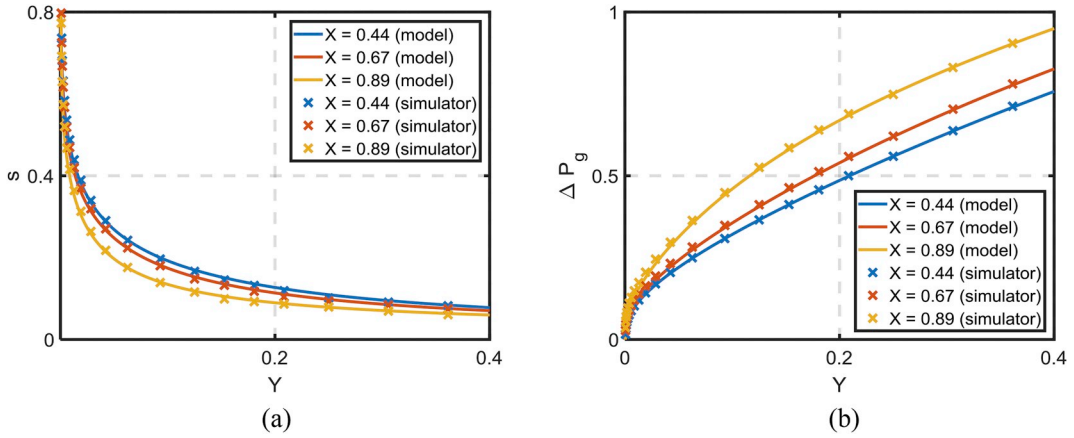

Fig. 2. Comparison between the proposed analytical model and the reservoir simulator at 3 different cross sections: (a) water saturation; (b) dimensionless pressure drop.

2005):

$$S_{wb} = \frac{\pi kh}{q_g}\frac{z_{sc}T_{sc}}{p_{sc}T}(\psi(\bar{p}) - \psi(p_{wf})) - \ln\left(\frac{r_e}{r_w}\right) + 0.75 - S_f \tag{39}$$

Fig. 3 shows the comparison between the skin values determined from the proposed analytical model and the reservoir simulator.

At low flow rates, the water block region will spread out closer to the edges of the reservoir and the difference in reservoir shape factor causes a deviation in skin value calculated. However, good agreement was achieved between the proposed model and the reservoir simulator. R^2 varied from 0.94 to 0.95 for all curves. The close agreement with skin, saturation profiles and pressure profiles validates the analytical model given by Eq. (27).

4. Non-Darcy flows at high production rates and inertial effects

This section derives the approximate analytical model for inertial flow using streamline method, and validates the solution by comparison with the numerical model.

4.1. Derivation of non-Darcy skin

The model presented in Section 2 considered slow, capillary dominated flow. However, at higher flow rates, inertial forces are large and non-Darcy flow can occur. The additional pressure drop due to the non-Darcy effect is accounted for by adding the Forchheimer term to Darcy's law. The Darcy-Forchheimer law is expressed as:

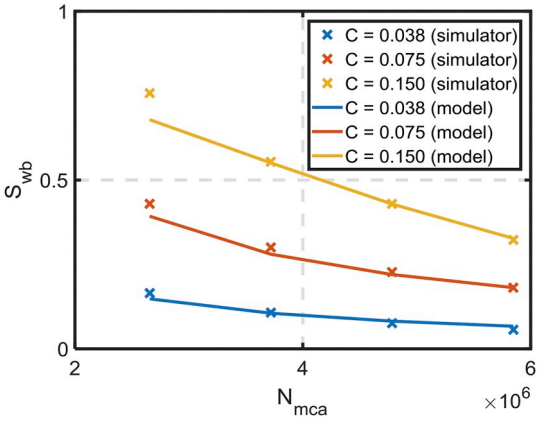

Fig. 3. Comparison of the water block skins calculated from the proposed analytical model and the reservoir simulator at 3 different dimensionless entry pressures.

$$\nabla p_g = uB_g(p_g)\left[\frac{\mu_g(p_g)}{kk_{rg}(s)k_{kg}(p_g)} + \beta|u|\frac{M}{R}\frac{p_{sc}}{z_{sc}T_{sc}}\right] \tag{40}$$

where β is the Forchheimer coefficient, M is the molar mass of the gas and R is the universal gas constant. From the streamline assumption (Eq. (17)), the modulus of velocity is:

$$|u| = u_\xi \tag{41}$$

From Eq. (21) and Eq. (23), we arrive at the modulus of velocity:

$$u_\xi = \frac{q_g}{h}\frac{G(\xi)}{x_f},\ G(\xi) = \left(\int_0^{2\pi}\sqrt{\sinh^2\xi + \sin^2\theta}\,d\theta\right)^{-1} \tag{42}$$

The quantity $G(\xi)/x_f$ is the inverse of the perimeter of the iso-potential line at the position ξ. As $\xi \to 0$, $G \to 1/4$ and Eq. (42) becomes the equation for velocity under linear flow. As $\xi \to \infty$, $G \to x_f/2\pi r$ and Eq. (42) becomes the equation for velocity under radial flow.

The streamline assumption (Eq. (17)) can reduce Eq. (40) to a single ordinary differential equation (ODE). The substitution of Eqs. (3), (41) and (42) the resultant ODE allows us to arrive at the following ODE:

$$\frac{ds}{d\xi} = N_{mca}\frac{B_g(p_g(s))}{J'(s)}\left[\frac{\mu_g(p_g(s))}{k_{rg}(s)k_{kg}(p_g(s))\mu_g(p_{wf})} + FG(\xi)\right] \tag{43}$$

where F is the dimensionless Forchheimer number:

$$F = \frac{q_g\beta k}{h\mu_g(p_{wf})x_f}\frac{M}{R}\frac{p_{sc}}{z_{sc}T_{sc}} \tag{44}$$

The boundary condition given by Eq. (25) can make the ODE (Eq. (43)) stiff. The implicit Klopfenstein –Shampine numerical differentiation formulae with quasi-constant step size (Shampine and Reichelt, 1997) are efficient at solving stiff ODEs, and are implemented into Matlab to solve Eq. (43).

The inflow performance equation accounting for the non-Darcy effects is:

$$q_g = \pi kh\frac{z_{sc}T_{sc}}{p_{sc}T}\left[\frac{\psi(p_e) - \psi(p_{wf})}{\ln(r_e/r_w) + S_f + S_{wb} + S_{nd}}\right] \tag{45}$$

where S_{nd} is the non-Darcy skin and is evaluated from:

$$S_{nd} = F\int_0^{\xi_e} G(\xi)k_{kg}(p_g(s(\xi)))\frac{\mu_g(p_{wf})}{\mu_g(p_g(s(\xi)))}d\xi \tag{46}$$

4.2. Numerical validation of the approximate analytical solution

The model accounting for non-Darcy effects (Eq. (43)) is compared

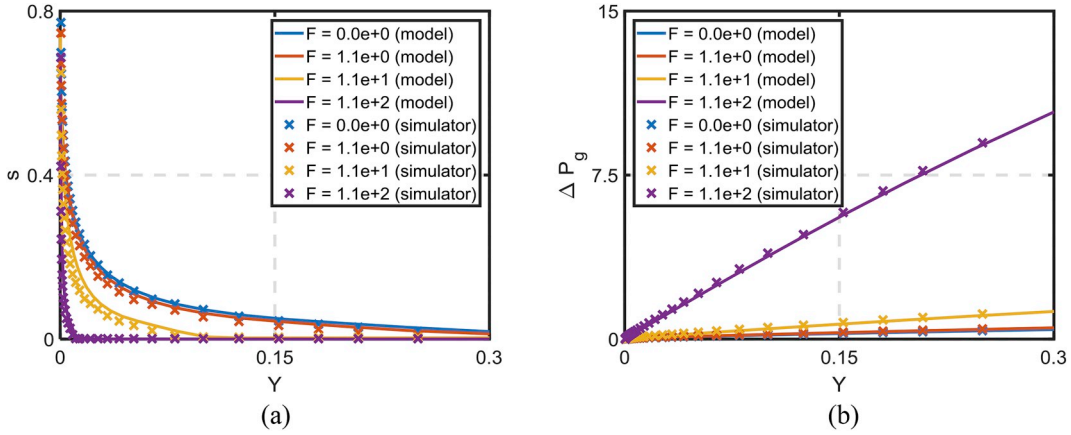

Fig. 4. Comparison between the proposed model and the reservoir simulator at the cross section $X = 0.44$ for 4 different dimensionless Forchheimer numbers: (a) water saturation; (b) dimensionless pressure drop.

to the numerical reservoir simulator IMEX. The reservoir has same characteristics as given in Section 3.1, and the technique used to validate the model is the same as given Section 3.1. The value for production rate and injection rate q_g was 0.58 m^3/s.

The sensitivity of saturation and pressure profile to F is given in Fig. 4. The blue curve represents Darcy flow, where $F = 0$. The value for the Forchheimer coefficient is determined from the empirical equation given by Pascal and Quillian (1980):

$$\beta = (1.0827 \times 10^{-5})k^{-1.176} \tag{47}$$

This equation gives a dimensionless Forchheimer number of $F = 9.4 \times 10^{-5}$. The crosses in Fig. 4 represent the numerical simulation results and the lines represent the model profile given by Eq. (43). The R^2 for all saturation and pressure profiles are within the range 0.97–0.99. The high agreement validates the semi-analytical model given by Eq. (43). The saturation gradient is influenced by both inertial and capillary forces. The inertial forces reduce the water saturation, and cause a reduction in water block.

The sum of water block and non-Darcy skin calculated by the numerical reservoir simulator and the proposed semi-analytic model for various dimensionless Forchheimer numbers is shown in Fig. 5. The close agreement ($R^2 = 0.99$) validates the semi-analytic model (Eq. (43)).

5. Comparison to linear and axisymmetric flow regimes

This section investigates the skin factor under the 1-D linear and radial flow regimes and compares it against the analytical model derived.

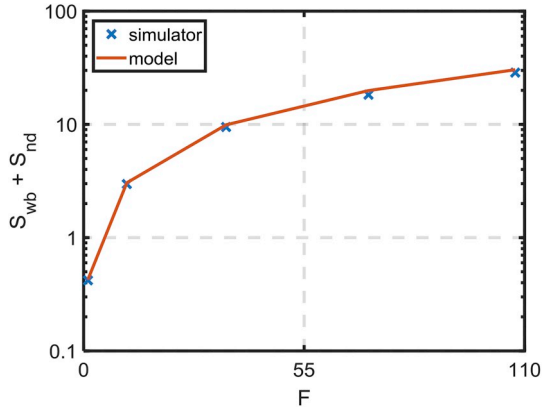

Fig. 5. Comparison between the sum of the water block skin and the non-Darcy skin calculated by the proposed model and the reservoir simulator.

5.1. Model for the linear flow regime

During the initial stage of production, the fractured well produces under a linear flow regime. The equations for saturation gradient ds/dx, water block skin S_{wb}, non-Darcy skin S_{nd} and the dimensionless drainage area A_d for linear flow are:

$$\frac{ds}{dx} = \frac{\pi N_{mca}}{2x_f}\frac{B_g(p_g(s))}{J'(s)}\left[\frac{\mu_g(p_g)}{k_{rg}(s)k_{kg}(p_g)\mu_g(p_{wf})} + \frac{F}{4}\right] \tag{48}$$

$$S_{wb} = \int_0^{L_e}\left[\frac{1}{k_{rg}(s(x))} - 1\right]dx \tag{49}$$

$$S_{nd} = \frac{\pi F}{8x_f}\int_0^{L_e} k_{kg}(p_g(s(x)))\frac{\mu_g(p_{wf})}{\mu_g(p_g(s(x)))}dx \tag{50}$$

$$A_d = \frac{4L_e}{x_f} \tag{51}$$

where L_e is the length from fracture face.

5.2. Model for the axisymmetric flow regime

When the pressure transient travels sufficiently far away from the fracture, the well flows under a radial flow regime. As it follows from Eqs. (1), (3) and (40) the equations for saturation gradient ds/dr, water block skin S_{wb}, non-Darcy skin S_{nd} and dimensionless drainage area A_d for radial flow are:

$$\frac{ds}{dr} = \frac{N_{mca}}{r}\frac{B_g(p_g(s))}{J'(s)}\left[\frac{\mu_g(p_g)}{k_{rg}(s)k_{kg}(p_g)\mu_g(p_{wf})} + \frac{Fx_f}{2\pi r}\right] \tag{52}$$

$$S_{wb} = \int_{x_f/2}^{r_e}\frac{1}{r}\left[\frac{1}{k_{rg}(s(r))} - 1\right]dr \tag{53}$$

$$S_{nd} = \frac{Fx_f}{2\pi}\int_{x_f/2}^{r_e}\frac{k_{kg}(p_g(s(r)))}{r^2}\frac{\mu_g(p_{wf})}{\mu_g(p_g(s(r)))}dr \tag{54}$$

$$A_d = \pi\left(\frac{r_e^2 - (x_f/2)^2}{x_f^2}\right) \tag{55}$$

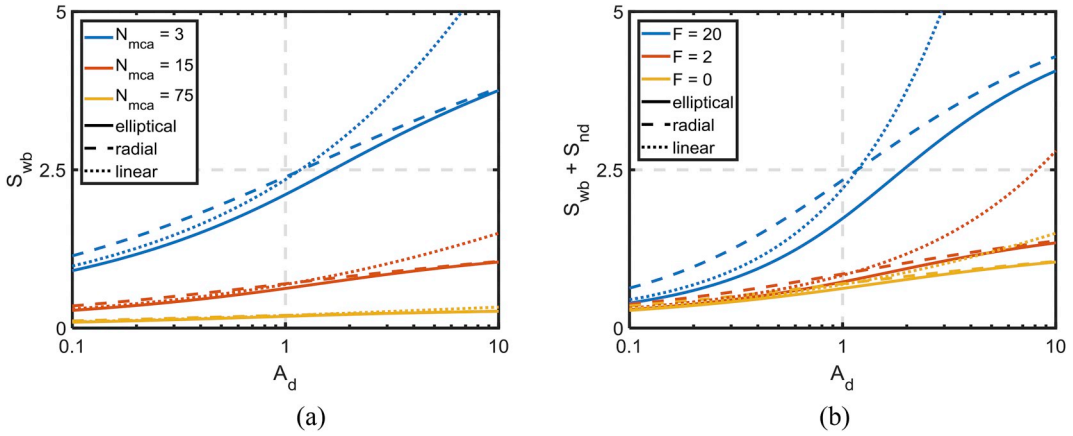

Fig. 6. Skin calculation comparison of for elliptical, radial and linear flows for varying dimensionless drainage area A_d: (a) the case of Darcy flow for different values of modified capillary number N_{mca}; (b) Non-Darcy flow at various dimensionless Forchheimer numbers F.

5.3. Comparison with the elliptic flow regime

In the intermediate of these two flow regimes, elliptic flow can occur. The dimensionless drainage area A_d for elliptic flow is:

$$A_d = \pi \sinh(\xi_e)\cosh(\xi_e) \tag{56}$$

Naik et al. (2018) provide the analytical models for radial and linear flows towards a well. Comparison of the presented model to the linear and radial flow models is provided in Fig. 6. Fig. 6a shows that the deviation between linear 1D flow and 2D flow towards fractured well increases as the drainage volume increases. However, at large drainage zones, where the fracture length is small in comparison with the drainage radius ($A_d > 10$), the flow towards the fracture converges to the radial flow. The higher is the modified capillary number N_{mca}, the higher is the rate, and the lower is the deviation between the three flows with different geometry.

Fig. 6b exhibits similar effect for non-Darcy flows: convergence of the fractured-well and axi-symmetric flows at large drainage areas, large deviation between the linear and fractured-well flows at large drainage areas, and high Forchheimer numbers.

6. Sensitivity analysis

This section investigates the sensitivity of the skin, and the radius of damage to various parameters which characterize the flow. The parameters investigated include the dimensionless Forchheimer number, modified capillary number, dimensionless capillary entry pressure, and the pore size distribution index.

6.1. Sensitivity of non-Darcy and water block skin with respect to inertial, viscous and capillary forces

This paper establishes a new semi-analytical model with consideration of inertial, viscous and capillary forces. The influence of the aforementioned forces on the inflow performance of a naturally fractured gas well is investigated. The physical characteristics of the reservoir which have been considered are given in Table 4. The dimensionless Forchheimer number F defines the ratio of inertial to viscous forces and the modified capillary number N_{mca} defines the ratio of viscous to capillary forces.

Fig. 7 shows the influence of increasing F on the saturation profile, at a fixed N_{mca}. The blue line represents the smallest value for F. When F is increased, the gas pressure increases and the gas phase becomes compressed. The result is that water saturation increase, as indicated by the red curve. However, at some point, the effect of the inertial forces will begin to reduce the saturation, as indicated by the yellow curve.

Table 4
Reservoir properties used for the sensitivity analysis.

Parameter	Value
k (mD)	0.1
p_{wf} (MPa)	5.5
C	0.15
λ	1.5
η	2
N_{mca}	1.5×10^2

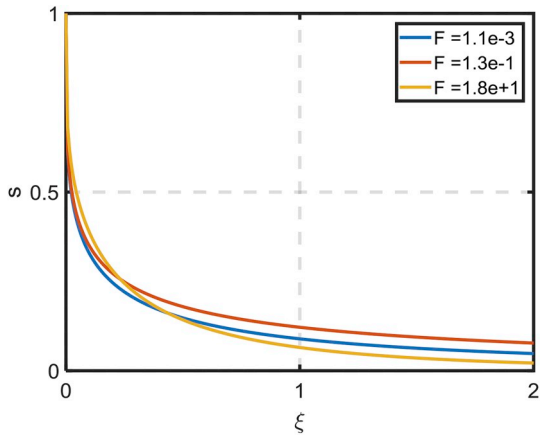

Fig. 7. Sensitivity of the saturation profile to the dimensionless Forchheimer number F. $N_{mca} = 1.5 \times 10^2$.

The final result is that there is some intermediate F where the saturation profile is largest.

Fig. 8 shows the sensitivity of S_{nd}, S_{wb} and their sum to N_{mca} and F. As expected S_{wb} is high when the N_{mca} is low. The non-monotonic relationship S_{wb} shares with F is the result of the competition between gas compression and inertial forces, as previously mentioned. Also, unsurprisingly, S_{nd} increases if F increases. However, the effect N_{mca} has on S_{nd} is not so straightforward. A decrease in N_{mca} causes a decrease in S_{nd}. This is due to the effect N_{mca} has on pressure drop. A decrease in N_{mca} causes an increase in pressure drop, which resultantly increases viscosity. The increase in viscosity is what reduces S_{nd}.

The sensitivity of S_{nd}, S_{wb} and their sum to C is presented in Fig. 9a. The Leverett J function and its derivative are proportional to C, which cause the water block skin to scale almost proportionally with C. Variation in C by ± 25% gives roughly 25% variance in water block skin.

The sensitivity of S_{nd}, S_{wb} and their sum to λ is presented in Fig. 9b.

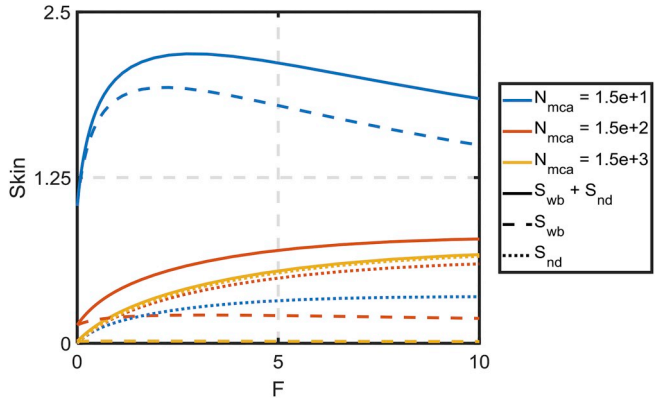

Fig. 8. Sensitivity of water block skin, non-Darcy skin and their sum to the dimensionless Forchheimer number and the modified capillary number.

A decrease in λ will increase the J function, which will increase S_{wb}. A decrease in λ by 25% can increase the skin by up to 80% and an increase in λ by 25% can decrease the skin up to 35%. Of the 2 parameters which define the forms of the Leverett J function, the skin due to water block is more dependent on the pore size distribution index λ. While the dimensionless parameters λ and C have a significant influence on the water block skin, they have a negligible influence on the non-Darcy skin.

6.2. Sensitivity of water block damage radius

Consider an iso-potential line given by ξ_D, such that 99% of skin due to water block results from water inside the region $\xi < \xi_D$:

$$0.99S_{wb} = \int_0^{\xi_D} \left[\frac{1}{k_{rg}(s(\xi))} - 1\right] d\xi \tag{57}$$

Let us define the radius of a circle with the same cross sectional area as this ellipse as the water block damage radius r_D. It can be found from the following equation:

$$\frac{r_D}{x_f} = \sqrt{\frac{\sinh \xi_D}{2}} \tag{58}$$

The ratio r_D/x_f is called the dimensionless damage radius and is useful for estimating volumes of chemical treatment for water block clean up.

The sensitivity of r_D/x_f to F and N_{mca} is shown in Fig. 10a. The domination of capillary forces over viscous and inertial forces causes water saturation to spread over a larger distance and increase water block skin. This means that the affected area is larger when both the dimensionless Forchheimer number and the modified capillary number are low. For the cases investigated the radius of damage is generally around 2 times the fracture half-length, but can be as large as 2.5 times the fracture half-length.

Due to the nature of the water saturation profile, more of the damage is closer to the fracture. For the case of $N_{mca} = 1.5 \times 10^2$, 70% and 50% of the water block comes from a dimensionless damage radius of less than 1/2 and 1/3, respectively (Fig. 10b).

7. Simplified analytical model for a fractured oil well

Generally, for oil flow, the compressibility of oil in the reservoir is neglected and inertial effects are not considered. Viscosity can also be approximated by a constant. Under these assumptions the water block skin equation simplifies to:

$$S_{wb} = \int_{s_{wf}}^{s_e} \frac{J'(s)[1 - k_{ro}(s)]}{N_{mca} B_o} ds \tag{59}$$

where B_o is the formation volume factor for oil. The comparison of the model for oil to the model for gas is given in Fig. 11. Under the aforementioned assumptions, water block skin is only dependent on the ratio of capillary to viscous forces. Capillary forces are affected by the Leverett J function and the dimensionless capillary number N_{mca}. The water block skin calculated by the model for gas is larger than the model for oil due to the effects gas compression has on water saturation. Oil generally has higher viscosity than gas, which increases the capillary number. For this reason there is generally higher research into water blocking for gas wells than oil wells.

8. Case study: model application to production data

Using the analytical model developed in Section 4, here we aim to determine the relative permeability and Leverett J curves which replicate the skin observed in one hydraulically fractured gas well. This allows us to test whether water block is a reasonable explanation for the increasing skin observed in the aforementioned well.

8.1. Properties of the well and reservoir

Well C in the Cooper Basin was selected for this case study. It is a vertical well intersecting multiple production intervals. One of its primary zones is the Patchawarra sand. This zone was hydraulically fractured. The model was tuned to fit measured production data to investigate opportunities for enhancing gas rate. The result of the tuned parameter values and the goodness of fit can give insight into how

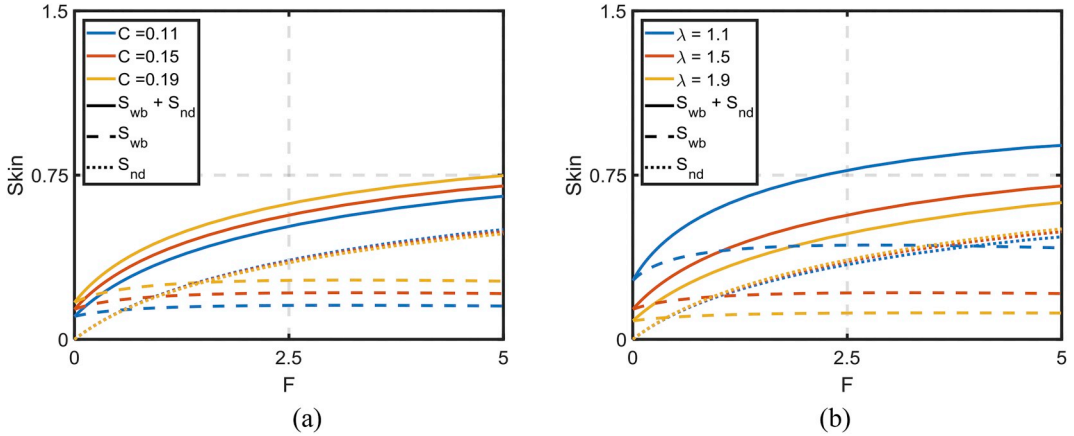

Fig. 9. Sensitivity of water block skin, non-Darcy skin and their sum to the dimensionless Forchheimer number and the Leverett J function parameters: (a) dimensionless entry pressure; (b) pore size distribution index.

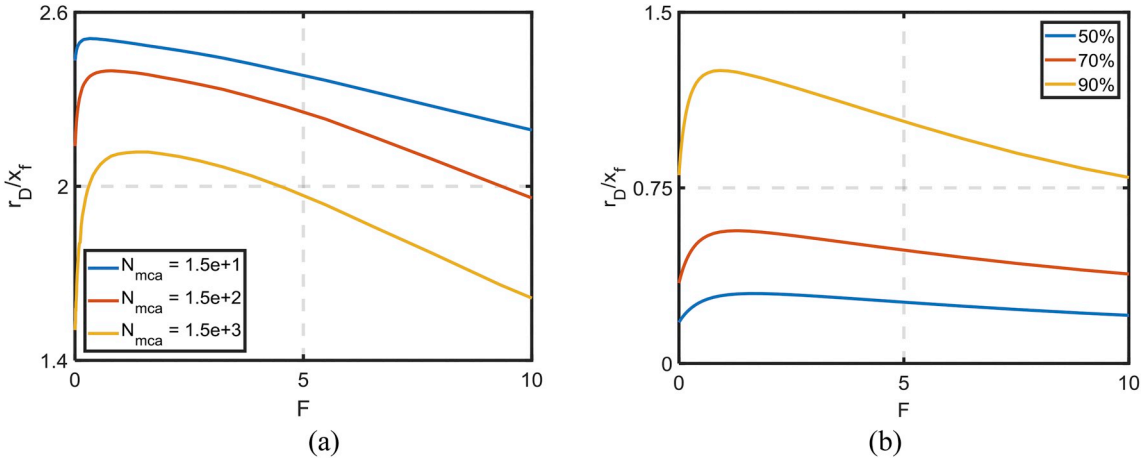

Fig. 10. Sensitivity of the dimensionless damage radius to the dimensionless Forchheimer number: (a) at varying modified capillary number; (b) for different percentages of water block.

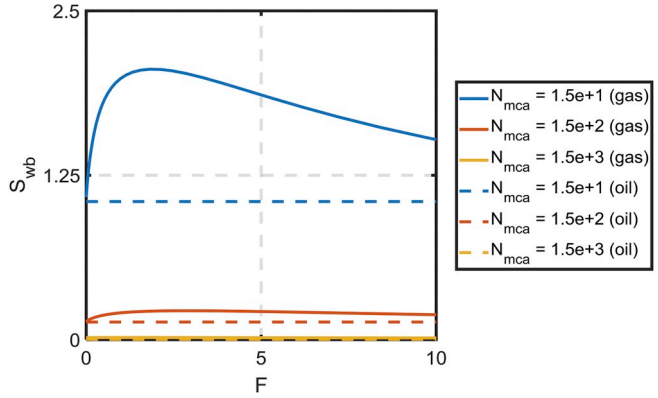

Fig. 11. Comparison of the water block skin calculated using the model for gas to the model for oil.

likely it is that water block is present.

After completion, a memory production logging tool (MPLT) test was performed. It gives the downhole measurements of pressure and rate during a short period of shut-in and production. The MPLT test is used to determine rate allocated to each production interval and is also used to give an indication of pressure drop during production of well life and shut in periods.

The well had a period where it was shut-in for a few days. The bottom-hole pressure during the shut-in is calculated from measured tubing head pressure and adding the same pressure drop determined from the MPLT shut-in test. The bottom-hole pressure during build-up is used to estimate initial reservoir pressure using pressure transient analysis equations implemented in the KAPPA software package Saphir. Pressure transient analysis equations are presented in Appendix A. The initial reservoir pressure determined was 14.7 MPa.

During the production period, the wellhead pressure and gas flow rate were measured every 4 h. The pressure drop from wellhead to the bottom-hole was calculated using Gray's correlation (Gray, 1974) implemented in Petroleum Experts' software PROSPER.

The production rate and bottom-hole flowing pressure data are used to calculate the permeability and drainage area using the rate transient analysis equations implemented in the KAPPA software Topaz. The rate transient analysis equations are presented in Appendix B. The determined interval permeability and drainage area were 0.0875 mD and 3.57×10^4 m^2 respectively.

The well has radius $r_w = 0.0787$ m and logging tools give porosity estimate of $\phi = 0.1$ and height $h = 6.1$ m. Since there is no well test to determine the fracture half-length of this particular interval, fracture half-length given from simulation results is used. Fracture stimulation simulation estimated an effective fracture half length of 17.4 m.

Core samples of the Patchawarra sand were taken from seven nearby wells. From these core samples mercury injection capillary (MICP) tests were performed. The Leverett *J* function was calculated for all of the cores.

8.2. Depletion model

The original gas in place (*OGIP*) is determined using initial reservoir pressure and drainage area from the following equation:

$$OGIP = Ah\phi(1 - s_{wi})\frac{p_i T_{sc} z_{sc}}{p_{sc} T z_i} \tag{60}$$

where A is the drainage area. The subscript i represents initial reservoir conditions. Volumetric drive with no water drive is assumed. The average reservoir pressure $\bar{p}$ is determined from the material balance equation:

$$\frac{\bar{p}}{\bar{z}} = \frac{p_i}{z_i}\left(1 - \frac{Q_p}{OGIP}\right) \tag{61}$$

where Q_p is the cumulative volume of gas produced. The measured gas flow rate q_g, calculated bottom-hole pressure p_{wf} and the calculated average reservoir pressure during the first year of production are given in Fig. 12a. The plot of $\bar{p}/\bar{z}$ against cumulative produced volume is given in Fig. 12b. The estimated depletion during the production period is given by the blue line.

8.3. Evaluating skin from production data

During the infinite acting radial flow regime the skin can be determined from (Bourdet, 2002):

$$S = \frac{1}{0.87}\left[\frac{2\pi kh}{q_g}\frac{z_{sc} T_{sc}}{p_{sc} T}(\psi(p_i) - \psi(p_{wf})) - \log\left(\frac{kt}{\phi\mu_g c_t r_w^2}\right) + 3.23\right] \tag{62}$$

where t is the production time and c_t is the total compressibility. The time for pseudo steady state to be reached is (Bourdet, 2002):

$$t_{PSS} = \frac{\phi\mu c_t r_e^2}{4k} \tag{63}$$

After pseudo steady state is reached, the equation for skin can be determined from (Ahmed and McKinney, 2005):

$$S = \frac{\pi kh}{q_g}\frac{z_{sc} T_{sc}}{p_{sc} T}(\psi(\bar{p}) - \psi(p_{wf})) - \ln\left(\frac{r_e}{r_w}\right) + 0.75 \tag{64}$$

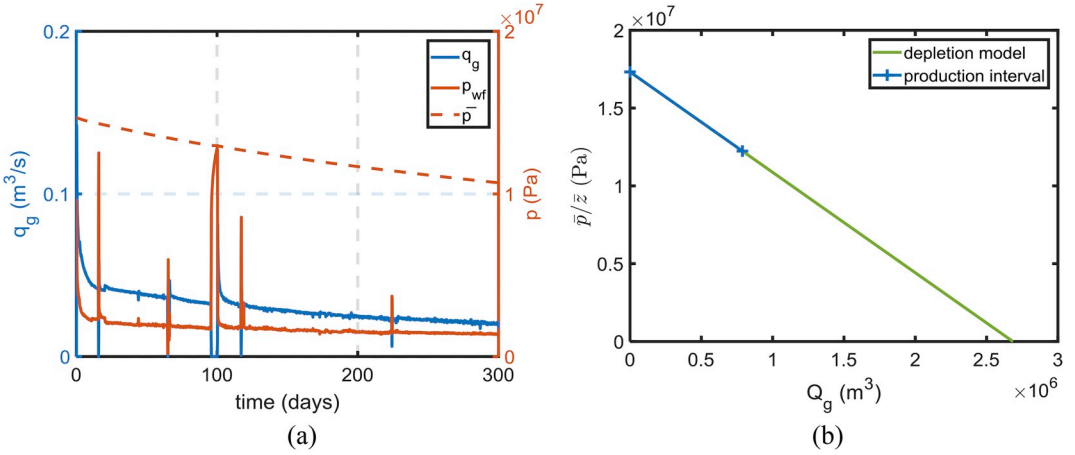

Fig. 12. Data from Cooper basin well and its estimated reservoir pressure: (a) measured gas flow rate, calculated bottom-hole pressure and calculated reservoir pressure; (b) The $\bar{p}/\bar{z}$ plot assuming volumetric depletion.

8.4. Tuning of well data by the analytical model

The model parameters C, λ and η are not known. With these parameters the model can give estimates of skin due to water block and non-Darcy flow. However, there can be more skin present due to other reasons, for example, drilling mud loss, proppant crushing and reservoir shape factor. When tuning the model to fit well production data, we added another constant, S_a, which represents the unaccounted for skin:

$$S = S_f + S_{wb} + S_{nd} + S_a \tag{65}$$

Parameters C, λ, η and S_a are tuned to fit the field estimate of skin. The results of tuning are presented in Fig. 13. Fig. 13a shows the comparison between modelled skin and calculated skin from production data and Fig. 13b shows comparison between tuned Leverett J function and the Leverett J function determined from mercury injection capillary pressure (MICP) tests.

Good fits were obtained for skin and the average J curve (i.e. $R^2 = 0.8$ for both cases) using the following parameter values: $C = 0.2$, $\lambda = 1.2$, $\eta = 13.95$, $S_a = 0.8$. The capillary pressure properties are within the same ranges as those in literature: C is between 0.01 and 0.6 (Desbarats, 1995; Thungsuntonkhun and Engler, 2004), and λ is between 0 and 7 (Leverett, 1941). For an irreducible water saturation range between 0 and 0.4, the empirical correlation given by Huet et al. (2005) gives C values between 0.11 and 0.17 and λ values between 0.85 and 0.9. These empirical values are not unreasonably far from the tuning results.

The tortuosity coefficient $\eta = 13.95$ is high compared to literature values, which are typically given as 0.5 or 2 (Mualem, 1976). However, when compared to the measured relative permeability in an analogous core, it has similar curvature, albeit a much smaller irreducible water saturation. The relative permeability comparison between the analogous core and the model is given in Fig. 13c.

9. Discussion

9.1. Discussion of the case study

The case study shows that water block can increase as the well depletes. As the gas flow rate decreases with well life, the modified capillary number and the dimensionless Forchheimer number will decrease, which can cause water block skin to increase. Thus, water block can be a reasonable explanation for the increase in skin. The water which forms the water block can come from more than one source, such as from the hydraulic fracturing operation or from the reservoir. During shut-in periods water from other intervals can also imbibe into the formation from the wellbore.

However, in order for water block skin to explain all of the increase in skin for the case study well, the tortuosity index in the relative permeability curve needs to be higher than that given in literature. This indicates that there may be additional skin effects not accounted for, such as scaling or depletion of other flow intervals, which can also contribute to the rise in skin. The existence of other factors contributing to skin is expected and the modelling results show that water block is a potential contributor.

Another explanation for the high tortuosity index is that the relative permeability model used does not account for any change in irreducible water saturation. Given that tight sands can sometimes exhibit sub-irreducible water saturations, they can be more sensitive to non-native water introduced from the fracture (Bennion and Thomas, 2005). Not accounting for this effect can cause the model to under-estimate water block skin if given a lower tortuosity index.

The case study does not conclusively prove that water block is the only cause of increasing skin. However, water block has been shown to be a potential explanation for this phenomenon. The model can be applied for estimating if the water block is significant enough to warrant intervention.

9.2. Applications of the models

In this paper we have converted the model for inflow of compressible gas with capillary entrapped water, given by Eqs. (1)–(3) to the Laplace equation. We have used the solution of the Laplace equation to calculate inflow performance of a fractured well in an ellipsoid reservoir. The method of conformal mapping and the Schwarz–Christoffel integral allow deriving the exact solutions for multiple well placement geometries and reservoir shape factors (Lavrentev and Shabat, 1977; Bedrikovetsky, 2013).

This work allows for estimating the improvement of productivity index from coreflood tests. Parvazdavani et al. (2014) presented the effect of nanoparticles which decrease the interfacial tension by 8 mN/m and improve relative permeability to oil. Results of the relative permeability measured before and after nano-fluid injection are presented in Fig. 14a. Substitution of the relative permeability curves and the interfacial tension values before and after treatment into Eq. (59) allow for the determination of skin improvement. Water block skin values for before and after treatment are presented in Fig. 14b.

The dimensionless numbers, F and N_{mca}, presented in this paper can be used as a screening criterion for well candidates in re-fracture treatments and chemical treatments. At high dimensionless Forchheimer numbers, re-fracturing can give the additional benefit of reducing non-Darcy skin on top of increasing half-length. Surfactant or

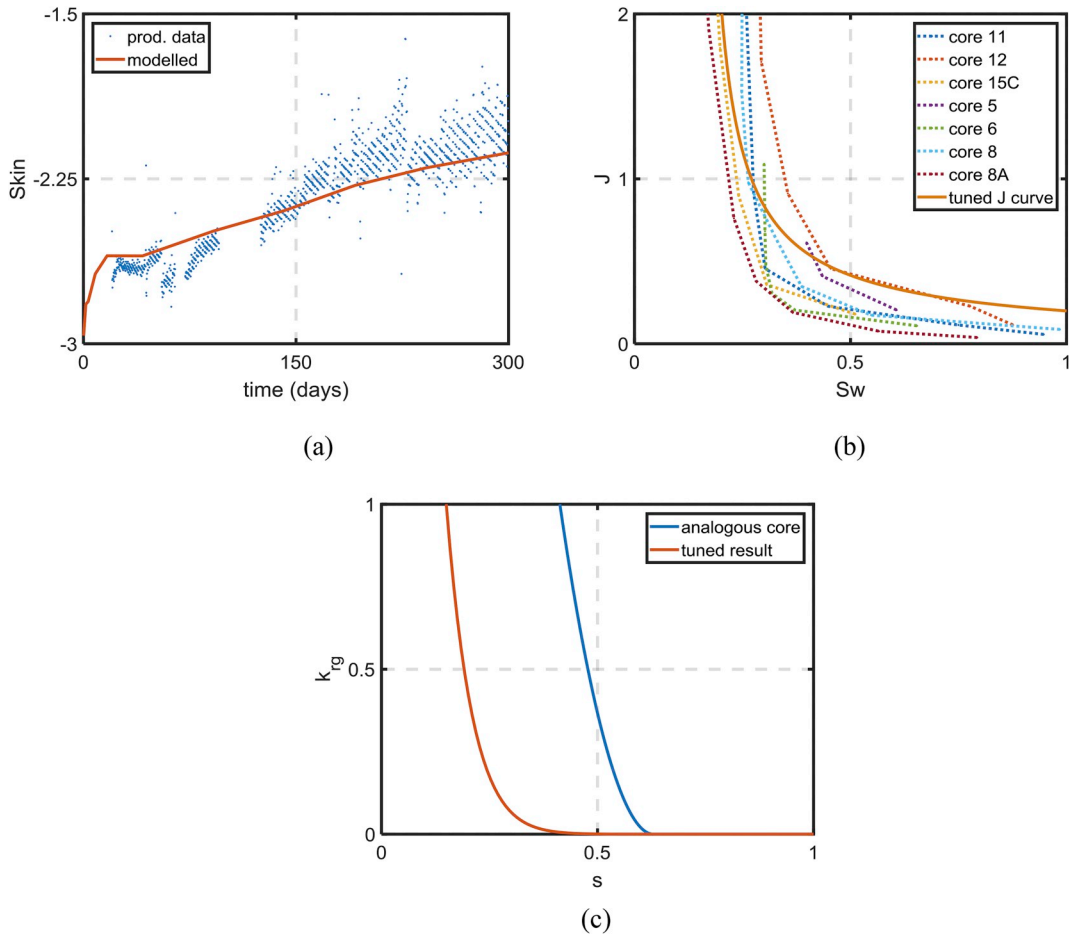

Fig. 13. Tuning the semi-analytical model to match the skin in fractured well: (a) skin for the well; (b) tuned Leverett *J* function curve; (c) comparison of relative permeability for the Cooper well to an analogous core.

nanoparticle treatment will reduce the capillary trapping of water (Towler et al., 2017; Xie et al., 2009; Ni et al., 2016), which is useful at low modified capillary numbers.

We show that the ratio of viscous to capillary forces and the magnitude of the Leverett *J* function control the water block skin. The values for the Leverett *J* function constants and the relative permeability tortuosity term can vary greatly and are the most important parameters to determine the likelihood of water block under steady flow. Generally in literature it has been reported that low permeability rocks can exhibit high skin due to water blockage (Bazin et al., 2010; Bahrami et al., 2011). This can be due to low permeability correlating with high dimensionless entry pressure and low pore size distribution index (Huet et al., 2005).

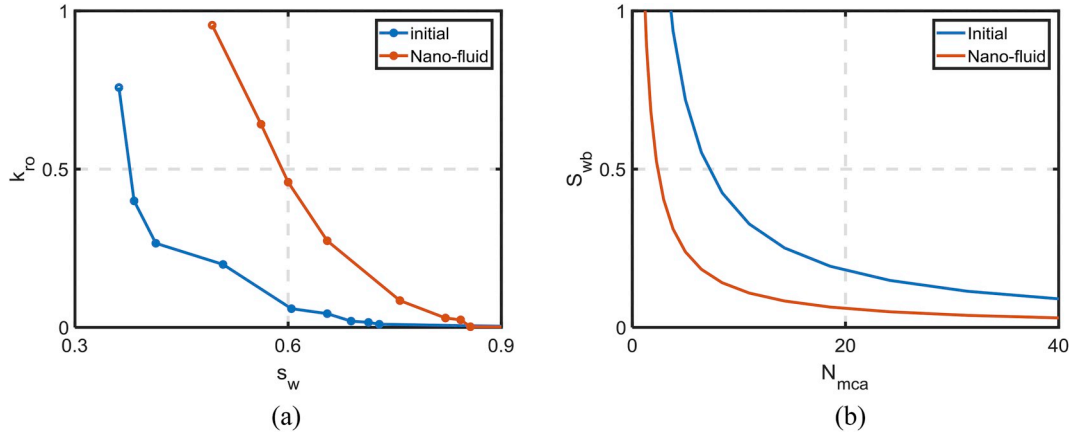

Fig. 14. Example case of core flood data used to estimate water block skin reduction: (a) measured relative permeability; (b) prediction of skin reduction due to application of Nano-fluid. Experimental data taken from Parvazdavani et al. (2014).

9.3. Limitations of the model

The model applied in this study (Eq. (43)) assumes infinite fracture conductivity and neglects pressure variation inside the fracture. The method of extending the model to account for hydraulic fracture conductivity can be found in the work of Economides and Nolte (1989).

The proposed model only considers steady state flow. However, the transient flow regime can be longer in low permeability reservoirs. The dynamic drainage area during transient flow and inflow performance equations during transient flow regime are given by Yuan et al. (2016). The current work can be extended to account for transient flow via conformal mapping to the dynamic drainage volume during the transient flow regime.

The model only considers homogeneous permeability. As permeability heterogeneity can affect capillary pressures near to the fracture face, water saturations near to the fracture will also be affected. The fracture flow back period and transient effects accounting for permeability heterogeneity and capillary pressure effects can be studied using a numerical reservoir simulator.

The model describes saturation distribution around the fractured production well and the skin factor accounting for capillary entrapped water. The model is not affected by the source of the water. However, the relative permeability and capillary pressure forms can be adjusted to account for the water source. In the case of fracture fluid leak off, fracture fluid first imbibes into the reservoir and then the gas will flow into the fracture. The gas inflow can be considered a secondary drainage process. The viscosity of the fracture fluid can change throughout this process. The hysteretic effects will need to be accounted for in the relative permeability and capillary-pressure curves.

After hydraulic fracturing, water block can be cleaned up from two dominant mechanisms; flow back and evaporation (Kamath and Laroche, 2003). Evaporative effects are dependent on flow rate, bottom hole flowing pressure and volatility of the gas. If the reservoir is completely dry, evaporative effects can remove the water film formed on the hydraulic fracture. This study neglects evaporative effects and is applicable for production after the clean-up of fracture fluid.

Adding energy conservation equation to the governing system (1–3) yield generalisation of this work for commingled production of water and steam from geothermal wells (Palabiyik et al., 2013; Tureyen et al., 2014).

The developed analytical model (30–33) does not account for fines migration, induced by shear from the fractured leak-off fluid, and consequent permeability decline (Bedrikovetsky et al., 2011, 2012). Another important permeability decline effect in fractured gas wells is the fracturing fluid leak-off containing suspended particles generated during fracture opening and propagation, yielding size exclusion, attachment and pore plugging (Bedrikovetsky et al., 2017).

Rock compressibility, which is very important for shale gas and oil reservoirs, can be implemented in the model by pressure-dependent porosity (Jiang and Younis, 2016; Huang et al., 2018).

10. Conclusions

This paper has extended the analytical models for 1D flow of compressible gas under the presence of capillary entrapped water derived by Naik et al. (2018) to 2D inertial and non-inertial flows around fractured wells. Besides revealing the saturation and pressure distribution around the fracture, the modelling was also able to unravel the impact of the interplay of capillary, viscous, inertial forces on the water block and non-Darcy skin. It allows us to conclude as follows:

1. The problem of 2-D non-inertial gas inflow towards a fractured well under the presence of capillary-trapped liquid allows for an exact solution. The explicit formulae for flow potential distribution is obtained by conformal mapping.
2. The solution defines implicit formulae for pressure and saturation distribution around the well. The skin as a result of water block around a hydraulic fracture is determined implicitly.
3. The competing effects of gas compression and inertial forces result in a non-monotonic relationship between water block skin and the dimensionless Forchheimer number.
4. Water block skin is sensitive to pore size distribution index λ and dimensionless entry pressure C. Skin due to water block can be small in low permeable formations despite high capillary pressure values if λ is large or if C is low.
5. The inflow-performance problem accounting for capillary-trapped fluid and gas inertia in the near-wellbore region can be solved using the stream-line method. Comparison with high-accuracy numerical solution exhibits high agreement ($R^2 = 0.97$).
6. There is a steep increase in water saturation close to the fracture face, which creates a major portion of the water block skin. The water block skin resulting from water inside some region close to the fracture face can be estimated implicitly from the model, which consequently provides an estimate for volume of chemical treatment required.

Acknowledgements

The authors would like to acknowledge the engineering students Emily Walker and Antreas Florentzou. Their honours research project assisted us in selecting the well candidate for the field case study. The authors are grateful to Eng. Mark Burgoyne (Santos Ltd) for the fruitful discussions. Many thanks are due to Dr. Themis Carageorgos and Mr. Thomas Russell for proofreading and providing feedback on the text.

Nomenclature

a	arc length, m
A	drainage area, m^2
A_d	dimensionless drainage area
b	Klinkenberg factor, Pa
B	formation volume factor
c_t	total compressibility, Pa^{-1}
C	dimensionless entry pressure
$\hat{e}$	unit vector
F	dimensionless Forchheimer number
G	inverse of dimensionless perimeter of ellipse
h	reservoir height, m
h_ξ	scale factor for the ξ coordinate
h_θ	scale factor for the θ coordinate
$OGIP$	original gas in place, m^3
J	Leverett J-function
k	permeability, m^2

k_{kg}	Klinkenberg correction coefficient
k_{rg}	relative permeability to gas
L_e	drainage boundary for linear flow model, m
M	molar mass, kg/mol
N_{mca}	modified capillary number
p	pressure, Pa
$\overline{p}$	average reservoir pressure, Pa
p_{ws}	bottom-hole shut-in pressure, Pa
P	dimensionless pressure, Pa
q_g	flow rate, m^3/s
Q_p	cumulative volume of gas produced, m^3
r	radius, m
r_w	wellbore radius, m
R	universal gas constant, 8.3144621 J/Mol·K
s	water saturation
s_n	normalised water saturation
s_e	boundary saturation\
s_{gr}	irreducible gas saturation
s_{wirr}	irreducible water saturation
S	skin
S_a	summation of the unaccounted skin
S_{wb}	water block skin
S_f	hydraulic fracture skin
S_{nd}	non-Darcy skin
t	time, s
t_{MB}	material balance time, s
t_{PSS}	beginning of pseudo-steady state time, s
t_{sup}	superposition time, s
T	temperature, K
u	velocity at surface conditions, m/s
x	Cartesian coordinate parallel to fracture, m
X	dimensionless Cartesian coordinate parallel to fracture
x_f	facture half length, m
y	Cartesian coordinate perpendicular to fracture, m
Y	dimensionless Cartesian coordinate perpendicular to fracture
z	compressibility factor

Greek Letters

β	Forchheimer coefficient, m^{-1}
η	tortuosity index
θ	elliptic coordinate which scales with the stream function
ϕ	porosity
λ	pore size distribution index
μ	viscosity, Pa·s
ξ	elliptic coordinate which scales with the potential
σ	interfacial tension, N/m
Φ	potential, m^2/s
ψ	modified pseudo-pressure, Pa/s

Subscripts

e	drainage boundary
D	water block damage boundary
i	initial reservoir conditions
g	gas
k	time period
o	oil
sc	standard conditions
w	water
wf	bottom-hole at flowing conditions
θ	in the direction of elliptic coordinate θ
ξ	in the direction of elliptic coordinate ξ

Appendix A. Pressure transient analysis equations

The build-up period can be preceded by multi-rate production. During build up, the difference between initial reservoir pseudo pressure, $\psi(p_i)$, and current static bottom-hole pseudo pressure $\psi(p_{ws})$, is given by (Bourdet, 2002):

$$\psi(p_i) - \psi(p_{ws}) = \frac{p_{sc}T}{z_{sc}T_{sc}}\frac{t_{\sup}}{2\pi kh} \tag{A-1}$$

where t_{sup} is the multi-rate superposition time expressed as:

$$t_{\sup} = \sum_{k=1}^{k=n} (q_k - q_{k-1})\log(t_c + \Delta t - t_{k-1}) \tag{A-2}$$

where q_k is flow rate during period k and t_k is time at end of period k.

Appendix B. Rate transient analysis equations

To identify flow regimes and characterize reservoir properties, production data can be plotted on a diagnostic plot. The diagnostic plot is a log-log plot of the derivative of the difference between the initial reservoir pseudo pressure ψ(pi) and the current flowing bottom hole pseudo pressure ψ(Pwf) against material balance time tMB. The usage of material balance allows for conversion of production data into an equivalent constant rate drawdown with rate qe (Ahmed and McKinney, 2005):

$$t_{MB} = \frac{Q_p}{q_e} \tag{B-1}$$

where Q_g is the cumulative volume of gas produced. Let us define the pseudo pressure drop derivative as:

$$\psi' = t_{MB}\frac{d(\psi(p_i) - \psi(p_{wf}))}{dt_{MB}} \tag{B-2}$$

From the diagnostic plot the pseudo radial flow regime can be determined from a constant value of the derivative plot (Ahmed and McKinney, 2005). The value of the constant can be used to determine permeability:

$$\log(\psi') = \log\left(\frac{1}{2\pi kh}\frac{p_{sc}T}{z_{sc}T_{sc}}\frac{1}{\ln(10)}\right) \tag{B-3}$$

References

Ahmed, T., McKinney, P., 2005. Advanced Reservoir Engineering. Elsevier, Burlington, MA.

Bahrami, H., Rezaee, M.R., Nazhat, D.H., Ostojic, J., Clennell, M.B., Jamili, A., 2011. Effect of water blocking damage on flow efficiency and productivity in tight gas reservoirs. In: Paper SPE-142283, Presented at the SPE Production and Operations Symposium, Oklahoma, USA, pp. 27–29 (March).

Barenblatt, G.I., Entov, V.M., Ryzhik, V.M., 1989. Theory of Fluid Flows through Natural Rocks. Springer, Amsterdam, The Netherlands.

Bazin, B., Peysson, Y., Lamy, F., Martin, F., Aubry, E., Chapuis, C., 2010. In-situ water-blocking measurements and interpretation related to fracturing operations in tight gas reservoirs. SPE Prod. Oper. 25 (4), 431–437.

Bear, J., 2013. Dynamics of Fluids in Porous Media. Dover Publications, New York.

Bedrikovetsky, P., 2013. Mathematical Theory of Oil and Gas Recovery: with Applications to Ex-USSR Oil and Gas Fields, vol. 4 Springer Science & Business Media.

Bedrikovetsky, P., Siqueira, F.D., Furtado, C., de Souza, A.L.S., 2011. Modified particle detachment model for colloidal transport in porous media. Journal of Transport in Porous Media 86, 353–383.

Bedrikovetsky, P., Zeinijahromi, A., Siqueira, F.D., Furtado, C., de Souza, A.L.S., 2012. Particle detachment under velocity alternation during suspension transport in porous media. Journal of Transport in Porous Media 91 (1), 173–197.

Bedrikovetsky, P., You, Z., Badalyan, A., Osipov, Yu, Kuzmina, L., 2017. Analytical model for straining-dominant large-retention depth filtration. Chem. Eng. J. 330, 1148–1159.

Bennion, D.B., Thomas, F.B., 2005. Formation damage issues impacting the productivity of low permeability, low initial water saturation gas producing formations. J. Energy Resour. Technol. 127 (3), 240–247.

Bourdet, D., 2002. Well Test Analysis – the Use of Advanced Interpretation Models. Elsevier, Amsterdam, The Netherlands.

Brooks, R.H., Corey, A.T., 1964. Hydraulic Properties of Porous Media. Hydrology Paper No. 3. Colorado State University, Fort Collins, Colorado, pp. 22–27.

Civan, F., 2015. Reservoir Formation Damage, third ed. Gulf Professional Publishing, Huston, TX.

Dake, L.P., 2013. The Practice of Reservoir Engineering, vol. 36 Elsevier, Amsterdam, The Netherlands.

Desbarats, A.J., 1995. Upscaling capillary pressure-saturation curves in heterogeneous porous media. Water Resour. Res. 31 (2), 281–288.

Economides, M.J., Nolte, K.G., 1989. Reservoir Stimulation, vol. 2 Prentice Hall, Englewood Cliffs, NJ.

Gray, H.E., 1974. Vertical Flow Correlation in Gas Wells. User Manual for API14B, Subsurface Controlled Safety Valve Sizing Computer Program.

Hale, B., Evers, J.F., 1981. Elliptical flow equations for vertically fractured gas wells. J. Pet. Technol. 33 (12), 2489–2497.

Huang, S., Ding, G., Wu, Y., Huang, H., Lan, X., Zhang, J., 2018. A semi-analytical model to evaluate productivity of shale gas wells with complex fracture networks. J. Nat. Gas Sci. Eng. 50, 374–383.

Huet, C.C., Rushing, J.A., Newsham, K.E., Blasingame, T.A., 2005. A modified purcell/burdine model for estimating absolute permeability from mercury-injection capillary pressure data. In: Presented at the International Petroleum Technology Conference, Doha, Qatar, pp. 21–23 (November).

Jiang, J., Younis, R.M., 2016. Compositional modeling of enhanced hydrocarbons recovery for fractured shale gas-condensate reservoirs with the effects of capillary pressure and multicomponent mechanisms. J. Nat. Gas Sci. Eng. 34, 1262–1275.

Jones, F.O., Owens, W.W., 1980. A laboratory study of low-permeability gas sands. J. Pet. Technol. 32 (9), 1631–1640.

Kamath, J., Laroche, C., 2003. Laboratory-based evaluation of gas well deliverability loss caused by water blocking. SPE J. 8 (01), 71–80.

Lake, L.W., Johns, R.T., Rossen, W.R., Pope, G.A., 2014. Fundamentals of Enhanced Oil Recovery. Society of Petroleum Engineers, Richardson, TX, USA.

Lavrentev, M.A., Shabat, B.V., 1977. Hydrodynamics Problems and Their Mathematical Models. Moscow, Russia.

Lee, J., 1982. Well Testing. Society of Petroleum Engineers, Richardson, TX, USA.

Leverett, M., 1941. Capillary behavior in porous solids. Transactions of the AIME 142 (01), 152–169.

Mualem, Y., 1976. A new model for predicting the hydraulic conductivity of unsaturated porous media. Water Resour. Res. 12 (3), 513–522.

Naik, S., You, Z., Bedrikovetsky, P., 2015. Rate enhancement in unconventional gas reservoirs by wettability alteration. J. Nat. Gas Sci. Eng. 26, 1573–1584.

Naik, S., You, Z., Bedrikovetsky, P., 2018. Productivity index enhancement by wettability alteration in two-phase compressible flows. J. Nat. Gas Sci. Eng. 50, 101–114.

Ni, G., Cheng, W., Lin, B., Zhai, C., 2016. Experimental study on removing water blocking effect (WBE) from two aspects of the pore negative pressure and surfactants. J. Nat. Gas Sci. Eng. 31, 596–602.

Palabiyik, Y., Tureyen, O.I., Onur, M., Deniz, M., 2013. February. A study on pressure and temperature behaviors of geothermal wells in single-phase liquid reservoirs. In: Proceedings of the Thirty-Eighth Workshop on Geothermal Reservoir Engineering.

Parvazdavani, M., Masihi, M., Ghazanfari, M.H., 2014. Monitoring the influence of dispersed nano-particles on oil–water relative permeability hysteresis. J. Pet. Sci. Eng. 124, 222–231.

Pascal, H., Quillian, R.G., 1980. Analysis of vertical fracture length and non-Darcy flow coefficient using variable rate tests. In: SPE Annual Technical Conference and Exhibition. Society of Petroleum Engineers.

Prats, M., 1961. Effect of vertical fractures on reservoir behavior-incompressible fluid case. Soc. Petrol. Eng. J. 1 (02), 105–118.

Shampine, L.F., Reichelt, M.W., 1997. The matlab ode suite. SIAM J. Sci. Comput. 18 (1), 1–22.

Tang, K.T., 2007. Mathematical Methods for Engineers and Scientists, vol. 1 Springer, New York.

Thungsuntonkhun, W., Engler, T.W., 2004. Applying NMR-hydraulic flow unit technique to estimate J-function and capillary pressure. In: Paper SPWLA-2004-EE, Presented at the SPWLA 45th Annual Logging Symposium, Noordwijk, Netherlands, pp. 6–9 (June).

Towler, B.F., 2002. Fundamental Principles of Reservoir Engineering. SPE Textbook Series, (8).
Towler, B.F., Lehr, H.L., Austin, S.W., Bowthorpe, B., Feldman, J.H., Forbis, S.K., Germack, D., Firouzi, M., 2017. Spontaneous imbibition experiments of enhanced oil recovery with surfactants and complex nano-fluids. J. Surfactants Deterg. 20 (2), 367–377.
Tureyen, O.I., Sarak, H., Gulgor, A., Erkan, B., Satman, A., 2014. February. A study on the production and reservoir performance of the Germencik geothermal field. In: Proceedings of the Thirty-Ninth Workshop on Geothermal Reservoir Engineering.
Van Duijn, C.J., Molenaar, J., De Neef, M.J., 1995. The effect of capillary forces on immiscible two-phase flow in heterogeneous porous media. Transport Porous Media 21 (1), 71–93.
Xie, X., Liu, Y., Sharma, M., Weiss, W.W., 2009. Wettability alteration to increase deliverability of gas production wells. J. Nat. Gas Sci. Eng. 1 (1–2), 39–45.
Yuan, B., Wood, D.A., 2015. Production analysis and performance forecasting for natural gas reservoirs: theory and practice (2011–2015). J. Nat. Gas Sci. Eng. (26), 1433–1438.
Yuan, B., Wood, D.A., Yu, W., 2015. Stimulation and hydraulic fracturing technology in natural gas reservoirs: theory and case studies (2012–2015). J. Nat. Gas Sci. Eng. (26), 1414–1421.
Yuan, B., Moghanloo, R.G., Shariff, E., 2016. Integrated investigation of dynamic drainage volume and inflow performance relationship (transient IPR) to optimize multistage fractured horizontal wells in tight/shale formations. J. Energy Resour. Technol. 138 (5).

9. Conclusions

The analytical modelling and laboratory experiments of one-phase transport accounting for chemical reactions, fines detachment, transport and capture, and two-phase transport accounting for capillary end effects in porous media led to the following conclusions:

1. Modelling the reactions of a one-dimensional (1D) nonlinear problem for reactive flow in porous media with large solid deposits allows for an exact solution. This is expressed by implicit formulae for reactants and precipitate concentrations, and for pressure drop across the core.
2. Contrary to the linear problem for reactive flow in porous media, when modelling the reactions with large precipitates, the breakthrough concentrations are not steady-state, and pressure drop across the core varies nonlinearly with time. This allows the extension of the three-point pressure method to the system.
3. The three-point pressure method provides a good match to laboratory data containing three sets of pressure drops and outlet concentration of one species when a non-linear chemical reaction model is used.
4. Identifiability analysis shows that the four model parameters can be determined using any subset of at least two data sets from those used in the laboratory section. Confidence intervals determined for each parameter demonstrate that including outlet concentration data significantly decreases parameter uncertainty. The large parameter uncertainties without using outlet concentration arise due to the inability for the model to distinguish between a set of deposit profiles.
5. Only the product of the formation damage coefficient with the number of released fines can be determined from the pressure drop data using the three-point pressure method applied to fines migration in porous media. It is necessary to determine

these values separately to characterise the system. Therefore, measurements of the additional pressure drop do not substitute the measurements of breakthrough concentrations of the produced fines.

6. A study of the three-dimensional (3D) effects on the laboratory steady-state-transient test (SSTT) was conducted. Of the two investigated inlet distributor geometries, the half-moon inlet distributor exhibits greater 3D effects than the spiral (or concentric-circle) distributor.
7. A laboratory experiment was conducted to validate the SSTT to determine relative permeabilities and capillary pressure. It included a secondary imbibition SSTT procedure followed by a continuous tertiary imbibition. The matched and predicted modelling exhibit high agreement with the experimental data.
8. An exact analytical solution, using conformal mapping, was obtained for the two-dimensional (2D) two-phase flow for well inflow performance with one immobile phase. The solution comprised implicit formulae for saturation distribution and skin factor around a fractured well to account for formation damage due to waterblock.

Recommendations

- Extend analytical solutions for chemical reactions, presented in Chapter 3, and fines migration, presented in Chapter 5, for the case of fractured well, as it was performed in Chapter 8 for two-phase flow towards fractured well.
- Extend the three-point pressure method developed in Chapter 3 for reaction flows and in Chapter 5 for colloidal suspension flows to two-phase flow in porous media. These developments can include steady-state-transient test (SSTT) method, developed in Chapter 7. It can also be performed for JBN method under small capillary end effects. However, significant experimental efforts must be

invested to achieve the result of applying the three-point pressure method to traditional waterflood tests and recommending it for use at industrial scale.